An Experimental Characterization of a High Degree of Freedom Spark-Ignition Engine to Achieve Optimized Ignition Timing Control

by

Robert G. Prucka

A dissertation submitted in partial fulfillment
of the requirements for the degree of
Doctor of Philosophy
(Mechanical Engineering)
in The University of Michigan
2008

Doctoral Committee:

Professor Dionissios N. Assanis, Co-Chair
Research Associate Professor Zoran S. Filipi, Co-chair
Professor Charles W. Kauffman
Gregory L. Ohl, Chrysler LLC

ACKNOWLEDGMENTS

It is impossible to recognize all of the people who have made significant contributions to my research. I would like to acknowledge Professor Dennis Assanis and Professor Zoran Filipi of the University of Michigan. Their guidance and support throughout this process has significantly enhanced my life, both personally and professionally. I am truly thankful that they provided me with the opportunity to continue my engineering education. My fellow lab-mates at the W.E. Lay Automotive Laboratory have made this experience very enjoyable, and their efforts are greatly appreciated.

Funding and technical support for this dissertation was provided by the Chrysler LLC. Specifically, I would like to thank Dr. Gregory Ohl, Denise Kramer, Michael Prucka, Gene DiValentin, Fadi Kanafani, and Roger Vick of Chrysler LLC. Without their exceptional guidance and expertise this project would not have been possible.

My family and friends have given invaluable support and encouragement. They have provided me with a great deal of motivation, and I am very appreciative of their kindness. For my parents, Robert and Marilyn, this dissertation signifies the seventh degree that their three children have earned from the University of Michigan. Finally, I am especially grateful to my wife Tammy for her unconditional support and understanding throughout this difficult process. Go Blue!

TABLE OF CONTENTS

LIST OF FIGURES

LIST OF TABLES

LIST OF APPENDICES

LIST OF ACRONYMS

ABDC	After Bottom Dead Center
AFR	Air-to-Fuel Ratio
ANN	Artificial Neural Network
ATDC	After Top Dead Center
BDC	Bottom Dead Center
BMEP	Brake Mean Effective Pressure
BTDC	Before Top Dead Center
CAD	Crank Angle Degree(s)
CA10	Location of 10% Mass Fraction Burned
CA50	Location of 50% Mass Fraction Burned
CA90	Location of 90% Mass Fraction Burned
CFD	Computational Fluid Dynamics
CLD	Chemi-Luminescence Detector
CMCV	Charge Motion Control Valve
CO	Carbon Monoxide
CO_2	Carbon Dioxide
COV	Coefficient of Variation
DMT	Density Modifier Term
ECU	Engine Control Unit
ETK	Emulator Test Probe
ECL	Exhaust Cam Location
EGR	Exhaust Gas Recirculation

EVC	Exhaust Valve Closing
EVO	Exhaust Valve Opening
FEGR	Fictitious Exhaust Gas Recirculation
FFID	Fast Flame Ionization Detector
FID	Flame Ionization Detector
FMEP	Friction Mean Effective Pressure
HC	Hydrocarbon
H_2O	Water
IBDC	Intake stroke Bottom Dead Center
ICL	Intake Cam Location
IMEP	Indicated Mean Effective Pressure
IMEPg	Gross Indicated Mean Effective Pressure
IMEPn	Net Indicated Mean Effective Pressure
IVC	Intake Valve Closing
IVO	Intake Valve Opening
LPP	Location of Peak Pressure
MAP	Manifold Absolute Pressure
MBT	Maximum Brake Torque
MEP	Mean Effective Pressure
MFB	Mass Fraction Burned
MPS	Mean Piston Speed
NDIR	Non-Dispersive Infra-Red
NO	Nitric Oxide
OF	Overlap Factor
OLV	Overlap Volume
PMEP	Pumping Mean Effective Pressure
RDT	Rapid Distortion Theory

RGF	Residual Gas Fraction
RMSE	Root Mean Squared Error
RPM	Revolutions Per Minute
SAE	Society of Automotive Engineers
SCP	Signal Conditioning Platform
SIS	Spark Ignition Simulation
TDC	Top Dead Center
VCT	Variable Cam Timing
VE	Volumetric Efficiency
VVA	Variable Valve Actuation
VVT	Variable Valve Timing

ABSTRACT

Pressure to improve fuel economy and emissions allows for the introduction of more complex and expensive spark-ignition engine technologies. As engine complexity increases, traditional ignition timing control methods become restrictive, creating a need for new approaches based on analytical techniques and experimental insight. The addition of variable valve actuation and other intake charge motion altering devices provides unprecedented opportunities for improving engine attributes, but poses significant challenges for developing robust control systems. In particular, internal residual fraction and turbulence level vary over a much broader range than in a traditional engine and have a critical impact on combustion. Hence, the goals of this thesis are two-fold. First, new diagnostic procedures that experimentally characterize key combustion parameters are developed. Then, the new information is used to create a universal physics-based ignition timing prediction model valid over a wide range of residual and in-cylinder turbulence levels.

Residual gas fraction is experimentally quantified using several different methods that incorporate fast response emissions analyzers, such as the Fast FID analyzer for unburned hydrocarbons, and a fast NDIR analyzer for CO_2. A technique relying on simultaneous measurement of in-cylinder and exhaust CO_2 concentration is demonstrated, and proves to be the most accurate and reliable. Turbulence intensity is quantified using a newly developed inverse-model of turbulent flame entrainment in conjunction with experimental combustion diagnostics. Experimental findings are subsequently used to generate semi-empirical models for residual fraction and turbulence intensity capable of running real-time within an engine controller.

The newly developed experimental techniques and semi-empirical models enable the development of a physics-based ignition timing control model. The proposed algorithm is loosely based on a well-established turbulent entrainment combustion model, ensuring robust and universal application. The model is divided into two sub-sections; one to predict combustion duration and another for combustion phasing. The duration sub-model predicts the time from ignition to fifty percent mass fraction burned for each operating condition, using an estimated flame entrainment rate, with an RMSE of 2.3 CAD. The combustion phasing sub-model is then used to determine required ignition timing, based on a desired location of fifty percent mass fraction burned.

CHAPTER 1

INTRODUCTION

1.1 Motivation

Continuous global population increase and economic development drives increased demand for energy resources. Consequently, soaring energy demand drives higher energy prices and has the potential to increase global pollution levels. These circumstances place the automotive industry under perpetually increasing social and political pressure to produce cleaner and more fuel-efficient vehicles. However, technologies that enable clean and efficient operation can greatly increase vehicle cost. Vehicle cost increases can outweigh the economic benefits of improved fuel economy and make such improvements undesirable in the marketplace. For these reasons, it is important to maximize the benefit of existing or additional low-cost technologies to produce cleaner vehicles that are also more fuel efficient.

In 2006 over 13.1 million (97%) cars and light trucks sold in the United States where powered by spark-ignition gasoline-fuelled internal combustion engines (Ward's Automotive Yearbook 2007). Worldwide, spark-ignition engines comprise over 50% of the automotive engine market with compression-ignition internal combustion engines being the second most common. Spark-ignition engines have proven to be inexpensive yet they are small, robust, and reliable, making them a prime choice for use as automotive power plants. Internal combustion engines convert chemical energy released from the combustion of fuel and air into mechanical energy that can be used to propel

automobiles. The efficiency with which chemical energy is converted to mechanical energy is directly related to vehicle fuel economy along with several other factors such as vehicle size and weight.

Pressure to improve fuel economy and emissions has paved the way for more complex and expensive engine technologies to enter the market. The addition of mechanical features, such as variable valve timing and charge motion control valves, offer improved engine performance and emissions, but add complexity to engine calibration and control. Individually, most devices influence combustion in a predictable and bearable manor throughout the engine operating range. However, combining several devices on a single engine significantly increases complexity and clouds the influence of each component. While calibration of optimal ignition timing for simple low degree of freedom engines is a well established process, traditional control methods become cumbersome as the number of control actuators increases. For these reasons it is vital to develop engine control algorithms capable of optimally handling these highly complex engine architectures.

Updated control algorithms must be accompanied by new experimental methods that aid in the assessment of added degrees of freedom. Increasing the number of degrees of freedom makes experimental data difficult to interpret and techniques must constantly evolve to enable evaluation new technologies. To properly characterize the impact of new engine technologies on ignition timing, experimental techniques must be developed to quantify changes in combustion. New experimental methods are required to be accurate, economical, and require little engine modification.

To formulate new ignition timing prediction and control strategies it is first important to study their evolution throughout the history of engine development. Innovations in spark timing control have been primarily driven by the continuous need to improve performance, fuel economy, and emissions. The following section provides a historical review of spark timing control for use in internal combustion engines.

1.2 Historical Review of Spark Timing Control

Electrical ignition systems where first used on engines in the 1780's and proved to be highly unreliable (Hardenberg 1999). In 1860 Lenoir developed a system to ignite air and fuel mixtures using a spark (Obert 1968). Lenoir also invented the first spark distributor (Hardenberg 1999). Nikolaus Otto is credited with developing what is now known as the four-stroke spark-ignition in 1876 (Hardenberg 1999). Initially, four-stroke engine combustion was started using a heated rod contained in the combustion chamber. Improvements to spark ignition systems shortly followed the advent of the first gasoline powered engines in 1880's and 1890's. Karl Benz developed the first reliable spark ignition systems to be used on four-stroke engines and is often credited for the invention of the modern spark plug (Hardenberg 1999). Additionally, Nikola Tesla was awarded U.S. Patent Number 609,250 in 1898 for his electrical ignition system. Early spark ignition systems produced fixed spark timing throughout the engine operating range. The preset spark timing was required to provide effective cold starting as well as high power performance. Without spark adjustment, engine versatility was severely compromised. By the 1920's most vehicles contained manual spark advance adjustment using a spark lever mounted on the steering column (Page 1921) greatly improving the useful operating range.

Manual spark control was eventually replaced by mechanical advance systems. Mechanical control systems were developed to compensate for engine speed and load variations. Centrifugal advance mechanisms were located inside the distributor system to vary spark timing with engine speed; shape, weight, and spring rate of the advance system were tailored to each specific application. Mechanical spark adjustment with engine load was controlled by a vacuum advance system. Vacuum spark advance systems were connected directly to the intake manifold. Intake manifold pressure is a strong function of engine load in a spark-ignition engine with a throttle plate.

Mechanical temperature compensation mechanisms were also developed to improve cold engine operation.

In the 1970's mechanical spark timing controls were replaced by electronic systems. The electronic spark timing control allows for greater flexibility than mechanical systems, improving engine emissions, efficiency, power, and responsiveness. Winstead (1977) developed an open-loop microprocessor based ignition timing control strategy. A matrix, or map, of base spark timing with respect to both engine speed and intake manifold vacuum was stored in the controller. In addition to the base spark map, a correction was applied to account for engine coolant temperature variations. Unlike mechanical advance systems, the electronic spark map is capable of capturing highly non-linear engine phenomena. The improved resolution greatly enhances engine performance over the entire operating range, including transients. Open-loop electronic control systems prove to be a great improvement over mechanical setups; however they still cannot adjust to spark adjustment variations brought about by engine aging and production variation.

Schweitzer and Collins (1978) introduced an electronic ignition timing control using closed-loop feedback. Feedback mechanisms for knock and engine torque were used allowing further engine efficiency gains. The control system did not rely on a pre-programmed base spark map; it determined optimum spark timing by continuously advancing and retarding spark while monitoring engine speed. If engine speed increased when ignition timing was moved it was closer to the optimum, and if speed decreased the spark was moving away from the optimum. Closed-loop operation allows spark timing adaption to account for engine aging and variation in production from engine to engine. The system demonstrated fuel economy improvements in the range of 5-30% as compared to cars with mechanical spark control systems. Efficiency gains were large because mechanical systems were often setup with spark timings far retarded from optimum to avoid engine-damaging knock. NOx emissions increased because higher

cylinder pressures were generated by the improved spark timing. Without a pre-programmed base spark timing map the system was subject to large errors during transient operation.

The need to improve engine emissions drives the constant improvement of sensor technologies used for spark timing control. Sensing improvements such as improved engine speed determination (Tang et al. 1994), accurate knock evaluation (Ham et al. 1996), and individual cylinder spark control (Ribbens and Badalament 1997), among others, have added additional accuracy to spark timing control. Ionic current measurement using special spark plugs have been developed to monitor combustion phasing and allow for closed-loop ignition timing control (Shimasaki et al. 2004; Zhu et al. 2007). Ionization current feedback systems are capable of quickly and accurately characterizing combustion conditions such as knock and misfire. The development of production-intent cylinder pressure sensors has also allowed for new ignition timing control strategies (Sellnau et al. 2000; Yoon et al. 2000; Zhu et al. 2003). Closed-loop control is possible using cylinder pressure sensing, but sensor durability and increased cost remain large challenges for this technology. Immense progress in computing technology has also aided the development of new ignition timing control systems.

Engines without a large number of control actuators, such as a fixed cam engine, can be effectively controlled using a feed-forward approach based on engine speed and load with corrections for things such as ambient conditions and knock. Adding control variables (e.g. variable valve timing) greatly complicate the traditional speed/load based spark timing maps. Changes in valve timing may alter combustion in a manner that does not allow for the use of simple correction equations based on traditional control variables (i.e. RPM, MAP, AFR, etc.), and additional spark maps may be required. To address the limitations of speed/load spark timing maps in engines with a high number of control actuators model-based ignition timing predictions techniques have been developed. Model-based techniques predict spark timing real-time within the engine controller using

physical principles; however, the models are simplified to allow for fast execution. Many model-based methods combine physics-based principles with complex empirically determined equations to model the combustion process (Onder and Geering 1995; Lygoe 1998; Bozza et al. 2002; Guerrier and Cawsey 2004; Cavina and Suglia 2005; Suzuki et al. 2006). The level of complexity and the amount of experimental information required for each method varies significantly. Also, artificial neural networks have proved capable of handling complicated interactions caused by the increased number of control actuators found in high degree of freedom engines (Wu et al. 2004; Wu et al. 2005; Hassaneen 2006; Wu et al. 2006).

1.3 Investigative Methodology

A robust spark timing prediction model must be capable of handling all the interactions affecting combustion when the number of control actuators increases. A traditional map-based approach can become restrictive as the number of control actuators increases. Populating a traditional spark map for an engine with a high number of control variables would require that all other actuator set points be established in advance of spark timing. For example, at each operating point strict camshaft timing, charge motion control valve (CMCV) state, throttle position, exhaust gas recirculation (EGR) valve position, etc. combinations would be strictly prescribed prior to optimal spark determination. Such a methodology may restrict the use of adaptive, or intelligent, engine control strategies.

While certain aspects of engine control (e.g. variable valve timing, air mass estimation, etc.) may be handled by neural networks or other methods, ignition timing prediction requires special treatment due to complex interactions with multiple engine variables and possible departure from design conditions. Ignition timing prediction is required to be done somewhat independently of other engine variables to achieve desired

engine output characteristics (i.e. high efficiency, exhaust gas temperature control, emissions constraints, knock suppression, etc.). In addition, the nature of artificial neural networks and other methods using complex equation fitting do not allow flexibility to make adjustments to a single aspect without complete retraining. For these reasons, it is desirable to develop compact physical models suitable for controlling ignition timing prediction in high degree of freedom engines.

The objective of this thesis is to develop new diagnostic techniques that experimentally characterize key combustion parameters and then use the new information to create a universal physics-based ignition timing prediction model that is suitable for high degree of freedom engine applications. Specifically, the influence of new technologies on turbulence intensity and residual gas fraction will be quantified using a combination of direct experimental measurements and data processing routines. Experimental results will be used to generate semi-empirical models for each parameter that are capable of running real-time within an engine controller. The new input parameters of turbulence intensity and residual gas fraction are then used by a simplified physics-based combustion model to predict ignition timing.

Relating each technology to specific combustion-controlling characteristics facilitates the creation of new ignition timing prediction algorithms. Focus on the experimental measurement of residual gas fraction and turbulence intensity is of interest because both parameters can alter drastically on engines equipped with variable valve phasing or charge motion control valves. Residual gas fraction is quantified experimentally using several different methods that incorporate fast response emissions analyzers. All methods are simultaneously measured to allow for direct comparison of accuracy and variability. Turbulence intensity is quantified using a newly developed inverse-model in conjunction with experimental data. The developments of experimental techniques that quantify residual gas fraction and turbulence intensity are key enablers for the introduction of physics-based combustion models for ignition timing control.

Formulating new spark timing control algorithms that accommodate a wide range of new engine technologies requires new focus on the fundamental principles of spark-ignition engine combustion. A commonly used spark-ignition engine combustion model that incorporates many aspects of spark-ignition engine combustion is used as a starting point and subsequently tailored for this purpose. The combustion model was developed by Tabaczynski et al. (1977), and it introduced the concept of turbulent flame entrainment. The model is capable of capturing the effects of flame/wall interaction, global turbulence level and the residual gas fraction on burn rate. The model was validated against experimental data and extensively used for combustion chamber design and engine system studies (Filipi and Assanis 1991; Filipi 1994; Filipi and Assanis 2000). The new spark timing prediction algorithm developed in this thesis is loosely based on the turbulent entrainment combustion model.

1.4 Dissertation Outline

The dissertation is composed of seven Chapters. Chapter 2 describes the experimental setup and data analysis techniques used to acquire engine data. Chapter 3 exposes, with experimental data, the challenge of ignition timing prediction in a high degree of freedom engine. The shortcomings of previous research on the subject are discussed and the new methodology based on a turbulent flame entrainment combustion model is introduced. The fourth Chapter focuses on residual gas fraction measurement and prediction for the purpose of calculating laminar flame speed. Several residual gas fraction measurement methods are developed and compared for accuracy and feasibility. Chapter 5 describes the experimental and analytical techniques used to quantify turbulence intensity over a wide range of operating conditions. The new spark timing prediction model is developed and validated in Chapter 6 using the methods and data

discussed in Chapters 3-5. Finally, conclusions and future recommendations are given in Chapter 7.

CHAPTER 2

EXPERIMENTAL SETUP AND DATA ANALYSIS

2.1 Test Engine Description

A 2.4L inline four cylinder engine was used to acquire experimental data for this project. Engine specifications are given in Table 2.1, Table 2.2, and Table 2.3. The engine has a dual overhead camshaft layout with 4 valves per cylinder (2 intake and 2 exhaust). The aluminum cylinder head has a pent-roof style combustion chamber with a center mounted sparkplug, as shown in Figure 2.1. Aluminum pistons have a shaped crown with machined recesses for the intake valves (Figure 2.2). The end cylinders (1 and 4) have the same relative crankshaft orientation and are 180˚ out of phase with the center cylinders (2 and 3); firing order is (1-3-4-2). Two balance shafts are chain-driven off of the crankshaft and are located in the oil pan beneath the crankshaft on the front of the engine. Exhaust system layout consists of four separate runners combining into a single collector at the same location.

Engine load is controlled by an electronic throttle plate. Fuel is injected into the intake port by a single fuel injector located in each intake runner. Upstream of the fuel injectors in the intake manifold is a charge motion control valve (CMCV). The CMCV is designed to generate high levels of charge tumble within the cylinder. Activating, or blocking, the CMCV reduces intake manifold flow area by approximately two thirds.

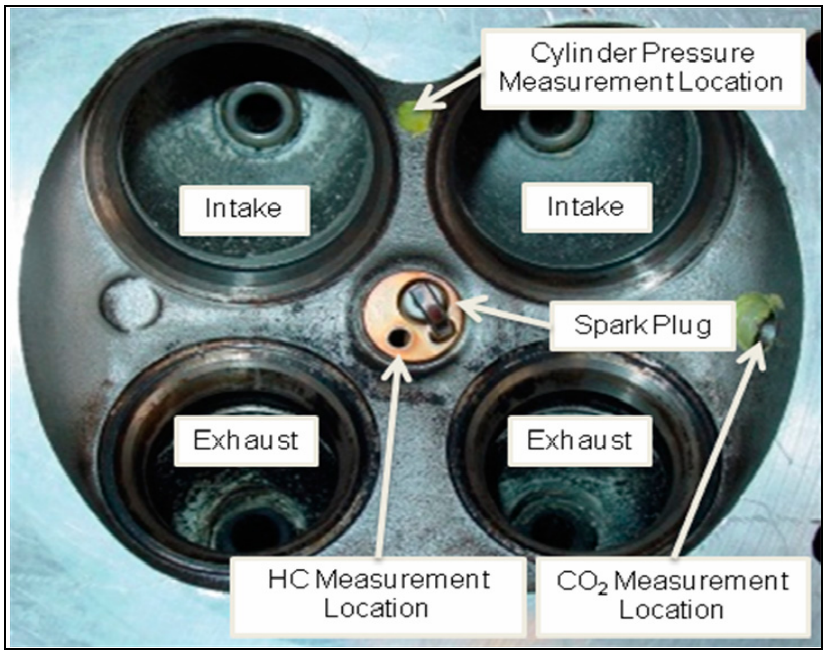

Figure 2.1: The pent-roof combustion chamber with two intake valves (top), two exhaust valves (bottom), and a central-mounted sparkplug.


Figure 2.2: The piston is crowned with valve reliefs cut for each intake valve. This piston is shown at top dead center (TDC) location.

The Engine Control Unit (ECU) is equipped with an ETAS ETK (Emulator Test Probe) which allows the engine to be recalibrated through the use of INCA software. Engine parameters such as camshaft position, throttle location, injector pulse width,

ignition timing, etc., are accessible using the ETAS hardware and software. The software allows access to all engine variables for monitoring and data acquisition during engine operation. 2.4 liter I-4 Intake Valve Parameters

Table 2.1: 2.4 liter I-4 test engine specifications

Number of Cylinders	4
Cylinder Arrangement	Inline
Total Displacement	2429 cm^3
Firing Order	1-3-4-2
Compression Ratio	9.4:1
Bore	87.5 mm
Stroke	101.0 mm
Bore/Stroke	0.866 (under-square)
Connecting Rod Length	151 mm

Table 2.2: 2.4 liter I-4 Intake Valve Parameters

Number of Intake Valves	2
Intake Valve Head Diameter	34.8 mm
Intake Valve Stem Diameter	6 mm
Maximum Intake Valve Lift	8.25 mm
Intake Valve Duration (0.15 mm lift)	244 CAD
Intake Valve Opening Range (0.15mm lift)	-41 to 19 (°ATDC gas exchange)
Intake Valve Closing Range (0.15mm lift)	203 to 263 (°ATDC gas exchange)

The test engine is equipped with a hydraulically activated dual-independent variable valve phasing mechanism. Variable valve phasing systems shift camshaft location with respect to the crankshaft. Valve duration and lift of the camshaft are not altered when the camshaft is moved; only the relative phasing of valve events with respect to piston motion change. Intake and exhaust cam location, ICL and ECL respectively, are defined as the number of crank angles between gas exchange TDC and the valve lift centerline. Valve lift centerline is defined by the crank angle of maximum valve lift. The maximum ranges of both ICL and ECL are illustrated in Figure 2.3.

Intake valve opening (IVO) and closing (IVC) occur 120° before and 124° after ICL respectively (valve timings are reported at 0.15mm lift). Exhaust valve opening (EVO) occurs 120° before and exhaust valve closing (EVC) 127° after ECL.

Table 2.3: 2.4L I-4 Exhaust Valve Parameters

Number of Exhaust Valves	2
Exhaust Valve Head Diameter	30.5
Exhaust Valve Stem Diameter	6 mm
Maximum Exhaust Valve Lift	6.60 mm
Exhaust Valve Duration (0.15 mm lift)	247 CAD
Exhaust Valve Opening Range (0.15mm lift)	-194 to -254 (°ATDC gas exchange)
Exhaust Valve Closing Range (0.15mm lift)	51 to -7 (°ATDC gas exchange)

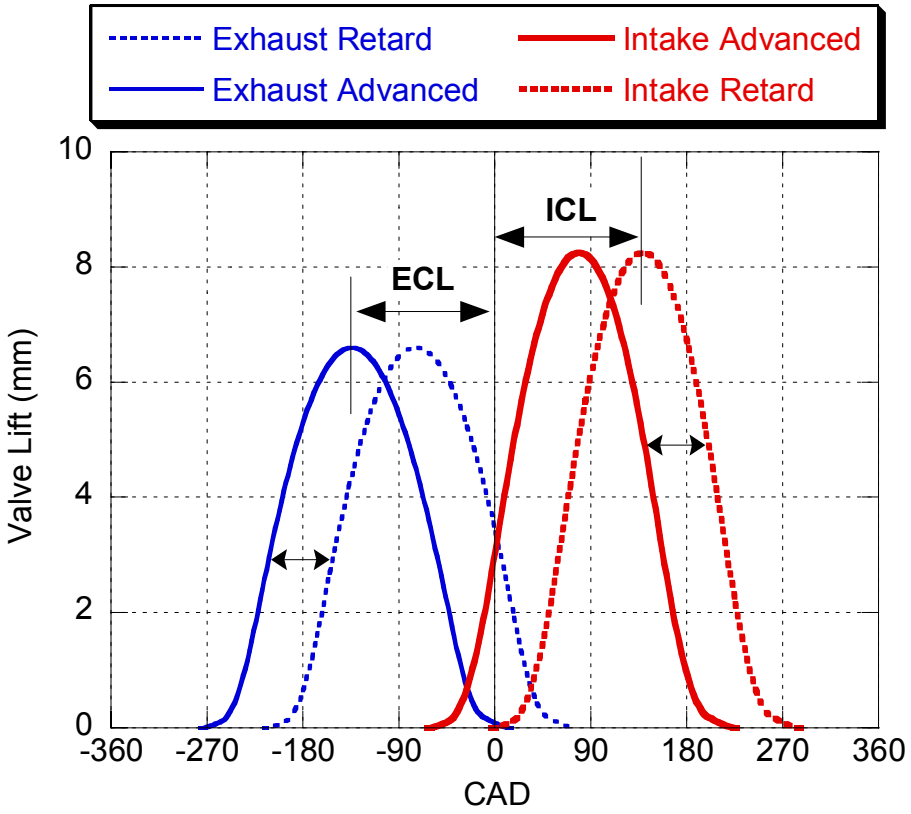

Figure 2.3: Intake and exhaust camshaft location is reported from centerline location to TDC of gas exchange.

2.2 Experimental Test Cell Setup

A Westinghouse 200hp DC dynamometer is used to absorb power and regulate engine speed. A Dyne Systems DYN-LOC IV is used for dynamometer control. Engine torque is measured using a Lebow Products load cell (200lbs maximum) attached to lever arm on the dynamometer shell. Calibration weights are used to calibrate engine torque prior to testing. Dynamometer speed is measured using a Hall-effect type sensor that reads in 6° intervals.

The test engine is coupled to the dynamometer using a DynoTech torsional damper assembly. The DynoTech system utilizes a solid driveshaft coupled to a special flywheel equipped with a damping system. Use of the damping system ensures proper engine speed control from 800 to 10,000 RPM, without oscillations arising from the engine-dynamometer coupling natural frequency.

Engine and coolant and oil temperatures are controlled using shell and tube heat exchangers containing tap water. Regulation of water flow rate through the heat exchangers is achieved using Omega CN76000 temperature controllers to activate solenoid valves. Coolant flow rate was calculated from a measured pressure drop across at venturi-style flow meter.

A Pierburg fuel system is used for fuel conditioning. The Pierburg system controls fuel pressure and temperature. Fuel flow rate is measured with a Pierburg PLU 103A positive displacement flow meter. Fuel flow rate along with the exhaust lambda sensor output are used to calculate total air flow rate into the engine. A Bosch broad-band lambda sensor unit with an ETAS LA3 controller measured exhaust lambda. Indolene fuel was used for all measurements. Paragon Laboratories, Inc. analyzed a fuel sample; analysis results are given in Table 2.4.

Table 2.4: Indolene fuel analysis results determined by Paragon Laboratories Inc.

Chemical Composition	$C_{1.0}\,H_{1.762}\,O_{0.0}$
Research Octane Number	97.4
Motor Octane Number	88.3
Density	0.7493 g/mL
Lower Heating Value (Q_{LHV})	43.346 MJ/kg

All temperature measurements are made with K-type thermocouples. Each thermocouple is calibrated with an OMEGA CL950 Hot Point Cell calibration unit. Special shielded probes are used to measure exhaust gas temperature. The exhaust gas temperature probes are surrounded by a radiation shield to reduce measurement errors produced by high heat transfer. Temperature sensor locations are shown in Figure 2.4.

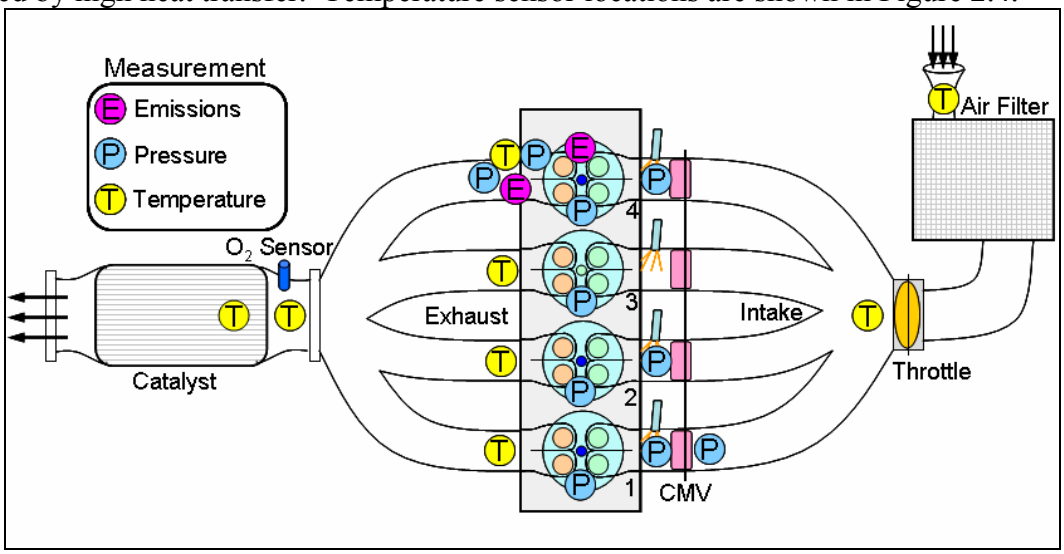

Figure 2.4: Sensor measurement locations on the 2.4L Chrysler test engine

2.2.1 Data Acquisition Systems

Engine data is collected on both a cycle-resolved and time-basis by two separate data acquisition systems. Cycle-resolved measurements, such as cylinder pressure, are collected by a Tektronix VXI-MXI-2 16-bit/16 channel system. The Tektronix system is linked to National Instruments LabVIEW program for data viewing and analysis. Time-resolved measurements (e.g., temperature and flow rates) are collected by a University of Michigan built 48-channel data acquisition system. Each channel has an isolation

module specific to the measured variable. Measured signals are transmitted to an in-house-developed National Instruments LabVIEW program. If required, MATLAB routines are written for additional post-processing.

Cycle-resolved measurements are recorded once per crank-angle degree. A Kistler Type 2612 crank encoder, mounted on the front of the crankshaft, provides the clock signal for measurement. All four combustion chambers are instrumented with Kistler Type 6052B piezo-electric passage mounted transducers. The cylinder pressure measurement passage is located between the intake valves; the location is visible near the top of Figure 2.1. Cycle-resolved intake and exhaust pressure measurements were made by a series of Kistler Type 4045A2 piezo-resistive transducers (See Figure 2.4). A special cooling adapter (Kistler Type 7511) is used to manage the exhaust sensor temperature. The piezo-resistive manifold transducers are used for cylinder pressure referencing (See Section 2.3.2) and flow calculations. All Kistler sensors are transmitted through a Kistler Signal Conditioning Platform (SCP) that contains and array signal conditions and charge amplifiers specific for each application.

2.2.2 Cycle Resolved Emissions Measurement

Exhaust port and in-cylinder CO_2 concentrations are acquired using Cambustion NDIR500 fast response analyzers. The sample probes use a non-dispersive infra-red (NDIR) technique to detect wet molar fractions of both CO and CO_2 concentration with a very fast response-time. Standard NDIR CO/CO_2 analyzers use a system to filter water from the sample gases prior to measurement (dry basis) to avoid overlap with the IR absorption ranges of CO and CO_2. The NDIR500 uses a special filter system to measure both CO and CO_2 on a wet basis (the sample contains water). A 10-90% response time on the order of 6 ms (Sutela et al. 1999) is achieved by significantly modifying the standard NDIR detector. Specific details pertaining to the NDIR measurement technique

are found in (Heywood 1988; Sutela et al. 1999; Sutela et al. 2000; Hands et al. 2001; Iizuka et al. 2004; Davis and Peckham 2006)

The Cambustion NDIR500 instrument consists of two sample probes. One sample probe is configured for in-cylinder measurement, while the second probe is used for exhaust gas measurement in the exhaust port. The probes are configured to provide high accuracy for the specific conditions at each measurement location. NDIR measurement accuracy is dependent upon the overall pressure level within the sample chamber as well as the level of pressure fluctuation. In general, higher sample chamber pressures with low pressure fluctuation provide the most accurate species concentration reading (Sutela et al. 2000). The exhaust port mounted probe is configured with a higher sample chamber pressure than the in-cylinder probe for higher accuracy. Sample chamber pressure for the in-cylinder NDIR sample probe must be maintained lower than manifold absolute pressure (MAP) to ensure that sample flow into the probe does not reverse during the intake stroke. The in-cylinder NDIR chamber volume is expanded by 2.5L to dampen pressure fluctuations which induce measurement error. Specific set points for each of the sample probes are given in Table 2.5.

Table 2.5: Cambustion NDIR500 CO/CO2 Configuration

	Exhaust Probe	In-Cylinder Probe
Chamber Pressure	550 mbar	200 mbar
Sample Probe I.D.	1.07 mm	0.41 mm
Sample Probe Temperature	120°C	120°C
Sample Chamber Temperature	150°C	150°C
Filter Wheel Speed (RPM)	15,000	20,000

In-cylinder and exhaust port hydrocarbon concentrations are measured on a crank-angle resolved basis using a Cambustion HFR500 fast response flame ionization detector (FID). Each measurement probe has a 10-90% response time on the order of 1.5 ms. A 2.5L expansion volume is added to the in-cylinder measurement probe to dampen

pressure fluctuations in the sample chamber. Measurement settings for each measurement location are given in Table 2.6. In-cylinder samples are measured through the body of a specially designed Kistler sparkplug with an offset central electrode. Calibration of the in-cylinder probe is done with a span gas containing 40,000 ppm propane (C_3H_8) with the balance comprised of N_2.

Table 2.6: Cambustion HFR500 FID Configuration

	Exhaust Probe	In-Cylinder Probe
Sample Probe I.D.	1.07 mm	0.33 mm
FID Chamber Pressure	500 mbar	440 mbar
CP Chamber Pressure	590 mbar	530 mbar
Sample Probe Temperature	235°C	235°C
Sample Head Temperature	150°C	150°C

A FID measures HC concentration by counting the number of carbon atoms found in a hydrocarbon sample. The actual hydrocarbon composition is not measured therefore the carbon to hydrogen ratio and average number of carbon atoms per hydrocarbon molecule must be determined by a different means. Fuel properties are used for in-cylinder measurement, and a smaller molecular composition is usually assumed for exhaust hydrocarbons.

2.3 Data Processing Routines

2.3.1 Engine Performance Parameters

Several common indicators are used throughout this report to quantify engine performance. Data that is independent of engine design and configuration is used where possible to allow comparison with future work using different engines. Parameters that quantify engine load, combustion variability and fuel efficiency are described in the following sections.

Mean Effective Pressure

The primary metric used to determine engine load is mean effective pressure (MEP). Mean effective pressure allows for comparison between engines having different displaced volumes because larger engines generally produce more torque than smaller engines. The mean effective pressure is defined as work per cycle divided by displaced volume, yielding a value with units of pressure, and is calculated by integrating cylinder pressure versus volume (P-V) data. Numerical integration of the P-V data is done in LabVIEW using the midpoint rule. Analysis of cylinder pressure is done using three indicated mean effective pressure metrics; gross, net, and pumping (See Figure 2.5). The gross mean effective pressure, IMEPg, calculated using only the compression and expansion strokes of the cycle. Net indicated mean effective pressure, IMEPn, is the IMEP of the entire 4-stroke cycle. The difference between the net and gross IMEP values is called the pumping mean effective pressure or PMEP.

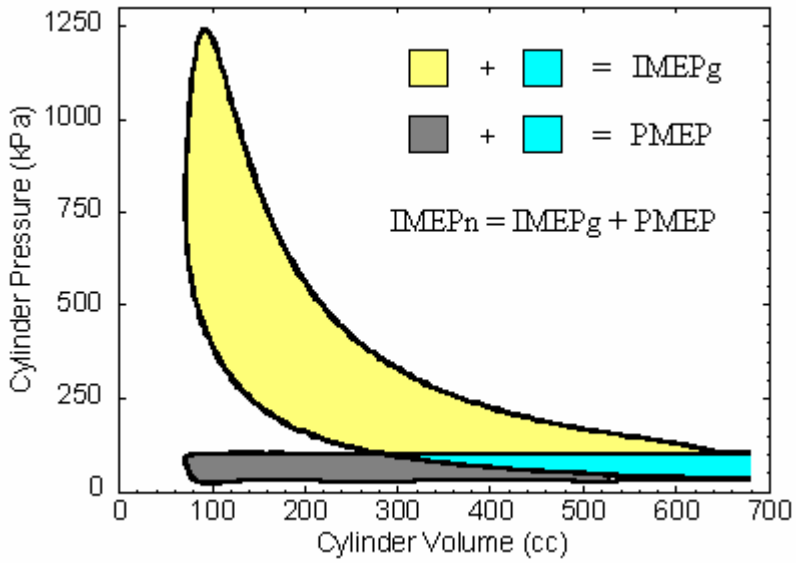

Figure 2.5: IMEP is calculated by integrating the pressure versus volume data over specific intervals. Clockwise loops yield positive work and counter-clockwise loops give negative work.

Indicated mean effective pressures represent the thermodynamic work available to the engine. The actual work output from the engine is less than the indicated value due to

losses from friction. The engine output work quantified using brake mean effective pressure (BMEP) using Equation (2.1). The difference between BMEP and IMEPn represents the amount of work lost to friction, also known as the FMEP.

$$BMEP = \frac{4\pi T}{100{,}000\, V_d} \tag{2.1}$$

Where: BMEP has units of bar

T = engine torque in N-m

V_d = displaced volume expressed in m^3

Coefficient of Variance of IMEP

Cycle-to-cycle variability is directly related to the drivability and harshness of an engine. For this reason, it is important to quantify the amount of cycle-to-cycle variability created at certain operating conditions. A common measure of cycle-to-cycle variability is the coefficient of variance of IMEP or COV_{IMEP}. COV_{IMEP} is defined as the standard deviation of IMEPn values from a sample set divided by the average IMEPn from that same set. There is not a standard regarding acceptable levels of COV_{IMEP}, however levels below 10% are generally considered acceptable (Heywood 1988).

Brake Specific Fuel Consumption

The brake specific fuel consumption (bsfc) is a measure of engine efficiency; it quantifies the amount of fuel used over a given time to generate one unit of power. Brake specific fuel consumption is reported with the units g/kW-hr using Equation (2.2) In general, lower values indicate more efficient operation.

$$bsfc = \frac{3600\, \dot{m}_{fuel}}{Power} \tag{2.2}$$

Where: $\dot{m}_{fuel}$ is the fuel flow measured in grams per second (g/s)

Power is expressed in units of kilowatts (kW)

2.3.2 Cylinder Pressure Data Processing

Accurate processing of cylinder pressure data is a critical step in quality data analysis. Two critical processing steps involve phasing the cylinder pressure data with cylinder volume and determination of the absolute pressure level. Randolph (1990), Kuratle and Marki (1992), Davis and Patterson (2006), and others have identified the magnitude and impact of such errors. Their data suggests proper phasing of cylinder pressure with cylinder volume is critical to accurate determination of location of peak pressure (LPP), mean effective pressures (MEP), and compression and expansion ratios of specific heats. Pressure level referencing of piezo-electric transducers is required since the transducers only measure changes in pressure, not absolute pressure. For this reason the piezo-electric sensor must be referenced, or pegged, to a known pressure at some point in the thermodynamic cycle.

Phasing of cylinder pressure to cylinder volume can be achieved through several methods. Davis and Patterson (2006) suggest using a top dead center (TDC) sensor to be the most accurate and robust method of phasing. However, at TDC sensor was not available for this work, so a method using a thermodynamic loss angle was used. The thermodynamic loss angle is defined as the number of crank angle degrees prior to true TDC that peak motoring cylinder pressure occurs. Peak motoring pressure occurs prior to TDC due to heat transfer, blow-by, and valve leakage during the compression stroke. In this case a loss angle of 0.5° BTDC is assumed for all engine speeds. Since the crank angle encoder only has a single degree resolution the true location of peak pressure is determined by fitting a curved to five measurement points on either side of peak pressure. The actual loss angle will vary from one engine condition to the next depending upon the characteristics of heat transfer and mass loss mechanisms at each point. The error

produced by assuming a constant thermodynamic loss angle is on the order of one degree. Both Kuratle and Marki (1992) along with Davis and Patterson (2006) indicated an IMEP calculation error of about 4% for every degree of phasing error.

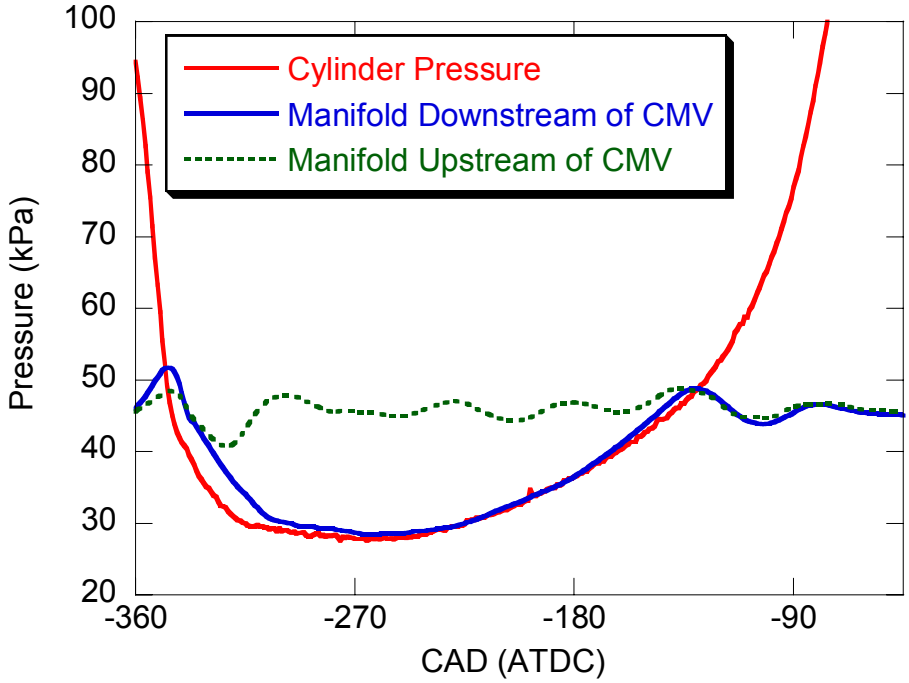

Figure 2.6: Cylinder pressure is referenced using the manifold pressure sensor downstream of the CMCV at BDC. Significant referencing errors can occur if cylinder pressure is referenced with a sensor located upstream of the CMCV.

Cylinder pressure referencing is performed using a Kistler 4045A2 pressure transducer placed close to the intake valve in the intake manifold. Randolph (1990) found that referencing cylinder pressure to manifold pressure at inlet bottom dead center (IBDC) was the most accurate technique available. This method relies on the assumption that flow velocity across the intake valve is zero at BDC; therefore pressure drop across the intake valve is zero. The manifold pressure transducer in the test engine was placed after charge motion valve (CMCV) and before the intake valve. There exists a significant pressure drop across the CMCV during the intake stroke, so proper transducer location is critical to accurate cylinder pressure referencing. Figure 2.6 shows measured pressure both upstream and downstream of the CMCV. Note that large pressure referencing errors

could occur if the transducer upstream of the CMCV were used as a reference. To minimize the affect of signal noise the measured values on either side of the IBDC for both the manifold and cylinder pressure were averaged prior to referencing.

Accurate pressure referencing allows extraction of additional information from cylinder pressure, specifically, compression and expansion ratios of specific heats. Some pressure referencing techniques require an assumed value of the ratio of specific heats during compression; however the technique employed in this work allows the ratio to be calculated and variable. Ratio of specific heat values will be used for various residual fraction calculation techniques discussed in this work.

2.3.3 Heat Release Analysis

Performing accurate heat release calculation using cylinder pressure data is an extremely important step in data analysis. Heat release data provides many useful insights into engine emissions, heat transfer, combustion efficiency, burn rates, along with many other important parameters. A good heat release calculation program will accurately account for the many different heat and mass transfer mechanisms that occur during an engine cycle. If many of the heat and mass transfer phenomena are well modeled, the First Law of Thermodynamics can be used to solve for the amount of chemical energy released due to combustion on a crank-angle basis.

Combustion analysis from cylinder pressure measurements has been developed extensively. Rassweiler and Withrow (1938) first developed a relatively simple method to calculate mass fraction burned profiles from cylinder pressure. Their method, which is still used today, provides reasonable results however it does not explicitly calculate heat release. Krieger and Borman (1966) later developed both single and dual- zone detailed heat release models. Gatowski et al. (1984) reported a simplified single-zone heat release model. The simplified model developed by Gatowski accounts for all major heat and

mass transfer mechanisms and shows reasonable accuracy when compared to the amount of fuel energy present in the cylinder.

The heat release equation is derived from the first law of thermodynamics. The basic differential form of the first law is derived by applying conservation of energy to an engine combustion chamber using an open-system single zone control volume. The final form of the first law that describes rate of heat release on a crank-angle basis is given in Equation (2.3) (Depcik et al. 2006). This derivation of the heat release equation accounts for internal energy, work, and heat transfer to and from the cylinder. Heat and mass transfer mechanisms that account for crevice flows and blow-by are neglected for simplicity.

$$\frac{dQ_{released}}{d\theta} = m_{total}\left[\frac{R}{\gamma - 1}\right]\left(\frac{dT}{d\theta}\right) + P_{cylinder}\left(\frac{dV}{d\theta}\right) + \frac{dQ_{Heat\,Transfer}}{d\theta} \tag{2.3}$$

Heat transfer between in-cylinder gases and the cylinder walls is modeled assuming convection heat transfer is the dominate mechanism. Radiation heat transfer becomes significant when soot generation is high, such as in compression ignition engines, and it is generally neglected in spark-ignition engines. Equation (2.4) represents the rate of convection heat transfer during the cycle. Surface area, heat transfer coefficient and average cylinder temperature are all computed on a crank-angle basis. Cylinder wall temperature is assumed constant during combustion. The surface area is continuously changing as the piston travels in the cylinder, and is related to crank angle by using the crank-slider equation. The heat transfer coefficient is averaged over the entire surface area of the cylinder, and is determined using experimental correlations. Several heat transfer correlations have been developed for internal combustion engines. The correlation developed by Hohenberg (1979), Equation(2.5), was found to be suitable for calculation in the test engine.

$$\frac{dQ_{Heat\,Transfer}}{d\theta} = A_{surface}\, h_{average}^{Hohenberg}\left(T_{cylinder} - T_{wall}\right) \tag{2.4}$$

$$h_{average}^{Hohenberg} = 3.26\left(V_{cylinder}^{-0.06}\right)\left(P_{cylinder}^{0.8}\right)\left(T_{cylinder}^{-0.4}\right)\left[\left(Sp + 1.4\right)^{0.8}\right] \tag{2.5}$$

The instantaneous ratio of specific heats, γ, is calculated as a function of in-cylinder species composition and average temperature. Species concentrations at each crank angle are calculated assuming complete combustion of burned gases. The constant pressure specific heat for each species is calculated as a function of temperature using correlations given by Sonntag (1998). Average in-cylinder gas temperature is calculated using the ideal gas law at each crank angle. The gas constant is calculated at each crank angle degree, as it is a function of species composition. The ratio of specific heats for the entire mixture is the mass-weighted average of the ratio for each chemical species, and is determined on a crank-angle basis.

Integrating heat release rate from Equation (2.3) yields total heat release as a function of crank-angle. Normalizing the total heat release curve by its maximum generates a mass-fraction-burned (MFB) profile. For consistency, the maximum heat release value is defined as the point where heat release rate drops to zero. This definition of maximum total heat release location provides consistent combustion parameter values by reducing the affects of noise within experimental data. The affect of signal noise is generally amplified when a noisy signal is differentiated.

With an accurate heat release model the total heat release at the end of combustion will reflect the total fuel energy available minus the heat lost by combustion inefficiency. Normalizing the total heat release curve by the value at the end of combustion generates a MFB profile based on the total mass that actually burns in the cylinder; energy lost due to combustion inefficiency is not reflected in the MFB profile. Combustion parameters, such as 10, 50, and 90 percent burned locations, are determined

directly from the MFB profile. The previously described heat release analysis method is used throughout this document.

2.4 Engine Test Point Description

Data was acquired over a large range of operating conditions to ensure that newly developed models were robust. Engine data is divided into two sets; one set for operating with the CMCV unblocked (non-active), and a separate set for blocked (activated) CMCV operation. The range engine speeds and loads tested for each CMCV activation state are shown in Figure 2.7. Engine speed was limited to 4000 RPM due to mechanical constraints of the dynamometer. In addition to engine speed and load variation, spark timing, air-to-fuel ratio along with valve overlap duration and centerline were varied at several operating conditions. Valve overlap duration was varied from -20° to +40° (crank angle degrees). Overlap centerline location was varied by 20° to either side of gas exchange top dead center.

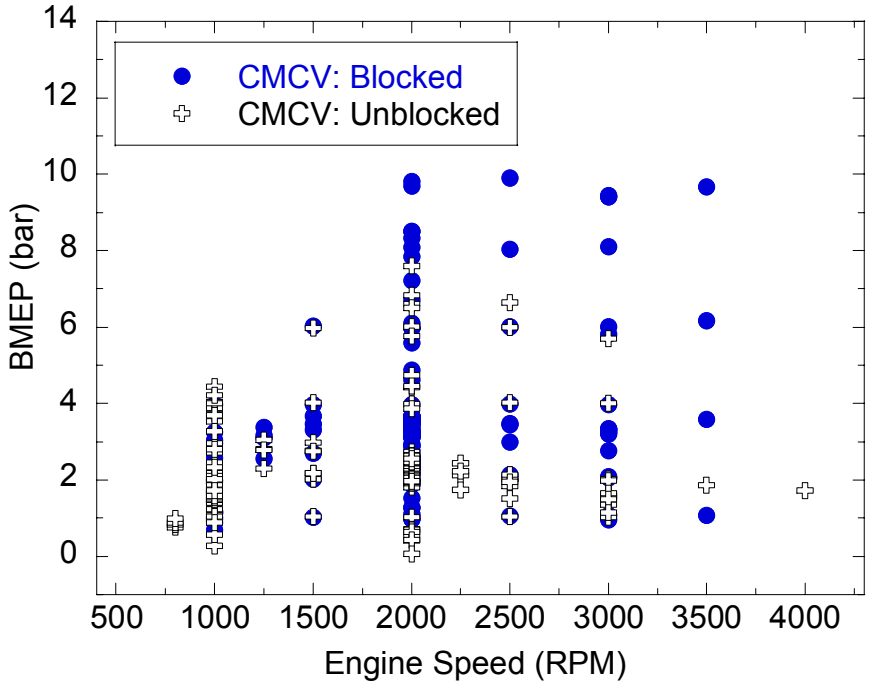

Figure 2.7: Engine speed and load operating conditions for experimental testing.

CHAPTER 3

THE CHALLENGE OF IGNITION TIMING PREDICTION IN A HIGH DEGREE OF FREEDOM ENGINE

Control strategies to predict required spark timing in a fixed cam engine considering engine speed, load, ambient conditions, and equivalence ratio are well established. Often, these strategies can be developed experimentally with little need to consider combustion fundamentals. For example, a base ignition timing surface can be generated over the entire engine speed/load range and corrections for ambient conditions and air-to-fuel ratio can be applied to the base value. The number of control actuators is small enough in this case so the full experimental characterization of each operating point is feasible. However, the number of possible actuator set-point combinations at a given engine speed and load increases dramatically when new control devices are added to the system. The test engine is equipped such that there are twenty-nine thousand actuator set-point combinations available at any given engine speed, load, and air-to-fuel ratio. Experimental characterization of each combination to generate optimal ignition timing maps is not feasible over the time period of a normal product development cycle.

To characterize a high degree of freedom engine for the purpose of developing an accurate ignition timing prediction model the fundamental processes impacting engine operation must be well understood. Every new control actuator can influence combustion in a specific manner, but the influence is not always unique to a single device.

Individually, certain devices will influence combustion in similar ways; however, combining several technologies may produce complicated interactions that are not easily discernable. To investigate complicated systems each actuator is first isolated and then its fundamental impacts on combustion are quantified. After each device is characterized it can be incorporated in an ignition timing prediction model that is based on fundamental combustion principles.

The following Chapter introduces the observed combustion characteristics of a high degree of freedom engine under a variety of operating conditions using several examples. Previous attempts to address control of high-content engines are then discussed and evaluated for implementation feasibility. Finally, based upon observed combustion trends and previously developed methods a new framework for ignition timing prediction is proposed.

3.1 Combustion Trends in a High Degree of Freedom Engine

The need to develop model-based ignition timing algorithms can be seen by examining a small slice of the engine operating range. The data in Figure 3.1 illustrates the challenge and importance of being able to predict the desired spark timing for any possible actuator set-point configuration. The combustion durations (10 to 90% MFB) in Figure 3.1 represent only a small fraction of the possible actuator set-point combinations at a single engine speed and intake manifold pressure. The data shows large differences in combustion duration from one set-point to another for a similar torque output. For example, at approximately 2.5 bar BMEP the combustion duration can vary over twelve crank angle degrees depending upon actuator configuration.

The wide range of combustion durations observed in Figure 3.1 were generated by altering charge motion control valve (CMCV) activation state in combination with intake and exhaust cam phasing. Each technology can be used to increase or decrease

combustion duration at any operating point. A brief introduction to the influence of each technology on combustion is provided in the following sections.

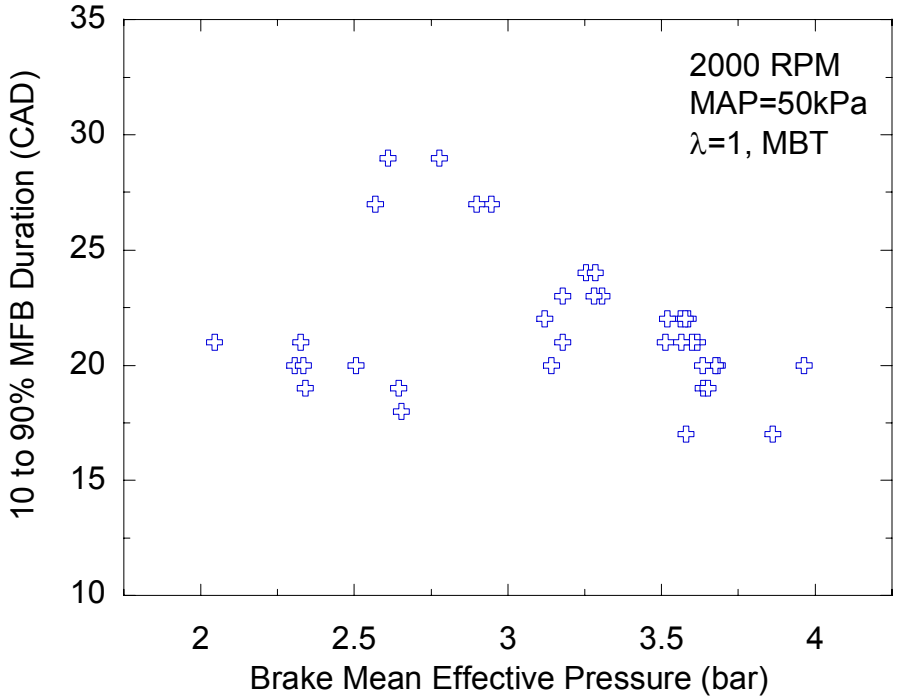

Figure 3.1: For a given engine speed and intake manifold pressure there are many possible actuator set-point configurations that produce similar torque output; however, they also yield a wide range of combustion durations.

3.1.1 Charge Motion Control Valve

Technologies that alter in-cylinder flow by means other than valve timing and valve lift are commonly referred to as Charge Motion Control Valves (CMCV). Charge motion control valves are generally placed in the intake system near the intake valves. The most common types of CMCV use specially shaped throttle-plate-like devices to either redirect flow within the intake ports or to disable/enable one intake port (Russ et al. Part 1: 1999; Russ et al. Part 2: 1999; Jung et al. 2004). Some systems combine intake port valves with a single specially designed intake port to change charge motion (Goldwitz and Heywood 2005). Charge motion devices are used to improve combustion

at operating conditions where high residual fraction and/or low charge motion occurs, such as low engine speed and load.

Russ and coworkers (Part 1: 1999) used a CMCV in an engine with a single intake valve. The charge motion valve blocked approximately three-quarters of the intake tract just prior to the cylinder head. It was found that the valve increases burn rate and decreases cycle-to-cycle variability significantly. Similar results were reported by Jung et al. (2004) as well as Goldwitz and Heywood (2005). NOx emissions did not change when the valve was used, so Russ concluded that residual fraction was not altered by the valve. Lower HC emissions were observed using the motion control valve, which was attributed to improved air and fuel mixing (Russ et al. Part 2: 1999).

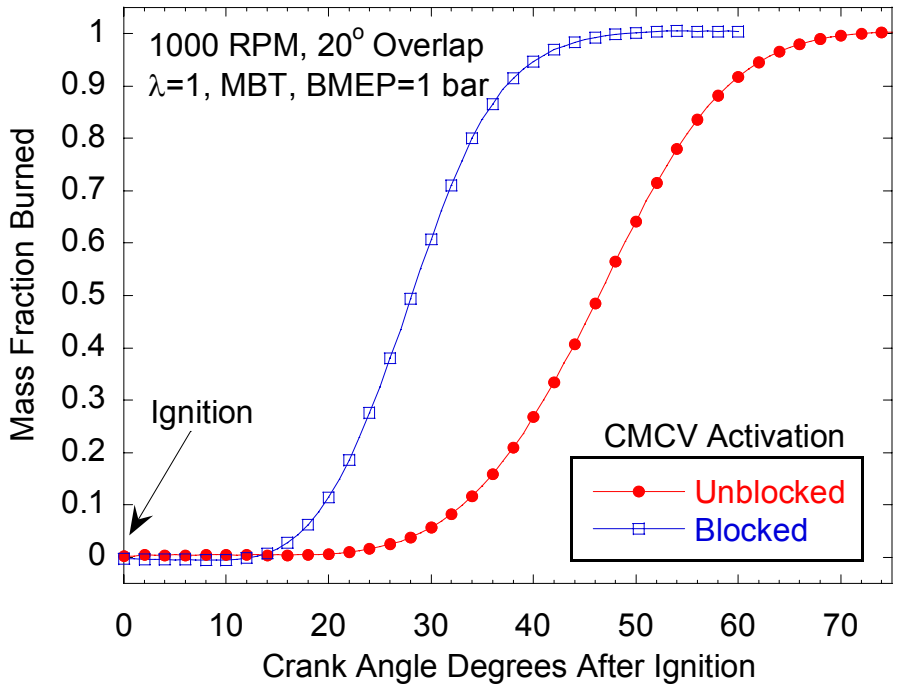

Figure 3.2: Activating the charge motion control valve (CMCV) increases the rate of combustion by approximately a factor of two, requiring spark timing compensation.

The charge motion control valve (CMCV) is used to increase in-cylinder fluid motion, leading to increased combustion rate. Reduction of the runner cross sectional area increases the mean flow velocity, thus increasing the mean kinetic energy and consequently leading to increased levels of in-cylinder turbulence. In general, increasing

combustion rate will decrease the COV_{IMEP} at a given operating condition. The relative improvement in combustion stability facilitates the use of efficient operating strategies at operating conditions where burn rates would be too low without the CMCV. Low engine speed operation (e.g. idle) is most benefited by using the CMCV because piston velocity generated flows are minimal.

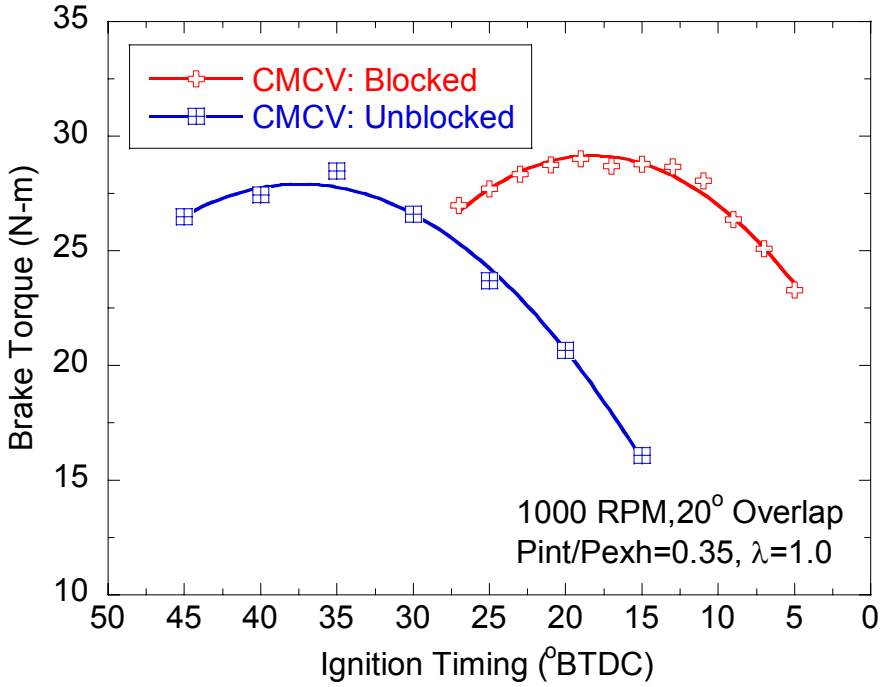

Figure 3.3: For a similar engine torque output the CMCV activation state greatly changes the required MBT spark timing.

MFB profiles with and without the CMCV are calculated at similar engine speed and load, and are shown in Figure 3.2. The MFB curves are shifted such that spark occurs at zero CAD in each case. The increased burn rate created by activating the CMCV is apparent from the short duration from the spark to ten percent mass fraction burned (CA10). The bulk of combustion (CA10 to CA90) also occurs faster when the CMCV is active, evident by the steep slope of the MFB profile. Burn duration decreases by approximately a factor of two when the CMCV is activated. Therefore, significant spark timing adjustments are required when switching between CMCV states to maintain desired combustion phasing.

The change in burn-rate generated by altering the CMCV activation state significantly influences MBT spark timing. Spark timing sweeps for similar operating conditions with each CMCV activation state are shown in Figure 3.3. At this particular operating condition the MBT spark timing changes by around 20 CAD when the CMCV is activated. Higher burn-rates caused by blocking, or activating, the CMCV require later spark timings to maintain proper combustion phasing. Further discussion of the influence of combustion phasing on engine operation is discussed in Appendix A.

3.1.2 Intake and Exhaust Valve Phasing

Dual-independent variable valve phasing systems allow for additional control of engine thermodynamic and gas exchange process as compared to fixed-cam designs. Additional control over these engine processes enables significant improvements in engine performance, fuel economy, and exhaust emissions. Thermodynamic performance is impacted through changes in pumping work, volumetric efficiency, along with compression and expansion ratios. The gas exchange process is affected by camshaft phasing through changes in valve overlap and phasing of valve events with piston motion. Further discussion of gas exchange and valve timing strategies is provided in Appendix B.

Valve overlap duration is known to affect the quantity of exhaust gases that remain trapped in-cylinder from cycle-to-cycle. High levels of positive or negative overlap tend to increase residual gas fraction, and reduce combustion rate. Experimental data confirms increasing combustion duration (from 10 to 90% MFB) for high levels of positive or negative valve overlap (See Figure 3.4). Combustion duration changes approximately twelve crank angle degrees from minimum to maximum for the operating condition in Figure 3.4. Increasing residual gas fraction levels is expected to be the primary driver of combustion duration in this case; however, valve timing also affects

charge motion and may contribute the observed trends. The pressure ratio across the cylinder ($P_{intake}/P_{exhaust}$) influences the magnitude of combustion duration change as a function of valve overlap. In general, combustion duration is less sensitive to valve overlap when operating at high pressure ratios than at low pressure ratio.

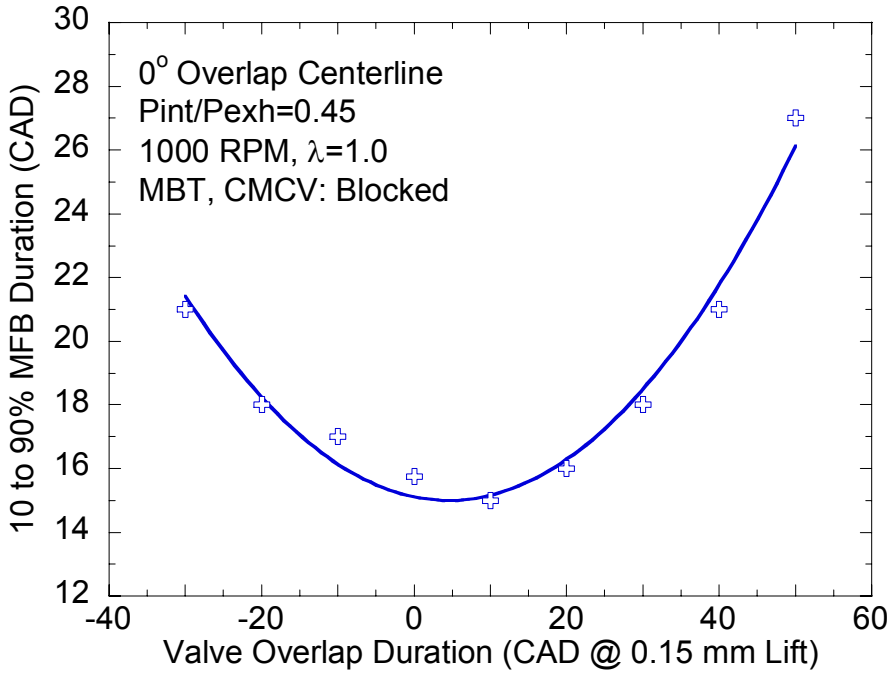

Figure 3.4: Valve overlap duration significantly impacts combustion duration because it affects the gas exchange process and residual gas fraction.

Another strategy that dual-independent valve phasing allows is the movement of valve overlap centerline location. Overlap centerline location influences engine operation by altering the phasing of overlap with piston motion. Moving valve overlap centerline away from TDC-gas exchange increases the net cylinder volume change during the overlap period. Net cylinder volume change depends on the direction (toward the intake or exhaust stroke) that overlap centerline is shifted and the amount that it is shifted. Combustion duration is affected by as much as five crank angle degrees depending upon valve overlap centerline for the operating conditions in Figure 3.5. The influence of valve overlap centerline on combustion duration increases further from TDC because of piston motion. The variation of combustion duration as a function of overlap

centerline is significant enough to require spark adjustment to maintain optimal combustion phasing.

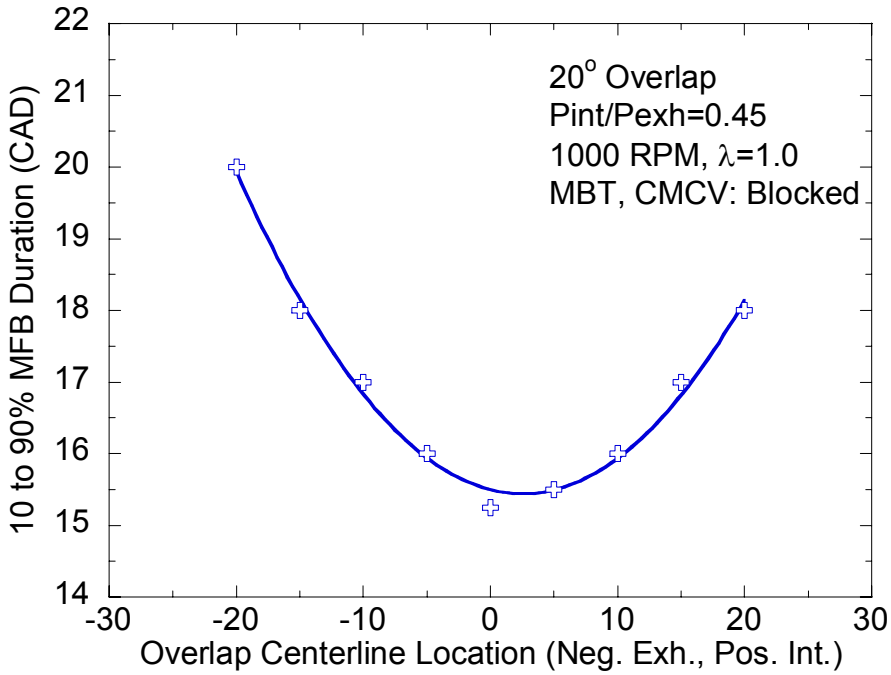

Figure 3.5: Moving overlap centerline location away from TDC increases combustion duration because it alters the phasing of valve overlap with piston motion.

The previous examples represent only a small subset of the possible actuator set-point configurations that are available throughout the engine operating range. An ignition timing prediction model must be capable of handling all of the complex interactions affecting combustion when the number of control actuators increases. The traditional speed/load map-based approach can become restrictive as the number of control actuators increases. The number of correction equations required to account for variations in actuator settings other than those of the base map could make this method cumbersome, and may restrict the use of adaptive or other intelligent engine control strategies. Many researchers have proposed model-based methods to address engine control issues in high degree of freedom engines. Model-based methods attempt to predict engine control parameters, such as ignition timing, without adding additional

engine sensors. A review of several of the proposed model-based methods is provided in the following section.

3.2 Background of Model-Based Ignition Timing Prediction

Model-based ignition timing prediction methods have been developed to address the complex control issues created by high degree of freedom engines. Many previously developed methods use physics-based models to generate traditional surface maps for engine control (Onder and Geering 1995; Lygoe 1998; Bozza et al. 2002; Guerrier and Cawsey 2004; Suzuki et al. 2006). The level of complexity and the amount of experimental information required for each method varies significantly. Several of the models use complexly fit equations to describe each response surface, as opposed to using a traditional matrix-style map. The use of complex equations can complicate calibration and restrict the flexibility of the model to adapt to new hardware configurations.

Cavina and Suglia (2005) developed a model-based ignition timing control method for an engine equipped with variable valve timing and a charge motion control valve. Their ignition timing prediction model is intended to run real-time in the engine controller. For a prescribed location of 50% MFB (CA50), the model calculates combustion duration based on measured engine parameters. Calculated combustion duration is used along with the desired CA50 to determine the required spark timing. Prediction of combustion duration is performed by an empirically-fit equation that considers residual gas fraction, engine speed, CMCV position, and total in-cylinder air mass. Ignition timing prediction using this method proved to be robust and accurate (±3°). The basic algorithm used for this model is very attractive for real-time ignition timing control in a high degree of freedom engine; however, physical meaning is lost using a purely empirical equation to predict combustion duration.

To improve upon previous research, an extensive experimental study is conducted to quantify two key factors that are significant to combustion in high degree of freedom engines, residual gas fraction and turbulence intensity. Prediction sub-models for each parameter are then developed using experimental results in conjunction with existing variables within an engine controller (i.e. RPM, MAP, ICL, ECL, etc.). The new models for residual gas fraction and turbulence intensity are then used to define a combustion model suitable for real-time engine control that is based on physical concepts.

Using a combustion model that is based on fundamental principles ensures the flexibility to accommodate a wide range of new engine technologies. A commonly used spark-ignition engine combustion model was originally introduced by Blizard and Keck (1974) and refined by Tabaczynski et al. (1977 and 1980), and is based on the concept of turbulent flame entrainment. The model consistently provides good agreement with experimental data, making it a good representation of combustion processes. Conceptually, pockets of the fresh air and fuel mixture are entrained by an advancing turbulent flame front. After a pocket of air and fuel is entrained it burns on the Taylor microscale level at the laminar flame speed of the mixture.

The new spark timing prediction algorithm developed in this thesis is loosely based on the turbulent entrainment combustion model. The prediction model is physics-based, but requires adjustments using experimental data. A background of the full turbulent flame entrainment combustion model is provided to properly define the required model inputs. The discussion indentifies the need for development of new experimentally-based methods to quantify turbulence intensity and residual gas fraction.

3.3 An Overview of a Turbulent Flame Entrainment Model for Spark-Ignition Engine Combustion

Spark-ignition engine combustion rate is primarily dictated by chamber geometry, turbulent flame entrainment rate, and the laminar flame speed of mixture burn-up (Poulos

and Heywood 1983). Laminar flame speed is a function of air-to-fuel ratio, pressure, temperature, and residual gas fraction (Turns 2000). In-cylinder turbulence and flow patterns are influenced by engine speed, intake parameters such as valve timing and port geometry, the length of compression stroke during which there is turbulence decay, and combustion. Combustion chamber geometry and spark plug location affect burn rate by altering flame front area determined by the interaction of the spherical flame front and combustion chamber walls (Poulos and Heywood 1983; Filipi and Assanis 2000). An accurate combustion model must therefore account for at least the affects of chamber geometry, laminar flame speed and in-cylinder turbulence.

The following controls-oriented model is developed based upon the quasi-dimensional turbulent flame entrainment concept first introduced by Blizard and Keck (1974) and refined by Tabaczynski et al. (1977 and 1980). Equation (3.1) describes the rate which unburned mass is entrained by the flame front. The flame is assumed to propagate though the unburned charge along Kolmogorov-scale vortices entraining turbulent eddies. Entrainment velocity is defined by the sum of a diffusive component, laminar flame speed, and a convective component, turbulence intensity. Flame front area is defined by the leading flame edge, not the total flame surface area enclosing the still unburned eddies. Of these parameters, mass entrainment rate is most influenced by turbulence intensity and flame front area (Filipi and Assanis 2000). Turbulence intensity is defined as the root-mean-squared velocity fluctuation within the cylinder (Tennekes and Lumley 1972; Munson et al. 2002); and is generally an order of magnitude larger than laminar flame speed.

$$\frac{dm_e}{dt} = \rho_{unburned} A_{flame} (u' + S_L) \tag{3.1}$$

Where: m_e = mass entrained by the flame

$\rho_{unburned}$ = density of the unburned charge ahead of the flame

A_{flame} = total flame front area

u' = turbulence intensity

S_L = laminar flame speed

After turbulent flame entrainment, mass burn-up rate can be described by Equation (3.2). Burn-up rate is proportional to the total unburned mass entrained behind the flame front. Entrained turbulent eddies are then assumed to burn-up at the laminar flame speed since the length scale is small. Eddy size is approximated as the Taylor microscale, which is the assumed length scale over which laminar diffusion occurs; justifying the use of laminar flame speed in this case (Tabaczynski et al. 1977). Taylor microscale is calculated using Equation (3.3). It is important to note that Taylor microscale is a function of turbulence intensity.

$$\frac{dm_b}{dt} = \frac{m_e - m_b}{\tau} \tag{3.2}$$

Where: m_b = total burned mass

$\tau = \lambda / S_L$, characteristic cell burn time

λ = Taylor microscale of turbulence

$$\frac{\lambda}{L} = \left(\sqrt{\frac{15}{\xi}}\right)\left(\frac{u' L}{\nu}\right)^{-\frac{1}{2}} \tag{3.3}$$

Where: ξ = 1 (Assumption made by Tabaczynski et al. 1977)

L = integral length scale

ν = kinematic viscosity

Prior to ignition, the integral length scale is assumed equal to the instantaneous combustion chamber height (Filipi and Assanis, 2000). After ignition, which is the period of interest here, unburned charge is compressed at such a rate that the rapid distortion theory (RDT) is assumed valid (Wong 1979). The rapid distortion theory is used when the timescale of turbulence distortion rate is much shorter than large eddy turnover or decay timescales (Durbin 1992). The RDT assumes that angular momentum

within the turbulent field is conserved, and that there is no interaction between turbulent eddies (Wong 1979). Rapid distortion theory defines the integral length scale during combustion by Equation (3.4). Instantaneous chamber height at the time of spark is calculated by dividing cylinder volume by bore area.

$$L = L_o \left(\frac{\rho_{uo}}{\rho_u} \right)^{\frac{1}{3}} \tag{3.4}$$

Where: L_o = chamber height at ignition

ρ_{uo} = unburned charge density at ignition

ρ_u = unburned charge density during combustion

3.3.1 Flame Front Area Calculation

Flame front area at each crank angle is interpreted from a geometrically calculated table. The flame-area table is generated using engine-specific combustion chamber geometry. Spherical coordinates, originating at the sparkplug, are used to calculate a flame front area and burned gas volume for a range of radii at each crank angle. Additional information, such as flame/wall interaction areas with the piston, cylinder walls, and cylinder head, is also generated.

3.3.2 Laminar Flame Speed Calculation

Knowledge of laminar flame speed is critical for both flame entrainment and burn-up. The key factors determining laminar flame speed are fuel type, air-to-fuel ratio, pressure, temperature, and residual gas fraction. All of these factors, with the exception of residual gas fraction, are either directly measured or could be calculated using basic relations during engine operation. However, laminar flame speed is very sensitive to residual gas fraction, as shown in Figure 3.6. Small variations in residual gas fraction can lead to large differences in calculated laminar flame speed, especially in the range of air-

to-fuel ratios common to spark-ignition engine operation (Φ~0.9-1.1). For these reasons, direct measurement of residual gas fraction is extremely important for the accurate prediction of spark timing. Residual gas fraction measurement and calculation techniques are the focus of Chapter 4. Experimentally measured residual fraction and equivalence ratios are used to determine laminar flame speed for the spark timing prediction model using the following procedure.

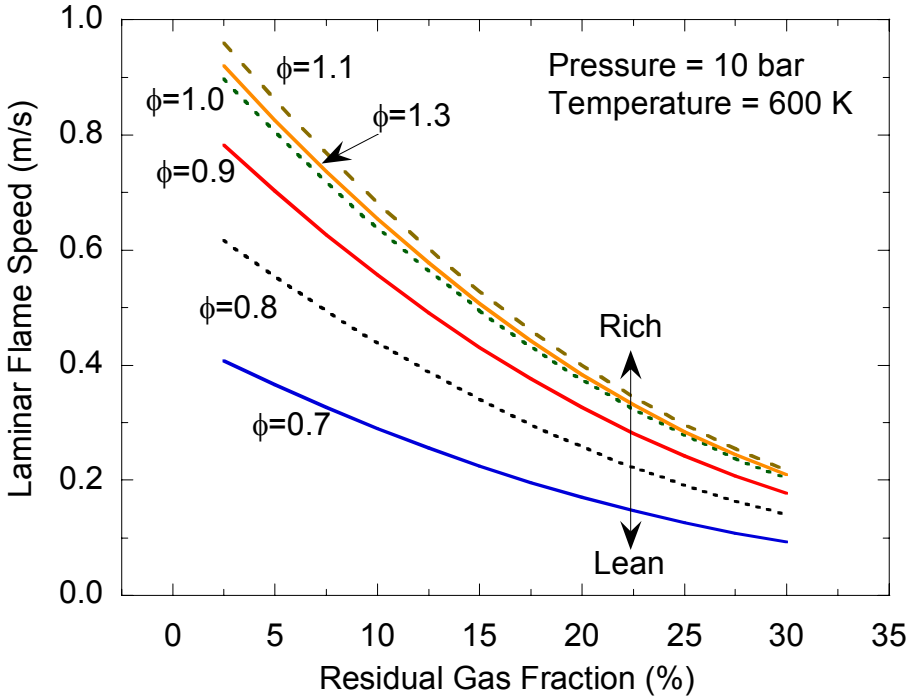

Figure 3.6: Laminar flame speed is a key factor determining the burn-up rate of entrained gases, and it is very sensitive to residual gas fraction.

Correlations relating the laminar flame speed of the mixture to equivalence ratio, residual fraction, pressure, and temperature have been developed. The effects of pressure and temperature have been fitted in the form of a power law in Equation (3.5) (Heywood 1988). Using this method, the reference laminar flame speed, $S_{L,O}$, is a function of fuel/air equivalence ratio, a separate correction is used to account for residual gas fraction.

$$S_L = S_{L,O}\left(\frac{T_u}{T_O}\right)^{\alpha}\left(\frac{p}{p_O}\right)^{\beta} \tag{3.5}$$

Where: $S_{L,O}$ = reference flame speed

T_O = reference temperature (298 K)

p_O = reference pressure (1 atm)

α = temperature compensation exponent for gasoline (Heywood 1988)

β = pressure compensation exponent for gasoline (Heywood 1988)

And:

$$\alpha = 2.4 - 0.271\,\phi^{3.51} \tag{3.6}$$

$$\beta = -0.357 + 0.14\,\phi^{2.77} \tag{3.7}$$

Equation (3.8) is used to adjust the reference flame speed for equivalence ratio. The values of the necessary parameters for gasoline were determined by Metghalchi (1976). The laminar flame speed from Equation (3.5) is then adjusted for residual gas content using Equation (3.9).

$$S_{L,O} = B_m + B_\phi(\phi - \phi_m)^2 \tag{3.8}$$

Where: B_m = 30.5 cm/s for gasoline

B_ϕ = -54.9 cm/s for gasoline

ϕ_m = 1.21, which is the maximum flame speed equivalence ratio for gasoline

$$S_{L,Corrected} = S_L\,(1 - 2.06\,\chi_b^{0.77}) \tag{3.9}$$

3.3.3 In-Cylinder Charge Motion and Turbulence Intensity Modeling

Large and small scale flows within the combustion chamber have a large influence on charge distribution and burn rate. In-cylinder charge motion is generally characterized by the mean or bulk flow and turbulence intensity. Bulk fluid flow describes the general motion (e.g. swirl, tumble, etc.) and the mean velocity of the in-

cylinder mixture. The level of in-cylinder turbulence is defined by the root-mean-squared velocity fluctuation, called turbulence intensity. In general, turbulence intensity is around an order of magnitude larger than laminar flame speed, and it can be greatly affected by the addition of new engine devices. Additionally, direct experimental measurement of turbulence intensity is difficult due to the extreme in-cylinder atmosphere. For these reasons it is important to develop methods to model turbulence intensity. To be used in a controls atmosphere the model for calculating turbulence intensity must be simple, fast, and accurate. An overview of turbulence intensity generation and modeling in spark-ignition engines is provided in the following sections.

The charge motion control valve (CMCV) position, valve overlap period and intake stroke initiate the general pattern of in-cylinder motion. Flow patterns then alter throughout the compression stroke to generate the in-cylinder conditions at ignition and during combustion. Since the intake stroke has a significant effect on in-cylinder charge motion, alterations to the intake process through either flow control or valve timing can greatly affect combustion characteristics. Turbulence intensity decays throughout the intake and compression strokes until ignition. Near the start of combustion, squish can also become a significant driver of turbulence intensity. Squish is gas motion that occurs when the piston surface comes in close proximity with certain cylinder head walls. The velocity of squish flow can be three to four times that of the mean piston speed, and is strongly dependent upon the distance between the piston the cylinder head wall (Heywood 1988).

Poulos and Heywood (1983) developed a zero-dimensional spark-ignition engine in-cylinder turbulence model based on the derivation of Mansouri et al (1982) for diesel engines. The model, based on conservation of energy, assumes that mean kinetic energy first becomes turbulent kinetic energy before changing into internal energy (heat) by viscous dissipation. Mean kinetic energy enters the cylinder through the valves. The process by which mean kinetic energy dissipates to turbulence is modeled after boundary

layer development over a flat plate. The rate of turbulent energy production is a function of several flow characteristics and is fit to experimental data by calibration of the turbulence dissipation constant. A combination of mean flow velocity, turbulence intensity, and instantaneous piston speed are subsequently used to calculate heat transfer to and from the cylinder walls. The turbulence 'cascade' model is used to model flow during all non-combustion events (e.g. intake, exhaust, and compression).

The zero-dimensional turbulence intensity prediction model was incorporated into a full cycle simulation at the University of Michigan (Filipi and Assanis 1991) called Spark-Ignition Simulation (SIS). Prediction results from the SIS program are used to provide insight into charge motion for the test engine. A method used to experimentally estimate turbulence intensity is derived in Chapter 5 and compared to the cycle simulation results. A model intended for engine controls to predict turbulence intensity over the engine operating range is also developed.

3.4 Conclusion

Observed combustion duration trends in a high degree of freedom engine demonstrate the need for improved ignition timing control strategies. Previous attempts to develop model-based ignition timing prediction models have relied on complicated empirical equations. The equations used did not provide sufficient physical insight into combustion, and tend to hinder localized adjustments. The use of a turbulent flame entrainment combustion model as a foundation for an ignition timing prediction was presented. In addition to conventional engine variables, both turbulence intensity and laminar flame speed are required inputs. Laminar flame speed was shown be a strong function of residual gas fraction, which requires experimental characterization (See Chapter 4). The importance of turbulence intensity model was also identified, and is the

focus of Chapter 5. The newly developed inputs are used in a simplified version of the turbulent flame entrainment model discussed in Chapter 6.

CHAPTER 4

RESIDUAL GAS FRACTION MEASUREMENT TECHNIQUES

Laminar flame speed is one of the primary mixture properties that determines combustion rate. As demonstrated in Figure 3.6, laminar flame speed is greatly influenced by residual gas fraction (RGF). Minor alterations in residual gas fraction can significantly impact laminar flame speed, and dual-independent variable valve timing systems are capable of generating high internal residual levels over a wide range of operating conditions. Sensors for residual gas fraction measurement are expensive and complex, making them impractical for use outside of the research environment. For these reasons it is important to quantify residual gas fraction over a wide range of operating conditions and develop prediction methods for use in engine controllers. Predictive capability of residual gas fraction (RGF) is required for spark and emission control.

Taking advantage of recent advents in diagnostic techniques, fast response emission analyzers are used to measure internal residual gas fraction by several different methods. Of primary interest are two techniques that use fast response analyzers to measure in-cylinder pre-combustion gases, one using HC concentration while the second relies on CO_2. A method using a single exhaust port-mounted fast response analyzer to quantify RGF is also discussed. Additionally, the feasibility of calculating residual gas fraction using cylinder pressure is examined. These experimental methods are described and compared using data acquired from the test engine. The relative impact of main operating parameters on residual fraction is also quantified and discussed.

Many researchers have developed residual gas fraction measurement techniques; however comparisons of these methods are not readily available. The availability of a particular instrument is generally a driving factor for choosing a RGF measurement method. In this case, fast response HC and CO_2 analyzers are simultaneously available, and were placed in the same cylinder. The presence of these analyzers allows for direct comparison of all methods used to estimate residual fraction.

4.1 Overview of Residual Gas Fraction Measurement

Experimental measurement of residual gas fraction is performed by either indicated cylinder pressure or emissions-based methods. While cylinder pressure-based methods are the least expensive they are subject to inaccuracy. Emissions based methods are generally more accurate but require more complicated experimental setups. The desire for highly accurate measurements focuses the current work on emissions-based methods; however the basic concepts of cylinder pressure-based techniques are discussed. Many experimental techniques have been developed for emissions-based and cylinder pressure- based techniques. The following sections provide an overview of internal residual gas fraction measurement techniques.

4.1.1 Cylinder Pressure-Based Residual Gas Fraction Measurement

Several pressure based residual fraction measurement techniques have been previously developed. Cains (1997) calculated RGF by comparing gross indicated mean effective pressures from cycles with and without residual. A cycle without residual was created by cutting the spark while continuing fuel injection for 8 to 10 cycles. Residual gases are slowly purged and filled with air and fuel mixture during the misfire period. When the spark is reinstated the first firing cycle occurs without residual, creating an increased IMEPg. Cains developed a routine to correct for relative spark location with

and without residual to generate a residual fraction measurement. The primary deterrent from this method is ensuring proper mixture preparation and air-to-fuel ratio after successive misfires. Mladek and Onder (2000) also developed a RGF estimate routine based upon cylinder pressure for engine control. Their method used measured temperatures and cylinder pressure along with empirical equations to estimate RGF. Results of the estimate model showed good agreement with engine simulations.

4.1.2 Emissions-Based Residual Gas Fraction Measurement

Emissions-based RGF measurement methods are defined by a combination of tracer species and measurement technique. The specific combination used dictates the versatility and accuracy of RGF data. The main selection criteria for tracer species are the level of mixing, relative concentration, required measurement technique, and physical state (liquid/gaseous). A good tracer species must be present in a sufficient concentration to ensure robust measurement and be relatively insensitive to sampling location (well mixed). Techniques used to measure tracer species are weighed against the following criteria; system complexity, engine modification, measurement type (single point or spatial), and cycle-by-cycle or cycle-averaged results. Several common tracer species and experimental configurations for measuring RGF are weighed against their respective selection criteria in Table 4.1 and Table 4.2.

For a tracer to be used to monitor residual gas content the molecular species must be formed or destroyed during combustion. This is the case because residual gas is comprised only of exhaust products, therefore the dilution level of exhaust products with fresh charge can be used to calculate residual fraction. Such a requirement makes it possible to use CO, CO_2, NO, H_2O, or HC among others as residual fraction tracer species. However, the availability of measurement devices for individual species limits the feasible species to CO, CO_2, NO, and HC for such a technique. Laser-based and

other optical measurements (Hinze et al., Quader and Majkowski 1999; Alger et al. 2004) allow further flexibility in tracer species and potentially provide information about spatial RGF distribution; however these techniques greatly increase complexity and engine modification, and are not discussed in the current work.

Table 4.1: Selection Criteria for Common RGF Tracer Species

Tracer Species	CO_2	CO	HC	NO	H_2O
Primary Origin	Exhaust	Exhaust	Intake Mixture	Exhaust	Exhaust
Secondary Origin	Ambient (0.04%)	Ambient (Very Low)	Residual Gas (Higher than Exhaust levels)	Ambient (Very Low)	Ambient (Humidity)
Physical State	Gaseous	Gaseous	Liquid/Gaseous	Gaseous	Liquid/Gaseous
Level of Mixing (Pre-Combustion)	Nearly Homogenous	Nearly Homogenous	Stratified	Nearly Homogenous	Unknown
Relative Concentration (Pre-Combustion)	High (1-4%)	Medium (<1%)	High (2-5%)	Low (<500 ppm)	High (1-4%)
Measurement Technique	NDIR inaccuracy with pressure fluctuations	NDIR (inaccuracy with pressure fluctuations)	FID (inaccuracy with pressure fluctuations)	CLD	Optical
Other Considerations			Air-to-fuel ratio fluctuations from cycle-to-cycle induce error	Concentration drops significantly at high residual gas levels	

Most common RGF measurement methods utilize either NO, HC, or CO_2 as the tracer species. The measurement technique is different for each species. Using NO or CO_2, RGF is calculated from the dilution level occurring when exhaust is mixed with fresh air and fuel during the intake and compression strokes. Measured HC concentration prior to ignition is compared with the HC level that would be attained if residual were completely purged from the system. The presence of residual gas reduces HC concentration and increases NO and CO_2 concentration in pre-combustion gases. CO_2 and HC exist in relatively higher pre-combustion concentrations than NO. However, it is

important to note that despite low in-cylinder concentrations, successful in-cylinder NO measurements are possible (Peckham et al. 1998; Ford and Collings 1999). Ultimately, the accuracy of the species measurement technique (e.g. NDIR, FID, etc.) determines the minimum acceptable species concentration.

Table 4.2: Emissions-Based Residual Gas Fraction Measurement Techniques

Experimental Configuration for Pre-Combustion Gas Measurement	Fast response analyzer directly measuring in-cylinder gases	Fast response analyzer behind a fast sample valve measuring in-cylinder gases	Single Fast response analyzer mounted in the exhaust port	Standard analyzer or gas chromatograph used with a fast sample valve	Optical or Laser based technique
Measurement Type	Single Point	Single Point	Exhaust Port	Single Point	Spatial Resolution
Cycle-by-cycle Measurements	Yes (Up to ~1500rpm)	Yes (All Engine Speeds)	No (misfire required)	No	Yes (All Engine Speeds)
Engine Modification	Minimal (Sparkplug mounting)	Dependant on sample valve design	Minimal (Mount analyzer probe in the exhaust port)	Dependant on sample valve design	Varies by method
System Complexity	Low	Medium	Low	Medium	High
Additional Considerations	1. Response time limits make misfires necessary at high engine speeds. 2. Pressure fluctuations can reduce analyzer accuracy	1. Sample valve timing must be closely controlled. 2. Measurement pressure can be controlled, improving analyzer accuracy	1. A model is required to account for over-expansion backflows that can occur during the misfire cycle	1. Low sample flow rates can complicate use of standard analyzers. 2. Gas chromatograph analysis will occur off-line	1. Optical access can require severe engine modification. 2. Can provide very high accuracy. 3. Spatial measurement is highly desirable

In-cylinder spatial distribution of a particular tracer species during the pre-combustion is an important factor in the selection of both the species and measurement technique. A well mixed species allows a measurement from a single point in the cylinder to be representative of the entire mixture. A poorly mixed species increases measurement variability when taken from a single point, and may require multiple sample locations. Spatial variations in CO_2 values have been found to be lower than

those of HC (Ishizawa 1997). Additionally, fuel condensation concerns generally limit use of HC as a tracer species to gaseous fuel operation only (Galliot et al. 1990; Cho et al. 1998).

Sampling of in-cylinder pre-combustion gases is commonly done with either a fast acting sample valve or continuously sampling fast response analyzers. These methods measure from a single point in the cylinder, therefore they rely on the assumption that contents are well mixed. In-cylinder samples removed with high speed valves are analyzed with either a gas chromatograph (Miller et al. 1998; Jang et al. 2004), standard analyzer (Toda et al. 1976; Sandquist et al. 1997; Kolmel and Spicher 1998; Schwarz and Spicher 2003; Albert and Ghandi 2004), or a fast response analyzer (Karagiorgis et al. 2006). Low sample flow rates from fast acting valves make the use of standard analyzers difficult, and cycle-by-cycle residual measurements are not possible unless fast response analyzers are used. Fast response analyzers continuously sample, either directly from the cylinder (Galliot et al. 1990; Ford and Collings 1999; Cho et al. 1998; Cho et al. 2001), or behind a fast acting valve (Karagiorgis et al. 2006), and offer cycle-resolved measurement. Large pressure fluctuations and response time issues can induce measurement error when measuring directly from the cylinder; however, proper setup, calibration, and robust data interpretation allow cycle-by-cycle residual fraction calculation.

A residual measurement method using a single fast response NO sensor in the exhaust port has been developed by Ford and Collings (1999). Their method requires the sensor be positioned in the exhaust port close to the exhaust valve. The engine is run and a steady-state NO reading in the exhaust port is recorded. A single misfire cycle is used and the pre-combustion gases, including residual, are purged during the exhaust stroke. This method avoids several of the complications in-cylinder sampling, however it has drawbacks. When the cylinder is misfired, the in-cylinder contents can be over-expanded prior to EVO under certain operating conditions. Over-expansion creates a backflow

from the exhaust manifold to the cylinder when the exhaust valve opens. The backflow of exhaust port gases from the previous firing cycle will mix with the in-cylinder gases and significantly increase the calculated residual fraction. Ford and Collings (1999) used a thermodynamic routine to estimate the quantity of backflow and calculate the expected NO concentration from the residual gas only. This method is more accurate at high engine load or when early EVO cam settings are used. Both conditions will minimize over-expansion of in-cylinder contents.

Giansetti et al. (2002) used a single Fast FID analyzer in the exhaust port to measure residual level. The residual calculation requires engine misfire, while still injecting fuel, and comparing the HC concentration of the first misfired cycle to the concentration several misfire cycles later. The HC level from the first cycle is lower than that of later cycles because the residual content within the cylinder decays once the spark is stopped. Several cycles after the misfire begins HC concentration reaches a steady-state, at this point it is assumed that all residual is purged from the cylinder. This process, similar to that performed by Ford and Collings (1999), is subject to over-expansion backflows and mixing with contents of the previous cycle. Giansetti (2002) did not consider the possibility that there may be over-expansion, and therefore back-mixing with the contents of the previous cycle. The sample FID signal trace given in the paper suggests that back-flows are indeed occurring and that this phenomenon should be considered. Failure to consider the effects of back-mixing will suggest artificially high residual levels. Additionally, as with all methods using a FFID and cycle misfire, a gaseous fuel is used to greatly reduce the possibility of fuel collection on the engine walls.

Of the previously mentioned work, only that of Karagiorgis et al. (2006) used CO_2 as a tracer species with the combination of a fast response analyzer mounted behind a sample valve to provide cycle-by-cycle RGF measurements with liquid fuel. The current work will use an experimental configuration using fast response CO_2 and HC

analyzers to directly measure in-cylinder gases, allowing accurate cycle-by-cycle measurements under certain conditions while reducing complexity. The HC-based method is modified to account for the use of liquid fuel. Additionally, a low complexity method using single exhaust port-mounted fast response CO_2 analyzer, in combination with misfire, is utilized. The use of cylinder pressure analysis to determine residual gas fraction is also discussed. All methods are measured simultaneously from the same engine cylinder using the experimental setup described in Chapter 2. Performing all measurements at the same time allows for direct comparison.

4.2 Emissions-Based RGF Calculation

Methods of calculating internal residual content from emissions are best described by first analyzing the in-cylinder chemical equations involved. Equation (4.1) describes the generic make-up of the in-cylinder mixture prior to combustion. The compositions of exhaust gas, internal residual, and EGR are given in Equations (4.2), (4.3), and (4.4) respectively. Although these three parts originate from exhaust gas it is important to separate them because they can have significantly different species compositions, especially during transient operation.

The left hand side of Equation (4.1) represents the gases measured in-cylinder prior to combustion. Exhaust gases measured by an exhaust port-mounted probe are represented by the right hand side of Equation (4.1). Note that wet mole fractions represented in Equations (4.2), (4.3), and (4.4) are the fractions within each component. For example the sum of all mole fractions in Equation (4.2) is equal to one. The same condition holds for Equations (4.2), (4.3), and (4.4) individually. The wet mole fractions found in these equations will be used in the same form to simplify future calculations.

Although re-circulated exhaust gases (EGR) and internal residual (RGF) originate from exhaust gases they may have different composition due to transient engine

conditions and engine design. Internal residual is assumed to be comprised of exhaust gases from the previous cycle whereas EGR may originate from several cycles previous depending on transit time through the EGR system. For example, if operation switches from rich to lean the internal residual could be comprised of lean exhaust species and the EGR comprised of rich exhaust species. Additionally, the fresh air and fuel inducted into the cylinder could also be at yet another AFR than the EGR and internal residual were created, making the final exhaust products a mixture of the three parts. In this case, calculating internal residual content or AFR from the measured exhaust composition may be invalid. This issue is generally neglected when dealing with spark-ignition engines, as the AFR does not alter greatly. However, compression ignition engines operate over a wide AFR range and may be significantly affected by such errors.

$$M_{FUEL}C_XH_Y + M_{AIR}(O_2 + 3.77N_2) + M_{EGR}[EGR] + M_{RGF}[RGF] \longrightarrow [Exhaust] \quad (4.1)$$

Where:

$$[Exhaust] = \chi_{H_2O}^{EXH}\ H_2O + \chi_{CO_2}^{EXH}\ CO_2 + \chi_{CO}^{EXH}\ CO + \chi_{O_2}^{EXH}\ O_2 \ldots \\ \ldots + \chi_{N_2}^{EXH}\ N_2 + \chi_{H_2}^{EXH}\ H_2 + \chi_{NO}^{EXH}\ NO + \chi_{HC}^{EXH}\ C_AH_B \quad (4.2)$$

$$[EGR] = \chi_{H_2O}^{EGR}\ H_2O + \chi_{CO_2}^{EGR}\ CO_2 + \chi_{CO}^{EGR}\ CO + \chi_{O_2}^{EGR}\ O_2 \ldots \\ \ldots + \chi_{N_2}^{EGR}\ N_2 + \chi_{H_2}^{EGR}\ H_2 + \chi_{NO}^{EGR}\ NO + \chi_{HC}^{EGR}\ C_AH_B \quad (4.3)$$

$$[RGF] = \chi_{H_2O}^{RGF}\ H_2O + \chi_{CO_2}^{RGF}\ CO_2 + \chi_{CO}^{RGF}\ CO + \chi_{O_2}^{RGF}\ O_2 \ldots \\ \ldots + \chi_{N_2}^{RGF}\ N_2 + \chi_{H_2}^{RGF}\ H_2 + \chi_{NO}^{RGF}\ NO + \chi_{HC}^{RGF}\ C_AH_B \quad (4.4)$$

Molar residual gas fraction is defined in Equation (4.5) using the number of moles of each in-cylinder constituent. Equation (4.5) only represents the fraction of internal residual in-cylinder. If the number of EGR moles is included in the numerator the total burned gas fraction would be represented. Molar residual fraction can be converted to a mass basis if the molecular weight of each constituent is known or approximated.

$$\chi_{RGF}^{Molar} = \frac{M_{RGF}}{M_{Air} + M_{Fuel} + M_{EGR} + M_{RGF}} \tag{4.5}$$

4.3 Residual Gas Fraction Measurement Using In-Cylinder CO_2 Concentration

Carbon dioxide (CO_2) is a commonly used tracer species for the calculation of RGF because is it well-mixed with intake air and fuel and it occurs in relatively high concentration. RGF calculation from CO_2 is done using a combination of pre-combustion and exhaust concentrations. In-cylinder pre-combustion and exhaust port post-combustion CO_2 concentrations are defined by Equations (4.6) and (4.7) respectively. Pre-combustion CO_2 concentration depends upon the species composition and total quantity of both EGR and internal residual. For post-combustion measurement the CO_2 concentration measured is a combination of CO_2 from internal residual, EGR, and the combustion of air and fuel. The CO_2 level produced by the air and fuel will reflect the cylinder air-to-fuel ratio (AFR). Under lean operation, air is recycled back into the cylinder as part of the internal residual and EGR, affecting global AFR.

$$\chi_{CO_2}^{Pre-Comb} = \frac{\chi_{CO_2}^{RGF} M_{RGF} + \chi_{CO_2}^{EGR} M_{EGR}}{M_{Air} + M_{Fuel} + M_{EGR} + M_{RGF}} \qquad \text{(Pre-combustion)} \tag{4.6}$$

$$\chi_{CO_2}^{Post-Comb} = \frac{\chi_{CO_2}^{RGF} M_{RGF} + \chi_{CO_2}^{EGR} M_{EGR} + \chi_{CO_2}^{AFR} M_{AFR}^{EXH}}{M_{AFR}^{EXH} + M_{EGR} + M_{RGF}} \qquad \text{(Post-combustion)} \tag{4.7}$$

Where:

$$M_{AFR}^{EXH} = \frac{M_{AIR} MW_{AIR} + M_{FUEL} MW_{FUEL}}{MW_{EXH}} \tag{4.8}$$

The pre-combustion CO_2 measurement equation is solved to yield an expression for the internal residual gas fraction in Equation (4.9). This equation does not assume that the CO_2 concentrations of the EGR and internal residual are equal; therefore it could be used for transient conditions. A problem is encountered since the number of RGF

moles is required to solve for the molar RGF, and iteration is required. However, if external EGR is not used or the engine is operated at steady-state the molar internal RGF is represented by Equation (4.10). In this case, the CO_2 concentration within the residual gases is assumed to be equal to that of the previous exhaust cycle.

$$\chi_{RGF}^{Molar} = \frac{1}{\chi_{CO_2}^{RGF}} \left(\chi_{CO_2}^{Pre-Comb} - \frac{\chi_{CO_2}^{EGR} M_{EGR}}{M_{Air} + M_{Fuel} + M_{EGR} + M_{RGF}} \right) \tag{4.9}$$

$$\chi_{RGF}^{Molar} = \frac{\chi_{CO_2}^{Pre-Comb}}{\chi_{CO_2}^{RGF}} = \frac{\chi_{CO_2}^{Pre-Comb}}{\left(\chi_{CO_2}^{EXH}\right)_{Previous\ Cycle}} \tag{4.10}$$

A typical in-cylinder CO_2 concentration profile measured with an NDIR500 is shown in Figure 4.1. CO_2 concentration decreases to pre-combustion levels during the compression stroke and is sampled until the flame traverses the measurement location, at which time the concentration rapidly increases to reflect exhaust gas levels. The measurement periods occurring before and after the pre-combustion period do not provide valid data. During combustion, cylinder pressure can rise too high for accurate measurement. The instrument will recover during the remainder of the expansion and exhaust strokes. During the intake stroke the pressure difference between the cylinder and measurement chamber can be low, reducing sample flow rate.

The in-cylinder CO_2 concentration used for RGF calculation in Equation (4.10) must be interpreted from the in-cylinder trace. To ensure a robust calculation method, an average of several crank angles around the minimum concentration is calculated. Since the in-cylinder probe is subject to error during the exhaust stroke a separate probe is used in the exhaust port to determine exhaust CO_2 concentration. The average exhaust stroke concentration measured in the exhaust port from the previous cycle is used in denominator of Equation (4.10).

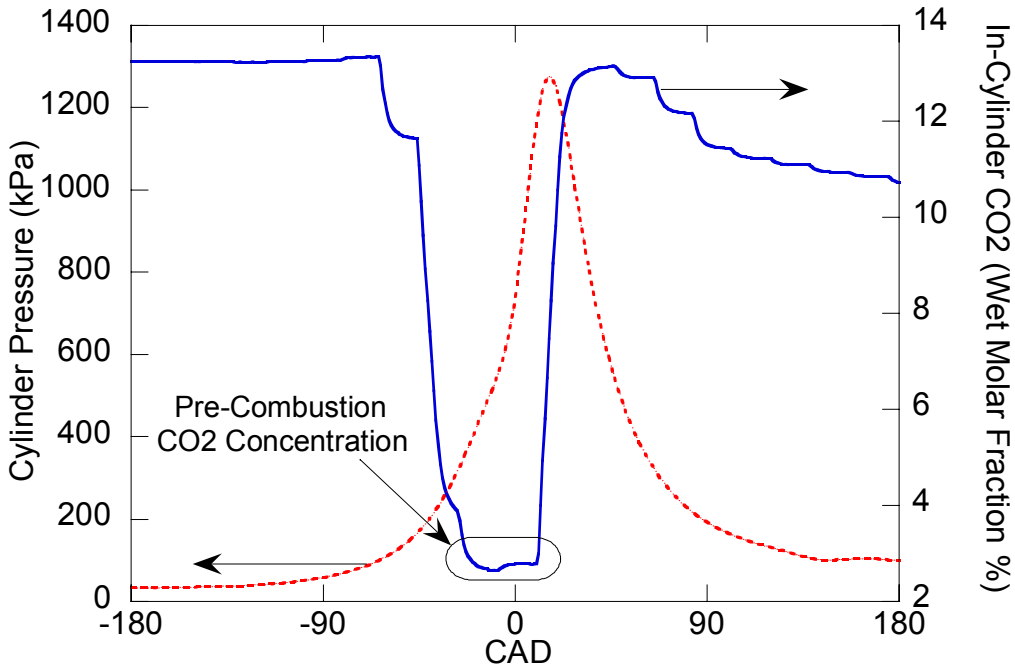

Figure 4.1: The in-cylinder CO_2 concentration profile indicates the pre-combustion level during the compression stroke

Calculated RGF values for 85 consecutive cycles at idle-like conditions are given in Figure 4.2. The exact origins of the cycle-to-cycle variation are not known, but they are suspected to be a combination of instrument error, measurement location dependence, and typical sources of cycle-to-cycle variation such as changes in air and fuel flow quantity. As engine speed rises, RGF standard deviation quickly increases to unacceptable levels as a percentage of average residual fraction. The sharp increase in standard deviation is a product of a relatively slow instrument response time. As engine speed increases less time is available for measurement of pre-combustion gases and a steady value is not reached (See Figure 4.3). If the instrument does not have ample time to stabilize, the residual calculation is subject to high variability and over-prediction. Measurement time prior to flame front arrival can be slightly extended by positioning the measurement location as far from the ignition source as possible. In this case the sample probe was located as far from the sparkplug as possible, near the cylinder wall, to increase the measurement window prior to flame arrival.

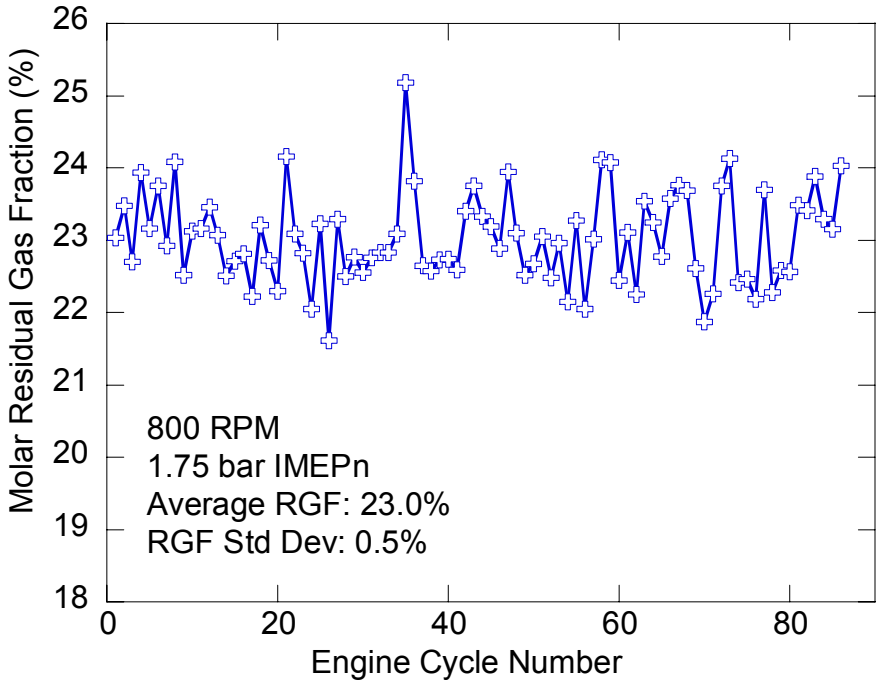

Figure 4.2: Cycle-by-cycle variations in calculated RGF from 85 consecutive cycles at idle-like conditions indicate a 95% certainty window of +/- 6% of the mean RGF

To address issues with slow instrument response time during continuous measurement intentional misfires are employed. An intentional misfire is created by cutting spark while continuing fuel injection. Without combustion there is significantly longer time for measurement of pre-combustion gases. The first misfire cycle contains a pre-combustion mixture that was formed under the same conditions as steady-state operation; exhaust temperature, exhaust pressure, manifold absolute pressure (MAP), and heat transfer characteristics are consistent with steady-state operation during compression of the first misfire cycle. Figure 4.3 compares in-cylinder CO_2 traces from continuous firing and intentional misfire, revealing two significant measurement observations. First, using intentional misfire allows the CO_2 concentration measurement to stabilize, reducing error. Secondly, the minimum CO_2 value reached during continuous firing can reflect a much higher concentration than is actually present in pre-combustion gases. The intentional misfire method is therefore required at high engine speed to maximize

accuracy; however care must be taken to avoid damage to the engine and after-treatment components.

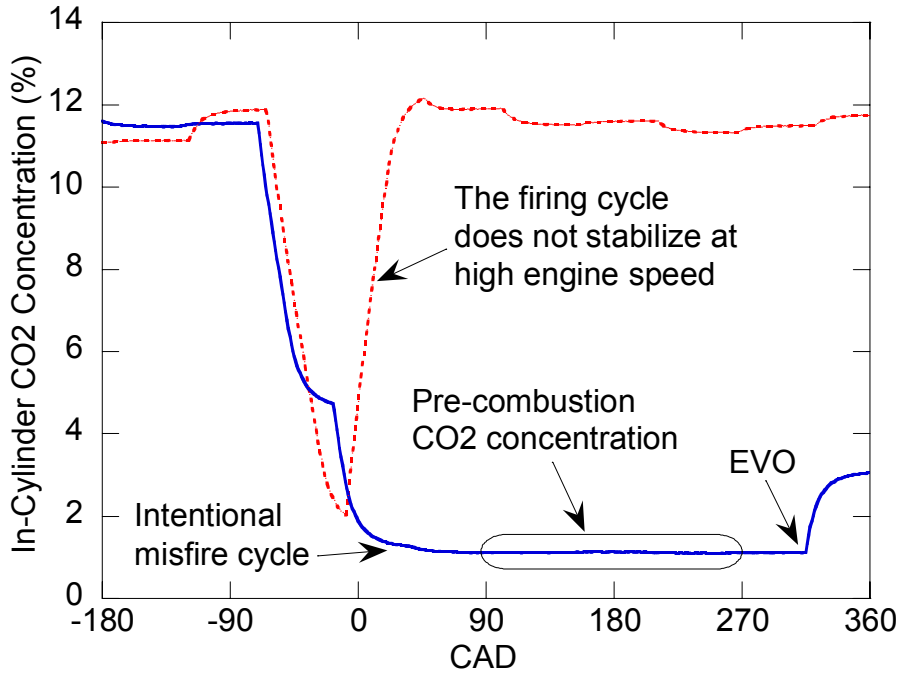

Figure 4.3: Intentional misfire extends the measurement window of pre-combustion gases

Variability in the intentional misfire method was determined by averaging five data sets at several engine operating conditions. Operating points were chosen to analyze performance over a range of possible error sources. The maximum standard deviation over the test range including a 1% instrumentation uncertainty was 5% of the average RGF value. A 95% confidence level of +/-10% of the mean, based on two standard deviations, is assumed for all skip-fire CO_2-based measurements. This uncertainty level represents a significant reduction as compared to measurement during continuous firing at high RPM, and is consistent with other RGF measurement methods (Alger and Wooldridge 2004). In general, variability is reduced when engine speed increases or when the CMCV is activated. These trends indicate that increased mixing of residual gas with fresh charge, caused by high charge motion, improves accuracy of the single point measurement. True cycle-to-cycle variation, indicated by COV_{IMEP}, also appears to

contribute to variation. Contributions to variability caused by either charge mixing or actual RGF variation cannot be distinguished in this case. Residual fraction magnitude is also significantly improved since the effect of slow instrument response time is eliminated, as shown in Figure 4.4. The error bars are based on a 95% confidence window (two standard deviations). In the current work the continuous firing method is used below 1500 rpm, while intentional skip-firing is used at and above 1500 rpm.

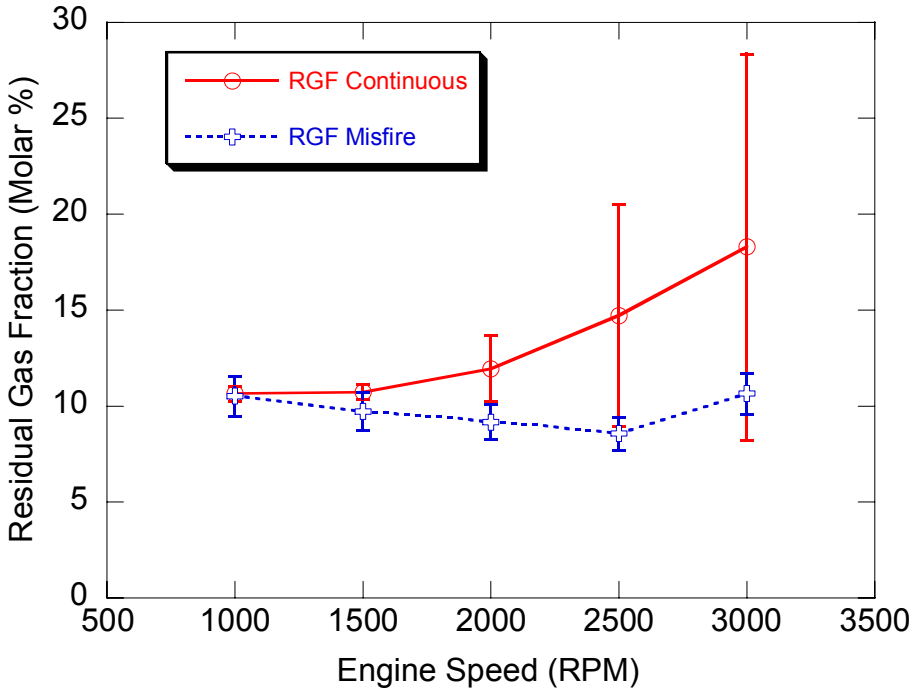

Figure 4.4: Using the intentional skip fire method greatly improves accuracy as compared to continuous measurement at high engine speeds

4.4 Residual Gas Fraction Measurement Using Exhaust Port CO_2 Concentration

A RGF measurement method using a single exhaust port-mounted fast response emissions analyzer was developed by Ford and Collings (1999). This method is desirable because fast response analyzers are generally more accurate when placed in the exhaust manifold because pressure fluctuations are much lower than in-cylinder measurement. Ford and Collings used NO as a tracer species; however CO_2 will be used in for this project. Both species share similar origins, however CO_2 is more plentiful, and an

exhaust port-mounted CO_2 analyzer was already in use. A single misfire is required to purge pre-combustion gases into the exhaust manifold. However, the method is complicated by the over-expansion of in-cylinder gases during the misfire cycle under certain operating conditions. In spark ignition engines, over-expansion during a misfire is common because manifold pressure is often below exhaust pressure. Unless the expansion ratio is proportionally less than the compression ratio to overcome the difference in intake to exhaust manifold pressure an over-expansion will occur. Over-expansion creates a backflow of exhaust gases into the cylinder at exhaust valve opening. Pre-combustion gases are diluted by the over-expansion exhaust backflow.

Ford and Collings developed a correction, Equation (4.11), to account for the backflow dilution to generate a RGF estimate. The correction equation requires data taken from three points; zero is located just after IVC, one is just before EVO, and two occurs at the end of the exhaust backflow, as shown in Figure 4.5. The main required assumption is that backflow gases are perfectly mixed with in-cylinder contents by the time the post backflow exhaust port CO_2 measurement is recorded.

$$\chi_{RGF} = \frac{p_o V_o T_e [CO_2]_{2:1} - (p_2 V_2 - p_1 V_1)(1 - [CO_2]_{2:1}) T_{inlet}}{p_o V_o T_e + (p_2 V_2 - p_1 V_1)(1 - [CO_2]_{2:1})(T_e - T_{inlet})} \tag{4.11}$$

Where:

$$[CO_2]_{2:1} = [CO_2]_{2:Post-Backflow} \Big/ [CO_2]_{1:Pre-Backflow} \tag{4.12}$$

The exhaust port-mounted NDIR analyzer is more accurate than an in-cylinder location because it is only subject to small pressure fluctuations. Further accuracy is gained because higher NDIR measurement chamber pressures can be used because the analyzer is not subjected to intake manifold pressure. Increasing measurement chamber pressure increases NDIR accuracy (Sutela et al. 2000). For these reasons instrumentation accuracy should be higher than using an in-cylinder analyzer. Variability in the post-

backflow exhaust port CO_2 concentration increases with engine speed. Increased variation at high engine speed is likely caused by a breakdown in the assumption that backflow gases perfectly mix with in-cylinder contents due to decreased mixing time. Additional uncertainty is added to this method via the backflow correction equation. The backflow correction equation requires accurate cylinder pressure, volume phasing, and temperature measurement. A variability, or precision, of approximately +/-20% (95% confidence) occurred at 3000 rpm and only slightly improved at lower engine speeds. However, this method is accurate and simple when the over-expansion backflow is not present, such a condition occurs at wide open throttle when intake manifold pressure is close to exhaust manifold pressure.

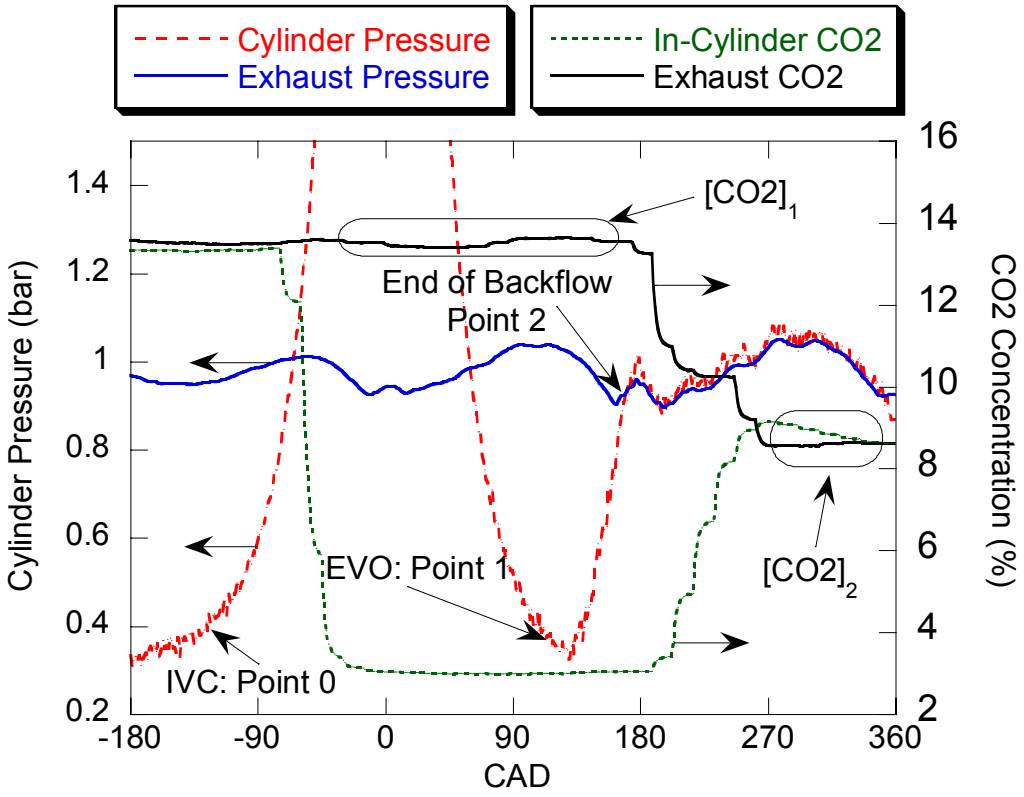

Figure 4.5: An example of measurement points used to calculate RGF with a single exhaust port-mounted fast response CO_2 probe

4.5 Residual Gas Fraction Calculation Using In-Cylinder HC Concentration

In-cylinder pre-combustion hydrocarbon concentration is a function of residual fraction and air-to-fuel ratio. The presence of residual gas lowers the pre-combustion HC concentration by displacing fresh air and fuel. It is important to note that air-to-fuel ratio is not influenced by residual fraction even though HC concentration changes with residual gas fraction. However, changes in air-to-fuel ratio also influence pre-combustion HC levels.

Residual gas fraction measurement using a fast response FID to perform in-cylinder HC measurements was initially developed by Galliot et al. (1990). Galliot and co-workers used propane fuel to ensure adequate mixing with intake air and to eliminate the possibility wall condensation affecting results. Liquid fuel is used in this experiment to assess the following method for use in common internal combustion engine applications.

In-cylinder conditions prior to combustion are represented by the left hand side of Equation (4.1). Measured in-cylinder hydrocarbon concentration prior to combustion is represented by Equation (4.13). Hydrocarbon concentration is a function of fresh fuel quantity, residual gas and EGR quantity and their respective hydrocarbons concentrations.

$$\chi_{HC}^{Pre-Combustion} = \frac{M_{EGR}\chi_{HC}^{EGR} + M_{RGF}\chi_{HC}^{RGF} + M_{Fuel}}{M_{EGR} + M_{RGF} + M_{FUEL} + M_{AIR}} \tag{4.13}$$

The test engine does not utilize external EGR, so it is not considered in this case. HC concentration in internal residual has been shown to be higher than exhaust levels (Ishizawa 1997), however it is neglected in this case for simplification. Combining Equations (4.1), (4.5), and (4.13) yields an expression relating pre-combustion HC molar fraction to residual gas fraction in Equation (4.14).

$$\chi_{RGF}^{In-Cylinder\ HC} = 1 - \chi_{HC}^{Pre-Comb}\left[1 + \lambda\left(x + \frac{y}{4}\right)\right] \tag{4.14}$$

Inspection of Equation (4.14) indicates that RGF is determined by the ratio of measured pre-combustion HC (Figure 4.6) and a reference HC level that would occur if no residual were present. The reference HC value is a function of both fuel composition and air-to-fuel ratio. This occurrence is used to simplify the RGF prediction equation to Equation (4.15).

$$\chi_{RGF}^{In-Cylinder\ HC} = 1 - \frac{\chi_{HC}^{Pre-Combustion}}{\chi_{HC}^{Reference}} \tag{4.15}$$

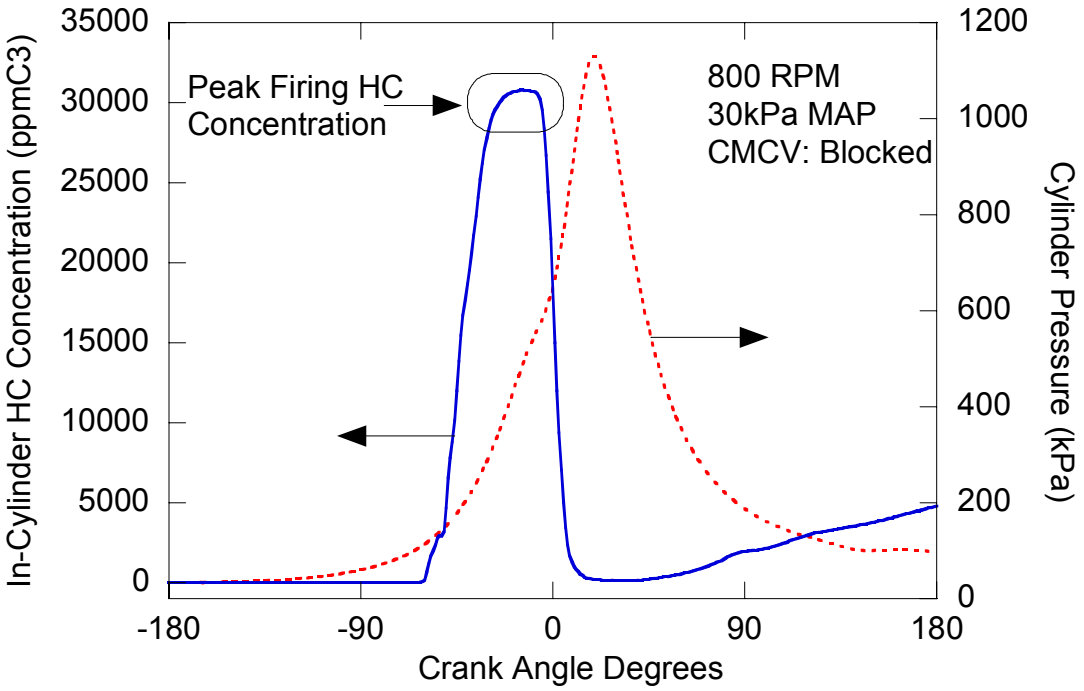

Figure 4.6: In-cylinder HC concentration increases to a peak value prior to combustion

The pre-combustion HC concentration of the first misfire cycle is used for residual gas fraction calculation. The first misfired cycle contains a mixture composition created during normal firing conditions, so effects from heat transfer and gas dynamics are maintained. Similar to the method using the NDIR500 measuring CO_2, the misfire

provides an extended measurement window to preventing errors from instrument response time. Even though the response time of the FFID is much faster than the NDIR500 there are still response time issues associated with the FFID. The measurement chamber pressure of the FFID must be relatively higher to maintain a stable flame; this slows sample speed through the system and can even create reverse flow situations during the intake stroke. While reverse flows are not significant enough to affect engine operation they do have the effect of narrowing the pre-combustion measurement window.

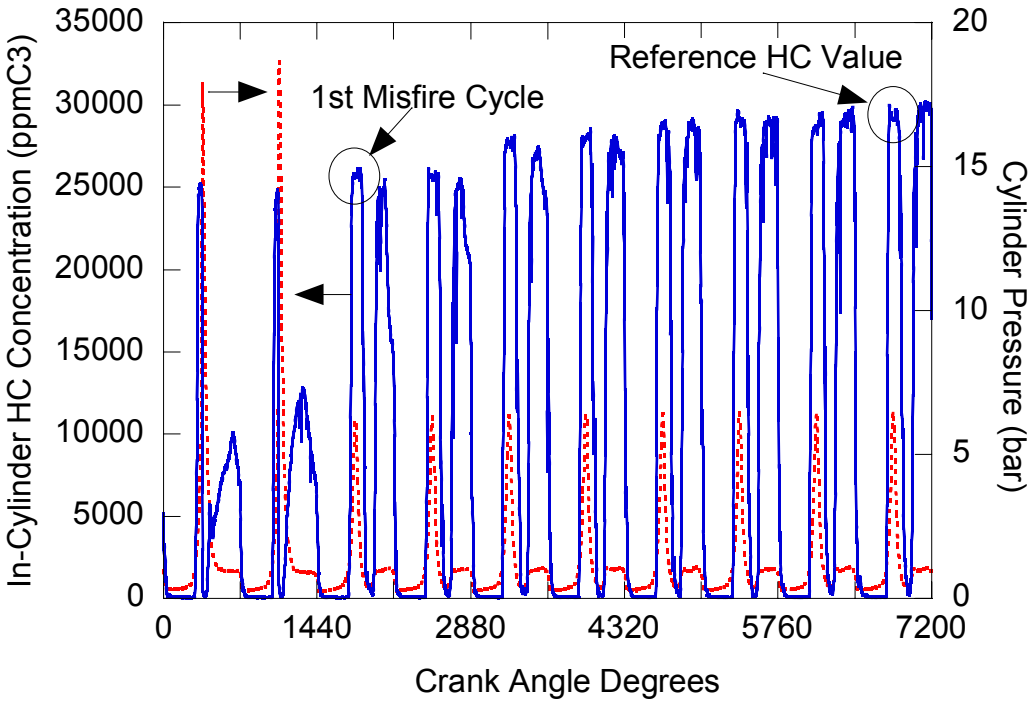

Figure 4.7: Consecutive misfires are used to purge residual gases from the cylinder allowing the measurement of a reference HC concentration

Determination of the reference HC concentration can be done using Equation (4.14) or experimentally. Experimental HC reference level measurement allows for flexibility in instrumentation calibration and other measurement errors, such as liquid fuel condensation. In this case HC reference level was determined experimentally from the in-cylinder FID after several misfires. In-cylinder hydrocarbon level reaches and maintains a peak value after approximately eight to ten consecutive misfire cycles (See Figure 4.7). Consecutive misfire cycles, created by cutting spark and continuing fuel

injection, purge residual from the cylinder and fill that space with only air and fuel at the operating air-to-fuel ratio.

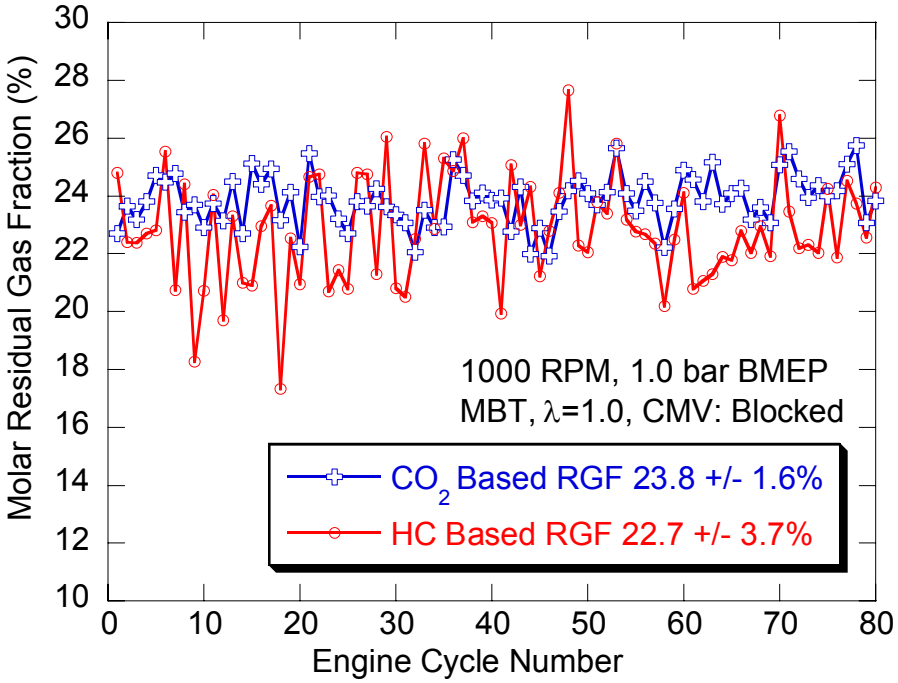

Figure 4.8: Simultaneous cycle-by-cycle RGF measurement shows higher variability for the HC-based method than the CO_2-based method

Variability, or precision, of the HC-based RGF measured over consecutive cycles is compared to that of the in-cylinder CO_2-based technique in Figure 4.8. The HC method shows more than double the variability as the CO_2 based method. The trend of increased variability for the HC-based method carries over the entire engine test range. Variability of approximately +/-20% of RGF (95% confidence) is representative of this technique throughout the testing range. The HC method is more susceptible to variability because HC concentration is a function of air-to-fuel ratio and RGF, whereas the CO_2 method is not dependent on AFR. Additionally, is has been shown that hydrocarbons generally exhibit more spatial variation that CO_2 because of the relatively shorter time for mixing prior to measurement (Ishizawa 1997).

4.6 Cylinder Pressure-Based Residual Gas Fraction Measurement

Residual gas fraction measurement using cylinder pressure is desirable because it is much less expensive than emissions-based methods. However, accuracy is generally compromised as compared to emissions-based methods due to the nature of the assumptions made to calculate RGF. The previously discussed method developed by Cains (1997) is relatively simple in concept, but obtaining consistent experimental data is difficult. The method requires measurement of a 'purged' firing cycle after several successive misfires and ensuring proper combustion for the re-fire cycle proved difficult. Although it is difficult to directly measure RGF from cylinder pressure there is still information imbedded in cylinder pressure data that can provide insight to mixture composition.

Numerous researchers have shown that compression of non-reacting in-cylinder gases is polytropic during the closed portion of the compression stroke, defined by Equation (4.16). The apparent polytropic exponent, n, of the mixture is a function of blow-by, heat transfer to and from the cylinder walls, along with species composition and temperature. The exponent is determined by calculating the slope of the linear portion of the log P vs. log V plot during the compression stroke. The relationship of the polytropic exponent to the log P-log V plot can be derived directly from Equation (4.16) and is shown in Figure 4.9. It is important to note that an accurate cylinder pressure referencing technique is required for precise polytropic exponent calculation. Davis and Patterson (2006) reported an error of approximately 5% (~0.06) in the polytropic exponent for every 25 kPa in pressure referencing error. To ensure proper cylinder pressure referencing an absolute pressure transducer was positioned near the intake valve and downstream of the CMCV (See Section 2.3.2).

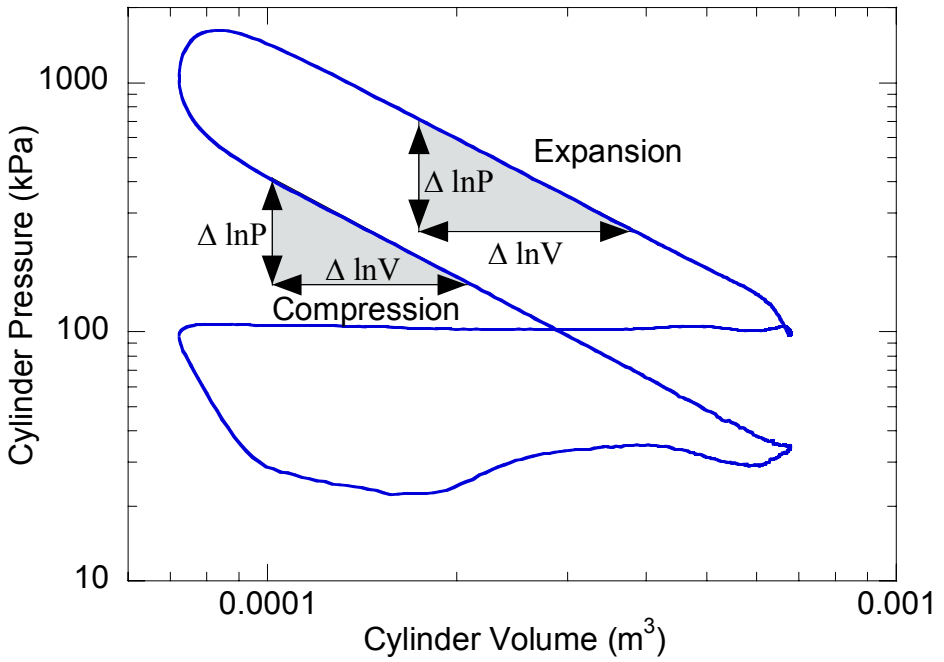

Figure 4.9: The polytropic exponent of compression or expansion is the slope of the log P vs. log V plot during those events.

$$\frac{P_2}{P_1} = \left(\frac{V_1}{V_2}\right)^n \quad solving\ for\ n \Rightarrow \quad n = \frac{\left(\ln P_2 - \ln P_1\right)}{\left(\ln V_1 - \ln V_2\right)} \tag{4.16}$$

The ratio of specific heats of the mixture, γ=Cp/Cv, is influenced by the species composition and temperature. Species with high molecular weights and/or containing more atoms tend to have higher specific heat than molecules containing fewer atoms and/or with lower molecular weight due to an increase in the translational energy along with a greater number of vibrational and rotational modes available store energy (Sonntag 1998). Increasing temperature also increases specific heat by activating more modes of energy storage. The difference between constant pressure and constant volume specific heat values is equal to the gas constant for a given. High molecular weight species have the effect of both lowering the gas constant and increasing specific heat, lowering the ratio of specific heats. In general, heat transfer out of the cylinder gases to the walls and blow-by will lower the polytropic exponent during compression. The combination of all

of the previously discussed effects yields an apparent polytropic exponent for the mixture.

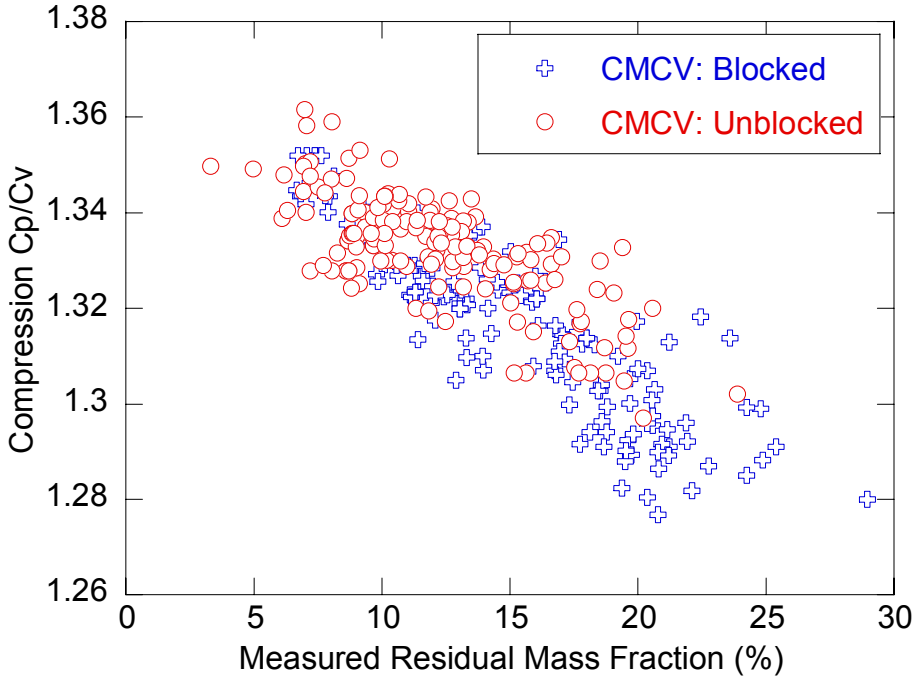

Figure 4.10: The polytropic exponent of compression is affected by residual gas fraction. Although the variability is high, RGF level can be estimated using compression polytropic exponent.

Exhaust gases have higher heat capacity than air because they are comprised of a higher percentage of tri-atomic molecules, such as H_2O and CO_2. The increased heat capacity of recycled exhaust gases (residual gas) has the effect of reducing the apparent polytropic exponent of compression from that of air and fuel alone. Therefore, increasing residual gas fraction will lower the polytropic exponent during compression. The correlation between residual gas fraction and the polytropic exponent during the compression stroke is given in Figure 4.10. The data indicates a good correlation between residual gas fraction and the compression exponent; however it is not of sufficient quality to use for accurate residual fraction prediction. The data trends also show the value of proper cylinder pressure referencing techniques. The range of data shown in Figure 4.10 is for engine conditions ranging from idle to high speed and load.

Exhaust gas temperatures for this data set range from approximately 400°C to 1000°C. Accounting for the large range of exhaust gas temperatures may improve the accuracy of residual fraction prediction using this method.

4.7 Comparison of Emissions-Based Measurement Methods

The preceding discussions only addressed precision, or variability, of each measurement method. The relative accuracy, in proximity to the true value, of each method is difficult to determine without a known reference; cycle accuracy can only be inferred from a combination of low variability and exhibition of consistent trends with engine operating parameters. Previous researchers have identified the important engine parameters that influence residual fraction (Toda et al. 1976; Galliot et al. 1990; Miller et al. 1998; Alger and Wooldridge 2003). Residual fraction origins are generally considered to be a combination of exhaust gases that backflow into the intake manifold which are re-inducted during the intake stroke and gases trapped within the cylinder volume at EVC. The major factors determining residual fraction are pressure ratio ($P_{intake}/P_{exhaust}$), engine speed, valve overlap duration, overlap centerline location, and compression ratio. Spark timing and air-to-fuel ratio have been found to have modest influence in RGF (Miller et al. 1998; Alger and Wooldridge 2003). The following section discusses RGF trends created by varying engine parameters and comparing the measurements from each experimental method.

Pressure ratio across the cylinder affects residual gas fraction by altering the magnitude of backflow from the cylinder to the intake manifold during valve overlap. Residual fraction decreases as pressure ratio increases due to reduced backflow (See Figure 4.11). Low engine pressure ratios create large backflows of exhaust gases from the cylinder into the intake manifold, increasing residual mass fraction. High valve overlaps are more influenced by pressure ratio than low overlap conditions because

backflow of exhaust gases into the intake occurs over a longer time-duration. The RGF method utilizing in-cylinder CO_2 illustrated the expected trend with pressure ratio. In-cylinder HC measurements do not give a consistent trend with pressure ratio.

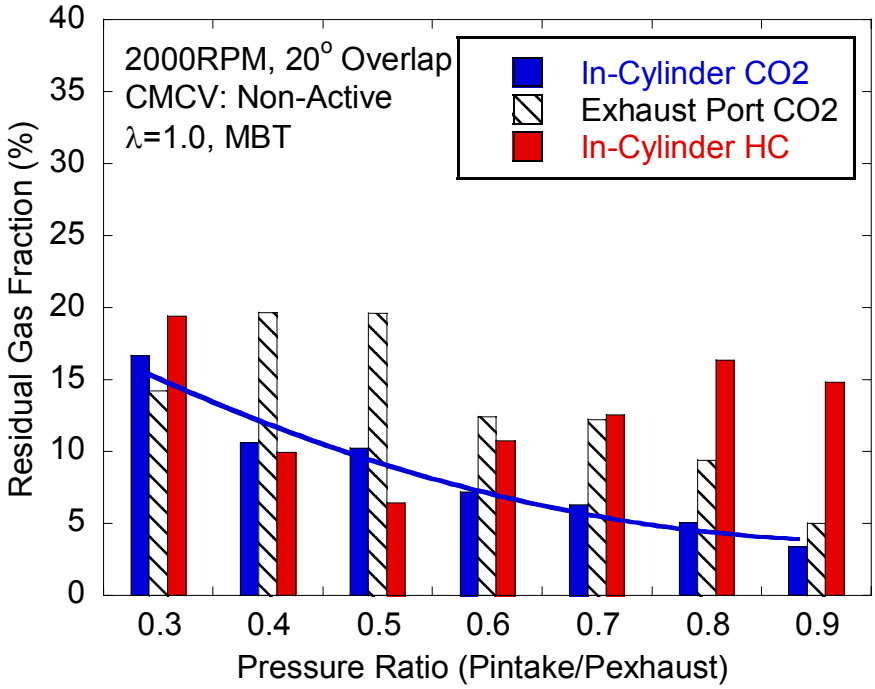

Figure 4.11: High residual fraction at low pressure ratios is caused by large backflows of exhaust gases into the intake manifold during overlap

Engine speed influences residual RGF by altering valve event time-scales. RGF as a function of engine speed is shown in Figure 4.12. The engine was operated at constant pressure ratio to separate the influence of time-scale changes on RGF. For positive overlap operation, low engine speeds provide relatively longer valve overlap time windows than high engine speeds; increasing backflow quantity and RGF at low engine speeds. It is important to note that residual fraction can increase at high engine speed due to valve timing. In this case, exhaust valve closing (EVC) occurs early enough that flow becomes restricted late in the exhaust stroke at high engine speeds, trapping more residual gases. Again, the in-cylinder CO_2 measurement provides the most consistent trend with engine speed.

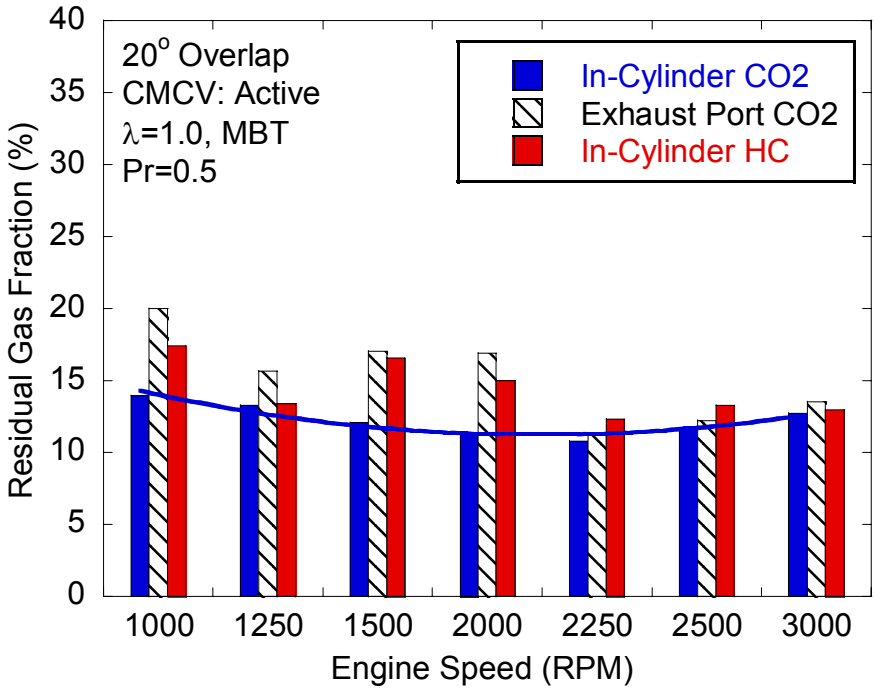

Figure 4.12: Engine speed influences the time-duration of valve overlap and therefore the size of the exhaust backflow

Residual gas fraction as a function of valve overlap duration is shown in Figure 4.13. Valve overlap duration is reported at 0.15 mm of valve lift (SAE Standard). RGF increases with positive overlap because backflow duration extends. Negative valve overlap increases residual fraction because the exhaust valve closes early in the exhaust stroke, trapping exhaust gases. Negative overlap is generally marked by a re-compression of exhaust gases near EVC and prior to IVO. Minimum RGF occurs around zero overlap, where backflows are small and exhaust valve closing is still sufficiently late to allow a full exhaust stroke. The overlap duration at which minimum residual fraction occurs will vary depending upon engine speed and load because time-scales and mass flow rates influence the gas exchange process. Specific details about valve events and gas exchange are well described by Asmus (1982 and 1991). All test methods predicted the proper RGF trend; however the in-cylinder CO_2 measurement method showed the least variability from point to point.

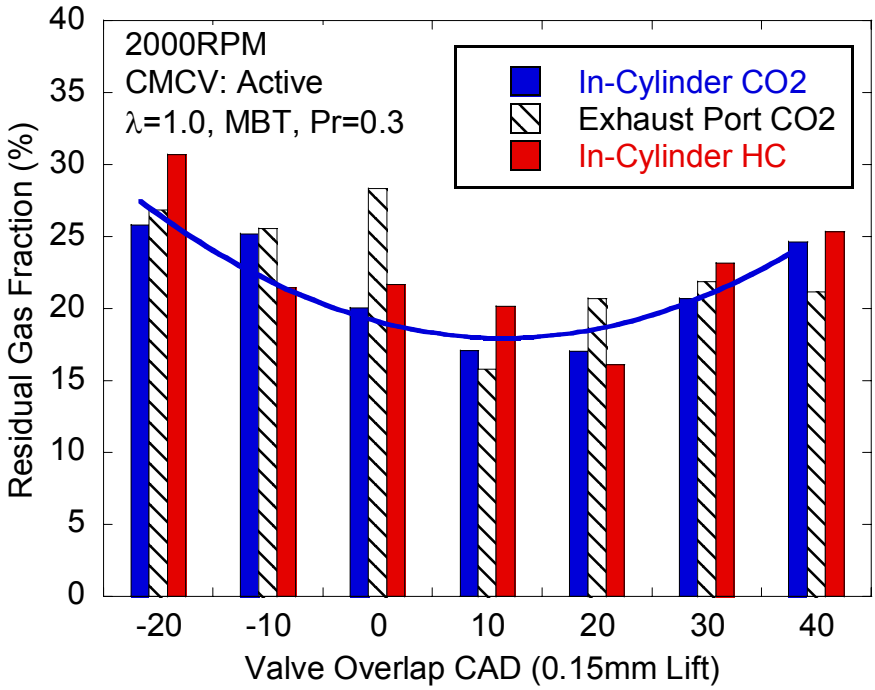

Figure 4.13: Residual fraction increases with high levels of either positive or negative overlap

Overlap centerline location influences RGF by altering the phasing of overlap with piston motion. Shifting overlap centerline away from TDC-gas exchange increases the net cylinder volume change during overlap. Moving centerline into the exhaust stroke decreases the net cylinder volume during overlap and piston motion aids backflow of exhaust gases into the intake manifold. A net increase in cylinder volume occurs during overlap when centerline is shifted into the intake stroke. During the intake stroke piston motion pulls exhaust gases from the exhaust port into the cylinder, increasing RGF. Residual gas fraction measurements for an overlap centerline bias sweep at a constant engine speed and pressure ratio are given in Figure 4.14. In-cylinder CO_2 based measurements confirm RGF increases when centerline is moved away from TDC. Exhaust stroke biased overlap produces higher residual gas fraction levels than a similar shift into the intake stroke. The influence of piston motion aiding backflow into the intake port during exhaust biased overlap is expected to be the prime reason for the difference in residual fraction from intake to exhaust overlap centerline bias. Both the in-

cylinder and exhaust port CO_2 methods captured the expected RGF trend with overlap centerline, with the in-cylinder CO_2 measurement showing the least variability.

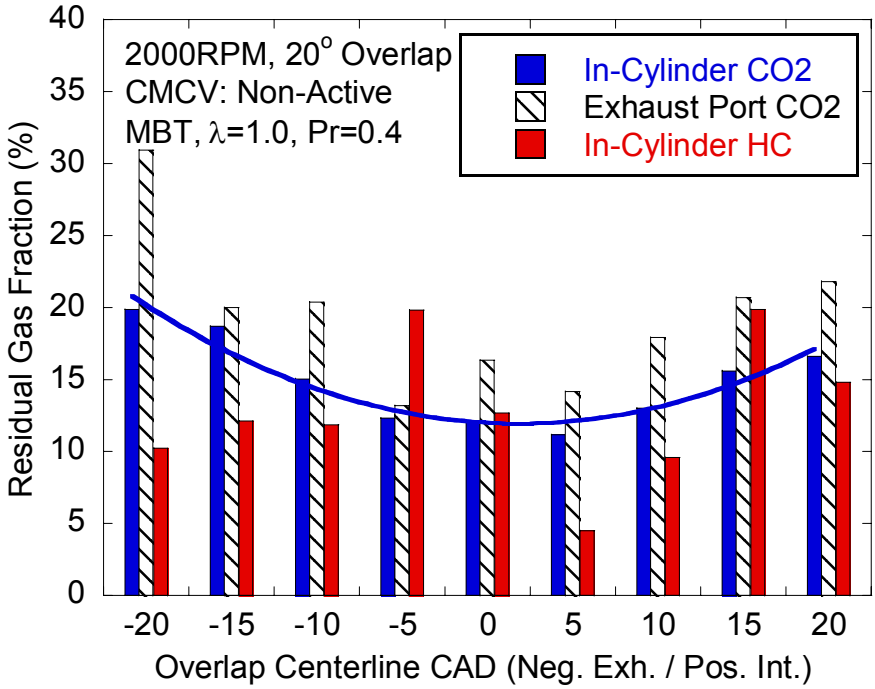

Figure 4.14: RGF increases as valve overlap centerline is shifted away from TDC. Shifting centerline into the exhaust stroke generates higher residual levels than an equal shift to the intake side due to the affect of piston motion on backflows.

Experimental data analysis suggests the in-cylinder CO_2 measurement method exhibits the lowest variability and most consistent trends, relative to engine variables, of the methods tested. For these reasons, the in-cylinder CO_2 measurement is used to compare the relative accuracy of the remaining two methods over all engine test points in Figure 4.15 and Figure 4.16.

Accuracy of residual fraction measurement using in-cylinder HC concentration, with respect to the in-cylinder CO_2 method, (Figure 4.15) shows a strong dependence on charge motion control valve state. Charge motion increases dramatically when the CMCV is active, when in-cylinder fuel distribution is expected to be more uniform than the case of a non-active CMCV. Perfect mixing of residual, air, and fuel is a main

assumption of any single point in-cylinder measurement, and high charge motion appears to significantly improve measurement results.

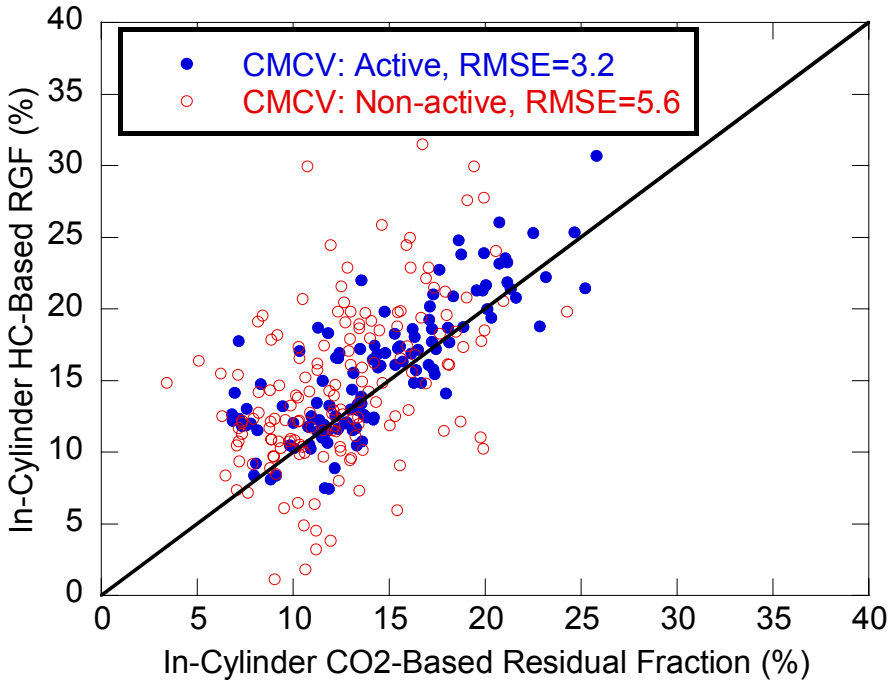

Figure 4.15: The in-cylinder HC method shows good agreement with the in-cylinder CO_2 method when the CMCV is active, but the correlation diminishes without the CMCV

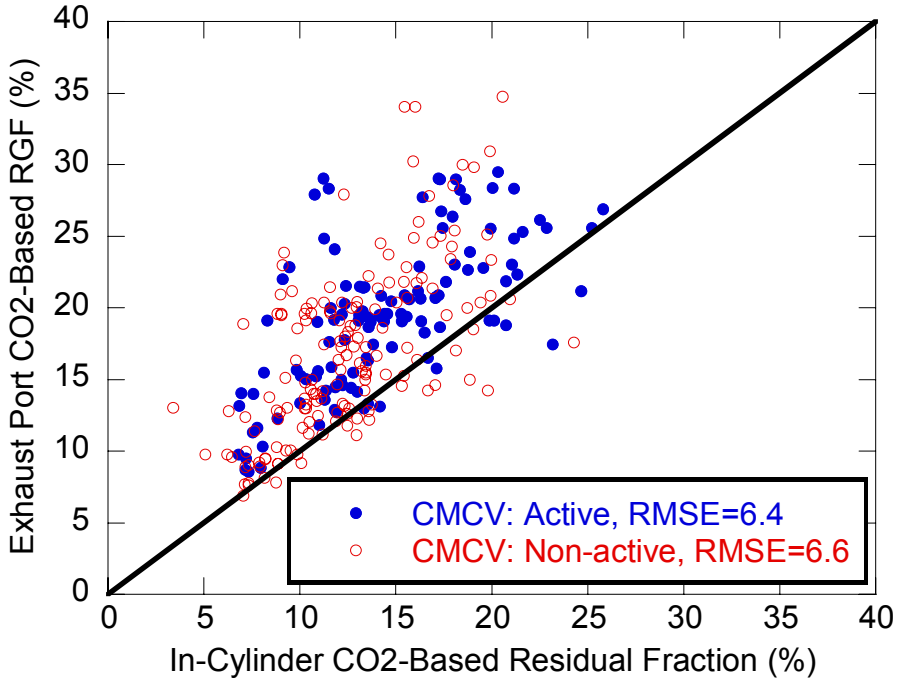

Figure 4.16: The single exhaust port-mounted CO_2 sensor over-estimates RGF as compared to the in-cylinder CO_2 method and shows little dependence on CMCV state

The exhaust port CO_2 based RGF measurement method is compared to the in-cylinder CO_2 method in Figure 4.16. Because this technique measures pre-combustion gases in the exhaust port, after a misfire, it is well-mixed and insensitive to CMCV state. In general, this method over-estimates RGF by several percent as compared to the in-cylinder CO_2 based method. The over-estimation is likely caused by poor mixing of exhaust backflow gases with pre-combustion gases and error in backflow quantity calculation. Overall, the accuracy of this method is not as good as using in-cylinder HC or CO_2 measurements.

4.8 Charge Motion Control Valve (CMCV) Influence on RGF

The affect of CMCV activation state on RGF is important to quantify for the purpose of engine control. Figure 4.17 shows the residual gas fraction as a function of pressure ratio for similar operating conditions. The pressure ratio calculation method is critical for proper comparison between CMCV states. Intake manifold absolute pressure (MAP) is calculated by averaging a crank-angle resolved pressure sensor during the intake stroke. The Kistler Type 4045A2 manifold pressure sensor and is located upstream of the intake valve but downstream of the charge motion valve. Sensor placement downstream of the CMCV is required for accurate MAP calculation because flow is throttled across the CMCV during the intake stroke. Average exhaust pressure is similarly calculated using a water-cooled exhaust port-mounted crank-angle resolved pressure sensor. Both blocked and unblocked CMCV states indicate the expected RGF trend with pressure ratio. When pressure ratio is calculated using an intake manifold pressure sensor downstream of the CMCV there is little RGF difference between CMCV activation states. If intake manifold pressure were calculated upstream of the CMCV a higher pressure ratio would be calculated when the CMCV was active, or blocked. The

alternate pressure ratio calculation would shift the blocked data curves to the right in Figure 4.17, increasing the observed RGF for a given pressure ratio.

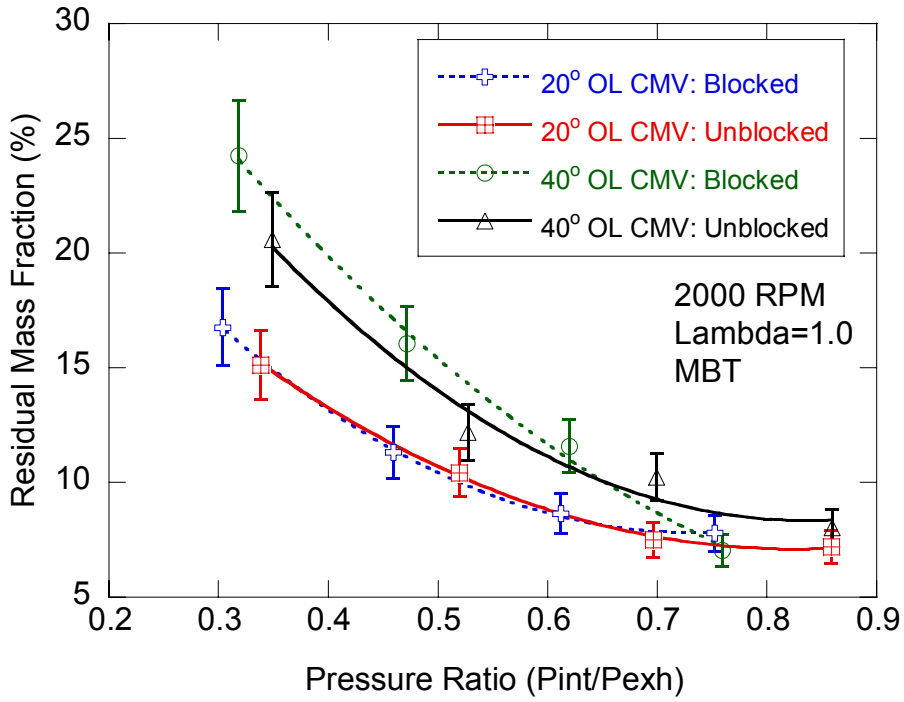

Figure 4.17: The CMCV activation state does not have a large affect on RGF as a function of pressure ratio.

4.9 Discussion of Negative Valve Overlap Operation RGF Trends

The previous discussion focused primarily on engine operation using positive valve overlap. Using negative valve overlap changes the mechanisms by which residual gas fraction is generated are different than during positive overlap operation. In-depth discussion of several engine parameters during negative overlap operation is provided in the following section. All RGF data is measured using the in-cylinder CO_2 measurement technique and an uncertainty of ±10% is assumed for all data points.

Negative valve overlap occurs when the exhaust valve(s) closes (EVC) prior to intake valve(s) opening (IVO). EVC prior to the end of the exhaust stroke creates a re-compression driven by piston motion, as in Figure 4.18. Re-compression begins prior to EVC due to flow restrictions at low valve lifts. Exhaust re-compression can also occur at

low values of positive overlap because valve flow areas are small and piston driven flows become restricted. Negative overlap with EVC occurring in the intake stroke is not possible with the test engine due to mechanical constraints. It is important to note that advancing the exhaust cam to generate negative overlap causes early blow-down and reducing expansion work (See Figure 4.18). The loss of expansion work may be balanced by a reduction in exhaust stroke pumping losses under certain operating conditions (Asmus 1982).

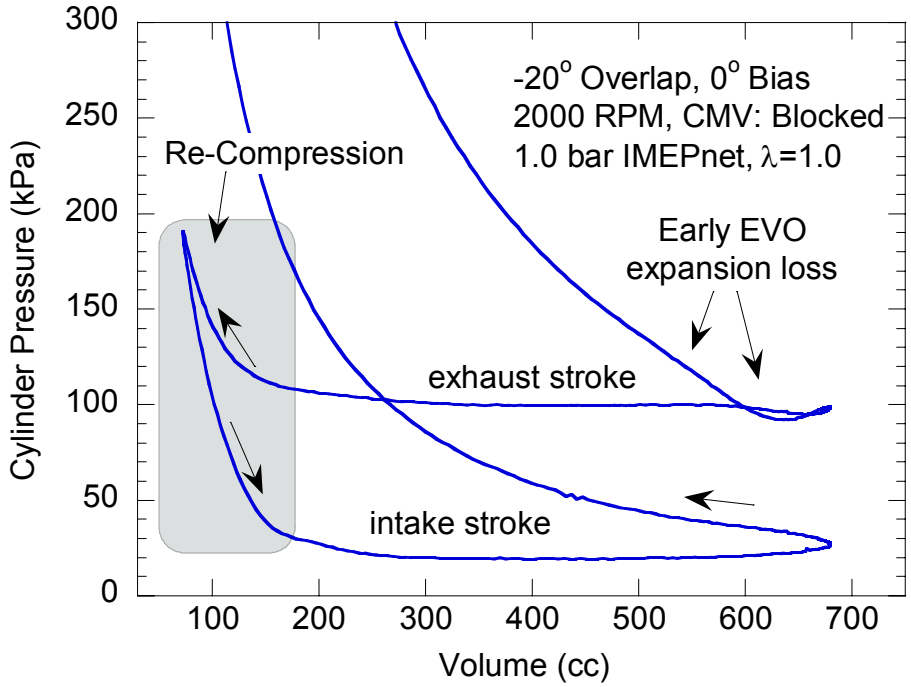

Figure 4.18: An example of exhaust re-compression created by the combination of negative valve overlap and piston motion

Negative overlap is an effective way to accurately control residual gas fraction. Unlike the case of positive overlap that has complicated backflows involving both intake and exhaust valves open concurrently, negative overlap strategies allow simpler residual mass prediction. The total residual mass for a given cycle is determined by the mass of exhaust gas in the cylinder at EVC. Any backflows that may occur after EVC are only between the cylinder and the intake system, and it is assumed that all exhaust backflows

into the intake manifold will re-enter the cylinder during the intake stroke of the same cycle during steady-state operation.

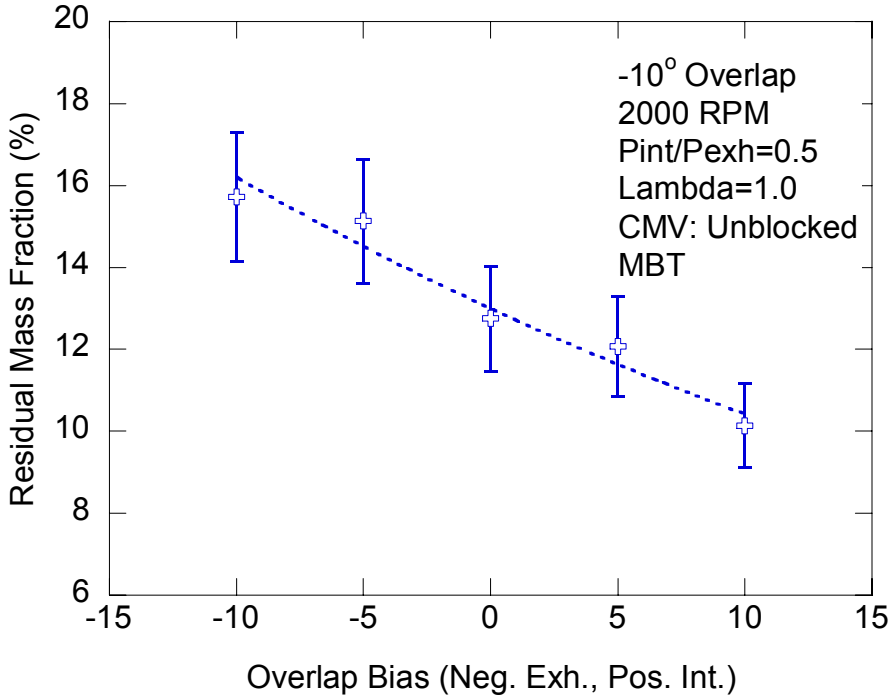

Figure 4.19: RGF decreases as overlap centerline is shifted from the exhaust to the intake stroke. Shifting centerline further into the intake stroke is expected to cause RGF to increase due to increasing cylinder volume at EVC.

Residual gas fraction measurements for an overlap centerline sweep at -10° overlap and a constant pressure ratio are shown in Figure 4.19. RGF decreases as overlap centerline is shifted to the intake stroke, following the trend of total cylinder volume at EVC. Further shifting of the centerline into the intake stroke is expected to cause RGF to increase due to a larger cylinder volume at EVC, but the phasing system is mechanically limited to the range in Figure 4.19. Increase in RGF with a centerline location in the intake stroke is not observed here because EVC only occurs slightly after TDC, where cylinder volume rate of change is small. In the most extreme case (10° intake bias) the exhaust valve only closes at 5° ATDC.

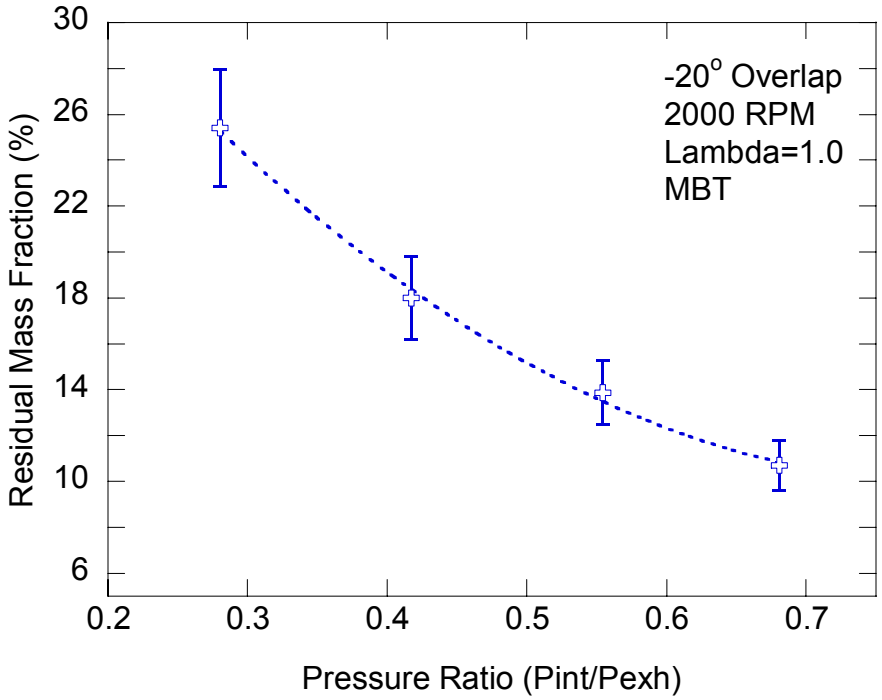

Figure 4.20: Increasing pressure ratio lowers RGF under negative overlap conditions

Increasing pressure ratio decreases RGF under negative overlap conditions. For the case of -20° overlap and 2000 rpm (Figure 4.20) residual fraction levels around 26% occur at a pressure ratio of 0.28. This level of residual approaches the stability limit for this particular engine. Masses of fuel, residual, and air per cycle for the data in Figure 4.20 are given in Figure 4.21. It is important to note that residual mass increases slightly with pressure ratio, but residual gas fraction decreases due to increased air mass. Total residual mass increases slightly due to higher exhaust pressures created by increased total mass flow rate (Figure 4.22). However, total residual mass does not change significantly with pressure ratio because the exhaust gas density within the cylinder near the end of the exhaust stroke does not vary greatly; similar amounts of residual mass are trapped at EVC regardless of pressure ratio.

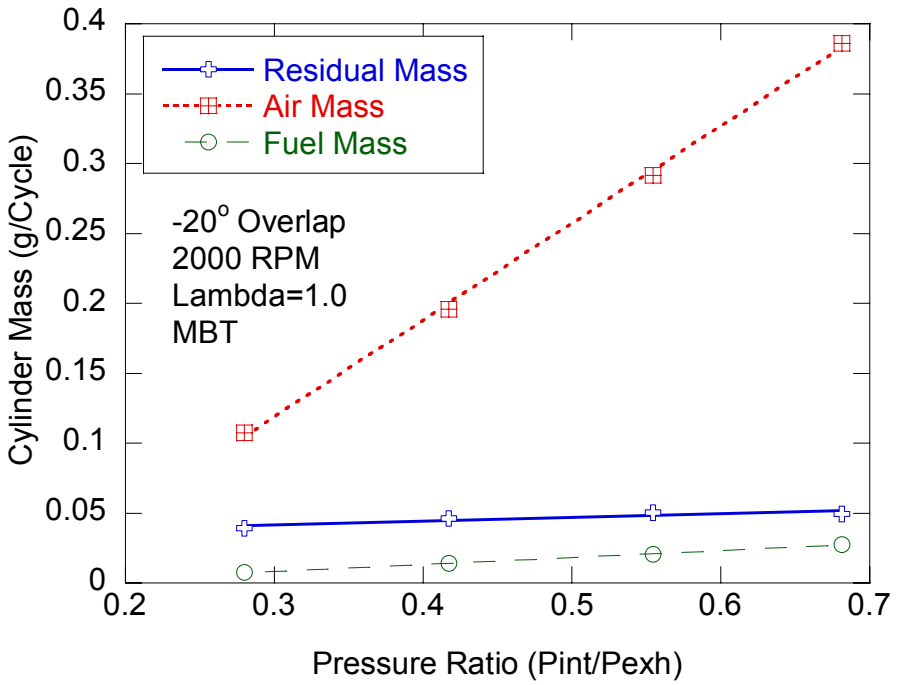

Figure 4.21: The increase in air mass per cycle overshadows a slight increase in residual mass as engine pressure ratio increases, reducing RGF

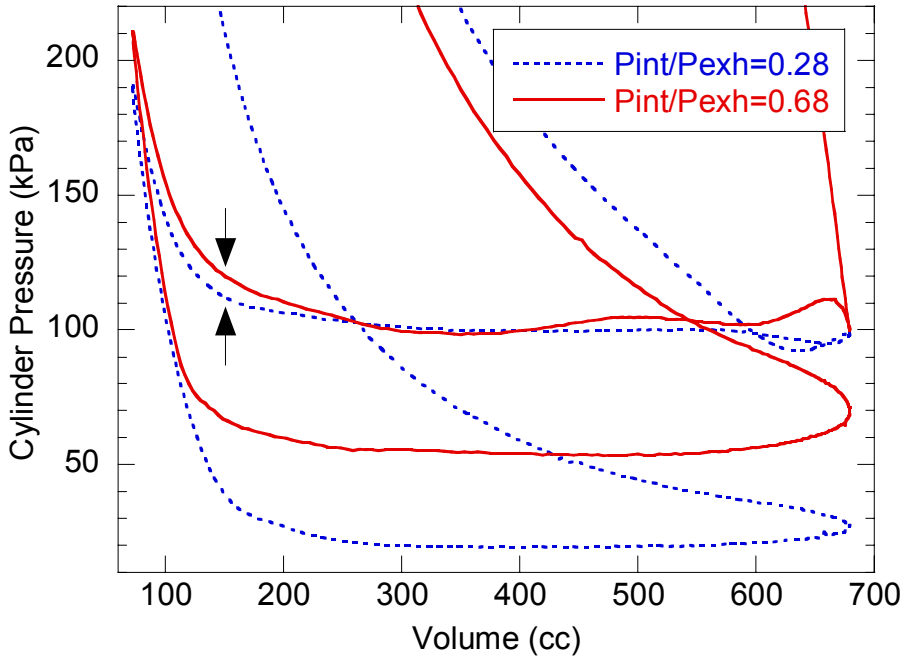

Figure 4.22: High exhaust flow rates elevate exhaust pressure and consequently total trapped residual mass at high pressure ratios

4.10 Residual Gas Fraction Prediction Model Correlation and Comparison

Prediction of residual fraction is essential for engine control strategies in high degree of freedom engines. Existing RGF prediction models vary in complexity from semi-empirical correlations (Fox et al. 1993; Shayler et al. 2000; Shayler et al. 2004; Amer and Zhong 2006) to three-dimensional CFD-based simulations (Senecal et at. 1996). Semi-empirical models are attractive for engine control purposes because they allow fast RGF prediction with relatively low computer processing time as compared to more complicated zero, one, or three-dimensional models. The experimental data acquired from the test engine using the in-cylinder CO_2 measurement method allows for the calibration and comparison of existing semi-empirical RGF prediction models. Commonly used models developed by Shayler et al. (2004), Amer and Zhong (2006), and Fox et al. (1993), are investigated for robust predictions over a wide range of operating conditions. The root mean squared error (RMSE) of predicted RGF to experimental measurement is used to gauge of the predictive ability of the models. RMSE accounts for variance in prediction as well as bias created by general under or over-prediction.

The semi-empirical model developed by Fox et al. (1993) separately calculates residual contribution of backflow during overlap from residual in-cylinder prior to overlap. The sum of both contributions is the total predicted residual fraction, as in Equation (4.17). Model constants C1 and C2 are determined by a linear fit to experimental data, as in Figure 4.23. The model is overly-sensitive to overlap factor (OF) at low overlap operating conditions (OF<=0.186 deg/m). Under these conditions residual fraction can be high due to restricted flow out of the cylinder near the end of the exhaust stroke. Additionally, both Albert and Ghandhi (2004) and Shayler et al. (2004) reported over-sensitivity to OF at overlap levels higher than those tested in this report. These observations are expected because the model was not originally formulated for such a large range of valve overlap. The re-calibrated model constants (C1: 0.235 and

C2: 0.6406) produced a RMSE of 2.6 as opposed to original model constants proposed by Fox (C1: 1.266 and C2: 0.632) which predicted with an RMSE of 6.5 to experimental data (See Figure 4.24). If low overlap data is excluded from calibration and prediction the RMSE of the Fox model significantly improves to 1.7.

$$Y_{RGF}^{Fox} = C_1 \frac{OF}{N}\left(\frac{p_i}{p_e}\right)^{-0.87}\sqrt{|p_e - p_i|} + C_2 \frac{\phi}{r_c}\left(\frac{p_i}{p_e}\right)^{-0.74} \tag{4.17}$$

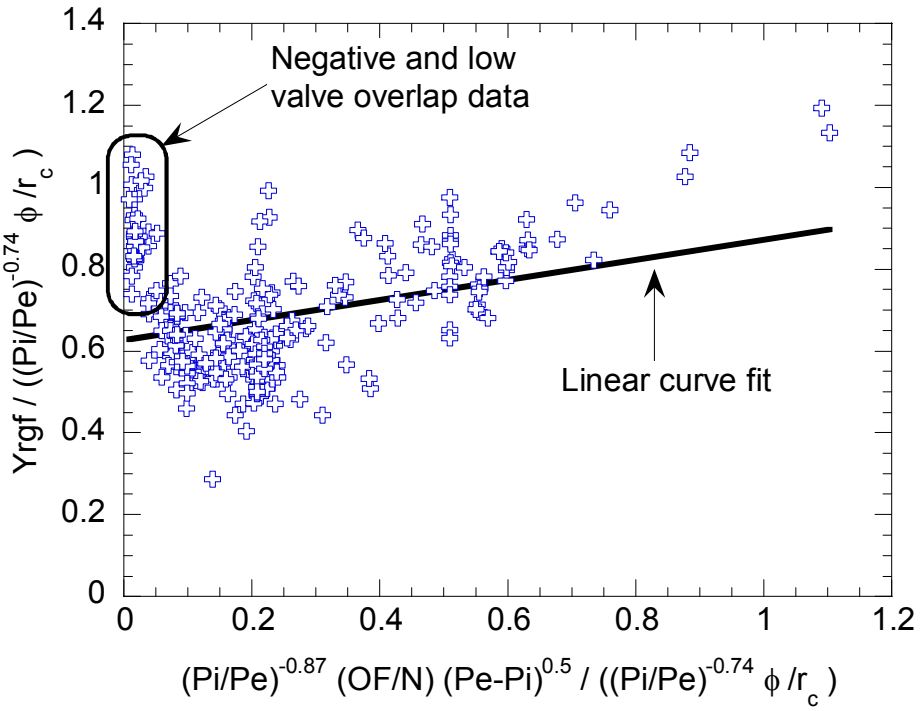

Figure 4.23: A linear fit of experimental data is used to calibrate constants C_1 and C_2 of the Fox model

Shayler et al. (2000) developed a residual fraction prediction model based on cylinder volumetric efficiency, pressure ratio, compression ratio, AFR, and EGR percentage. The model does not contain empirically fit constants (Equation (4.18)). Shayler et al. (2004) later expanded the model to better account for large backflow that occur when valve overlap is high. An equation, which is a function of valve overlap only, is fit to experimental data and then used to generate a fictitious EGR rate known as FEGR using Equation (4.20). The artificial FEGR is used along with the standard RGF

calculation to generate an improved prediction using Equation (4.19). RGF prediction using Equation (4.18) alone, without using FEGR, yields a RMSE of 2.5 to experimental data. Using the modified method with an overlap function fit to experimental data, Equation (4.21), generates RGF predictions with an RMSE of 2.4 (Figure 4.25). A slight improvement is gained using the FEGR approach; however the magnitude of backflow is under-estimated at low engine speeds, yielding low RGF predictions. Adding engine speed dependence to the FEGR calculation would likely improve predictive capability.

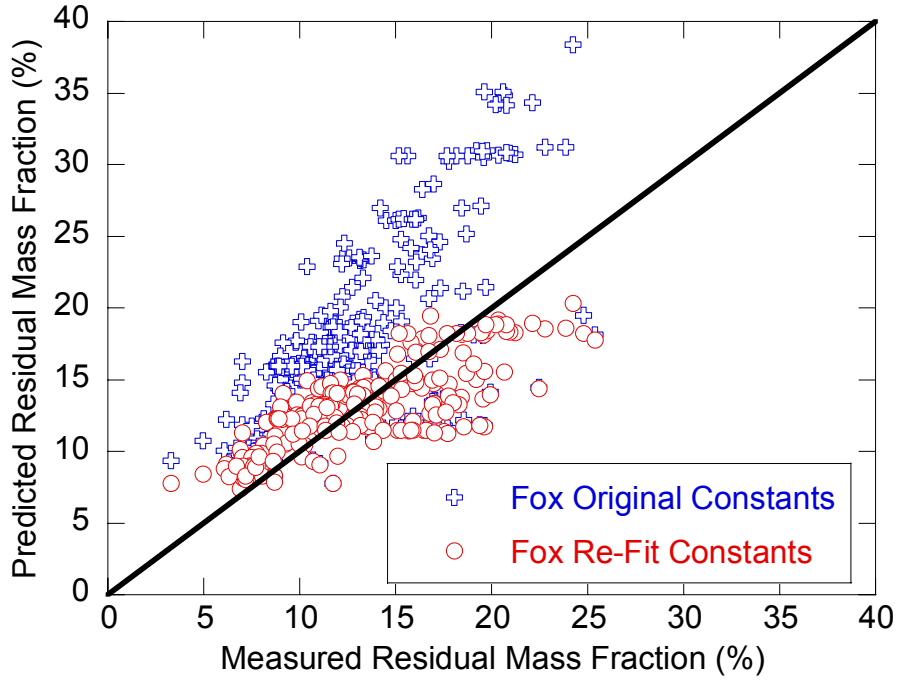

Figure 4.24: The Fox model prediction accuracy is greatly improved over the original model when the calibration constants are re-fit.

$$Y_{RGF}^{Shayler} = \frac{1}{1+2(r_c-1)\eta_v\left(\frac{AFR+1-EGR}{AFR(1-EGR)}\right)} \tag{4.18}$$

$$Y_{FEGR\_RGF}^{Shayler} = Y_{RGF}^{Shayler} + \frac{\left(1-Y_{RGF}^{Shayler}\right)\cdot AFR\cdot FEGR}{AFR+1-FEGR} \tag{4.19}$$

Where:

$$FEGR = \frac{fn(OL)}{\dot{m}_a + fn(OL)} \tag{4.20}$$

$$fn(OL) = 7\times10^{-7}(OL)^2 - 2\times10^{-5}(OL) - 0.0003 \tag{4.21}$$

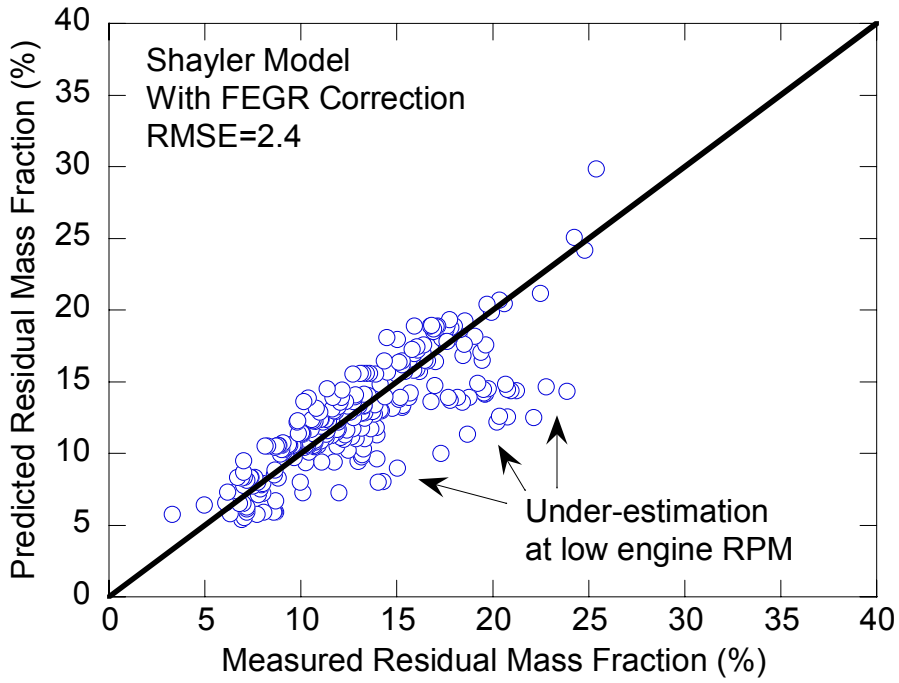

Figure 4.25: The model designed by Shayler yielded good predictive capability at medium to high engine speeds but under-predicted low RPM conditions.

Amer and Zhong (2006) made a modification to Equation (4.18) by removing the assumption that the product of engine temperature ratio and the ratio of clearance volume to displaced volume is constant, and equal to 2. The new variable, called the "density modifier term" or DMT, was fit to an equation relating RPM, overlap volume (OLV), volumetric efficiency (VE), and exhaust cam location (ECL). OLV is the integral of valve flow area over the crank-angle duration of overlap normalized by cylinder displacement (Asmus 1982). Typical units for OLV are (cm^2-CAD)/L. Figure 4.26, Figure 4.27, and Figure 4.28 confirm that DMT is a function of VE, OLV, ECL, and

RPM. The ideal density modifier terms where calculated using measured residual gas fraction and Equation (4.22). It is clear from the data that an equation fit to the density modifier term has the potential to improve the residual fraction estimate as compared to using a constant term.

$$Y_{RGF}^{Amer} = \frac{1}{1 + DMT\,(r_c - 1)\eta_v \left(\frac{AFR + 1 - EGR}{AFR\,(1 - EGR)} \right)} \tag{4.22}$$

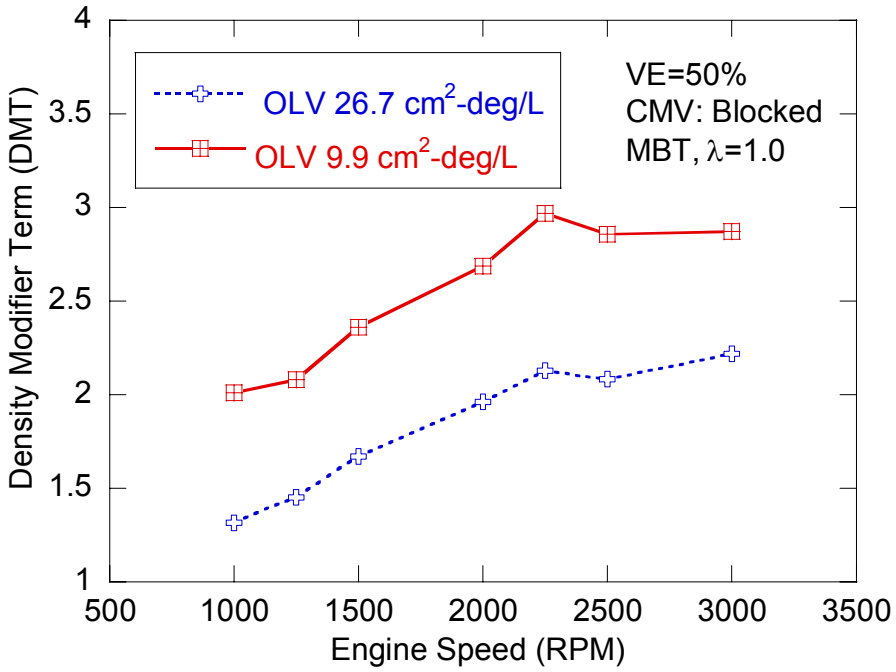

Figure 4.26: The density modifier term is a function of engine speed and overlap volume

The DMT equation proposed by Amer contained 25 constants that were fit using residual data generated with a 1-D engine simulation code. The exact details of the data fitting process where not disclosed, so a non-linear regression fit was used to generate a DMT equation from the data acquired for this report, using care to minimize over-fitting. The DMT model was calculated using a non-linear regression method in JMP statistical software. Only terms with a statistical significance level of less than 5% were considered for the equation fit. The predictors are centered about their mean values to create a more stable model. The model was calibrated using a random sampling of experimental data

(160 points), then used to predict RGF values for 160 new data points as well as the training data set. Table 4.3 lists the fit coefficients for each term of the equation. The DMT fit equation is assembled by adding together all ten Term/Coefficient products.

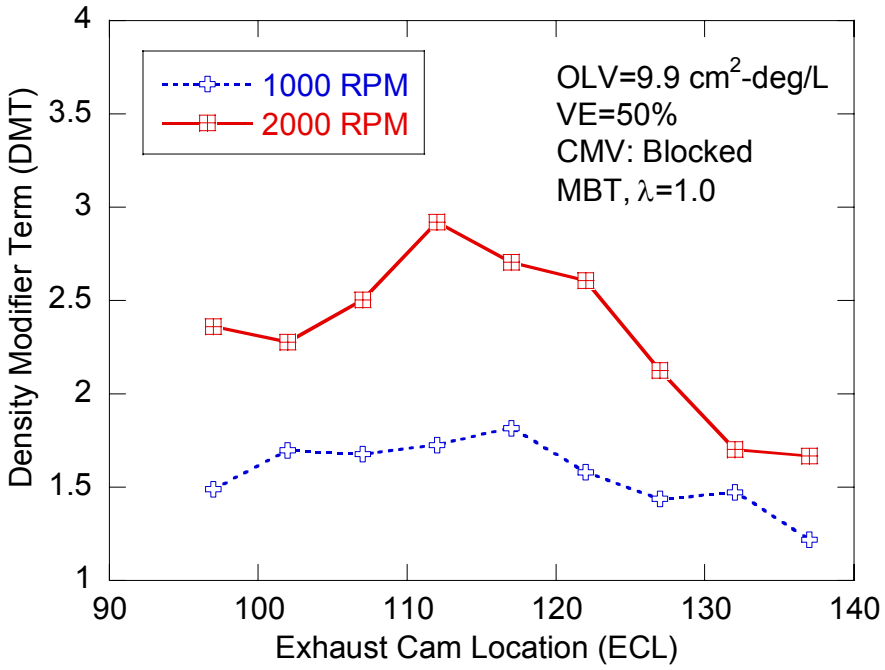

Figure 4.27: Exhaust cam location is related to valve overlap duration and centerline, both of which influence DMT

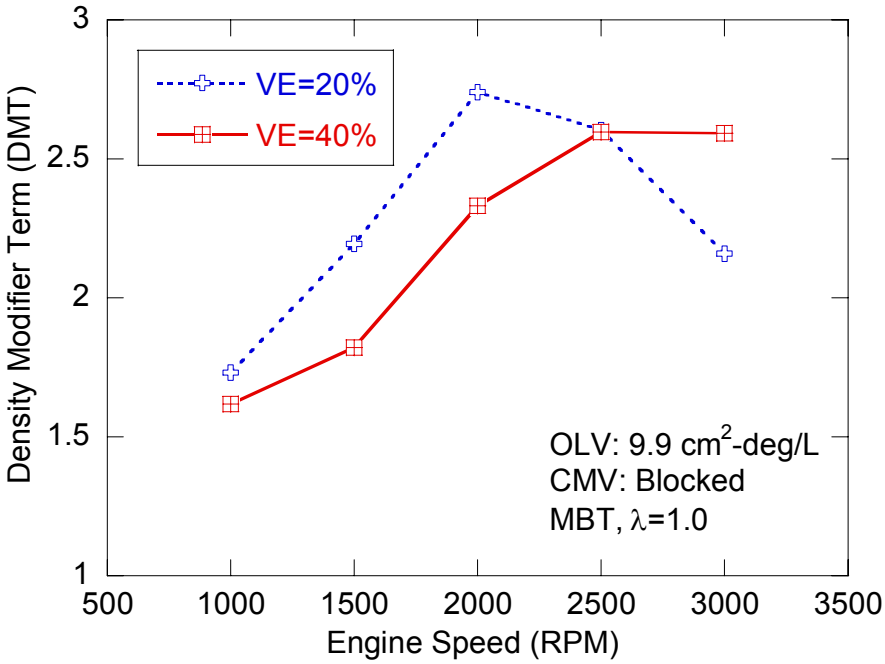

Figure 4.28: Volumetric efficiency variations alter the required density modifier term

Table 4.3: DMT Prediction Equation Terms

Coefficient	Term
5.630	Intercept
0.00019	RPM
-0.0262	ECL
-0.0153	OLV
-0.4467	VE
-1.962e-5	(RPM-2038.6)(ECL-119.7)
0.00286	(ECL-119.7)(OLV-10.0)
-0.000691	(RPM-2038.6)(VE-0.357)
0.6888	(OLV-10.0)(VE-0.357)
-3.487e-7	(RPM-2038.6)(RPM-2038.6)

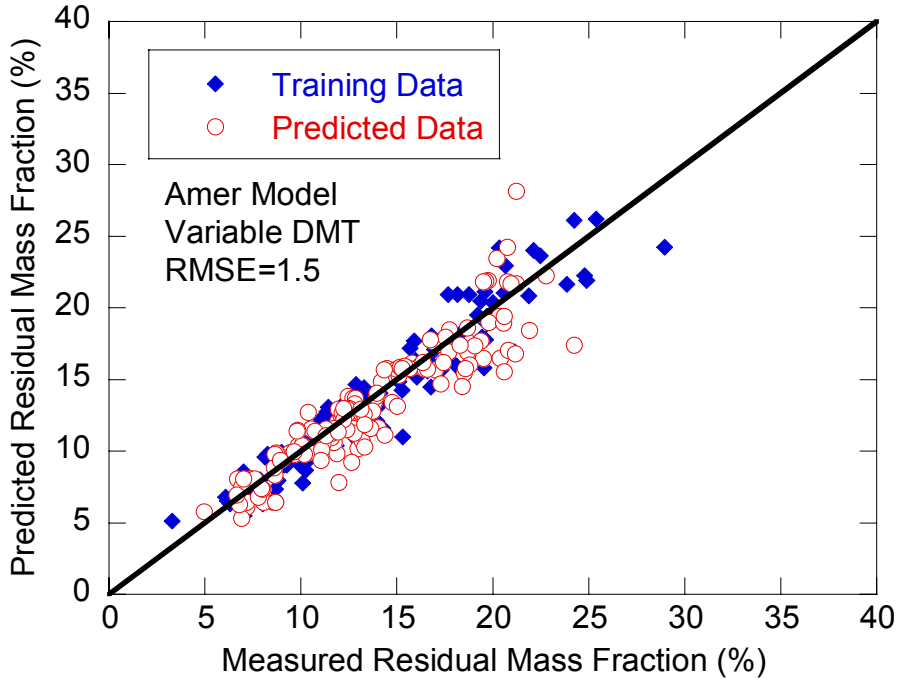

Figure 4.29: The RGF prediction method developed by Amer showed the lowest root mean squared error of all models tested

Predicted RGF data is plotted against experimental measurements in Figure 4.29. A RMSE of 1.7 for the predicted data points made this model the most accurate; however data over-fitting is a concern with such a complicated DMT equation. For this reason

large data sample sets and sound statistical analysis must be used when fitting the DMT equation. This model is used to calculate residual gas fraction for the ignition timing prediction model because it contains variables that are pre-existing within an engine controller and accuracy is sufficient.

4.11 Residual Gas Fraction Measurement Conclusion

High degree of freedom engines are capable of generating a wide range of internal residual gas fraction levels. It is important to quantify residual gas fraction because it significantly impacts laminar flame speed. Estimation of laminar flame speed is a critical input for spark timing prediction and combustion analysis. Several residual gas fraction measurement methods were described and compared in a liquid-fuelled variable valve timing engine. RGF measurements using each method were performed simultaneously in the same cylinder and engine cycle to ensure proper comparison. Variability of each technique was quantified by analyzing repeated measurements at each engine operating condition. Engine variables influencing residual gas fraction that are related to variable valve phasing were quantified and discussed. Conclusions pertaining to the accuracy of each method were assessed based on indicated RGF trends with the variation of engine speed, pressure ratio, valve overlap, and overlap centerline location. The effects of using the CMCV and negative valve overlap on RGF were also discussed. The recorded data was used to assess several existing semi-empirical models, and to calibrate the constants in the preferred model. Findings are summarized as follows:

- Response times of the NDIR500 and HFR500 are such that intentional misfire is required at or above 1500 rpm. The intentional misfire extends the available time for measurement of pre-combustion gases.
- Measurement variability for the in-cylinder CO_2 based method was determined to be +/- 10% (95% confidence level) for the method requiring

intentional misfire, the lowest of the three methods. Variability in both the in-cylinder HC and CO_2 based methods is greatly reduced when charge motion is high and the assumption of perfect mixing is valid.

- In-cylinder HC concentration is only a good indicator of RGF when charge motion is high. In this case, activating the charge motion control valve greatly improved measurement accuracy as compared to the results obtained using in-cylinder CO_2 measurement. Without the CMCV, in-cylinder HC levels were subject to large variability, producing inaccurate RGF results.
- Using a single exhaust port-mounted CO_2 sensor with an intentional misfire to measure pre-combustion gases produces high variability. The technique is simple, but it requires measurement compensation for over-expansion backflows that occur after the intentional misfire. In general, this method did not provide sufficiently accurate results as compared to the in-cylinder CO_2 based measurement.
- Measuring residual gas fraction using a fast response in-cylinder CO_2 sensor coupled with a separate exhaust port analyzer provided the lowest variability and consistent trend prediction.
- Operating with positive overlap, residual gas fraction is highly sensitive to pressure ratio across the engine. The highest RGF levels occur at low pressure ratios, where exhaust gas backflows are large. Overlap centerline location shifted to both side of TDC increases RGF, and exhaust biased centerline provides the highest residual levels. Increasing engine speed decreases the time available during overlap for backflows, therefore RGF reduces at high engine speeds
- The charge motion control valve (CMCV) activation state does not significantly affect measured RGF if pressure ratio is calculated using an

intake manifold pressure sensor located between the CMCV and the intake valve.

- Negative valve overlap operation allows for more predictable RGF because backflows are eliminated. Cylinder volume at EVC is the primary driver of RGF.
- Several semi-empirical RGF prediction models where examined. The model produced by Amer and Zhong (2006) provided the best predictive capability of the models tested. A formula for the density modifier term used in the Amer and Zhong model was calibrated based on the measurements from the 4-cylinder test engine equipped with variable valve timing.

CHAPTER 5

TURBULENCE INTENSITY CALCULATION ROUTINE

Devices such as variable valve timing, valve deactivation, and flow control valves can be used to significantly alter the rate of combustion. Prediction of optimal spark timing requires knowledge of the burn rate prior to combustion. Burn rate is strongly dependent on in-cylinder flows and charge composition along with several other factors. However, standard measurements acquired from an experimental test engine, such as cylinder pressure and emissions, do not characterize many important aspects of in-cylinder combustion. Added data processing routines, such as heat release analysis from cylinder pressure, are important for extracting the greatest amount of useable data from a certain set of measurements. However, heat release analysis only provides information about burn rate and does not provide specific combustion details, such as charge motion parameters or laminar flame speed. A data processing routine that provides insight into charge motion levels of experimental data is highly desirable from an engine control and calibration perspective. Such a method allows the separation of laminar flame speed and charge motion affects on combustion, providing greater versatility in ignition timing prediction and facilitating the addition of new engine technologies. The following sections propose a new calculation routine to estimate turbulence intensity from experimental data.

5.1 In-Cylinder Turbulence Calculation Routine

Single-zone heat release analysis does not explicitly describe or separate the effects of flame speed and in-cylinder turbulence on combustion. For this reason, heat release analysis alone does not provide all of the necessary information needed to describe the influence of flow altering devices (e.g. charge motion valves, variable valve timing, etc.) on combustion. In-depth combustion analysis is therefore required to separate the effects of turbulence intensity and laminar flame speed on burn rate. A method that combines experimental data with a turbulent combustion model would prove to be a powerful tool in predicting the effects of new technologies on engine operation. Experimentally determined burn rate and residual gas fraction values are used as inputs to a turbulent combustion model. The turbulent combustion model is then solved in reverse, yielding a representative value of in-cylinder turbulence. The following sections describe the derivation and results of the inverse-model used to calculate in-cylinder turbulence intensity.

5.1.1 Turbulence Intensity Calculation Derivation

The inverse-model is derived from the quasi-dimensional turbulent flame entrainment model introduced in Section 3.3. Equations (3.1) through (3.4) are solved for turbulence intensity using the following methodology. First, Equation (3.2) is solved for the entrained mass (See Equation (5.1) below). The derivative of Equation (5.1) is related to the rate of turbulent flame entrainment in Equation (5.2). The characteristic diffusive cell burn time, τ, is assumed constant during differentiation to simplify calculation.

$$m_e = m_b + \tau\left(\frac{dm_b}{dt}\right) \tag{5.1}$$

$$\underbrace{\left(\frac{d\tau}{dt}\right)\left(\frac{dm_b}{dt}\right)}_{Assume: d\tau/dt=0} + \tau\left(\frac{d^2m_b}{dt^2}\right) + \left(\frac{dm_b}{dt}\right) = \left(\frac{dm_e}{dt}\right) = \rho_{unburned}\, A_{flame}(u' + S_L) \tag{5.2}$$

To solve for u' Equation (5.2) is converted into a cubic polynomial (Equation (5.3)). The cubic polynomial can be solved graphically or numerically. Only positive real roots of the polynomial are acceptable solutions for u'. The mass-fraction burned curve from a single-zone heat release model is used as the input for the derivative of mass-burning rate. Flame front area, laminar flame speed, and unburned gas density and temperature are also calculated at each crank-angle.

$$u'^3 + 2\left(S_L - \frac{1}{\rho A}\frac{dm_b}{dt}\right)u'^2 + \left(S_L{}^2 + \frac{1}{(\rho A)^2}\left(\frac{dm_b}{dt}\right)^2 - \frac{2S_L}{\rho A}\frac{dm_b}{dt}\right)u' = \frac{15L\upsilon}{\xi(\rho A S_L)^2}\left(\frac{d^2m_b}{dt^2}\right)^2 \tag{5.3}$$

The calculation algorithm used to solve Equation (5.3) is shown in Figure 5.1. The process starts will the acquisition of engine data. Required data inputs include; bore, stroke, engine speed, equivalence ratio, fuel and air mass flow rates, ignition timing, residual fraction, and cylinder pressure phased with volume. The calculation interval starts with spark timing and finishes at the end of combustion. Heat release analysis provides the mass fraction burned profile for each operating condition. Burned and unburned mass at each crank angle is determined from the MFB profile and total air/fuel mass. Unburned gas volume is calculated using cylinder pressure, unburned gas temperature, mass and gas constant with the ideal gas law. Burned gas volume is determined from the difference of total cylinder and unburned gas volumes. The burned gas volume at each crank angle location is used along with an assumed flame thickness to look up a corresponding flame area using a geometrically determined look-up table. Turbulence intensity calculation during the flame development period is susceptible to error generated by noise in the cylinder pressure signal. To avoid erroneous results from signal noise the turbulence intensity calculation range is starts at two percent MFB and

continues until the end of combustion. The calculation starting location is determined arbitrarily.

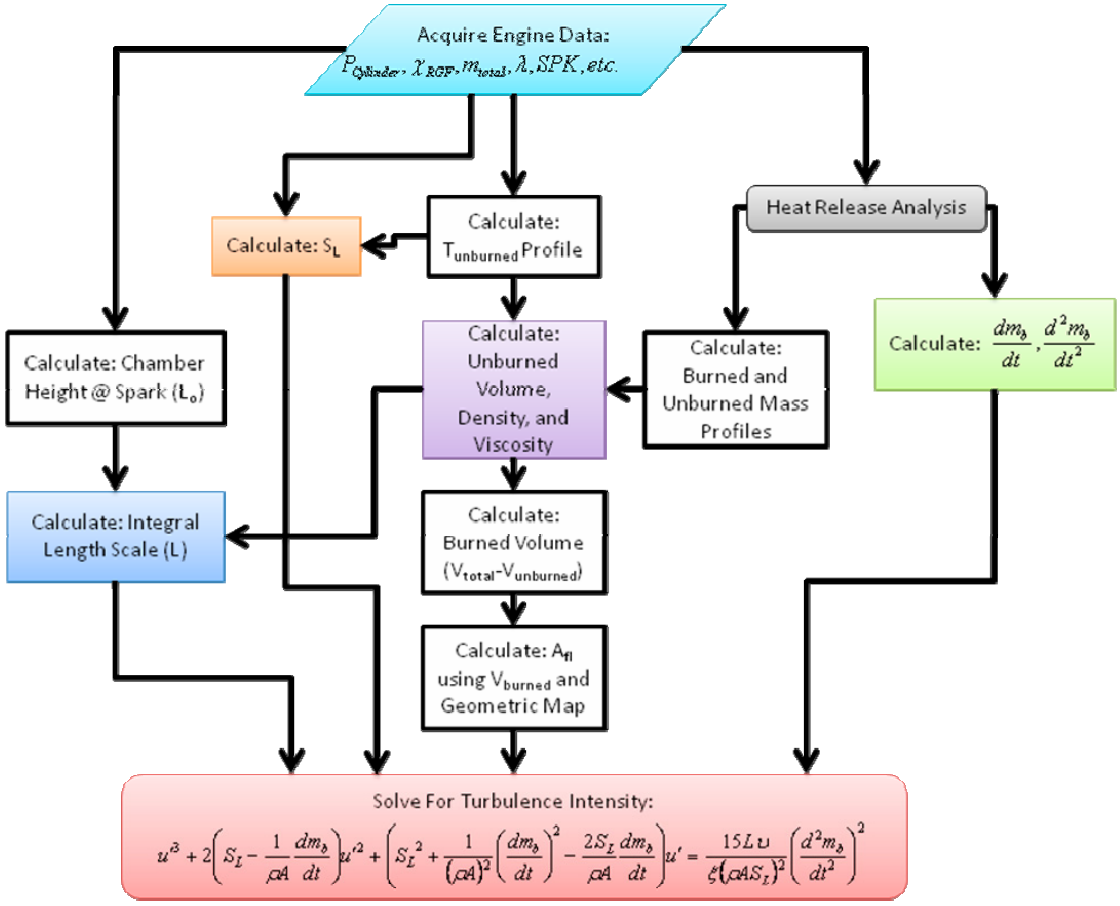

Figure 5.1: The turbulence intensity calculation algorithm

5.1.2 Gas Property and Flame Front Area Calculations

Cylinder contents are divided into two separate calculation zones, burned and unburned gases. Separate properties are calculated for each section. Several assumptions are made to calculate properties for both the unburned and burned zones. Unburned contents are assumed to compress in an isentropic manner during combustion. Burned zone properties are calculated using information from heat release analysis and unburned zone calculations. Specific calculation methods for each variable are described in the following section.

Burned and Unburned Mass as a Function of Crank Angle

A mass fraction burned (MFB) profile is required for the turbulence intensity calculation. The MFB profile can be determine either by a thermodynamic heat release routine or by a cylinder pressure based method, such as Rasswieler and Withrow (1938). Total unburned in-cylinder mass is calculated from fuel and air flow rates. Residual gas and EGR are assumed to be comprised solely of post-combustion gases, and therefore are not represented in the MFB profile. Burned mass at each crank angle is calculated from the product of the initial air and fuel mass and MFB. The unburned mass fraction profile is calculated from the difference of the initial air and fuel mass and the burned mass.

Unburned Charge Temperature Volume and Density

Pre-combustion gases ahead of the flame front are compressed during combustion because post-combustion gases have a lower density. The compression process is assumed isentropic with the ratio of specific heats determined from cylinder pressure data during the compression process (See Section 4.6). Unburned gas temperature is initialized as the average cylinder temperature calculated during heat release at the time of spark. During combustion, unburned gas temperature profile is calculated using Equation (5.4) for the duration of combustion. Unburned charge density is calculated using the ideal gas law and the known values of temperature, pressure, and gas constant. Unburned volume is calculated using the unburned mass profile that is determined from heat release analysis. Heat transfer is not considered during the turbulence intensity routine since it has already been accounted for during heat release analysis.

$$T_{unburned,i} = T_{cylinder}^{spark}\left(\frac{P_{cylinder,i}}{P_{cylinder}^{spark}}\right)^{\left(\gamma-1/\gamma\right)} \tag{5.4}$$

Burned Gas Volume Calculation

The volume of burned gas at each crank angle is required to generate an entrained flame area estimate. In this case, unburned volume is used to determine burned gas volume at each crank angle according to Equation (5.5), assuming flame volume is small. Post-combustion flame temperature can then be calculated using the ideal gas law because burned gas mass, volume, pressure, and gas constant are known.

$$V_{burned,i} = V_{cylinder,i} - V_{unburned,i} \tag{5.5}$$

Entrained Flame Area Estimation

A geometrically calculated flame area table, identical to that used for the cycle simulation, is employed in the turbulence intensity calculation. As discussed in Section 3.3.1, the flame-area table is generated using engine-specific combustion chamber geometry. The table relates a given entrained gas volume, at a specific crank angle, to a flame radius representing the distance of the flame-front leading edge from the ignition location. Flame front radius is geometrically related to the entrained flame area at each crank-angle. The difference in entrained radius and burned radius defines a flame thickness. The entrained volume contains both burned and some unburned gases, and is therefore larger than the burned-gas volume. Entrained volume, or radius, is required to determine the entrained flame area at each crank angle location. However, the entrained volume is not an output of heat release analysis, so it must be determined using the known burned gas radius and an assumed flame thickness. Flame thickness (assumed constant) is added to the burned gas radius to generate an entrained radius. The entrained radius is then mapped to an entrained flame area at each crank angle. The flame area relationships to entrained gas volume for a range of crank angle positions are shown in Figure 5.2. Flame area relationships were calculated for intervals of four crank angles for this report; linear interpolation is used for locations between the tabulated crank angles.

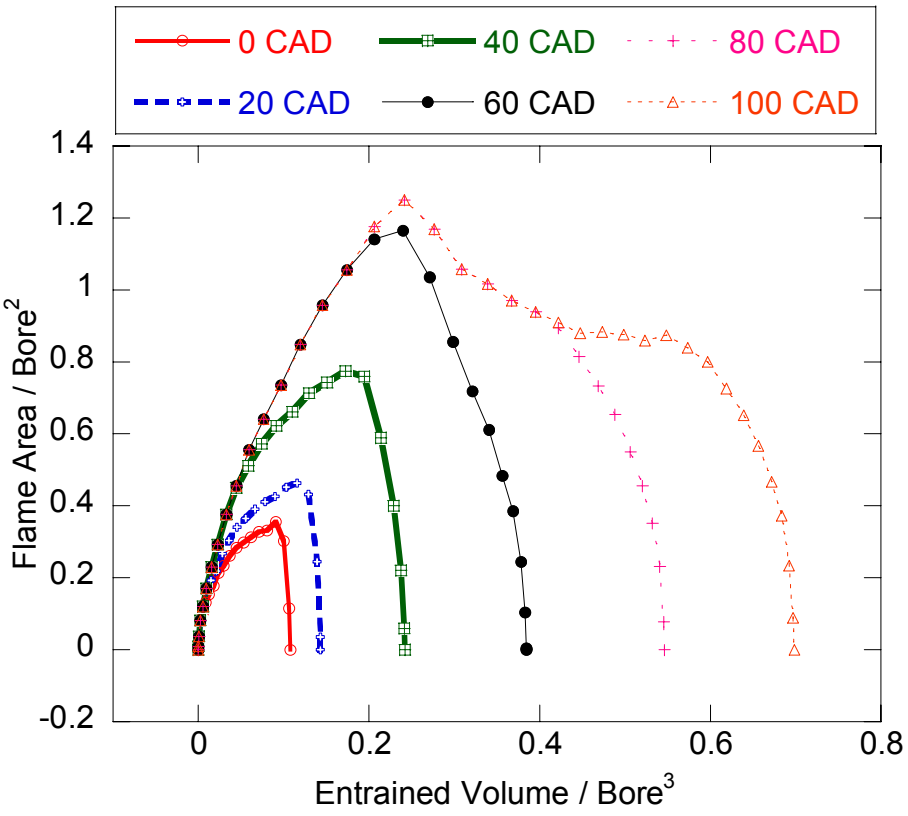

Figure 5.2: The geometrically calculated map is used to determine flame front area at each calculation step from the calculated entrained gas volume.

Integral Length Scale

The integral length scale is used to describe eddy size, and is the largest scale defined in a turbulent flow field. During combustion the integral length scale is calculated using Equation (5.6), and is based on the conservation of angular momentum and mass (Filipi and Assanis 2000). At ignition the integral length scale is initialized as the instantaneous combustion chamber height, determined by dividing cylinder volume by bore area. Instantaneous chamber height calculated over entire spark timing range of the test engine is shown in Figure 5.3. Unburned gas density calculation is calculated using the ideal gas law.

$$L = L_{o,spark}\left(\frac{\rho_{uo,spark}}{\rho_u}\right)^{\frac{1}{3}} \tag{5.6}$$

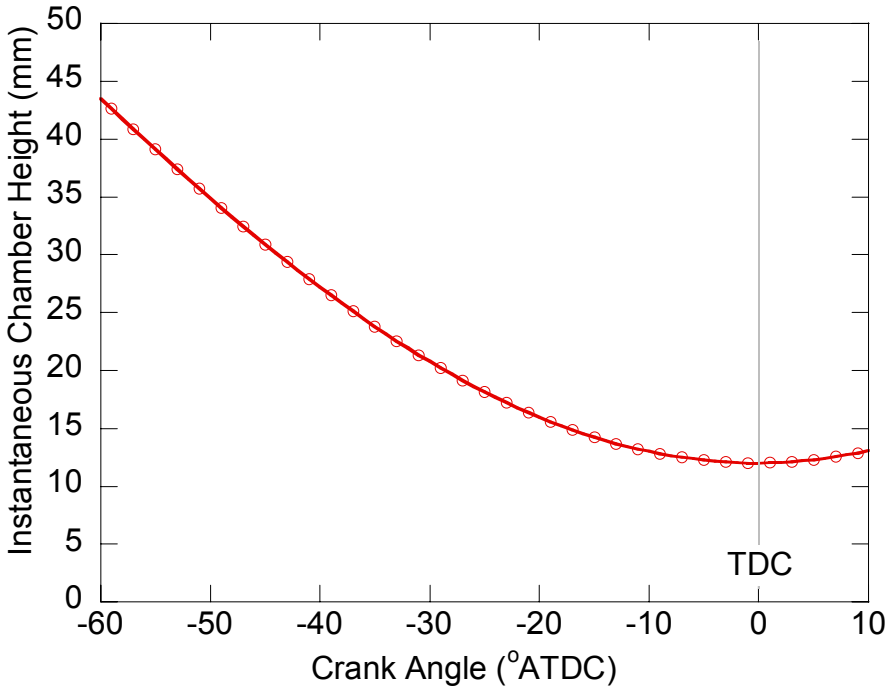

Figure 5.3: Instantaneous combustion chamber height, Lo, as a function of crank angle for the 2.4L test engine

Kinematic Viscosity

Kinematic viscosity, ν, of the unburned mixture is calculated by dividing dynamic viscosity, μ, by gas density. The dynamic viscosity of air is used to represent the unburned mixture because it is similar to that of an air/fuel mixture (Heywood 1988), and is described as a function of temperature in Equation (5.7). The unburned gas temperature and density are used to calculate kinematic viscosity.

$$\mu_{unburned}\left[\frac{kg}{m\cdot s}\right] = \left(3.3\times10^{-7}\right)T_{unburned,K}^{0.7} \tag{5.7}$$

Laminar Flame Speed

The laminar flame speed for the unburned mixture ahead of the flame front is calculated at each crank angle using the method described in Section 3.3.2. Flame speed is a function of residual gas fraction, air-to-fuel ratio, pressure and unburned gas

temperature. Of these factors, residual gas fraction has the largest impact on laminar flame speed (Heywood, 1988) (See Section 3.3.2). Laminar flame speed at conditions similar to those at ignition is shown as a function of residual gas fraction in Figure 3.6.

5.2 Validation of Turbulence Prediction Model

Turbulence intensity prediction model results are verified using a spark-ignition cycle simulation, described in Chapter 3. Experimental data is used to calibrate the cycle simulation by matching burn rate and IMEP, as described in Appendix C. The simulated combustion period is of primary interest because the inverse-model only calculates turbulence intensity during combustion. The spark-ignition simulation model calibrates to within a two percent of experimentally measured burn rates. The close correlation allows simulated results to be used in the place of data that is difficult or impossible to measure experimentally. The inverse-model turbulence intensity results are therefore compared with simulation levels to determine the relative accuracy of the new process. Inverse-model and cycle-simulation turbulence intensity results from 2% to 90% MFB for a single operating condition are shown in Figure 5.4

Turbulence intensity results from the inverse-model are close to simulated levels during early combustion. Late combustion prediction levels deviate significantly from simulated results. The deterioration in the turbulence intensity prediction after the early stages of combustion is caused by a combination of derivation assumptions and calculation methods. Assuming constant laminar burning time, τ, causes some of the discrepancy with simulation results. Calculated values for each of the three terms on the left-hand side of Equation (5.2) are plotted with respect to crank angle in Figure 5.5. The sum of these terms represents the rate of mass entrainment. The nature of the calculation is that higher mass entrainment rates will increase the turbulence intensity estimate. Neglecting the laminar burn-up time rate of change will increase the rate of mass

entrainment and therefore increase calculated turbulence intensity. Rates of mass entrainment with and without the assumption that laminar burn time is constant are shown in Figure 5.6 for the same operating condition in Figure 5.4. In general, neglecting $d\tau/dt$ has little affect on mass entrainment rate during early combustion, but the error increases to just under 20% during the middle and late combustion stages. The error generated by neglecting $d\tau/dt$ is not significant enough to account for the differences between turbulence intensity calculated from experimental data and simulation.

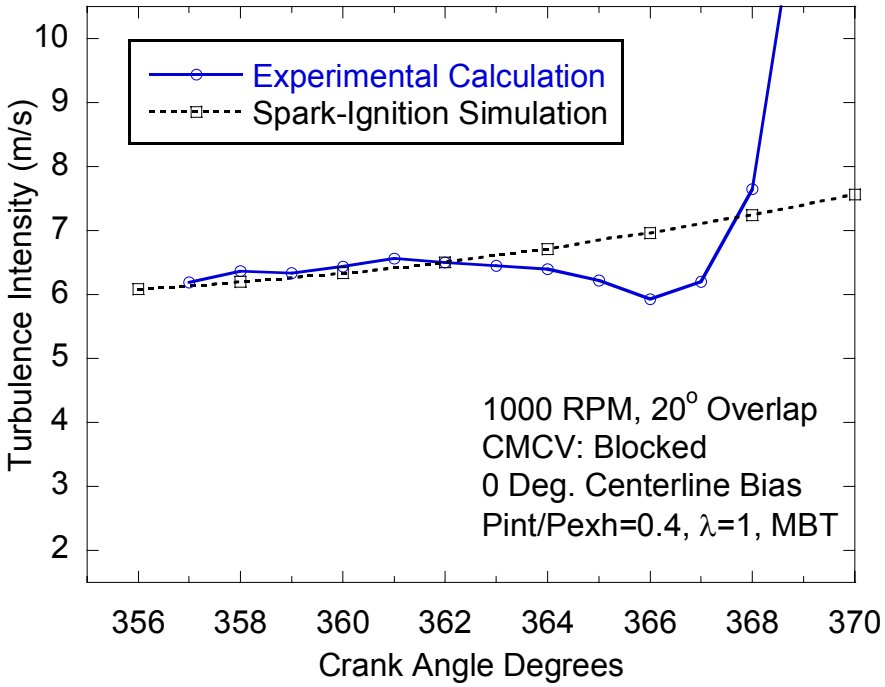

Figure 5.4: The experimental calculation agrees well with simulation results during the early stages of combustion. Calculation accuracy decreases later in the combustion process due to derivation assumptions.

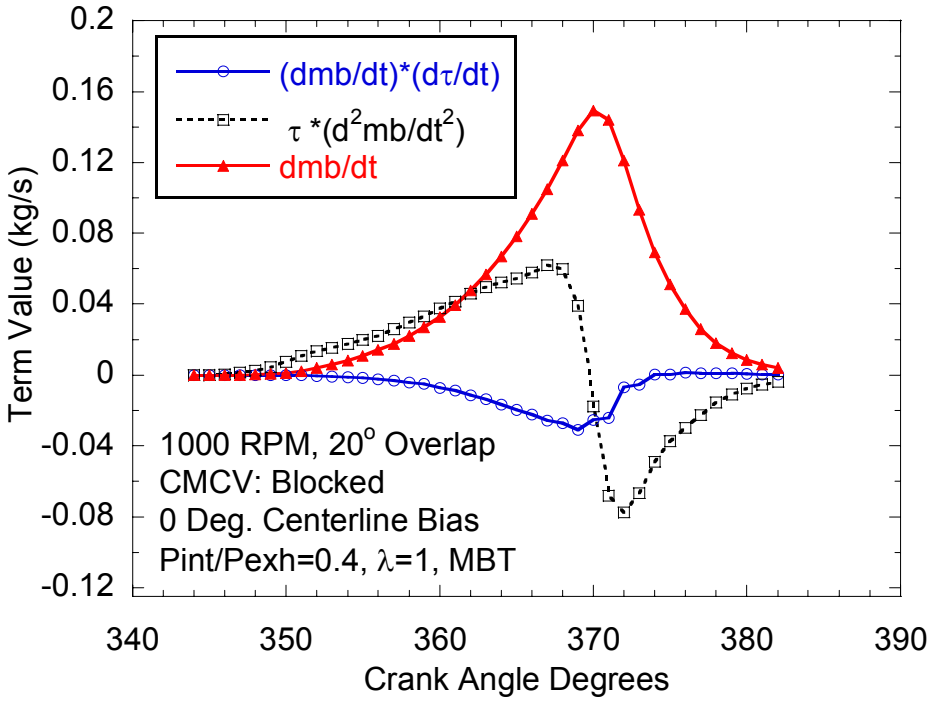

Figure 5.5: The three terms that sum to define the rate of mass entrainment on the left-hand side Equation (5.2). The first term, (dmb/dt)*(dτ/dt), is makes the smallest contribution to mass entrainment rate and is neglected for simplicity.

The entrained flame area is critical to the turbulence intensity calculation accuracy. In general, a flame area greater than the actual area will reduce the turbulence intensity estimate, and lowering flame area will increase the prediction. Predicted and simulated entrained flame front areas for the combustion process are shown in Figure 5.7. Using an assumed flame thickness of 6 mm provides good correlation with simulation results during early combustion, but underestimates area late in combustion. The assumed flame thickness value was determined by trial and error, and acts as a calibration constant for flame area. The flame thickness used is much higher than expected (1-3 mm is the typical range of flame thickness calculated in the cycle simulation); however, it is used to make up for errors in burned volume calculation early in combustion. The elevated flame thickness causes early flame/cylinder-wall contact, lowering predicted flame area late in combustion. The lower area late in combustion greatly increases the turbulence intensity estimate, and the estimation becomes invalid.

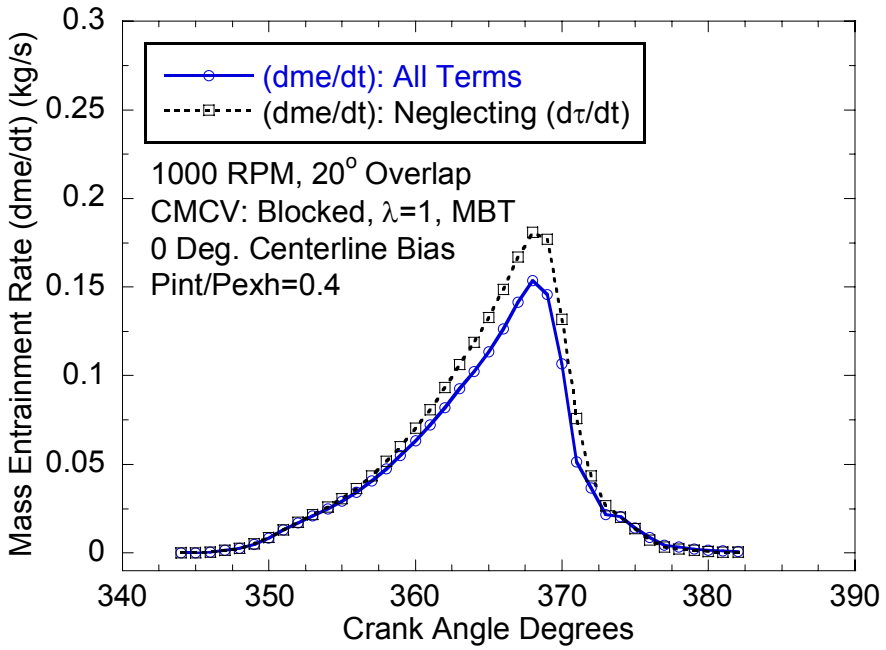

Figure 5.6: Neglecting the change in laminar burning time creates an over-estimate of mass entrainment rate. The assumption does not create significant error in early combustion, but error increases to around 20% during middle to late combustion.

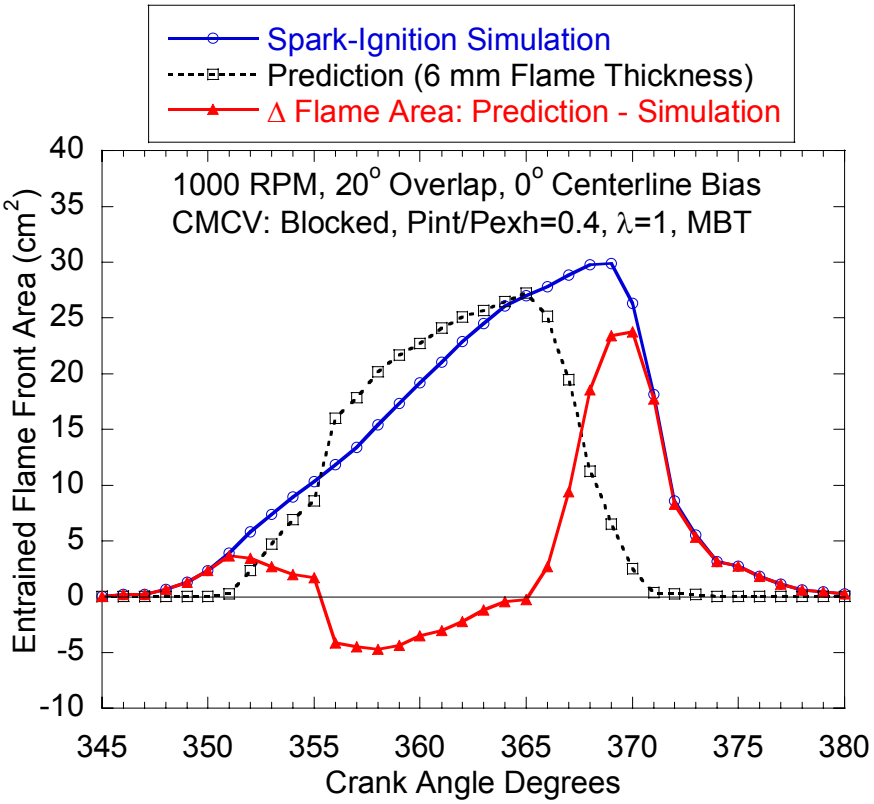

Figure 5.7: Predicted flame front area differs from the simulated value throughout the combustion process, and affects turbulence intensity prediction accuracy.

The sensitivity of the calculated turbulence intensity to the predicted entrained flame front area is shown in Figure 5.8. Predicted flame entrainment area depends upon the burned gas volume and flame thickness at each crank angle location. Burned gas volume is calculated based on unburned gas properties, so proper unburned gas treatment is critical. In general, decreasing unburned gas temperature will create a larger burned gas volume and entrained flame front area early in combustion. During middle to late combustion, when flame contact with walls becomes more significant, the flame area will decrease faster if unburned gas temperature (or density) is decreased. Flame thickness also influences the entrained flame front area prediction. Assuming a thicker flame will effectively shift the predicted entrained flame front area earlier in the combustion process, and a smaller flame thickness will shift the area profile later. The flame thickness was selected to match simulation results for early combustion (5-10% MFB).

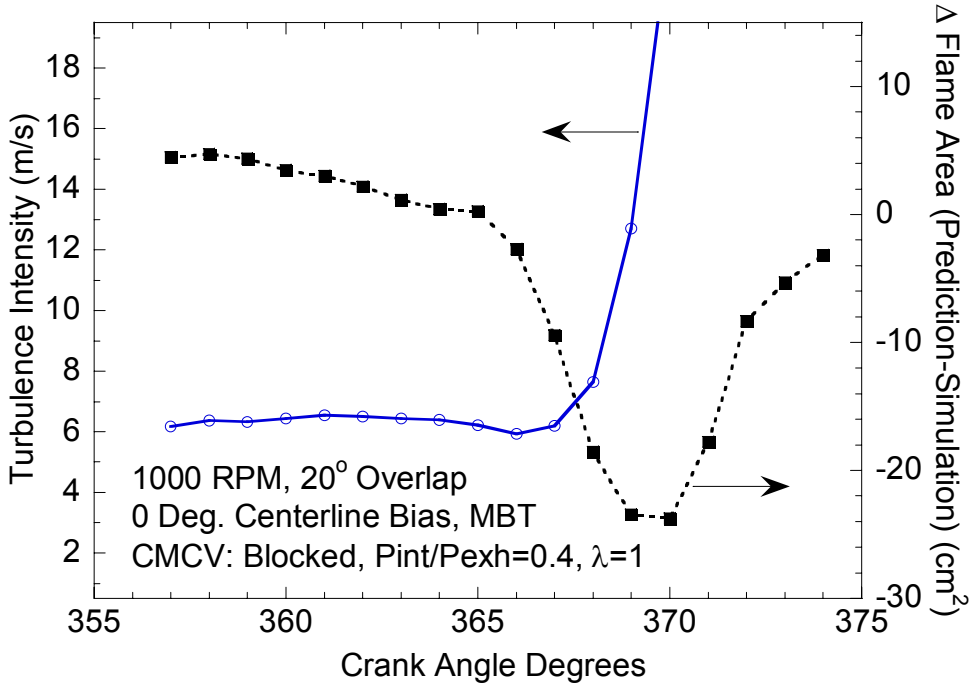

Figure 5.8: The turbulence intensity calculation is strongly related to the flame front area calculation. In general, predicted turbulence intensity is inversely proportional to entrained flame front area.

For the purpose of engine control a single value characterizing the turbulence intensity at each operating condition is desirable. A single turbulence intensity value for each condition was determined by averaging the prediction between 5% and 10% mass-fraction burned. The early-combustion average is used because a turbulence intensity value close to ignition is desirable for the prediction of spark timing and the predicted results agree well with simulation in this range.

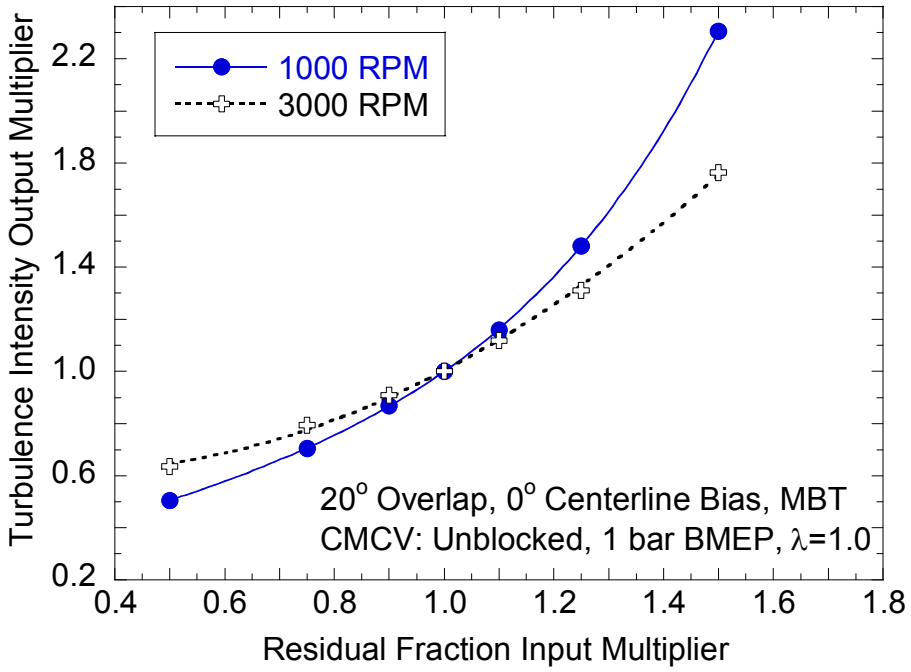

Figure 5.9: Low engine speed operation is more sensitive residual gas fraction input accuracy than high engine speed operation. A 10% change in RGF input creates approximately a 10% change in turbulence intensity prediction.

The uncertainty in turbulence intensity created by residual gas fraction input variation is shown in Figure 5.9. Increasing the input residual gas fraction lowers laminar flame speed, causing an increase in turbulence intensity prediction. Turbulence intensity prediction increases when laminar flame speed decreases because their combination must satisfy the burn rate for each operating condition. Low engine speed operation is more sensitive to residual gas fraction variation because overall turbulence intensity level is low, making laminar flame speed more significant to the rate of mass entrainment. The

relative uncertainty in RGF measurement was determined to be ±10% in Chapter 4. Turbulence intensity calculation changes approximately 15% with a 10% change in RGF input at 1000 RPM, and improves to 12% at 3000 RPM. Reported uncertainty in turbulence intensity values is assumed ±15% for all data to reflect the variation in RGF measurement.

Inverse-model turbulence intensity values, averaged from 5% to 10% MFB, compare well will results from the spark-ignition simulation over an engine speed sweep (See Figure 5.10). Turbulence intensity is a function of engine speed because it alters valve flow velocities during the intake stroke. Calculated turbulence intensity slightly overestimates simulated values, but still agree within 10%.

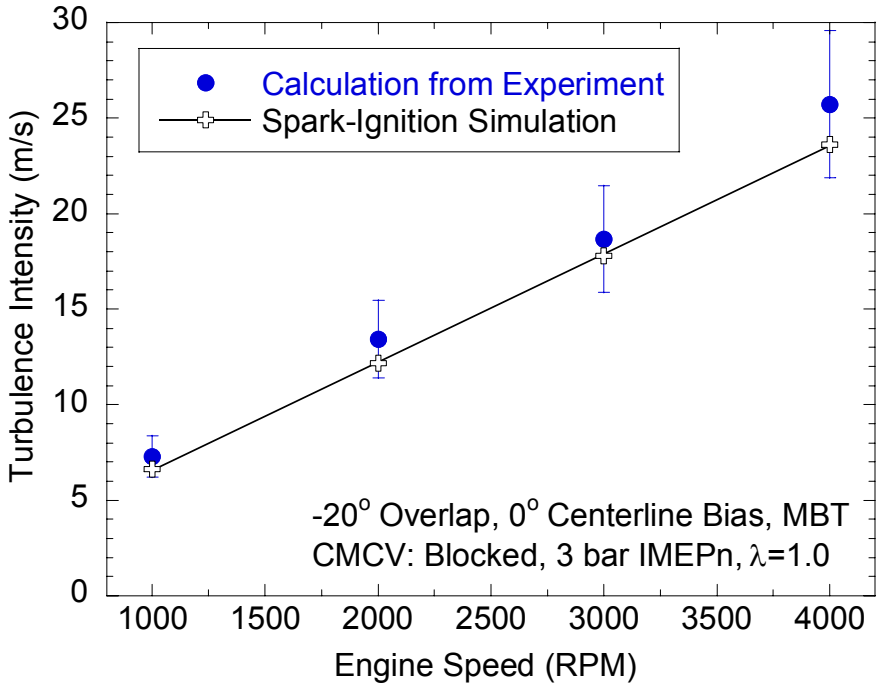

Figure 5.10: Calculated turbulence intensity, averaged from 5% to 10% MFB, agrees well with simulation results when engine speed is changed.

The results in Figure 5.11 indicate that turbulence intensity slightly decreases with increasing engine load. Overall, calculated u' levels agree well with the spark-ignition simulation results over the entire load sweep. A slight decrease in turbulence intensity is observed as load increases, likely caused by a relatively later spark timing at higher load

allowing more time for charge motion decay. Higher load operation is also subjected to increased energy dissipation rates, potentially reducing turbulence intensity.

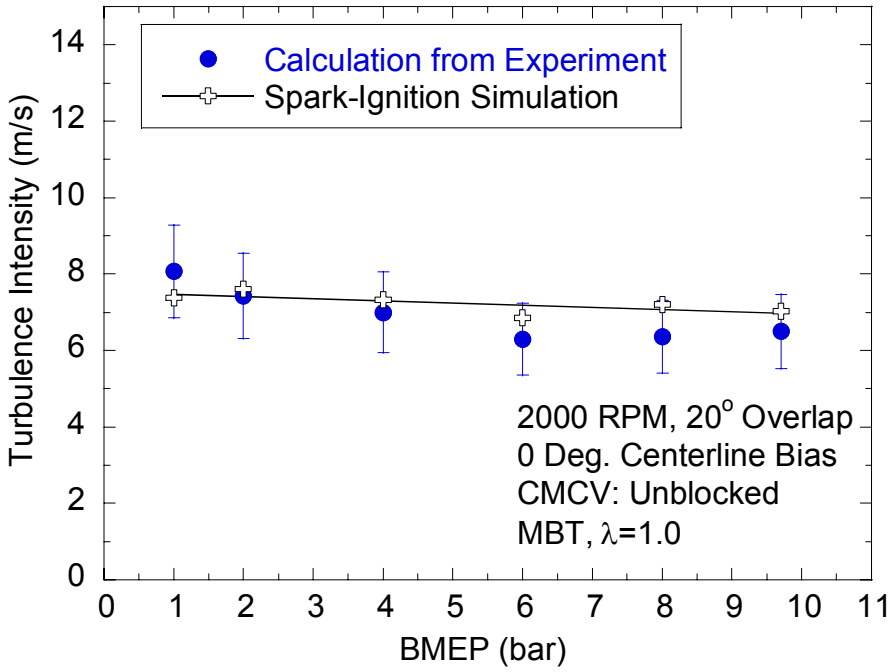

Figure 5.11: Variation in turbulence intensity as a function of engine load is properly captured by the proposed calculation method.

Turbulence intensity decays during the compression stroke, so delaying ignition will generally decrease charge motion levels during combustion. The results in Figure 5.12 show reduced charge motion levels when spark timing occurs closer to TDC. Calculated turbulence intensity values are lower than simulation values at later spark timings. The discrepancy between simulation and calculation is likely caused by flame area mapping assumptions used to simplify calculation (e.g. constant flame thickness). Flame thickness will change at later spark timings because more of the charge is burned during expansion, slowing combustion and increasing flame thickness.

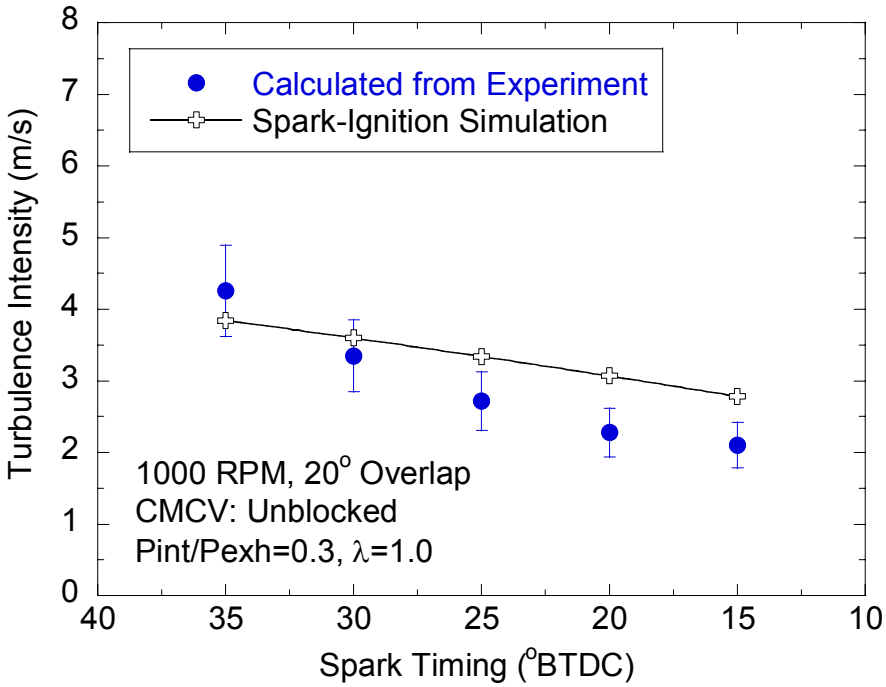

Figure 5.12: Turbulence intensity is a function of spark timing because charge motion decays during the compression stroke.

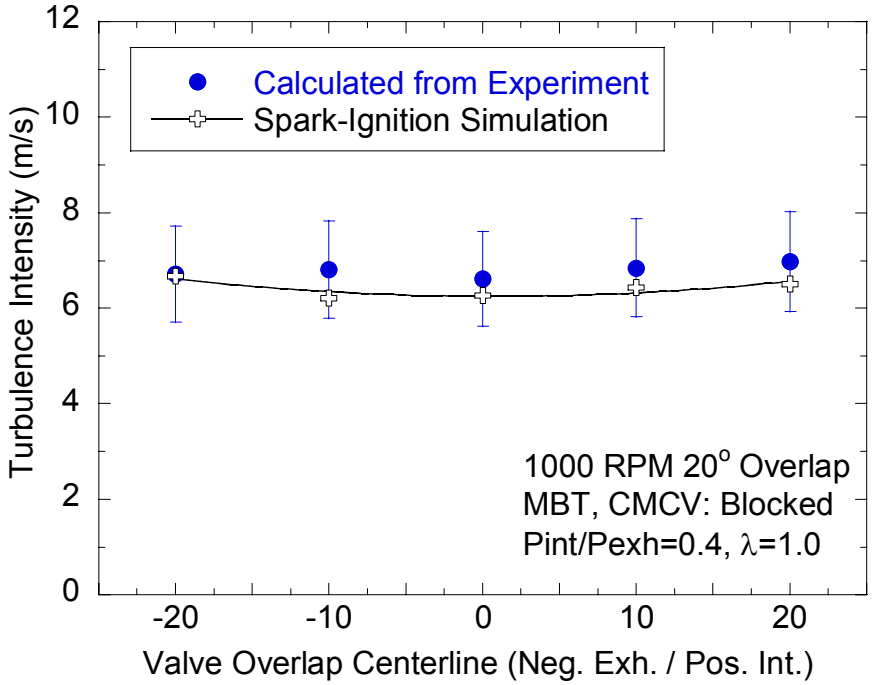

Figure 5.13: Turbulence intensity is not significantly affected by altering valve overlap centerline location. The u' calculation routine agrees well with spark-ignition simulation results over the range of valve overlap centerline locations.

Overlap centerline location determines the phasing of valve events with piston motion. Altering valve overlap centering phasing will influence piston driven flow velocity characteristics. However, the results in Figure 5.13 show little dependence of turbulence intensity on valve overlap centerline. Calculated turbulence intensity results are in good agreement with spark-ignition simulation predictions. Valve overlap centerline location appears to affect burn rate primarily through changes in residual gas fraction, as describe in Section 4.7.

5.3 Turbulence Intensity Model Results

Consistency of the inverse-model results with the spark-ignition simulation permits its use for engine characterization. As a primary factor determining flame entrainment rate, turbulence intensity trends must be quantified throughout the engine operating range. A simple model for turbulence intensity prediction is also desirable for real-time spark timing prediction in an engine controller. The following sections describe turbulence intensity trends throughout the engine operating range, and its impact on burn duration.

The flame development period of combustion occurs from the time of spark to 10% mass fraction burned. Many factors influence flame development duration, including turbulence intensity and residual gas fraction. The time-duration of flame development is plotted against turbulence intensity for all test points in Figure 5.14. High levels of charge motion correlate to short flame development durations. Lower levels of turbulence intensity have some impact on flame development, but other parameters, such as laminar flame speed, become more significant when charge motion decreases. In general, activating the charge motion valve increases turbulence intensity and reduces flame development duration.

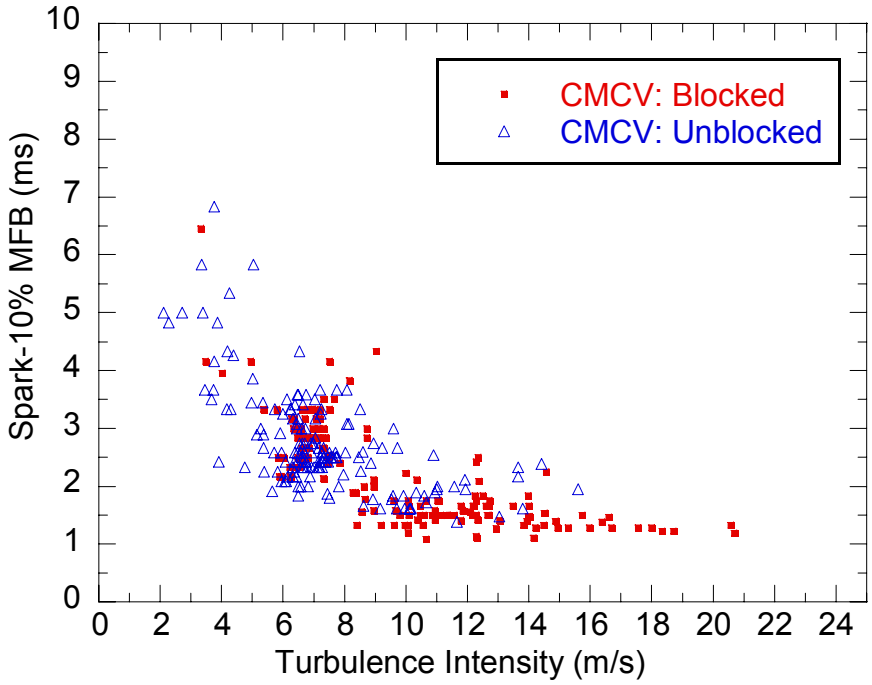

Figure 5.14: The flame development period is influenced by charge motion. At low levels of turbulence intensity other factors, such as residual gas fraction, contribute to flame development time.

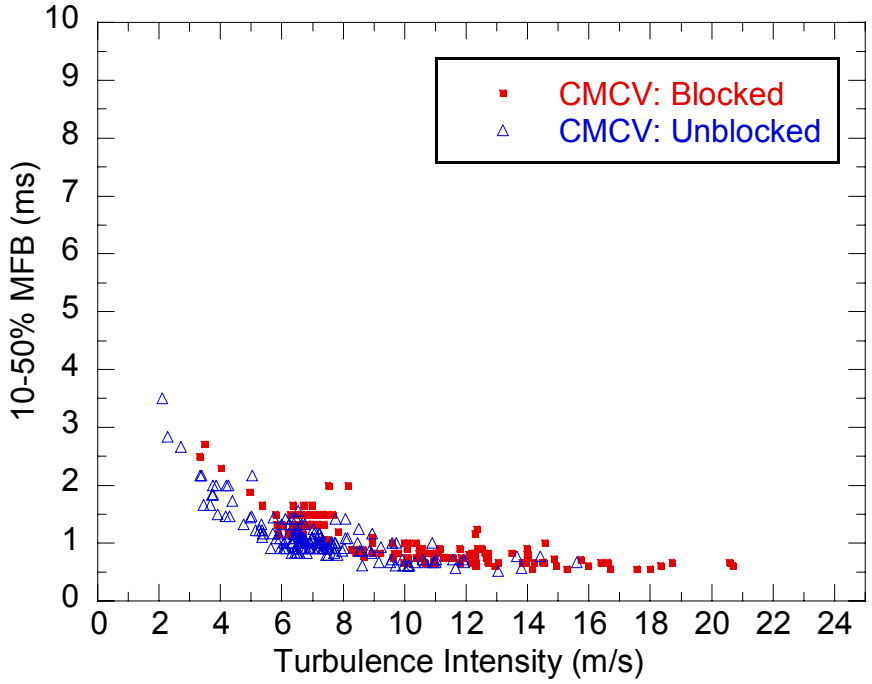

Figure 5.15: Combustion duration from 10% to 50% MFB is relatively constant for turbulence intensity levels above 10 m/s, reducing charge motion increases 10-50% combustion duration.

The time-duration from the end of the flame development period to 50% mass fraction burned (CA10 to CA50) for all test points is shown in Figure 5.15. CA10 to CA50 is significantly shorter than the flame development period. The flame entrainment rate during this period is very high because flame area, turbulence intensity, laminar flame speed, and unburned charge density are all increasing. Flame front area and turbulence intensity are the dominate factors determining flame entrainment (Filipi and Assanis 2000), yielding good correlation between charge motion and 10-50% MFB duration.

Previous researchers (Abraham et al. 1985, Heywood 1988) have demonstrated that turbulence intensity scales linearly with mean piston speed (MPS). The increase in turbulence intensity with engine speed occurs because the time duration of the intake stroke changes. For a given air and fuel mass, increasing engine speed will decrease the induction time and create high velocities at the intake valves. The slope of turbulence intensity with respect to mean piston speed varies with engine design and operating condition. Typical slope values range from approximately 0.4 to 1.7. Turbulence intensity predictions with respect to MPS for both CMCV activation states follow a linear trend (See Figure 5.16). The data is reported at MBT spark timing, constant valve overlap, stoichiometric air-to-fuel ratio, and fixed engine load to isolate the influence of engine speed. Activating, or blocking, the CMCV increases the slope by 30% and the offset by approximately 1.6 m/s as compared to the unblocked state. Valve overlap also affects the relationship between MPS and turbulence intensity; increasing valve overlap tends to decrease the slope and increase the intercept (See Figure 5.17). Valve overlap affects turbulence intensity because it determines the timing of valve events with respect to the piston as well as the size and strength of exhaust backflows into the intake.

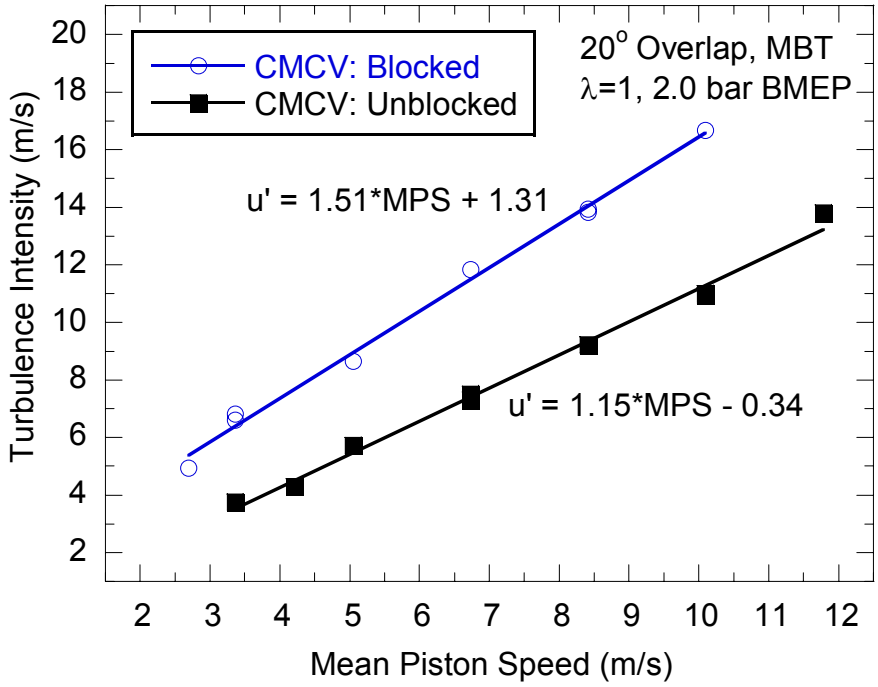

Figure 5.16: Turbulence intensity is linearly proportional to mean piston speed. Activating the charge motion control valve increases both the linear offset and slope.

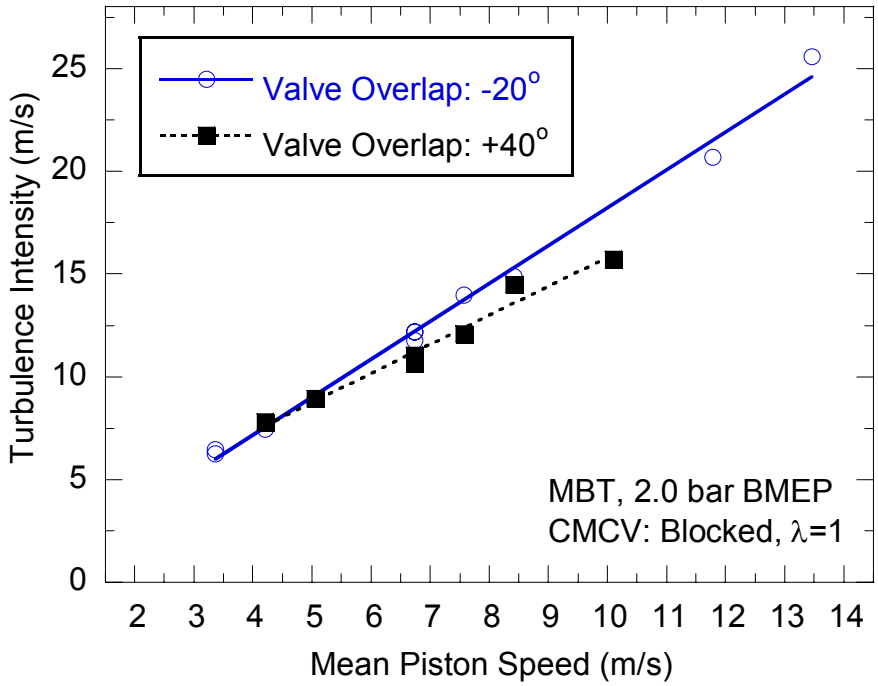

Figure 5.17: Valve overlap (reported @ 0.15 mm lift) affects the linear slope and intercept of turbulence intensity as a function of mean piston speed.

Turbulence intensity decay during the compression stroke leads to variation in initial levels as a function of spark timing. Later spark timings are subjected to lower turbulence intensity than advanced timings because viscous dissipation occurs for a longer period of time prior to ignition. Compression stroke turbulence decay is also dependent on engine speed because it affects the energy flow into the cylinder during the intake stroke. Higher energy levels decay faster than lower levels, so turbulence intensity will decay faster at high engine speeds than it will at lower engine speeds. Figure 5.18 illustrates the decay of turbulence intensity as a function of the location of 50% MFB (CA50) for a range of engine speeds at constant load. Turbulence intensity at 3000 rpm decays at nearly double the rate as 1000 rpm for a similar range of spark timings. It is important to note that squish, occurring late in compression near TDC, can increase turbulence intensity at retarded spark timings. This phenomenon was not observed because the test engine geometry creates minimal squish-induced charge motion.

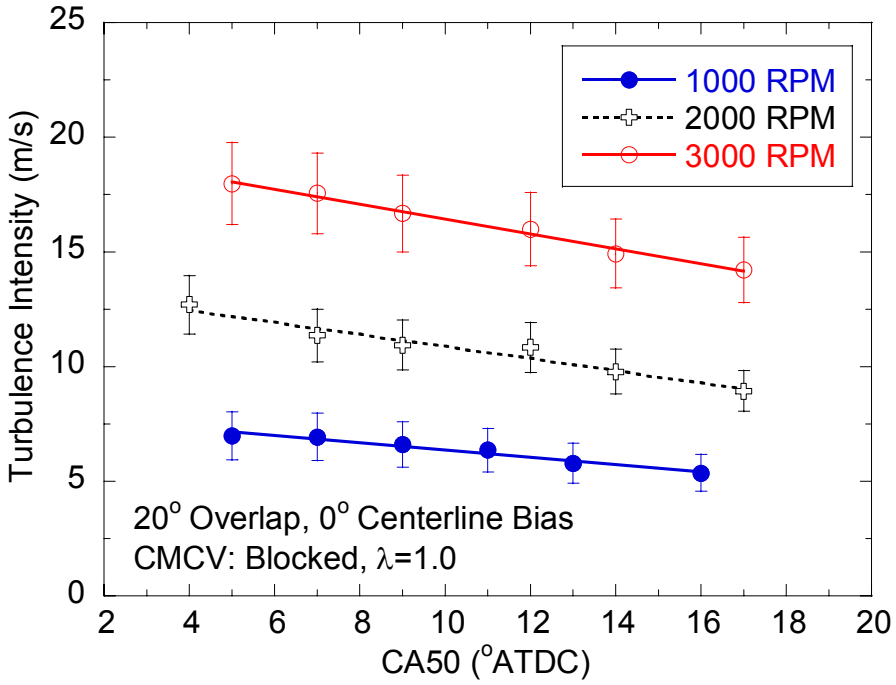

Figure 5.18: Turbulence intensity decays during the compression stroke, so later spark timings are subjected to lower turbulence intensity levels.

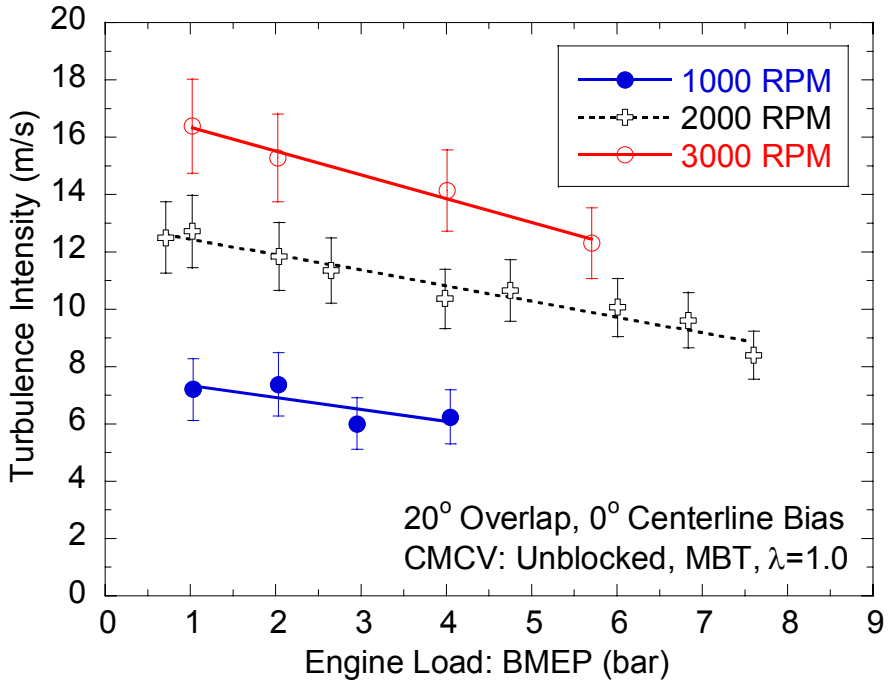

Figure 5.19: Turbulence intensity decreases with increasing engine load.

Initial (5-10% MFB) turbulence intensity levels are a function of engine load (See Figure 5.19). The decrease in charge motion at high loads is caused by the combination of later spark timing and increased viscous dissipation. As previously discussed, later spark timings allow more time during the compression stroke for decay. The decreasing burn duration at higher loads requires that spark-ignition occur closer to TDC to maintain proper combustion phasing. The dissipation rate of kinetic energy within the combustion chamber is a function total in-cylinder mass. The nature of high load operation is that more mass is trapped in-cylinder, increasing turbulent kinetic energy dissipation rate.

5.3.1 A Turbulence Intensity Model for Engine Controls

A model capable of fast turbulence intensity prediction is essential for facilitating physics-based ignition timing control strategies. The experimental data trends observed in the previous section are used to generate a turbulence intensity estimation routine. The modeling approach is to generate an initial estimate based on engine speed and valve

overlap. The initial estimate is then scaled to account for desired CA50 location and engine load. Separate sets of equations are developed for each CMCV activation state to accommodate differences in turbulence generation. The model consists of three basic steps, with each step utilizing experimentally fit constants.

The base turbulence intensity level is determined from mean piston speed, valve overlap, and charge motion control valve state using Equation (5.8). The linear relationships shown in Figure 5.16 and Figure 5.17 are the basis for the initial turbulence level. Linear slope and intercept are calculated as a function of valve overlap using experimentally fit Equations (5.9) and (5.10) depending upon CMCV activation state.

$$u'^{CMCV}_{BASE\_2bar\_MBT} = \left(Slope^{CMCV}_{Overlap}\right) \cdot MPS + Intercept^{CMCV}_{Overlap} \tag{5.8}$$

Where: (CMCV: Blocked)

$$\begin{aligned} Slope^{CMCV:Blocked}_{Overlap} &= -0.006 \cdot \left(Overlap^{CAD}_{0.15mm\ Lift}\right) + 1.654 \\ Intercept^{CMCV:Blocked}_{Overlap} &= 0.03 \cdot \left(Overlap^{CAD}_{0.15mm\ Lift}\right) + 0.614 \end{aligned} \tag{5.9}$$

or: (CMCV: Unblocked)

$$\begin{aligned} Slope^{CMCV:Unblocked}_{Overlap} &= -0.006 \cdot \left(Overlap^{CAD}_{0.15mm\ Lift}\right) + 1.261 \\ Intercept^{CMCV:Unblocked}_{Overlap} &= 0.025 \cdot \left(Overlap^{CAD}_{0.15mm\ Lift}\right) + 0.949 \end{aligned} \tag{5.10}$$

The data presented in Figure 5.16 and Figure 5.17 are at MBT spark timing (CA50 @ 8° ATDC) and a specific engine load, $BMEP_0$ (2 bar BMEP in this case). The base turbulence intensity level is adjusted for load variation using Equation (5.11), and the slope is a linear function with MPS. The correction scales with MPS because higher turbulence intensity levels have higher overall decay rates. Separate slope correlations are used for each CMCV state.

$$u'^{CMCV}_{BASE\_BMEP\_MBT} = \left(Slope^{CMCV}_{BMEP}\right) \cdot \left(BMEP_{Operating} - BMEP_0\right) + u'^{CMCV}_{BASE\_2bar\_MBT} \tag{5.11}$$

Where:

$$Slope_{BMEP}^{CMCV:Blocked} = -0.061 \cdot (MPS) - 0.186$$

$$Slope_{BMEP}^{CMCV:Unblocked} = -0.048 \cdot (MPS) + 0.093 \quad (5.12)$$

The final step corrects for turbulence intensity differences caused by combustion phasing. Charge motion decays during the compression stroke, so later spark timings are subjected to lower turbulence levels. The desired location of 50% mass fraction burned (CA50) is used to correct for spark timing variation because it is a pre-determined input to the ignition timing prediction model. Similar to engine load correction, the linear slope is itself correlated to mean piston speed. The relative location with respect to MBT CA50 (8° ATDC) is used to correct for spark timing differences. CA50 is set relative to MBT location because the baseline turbulence intensity value was determined at that combustion phasing.

$$u'_{Final} = u'^{CMCV}_{BASE\_BMEP\_CA50} = \left(Slope_{CA50}^{CMCV}\right) \cdot \left(CA50 - CA50_{MBT}\right) + u'^{CMCV}_{BASE\_BMEP\_MBT} \quad (5.13)$$

Where:

$$Slope_{CA50}^{CMCV:Blocked} = -0.024 \cdot (MPS) - 0.082$$

$$Slope_{CA50}^{CMCV:Unblocked} = -0.019 \cdot (MPS) \quad (5.14)$$

Model accuracy is verified against the inverse-model calculations in Figure 5.20. The fast turbulence intensity model re-predicts the inverse-model data with an RMSE of 0.91 m/s for blocked CMCV operation and 0.99 m/s for unblocked. Overall the simple model predicts turbulence intensity very well. The slopes and intercepts of each linear correlation should be calibrated specifically for each test engine. In this case the correction for engine load was based on BMEP, but other load indicating parameters, such as manifold pressure could be used if properly calibrated.

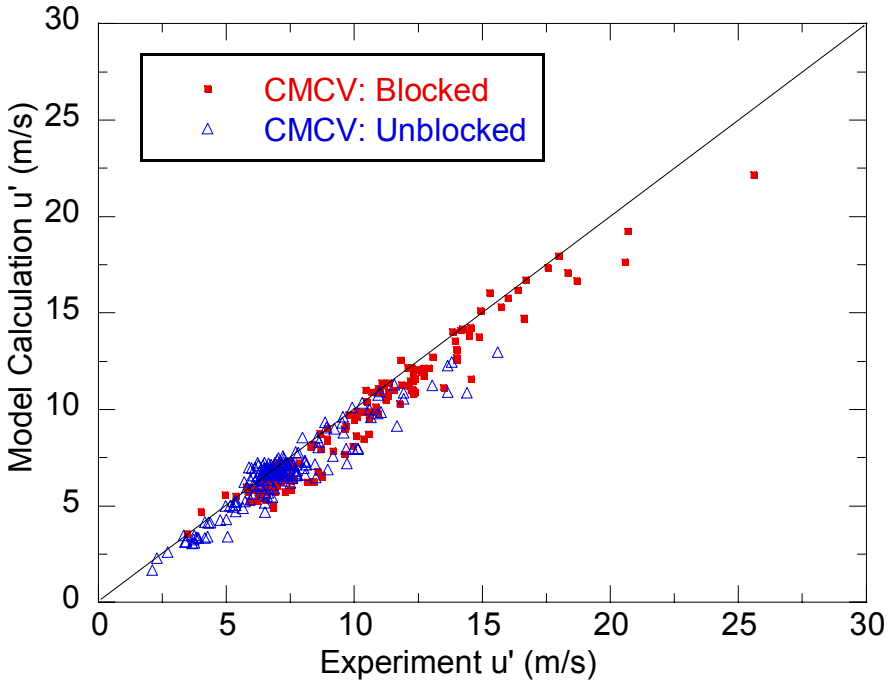

Figure 5.20: The turbulence intensity model predicts the experiment calculation with an RMSE of less than 1.0 m/s.

5.4 Summary and Conclusions

The basic architecture and calculation methods for calculating turbulence intensity from cylinder pressure data demonstrate excellent correlation with cycle simulation for the early stages of combustion. The calculated turbulence intensity for the range from 5% to 10% mass fraction burned is averaged to generate a single characteristic value at each operating condition. Calculated turbulence levels were within 10% of simulation results. Additionally, residual gas fraction input accuracy (±10%) scales about one-to-one with turbulence intensity uncertainty. Calculation results show that turbulence levels scale linearly with mean piston speed, which is in agreement with the observations of previous researchers. Spark timing, engine load, and valve overlap also have an impact on turbulence intensity. A model intended for use in an engine controller was generated, based on linear correlations, to calculate turbulence intensity

throughout the engine operating range. The prediction accuracy of the model matched experimentally calculated turbulence levels with a RMSE of less than 1.0 m/s.

CHAPTER 6

A MODEL-BASED SPARK TIMING PREDICTION ROUTINE

Development of a model-based spark timing prediction routine for the purpose of engine controls is critical for the optimization of high degree of freedom engines. The spark timing prediction model must be computationally efficient, flexible, accurate, and robust over the entire engine operating range. In order to use the method for real-time spark timing prediction it must have computationally efficient algorithm with minimal calculations. A modular architecture is desirable for flexibility, allowing engine and/or operating condition-specific calibration. Accuracy is primarily a function of combustion model design and input variability. Model robustness is ensured by selecting inputs that significantly impact combustion duration, including: laminar flame speed, turbulence intensity, charge density, and total mass. The following sections provide a background of model-based engine controls as well as describe a new spark timing prediction model designed to meet the above requirements.

6.1 Spark Timing Prediction Model Architecture

The primary objective of the prediction model is to generate a spark timing at any engine operating condition given a desired location of 50% mass fraction burned (CA50). The desired CA50 location is determined independently of the spark timing prediction model to meet vehicle and engine system objectives. The ignition timing model calculates a spark timing that will satisfy the defined CA50 by first predicting

combustion duration (spark to CA50) for a range of potential spark timings. Combustion durations are calculated over the entire window of potential timings and a single ignition location is determined to meet the desired CA50.

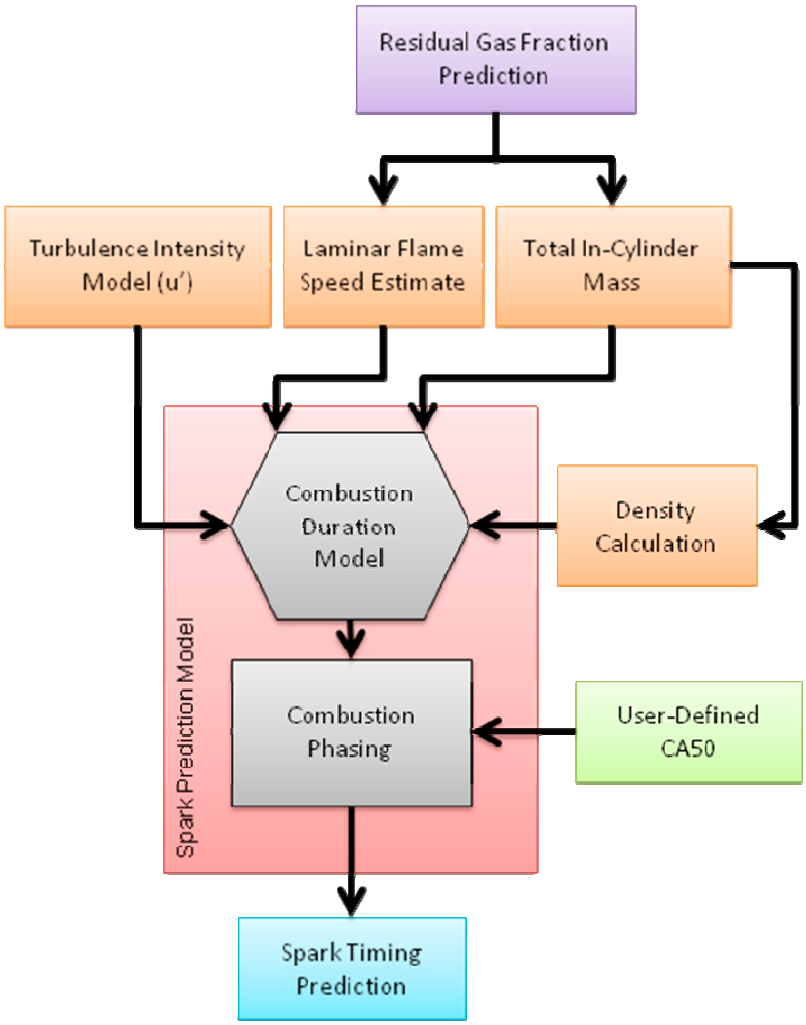

Figure 6.1: Architecture of the ignition timing prediction model

The basic structure of the prediction model is shown in Figure 6.1. It is divided into two sub-models; a combustion duration routine and a combustion phasing calculation. The ignition timing prediction model requires six inputs and the output is a single ignition timing that will satisfy the desired CA50. Direct model inputs are user-defined CA50, turbulence intensity, unburned density, laminar flame speed, and total in-

cylinder mass. Residual gas fraction is indirectly required for calculation of laminar flame speed and total in-cylinder mass.

6.1.1 Model Input Calculations

To calculate desired spark timing for any operating condition, inputs for turbulence intensity, unburned density, laminar flame speed, and total in-cylinder mass are required. Laminar flame speed and unburned charge density are calculated at each crank angle throughout the spark window. The range of spark window is dependent upon engine design. For the test engine it ranges from 50° BTDC to TDC with the CMCV unblocked and 35° BTDC to TDC with the CMCV blocked.

Turbulence intensity for each operating condition is estimated using the model developed in Section 5.3.1. Inputs to the turbulence intensity model are CA50, operating BMEP, valve overlap duration (CAD), and mean piston speed. All input variables are available within modern engine controllers. A single value is determined for turbulence intensity throughout the potential ignition timing range because the prediction model uses desired CA50 as an input.

A laminar flame speed array is calculated over the spark window to account for in-cylinder temperature and pressure variations during the compression stroke. Calculation of laminar flame speed is performed at each crank-angle location, using the model described in Section 3.3.2, based on residual gas fraction, air-to-fuel ratio, and in-cylinder pressure and temperature. Residual gas fraction is estimated using the model developed by Amer and Zhong (2006) that was fit to experimentally recorded data (See Section 4.10). In-cylinder pressure is calculated assuming polytropic compression from the intake manifold pressure at IVC to the time of spark using Equation (6.1). The polytropic coefficient is calculated as a function of residual gas fraction using a linear fit to the experimental data in Figure 4.10 (See Equation (6.2)). In-cylinder mixture

temperature is also calculated assuming polytropic compression using Equation (6.3). Temperature at intake valve closing (IVC) is estimated using the mass-weighted calculation and assuming the specific heats of intake and exhaust gases are equal, as in Equation (6.4). Residual gas temperature at IVC is assumed equal to exhaust temperature minus one hundred degrees (K) to account for heat transfer during the gas exchange process. The assumption that one hundred degrees in temperature is lost during gas exchange was determined by comparison with cylinder pressure-based heat release data. A more extensive heat transfer model could be developed to further improve accuracy; however, in-cylinder temperatures compared sufficiently well with heat release data using this assumption.

$$P_{SPK,i} = P_{MAP}\left(\frac{V_{IVC}}{V_{SPK,i}}\right)^{n} \tag{6.1}$$

$$n = -0.00369 * RGF(\%) + 1.39 \tag{6.2}$$

$$T_{SPK,i} = T_{IVC}\left(\frac{V_{IVC}}{V_{SPK}}\right)^{n-1} \tag{6.3}$$

$$T_{IVC} = \frac{m_{RGF}\left(T_{EXH} - 100\right) + m_{fuel}T_{fuel} + m_{air}T_{air}}{m_{total}} \tag{6.4}$$

Total in-cylinder mass is calculated from the residual gas fraction estimate along with air and fuel mass. Unburned charge density over the spark window is calculated by dividing total mass by cylinder volume. All input parameters are provided in array form to the combustion model for ignition timing calculation.

6.1.2 Combustion Duration Sub-Model

Within the ignition timing model the most important sub-model involves the prediction of combustion duration. Combustion duration is calculated using a simplified

version of the turbulent flame entrainment model described in Chapter 3. The model is simplified step-by-step using a series of assumptions, making sure accuracy is preserved at each step. Derivation of the combustion duration model is described in the following section.

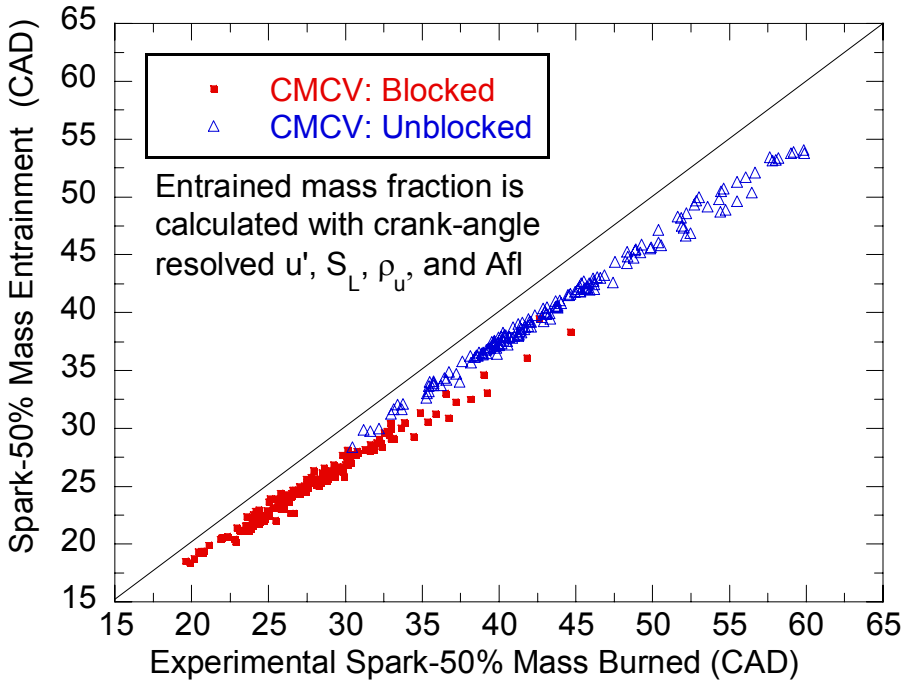

Figure 6.2: There is a linear relationship between the duration from spark to 50% mass fraction burned and entrained. The linear relationship allows the burn-up time to be determined without direct calculation, reducing computation time.

The first simplification to the turbulence flame entrainment model involves generating an approximation for the burn-up phase of combustion. The full combustion model is structured such that mass is first entrained by a turbulent flame, and then entrained mass burns according to a laminar time scale. Figure 6.2 shows the relationship between spark to 50% mass fractions burned and entrained from high fidelity crank angle resolved calculation. As expected, the spark-to-50% entrained mass duration is shorter than the full burn-up duration. The duration of spark to 50% mass entrainment is based on total in-cylinder mass (residual gas included) instead of just the fuel and air mass. The use of total in-cylinder mass in the calculation helps to create a linear relationship

between the entrained and burned durations and allows the burn-up process to be modeled by applying an offset to the entrained duration. Conceptually, using total mass in the calculation lengthens the total combustion duration as compared to considering air and fuel mass only. When residual gas fraction is high the burn-up process will be slow because laminar flame speed is low, using total mass compensates for slower burn-up. If only air and fuel mass were considered in the calculation a linear offset between entrained and burned spark-to-50% MFB burned may not be observed. Modeling the burn-up process by using a linear offset equation simplifies combustion duration calculation by removing the calculation several integrals. Without the need to explicitly solve for the burn-up process (Equation (3.2)) turbulent flame entrainment calculation becomes the primary focus for further simplification.

Turbulent flame entrainment, modeled by Equation (3.1), requires crank-angle resolved inputs of entrained flame area, unburned gas density, turbulence intensity, and laminar flame speed to generate a detailed mass fraction entrained profile. The requirement of the prediction model is to output the required spark timing to satisfy a desired CA50 location. Additional combustion information, such as CA10, is not required and therefore a detailed mass fraction entrained profile is not necessary. Accurate prediction of only a single parameter (spark to 50% mass fraction entrained) instead of the entire combustion process allows for addition method simplification. The mass fraction entrained spark to 50% duration in Figure 6.3 is calculated using constant values of laminar flame speed and turbulence intensity. Both laminar flame speed and turbulence intensity are held at their respective values at ignition throughout the calculation. Neglecting change in these properties during combustion slightly degrades the duration calculation, but significantly reduces calculation time. It is important to note that CMCV activation state also influences the relationship between burn and entrained duration. Separate correction equations are therefore required for each CMCV activation state (blocked and unblocked).

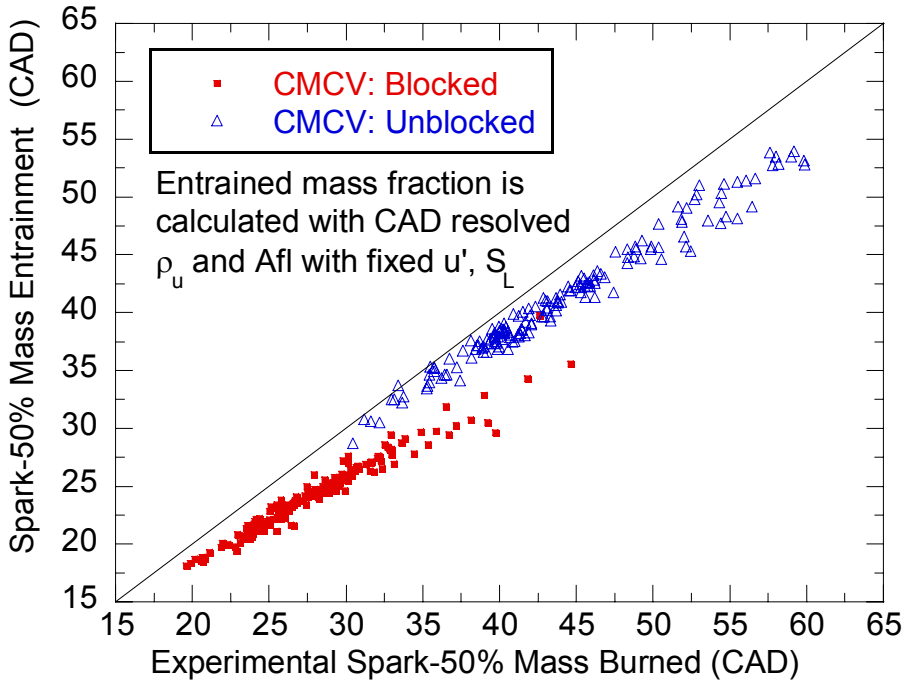

Figure 6.3: Assuming constant values for laminar flame speed and turbulence intensity during the mass fraction entrained calculation does not affect the linear relationship with mass fraction burned.

To further simplify the calculation of combustion duration a method utilizing a constant, or characteristic, mass entrainment rate is proposed. Using a characteristic flame entrainment rate eliminates the need for calculation of a crank-angle resolved integral to obtain combustion duration. Spark to 50% mass entrainment duration can be calculated by simply dividing the constant flame entrainment rate by the total in-cylinder mass. Figure 6.4 illustrates the concept of using a constant flame entrainment rate to determine combustion duration. Combustion rate detail is lost by using this method because inputs are tailored to predict a particular interval (i.e. spark to 50% mass entrainment); however, significant gains in computational efficiency can be achieved.

Input values for turbulence intensity and laminar flame speed are fixed at their respective values at the time of spark (As previously discussed.). Values for both entrained flame area and unburned gas density must be modeled at each operating condition so that the proper constant mass entrainment rate is calculated. Target values

for unburned gas density and entrained flame area were calculated from experimental data by determining their values at the combustion location were the instantaneous mass entrainment rate is equal to the ideal constant entrainment rate. Properties values at the crank angle location where instantaneous mass entrainment rate is equal to the ideal constant entrainment rate are denoted by '*', and generally corresponds to a mass fraction entrained value of around 5%.

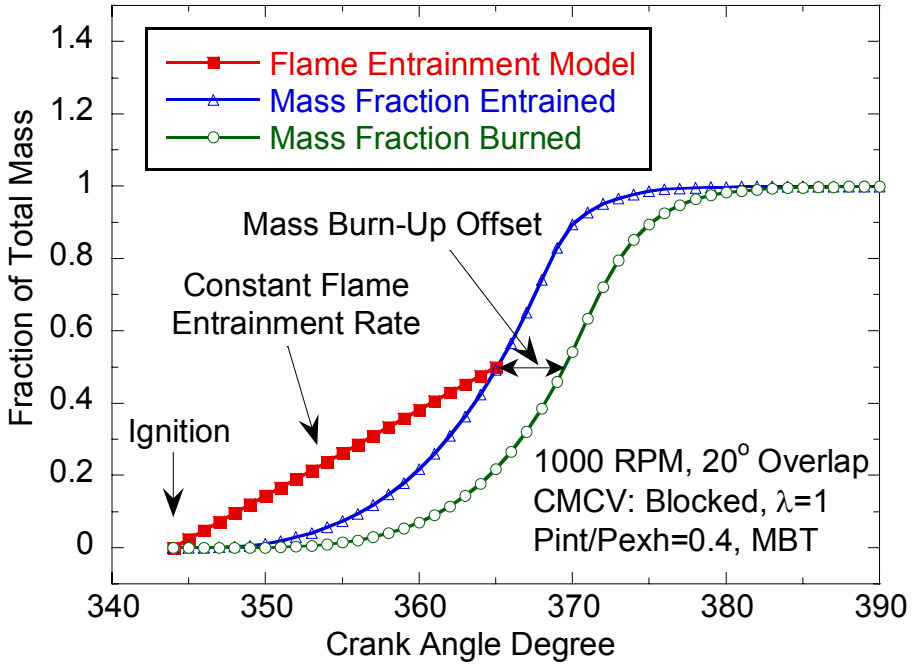

Figure 6.4: A constant flame entrainment rate model is used to predict the duration from spark to 50% mass fraction entrained. After calculation of spark to 50% mass entrainment duration an offset is added to account for the mass burn-up process.

To model the change in unburned charge density from the time of spark to the characteristic '*' location a normalized density multiplier is proposed. A relationship for an unburned gas density multiplier between the spark location and characteristic '*' location correlates well with combustion chamber height at the time of spark (See Figure 6.5). Instantaneous combustion chamber height is calculated by dividing total cylinder volume by piston bore area at each crank angle location. The relationship between density multiplier and combustion chamber height is founded in the fixed combustion

chamber geometry and the low mass fraction burned level at the '*' location. Low mass fraction burned levels produce only a small pressure rise due to combustion at the characteristic '*' location, allowing the density multiplier to be relatively independent of combustion and a primary function of engine geometry. Conceptually, the density multiplier trend is realistic because early spark timings create higher rates of pressure rise, increasing unburned charge density throughout combustion. Similar normalization concepts were found for cylinder pressure by Zeng et al. (2004).

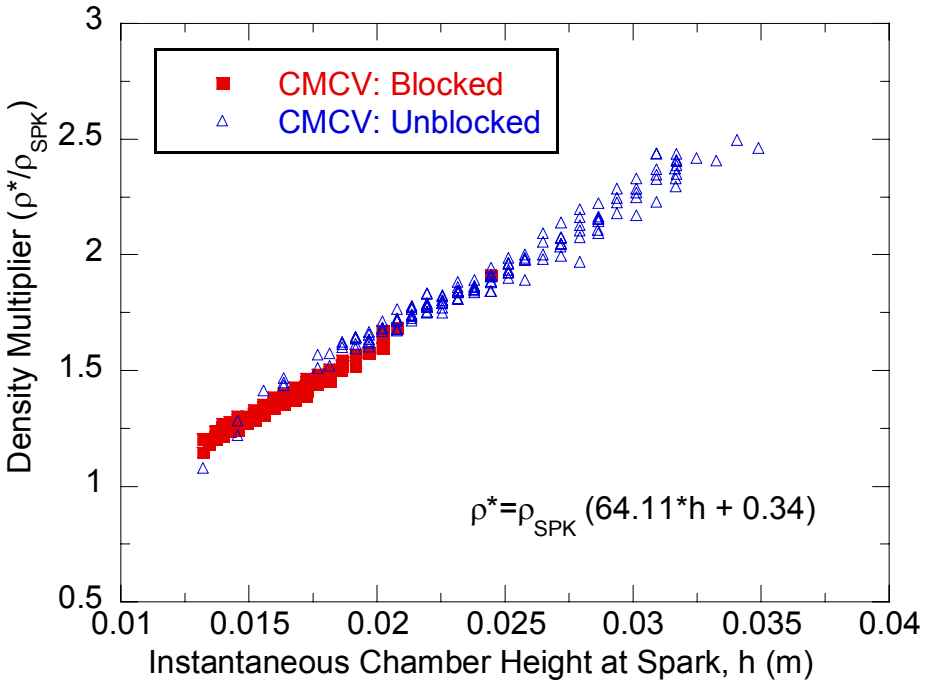

Figure 6.5: The density multiplier, assuming constant mass fraction entrainment rate, is a function of the instantaneous chamber height at the time of spark.

Calculation of entrained flame area to be used for calculating a constant mass entrainment rate requires a more complex model than unburned gas density. Flame entrainment area does not correlation well with any single parameter, so a linear regression was fit to experimental data using the LINEST function in Microsoft EXCEL. The flame area prediction equation uses inputs values at ignition timing for total in-cylinder mass, instantaneous chamber height, unburned gas density, turbulence intensity and laminar flame speed. Model coefficients for both CMCV activation states are given

in Table 6.1. The correlation between predicted flame entrainment area to experimental calculations are shown in Figure 6.6.

Table 6.1: Entrained flame front area (Afl*) is determined by summing each property term for the given CMCV activation state.

Property	CMCV: Blocked	CMCV: Unblocked
Unburned Gas Density [kg/m^3]	$-3.27\text{x}10^{-5} * (\rho_{u,SPK})$	$-1.28\text{x}10^{-4} * (\rho_{u,SPK})$
Instantaneous Chamber Height [m]	$-0.0249 * h_{SPK}$	$-0.0269 * h_{SPK}$
Laminar Flame Speed [m/s]	$3.75\text{x}10^{-4} * S_{L,SPK}$	$3.31\text{x}10^{-4} * S_{L,SPK}$
Turbulence Intensity [m/s]	$-9.23\text{x}10^{-6} * u'_{SPK}$	$-8.98\text{x}10^{-6} * u'_{SPK}$
Total In-Cylinder Mass [kg]	$0.935 * m_{total}$	$1.566 * m_{total}$
Intercept	0.00135	0.00168

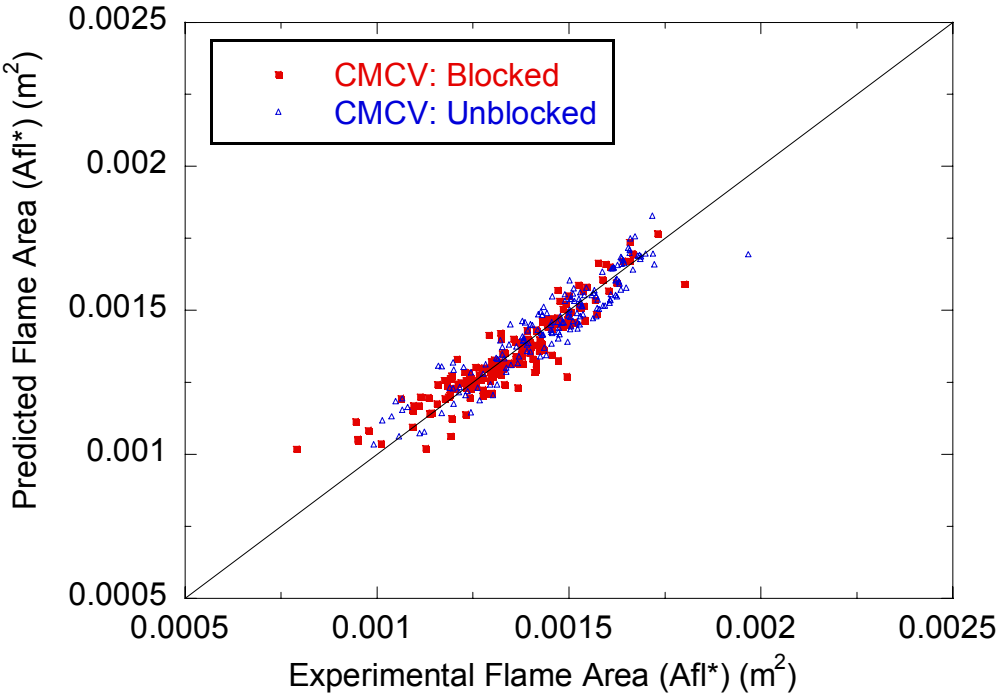

Figure 6.6: Entrained-mass flame area, for the case of constant flame entrainment rate, is predicted using a linear regression of several properties at the time of spark.

The time-duration from spark to 50% mass entrainment is calculated by dividing total in-cylinder mass by the predicted mass entrainment rate at each operating condition.

To account for the duration of mass burn-up, and convert entrained values to burned, linear corrections are used. The burn-up correction is determined from the time-based (instead of CAD-based) version of Figure 6.3. Burn-up correction equations are provided for each charge motion control value activation state in Equations (6.5) and (6.6). Burn-up corrected spark to 50% mass fraction burned durations are converted to a crank angle-basis using engine speed. Final spark to 50% mass fraction burned prediction duration has an RMSE of 2.3 with experimentally measured values (See Figure 6.7).

$$Time^{Burned}_{SPK\,to\,CA50}[ms] = 1.145 \cdot \left(Time^{Entrained}_{SPK\,to\,CA50}[ms]\right) + 0.006 \qquad \text{CMCV: Blocked} \tag{6.5}$$

$$Time^{Burned}_{SPK\,to\,CA50}[ms] = 1.100 \cdot \left(Time^{Entrained}_{SPK\,to\,CA50}[ms]\right) - 0.108 \qquad \text{CMCV: Unlocked} \tag{6.6}$$

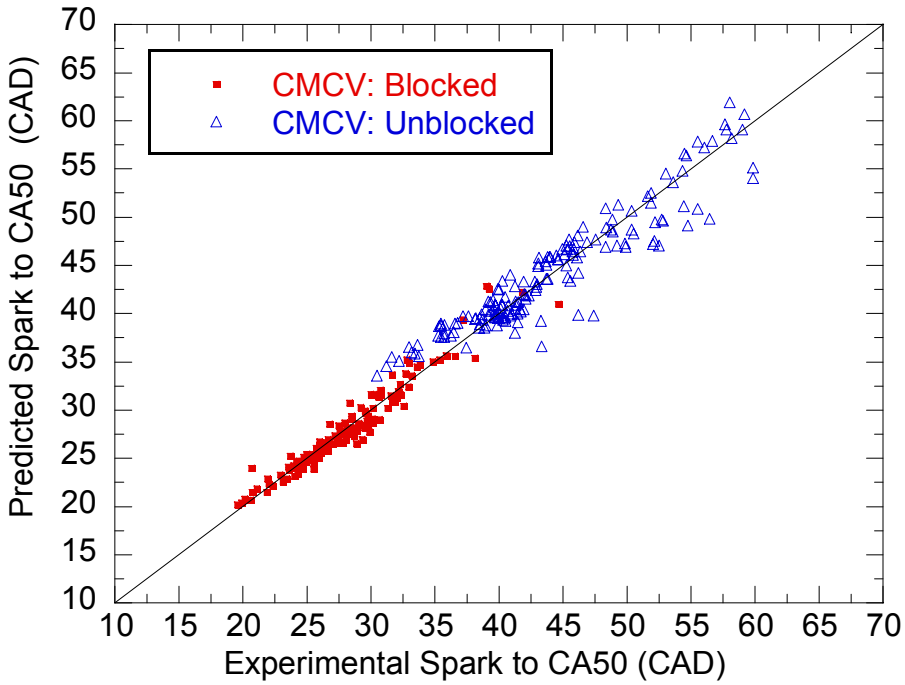

Figure 6.7: Combustion duration from the spark timing to 50% mass fraction burned is predicted with an RMSE of 2.3 with respect to experimental data.

6.1.3 Combustion Phasing Sub-Model

The combustion phasing sub-model is required to determine an ignition timing output based on combustion durations calculated over a pre-specified range of timings

known as the 'spark window.' Values of each parameter are modeled over the entire spark window using the same prediction equations developed for the combustion duration sub-model. Constant turbulence intensity is used for the entire spark window and it is predicted using the equations in Section 5.3.1. Laminar flame speed is calculated using the method described in Section 3.3.2. In-cylinder pressure and temperature during compression dictate the laminar flame speed profile over the spark window (See Figure 6.8). The entrained flame area (Afl*) input to the combustion duration sub-model is predicted to increase throughout the spark window.

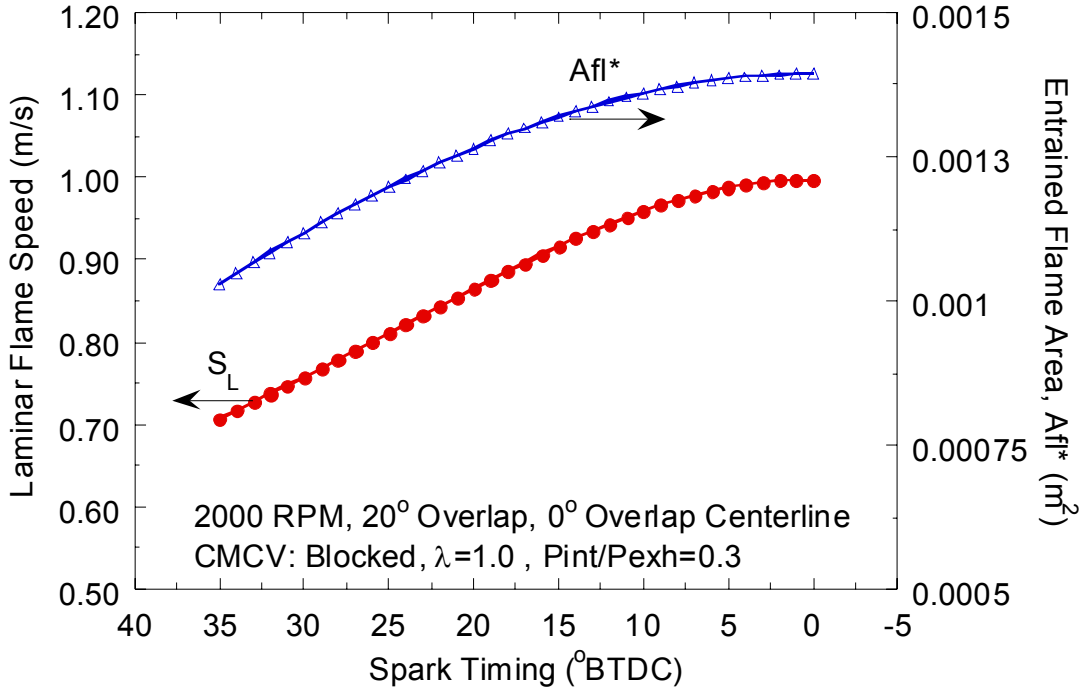

Figure 6.8: Both laminar flame speed (S_L) and entrained flame area (Afl*) increase during the compression stroke.

The unburned charge density value required for the combustion duration sub-model is the product of a base value and a multiplier. The base unburned charge density value increases during the spark window because the unburned mass is compressed into a smaller cylinder volume. The density multiplier value is proportional to the instantaneous chamber height at ignition (See Section 6.1.2). The product of the base and multiplier values produces a value that increases slightly throughout the spark window.

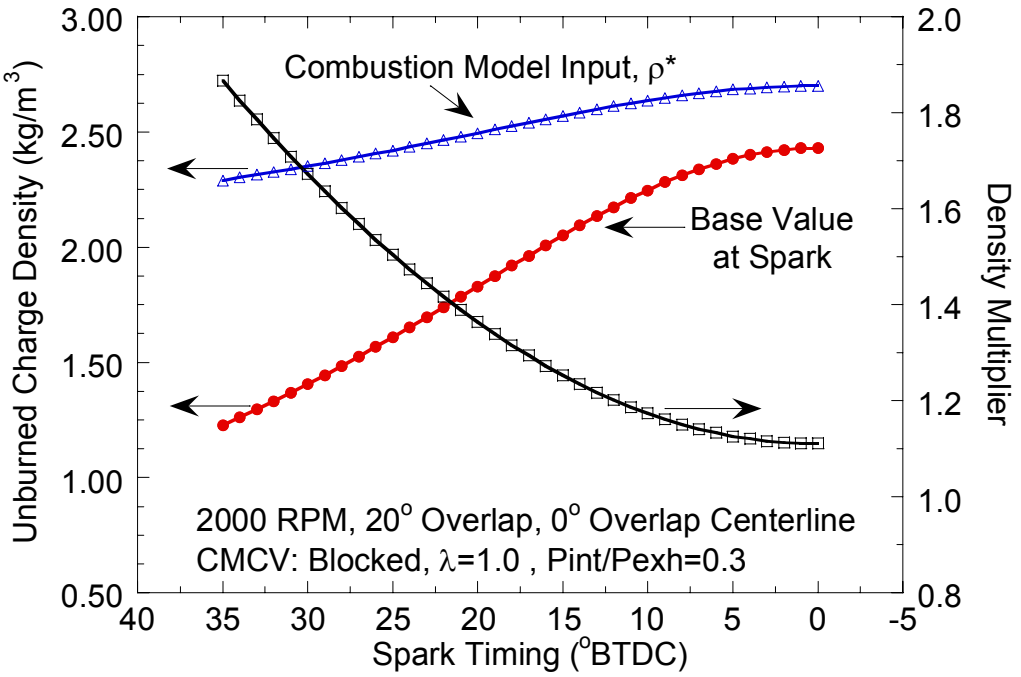

Figure 6.9: Unburned charge density increases and the multiplier decreases during the compression stroke. Their product (ρ*) slightly increases during compression.

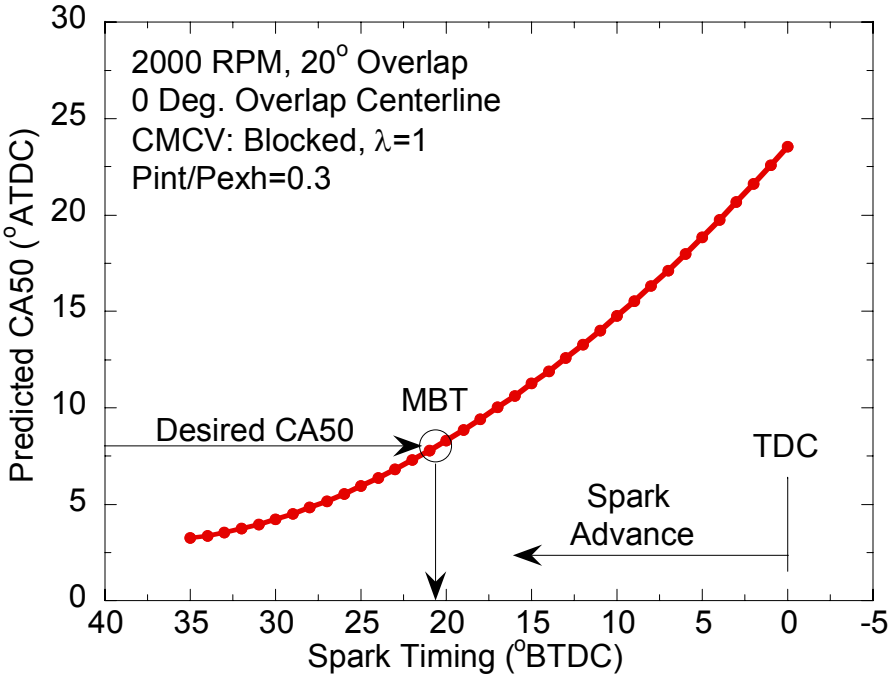

Figure 6.10: The combustion model predicts CA50 at each l within the spark window, and then desired CA50 is used to determine the required output timing.

A sample combustion duration sub-model output for a single operating condition is shown in Figure 6.10. The example demonstrates how the combustion duration sub-model predicts CA50 for a wide range of timings within a pre-described spark window. Model output is calculated by mapping the desired CA50 back to required ignition timing. The example in Figure 6.10 illustrates the ignition timing mapping process for a CA50 of 8° ATDC.

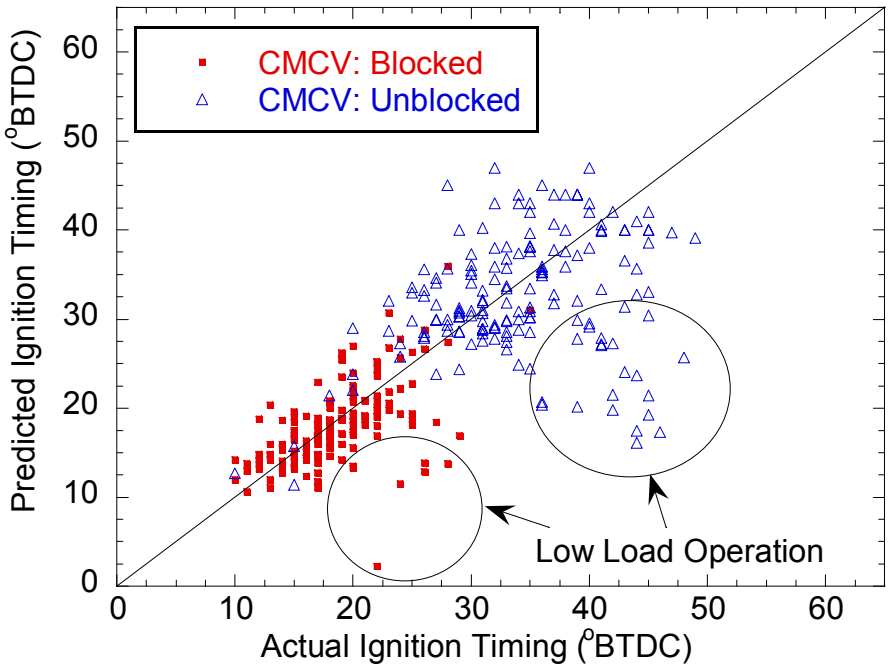

Figure 6.11: The spark timing selection routine re-predicts experiment values with a RMSE of 6.7 CAD. The data indicates that low load operation is particularly prone to prediction error.

To quantify ignition timing selection accuracy all of the experimental data recorded for this thesis is re-predicted. Ignition timing is calculated using the actual CA50, air mass, fuel mass, residual gas fraction, turbulence intensity, intake manifold pressure and BMEP for each operating condition. Predicted ignition timings for all data points are plotted against the experimentally measured values in Figure 6.11. The model only proves capable of predicting spark timing with an RMSE of 6.7 CAD. Low engine load operation seems to generate the largest prediction errors. The flame area prediction

model is suspected to be the primary cause of prediction uncertainty. The flame area model was fit to experimental data recorded at only one spark timing for each operating condition. Flame area trends calculated over the entire operating range were used to calibrate the model and it may not properly capture the correct trend over an entire spark window for a single operating condition. The assumption that a globally calibrated flame area is able to extrapolate values over any given spark window appears to break-down in this case.

6.2 Case Study: Predicting Combustion Duration over a Speed/Load Map

To further evaluate the combustion duration model's predictive capability an existing ignition timing map is regenerated. The original speed/load map from the base fixed-cam engine is used for comparison. The base ignition timing map was calibrated with an intake manifold that did not contain a charge motion control valve. The model was used to predict the combustion duration over a region of the spark map that is within the boundaries of recorded experimental data. None of the operating conditions represented by the base ignition timing map were previously recorded experimentally. The models developed for turbulence intensity and residual gas fraction were utilized to generate prediction inputs. The difference in combustion duration from calibrated to predicted values is within six crank angle degrees (See Figure 6.12). Predictions were not performed at low engine speed and high load, where knock is prone to occur. Experimental data was not recorded in the knock-region to avoid engine damage. Additionally, it is difficult to determine true MBT timing in the knock-region. Overall, combustion duration is predicted to within 10% of the actual value for operating conditions that were not used to calibrate the combustion model.

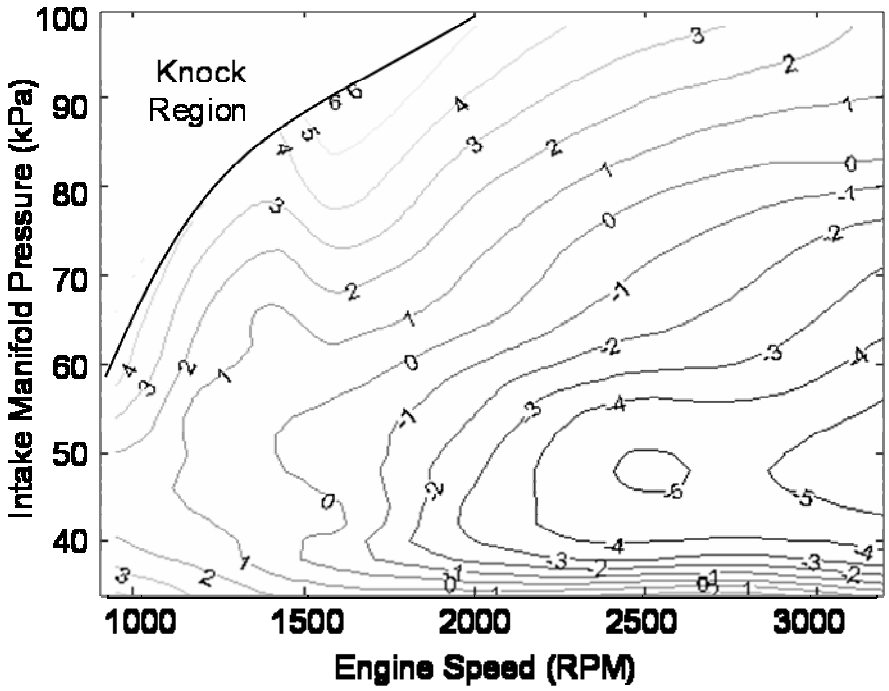

Figure 6.12: The difference in combustion duration from calibrated values to prediction is within six crank angle degrees over the operating range that the models were calibrated.

6.3 Conclusions

An algorithm for predicting ignition timing, given a desired CA50, in a high degree of freedom engine was developed and discussed. The model is intending to be capable of running real-time in an engine control unit. Main model inputs are laminar flame speed, turbulence intensity, unburned gas density, and total in-cylinder mass. The residual gas fraction estimate required to complete several of the input calculations is provided by the model discussed in Section 4.10.

The ignition timing selection model consists of two sub-models: one to predict combustion duration and another for combustion phasing. The duration sub-model is loosely based on a turbulent flame entrainment combustion model and is used to predict the crank angle duration from ignition to CA50 for each operating condition. A constant flame entrainment rate is generated for each operating condition by manipulating inputs to simplify calculation. Combustion duration is estimated based on total in-cylinder mass

(air, fuel, and residual). Using total in-cylinder gas partially accounts for changes in burn-up rate caused by different internal residual gas fraction quantities, and allows burn-up to be modeled by an offset that depends upon total entrainment duration. The method greatly simplifies calculation and it re-predicts combustion duration of experimental data with an RMSE of 2.3 CAD. The combustion phasing sub-model is used to determine the required ignition timing from combustion calculations performed over the entire spark window. While overall performance of the combustion phasing model was good, more work is required to improve model accuracy. Combustion phasing prediction at low engine loads requires improved accuracy. Of particular interest for improving accuracy is the flame area prediction over the spark window.

To further test the combustion duration sub-model a case study was investigated. Combustion duration using the base spark map from a fixed-cam version of the test engine was re-predicted. All of the operating conditions represented by the base ignition timing map were new and not previously recorded experimentally. Combustion duration is predicted to within six crank-angle degrees over a production engine ignition timing map which is within 10% of the actual value for each operating condition.

CHAPTER 7

SUMMARY AND CONCLUSIONS

7.1 Thesis Summary

The objective of this thesis is to develop new diagnostic techniques that experimentally characterize key combustion parameters and then use the new information to create a universal physics-based ignition timing prediction model that is suitable for high degree of freedom engine applications. Specifically, the influence of new technologies on turbulence intensity and residual gas fraction are quantified using a combination of direct experimental measurements and data processing routines. Experimental results are used to generate semi-empirical models for each parameter that are capable of running real-time within an engine controller. The new input parameters of turbulence intensity and residual gas fraction are then used to create simplified physics-based combustion model to predict ignition timing.

The newly formulated ignition timing prediction method is able to accommodate a wide range of new engine technologies because it is based on fundamental spark-ignition engine combustion principles. The algorithm is loosely based on a well-established turbulent entrainment combustion model. Model architecture places primary importance on new experimentally-based methods to quantify turbulence intensity and internal residual gas fraction. In response to this need, new routines that combine experimental measurement and engine simulation to quantify turbulence intensity and residual gas fraction were developed. The results are used to create sub-models for each

parameter that are capable of real-time operation in an engine control unit. Both turbulence intensity and residual gas fraction prove to be invaluable inputs to the combustion model and provide significant insight into new engine technologies.

The ignition timing selection model is divided into two sub-models; one to predict combustion duration and another for combustion phasing. The duration sub-model is used to predict the crank angle duration from ignition to CA50 for each operating condition. A single characteristic flame entrainment rate is generated for each operating condition by manipulating inputs to simplify calculation. The greatly simplified method re-predicts combustion duration of experimental data with an RMSE of 2.3 CAD. The combustion phasing sub-model is used to determine the required ignition timing from combustion calculations performed over the entire spark window of each operating condition. While overall performance of the combustion phasing model is good, more work is required to improve model accuracy.

7.2 Significant Conclusions and Findings

Contributions and improvements are realized in three distinct areas; (1) experimental residual gas fraction measurement, (2) turbulence intensity estimation using a combination of experimental data and simulation, and (3) the development of a physics-based model to predict combustion duration over the wide operating range that is intended for real-time engine control. Significant findings in each category are described separately in the following sections.

7.2.1 Internal Residual Gas Fraction Measurement

High degree of freedom engines are capable of generating a wide range of internal residual gas fraction (RGF) levels. It is important to quantify residual gas fraction because it significantly impacts laminar flame speed. Estimation of laminar flame speed

is a critical input for spark timing prediction and combustion analysis. Several residual gas fraction measurement methods were described and compared in a liquid-fuelled variable valve timing engine. RGF measurements using each method were performed simultaneously in the same cylinder and engine cycle to ensure proper comparison. Variability of each technique was quantified by analyzing repeated measurements at each engine operating condition. Engine variables influencing residual gas fraction related to variable valve phasing were quantified and discussed. Conclusions pertaining to the accuracy of each method were assessed based on indicated RGF trends with the variation of engine speed, pressure ratio, valve overlap, and overlap centerline location. The effects of using the CMCV and negative valve overlap on RGF were also discussed. Recorded data was used to assess several existing semi-empirical models, and to calibrate the constants in the preferred model. Findings are summarized as follows:

- Response times of the NDIR500 and HFR500 are such that intentional misfire is required at or above 1500 rpm. Intentional misfire extends the available time for measurement of pre-combustion gases.
- Measurement variability for the in-cylinder CO_2 based method was determined to be +/- 10% (95% confidence level) for the method requiring intentional misfire, the lowest of the three methods. Variability in both the in-cylinder HC and CO_2 based methods is greatly reduced when charge motion is high and the assumption of perfect mixing is valid.
- In-cylinder HC concentration is only a good indicator of RGF when charge motion is high. In this case, activating the charge motion control valve greatly improves measurement accuracy as compared to the results obtained using in-cylinder CO_2 measurement. Without the CMCV, in-cylinder HC levels were subject to large variability, producing inaccurate RGF results.

- Using a single exhaust port-mounted CO_2 sensor with an intentional misfire to measure pre-combustion gases produces high variability. The technique is simple, but requires measurement compensation for over-expansion backflows that occur after the intentional misfire. In general, this method did not provide sufficiently accurate results as compared to the in-cylinder CO_2 based measurement.
- Measuring residual gas fraction using a fast response in-cylinder CO_2 analyzer coupled with a second exhaust port mounted probe provided the lowest variability and most consistent trend prediction.
- Operating with positive overlap, residual gas fraction is highly sensitive to pressure ratio across the engine. The highest RGF levels occur at low pressure ratios, where exhaust gas backflows are large. Overlap centerline location shifted to both side of TDC increases RGF, and exhaust biased centerline provides the highest residual levels. Increasing engine speed decreases the time available during overlap for backflows, therefore RGF reduces at high engine speeds
- The charge motion control valve (CMCV) activation state does not significantly affect measured RGF if pressure ratio is calculated using an intake manifold pressure sensor located between the CMCV and the intake valve.
- Negative valve overlap operation allows for more predictable RGF because backflows are eliminated. Cylinder volume at EVC is the primary driver of RGF.
- Several semi-empirical RGF prediction models where examined. The model developed by Amer and Zhong (2006) provided the best predictive capability of all models tested. A formula for the density modifier term used in the Amer and Zhong model was calibrated based on the

measurements from the 4-cylinder test engine equipped with variable valve timing.

7.2.2 Turbulence Intensity Characterization

Single-zone heat release analysis does not explicitly describe or separate the affects of flame speed and in-cylinder turbulence. For this reason, heat release analysis alone does not provide all of the necessary information needed to describe the affects of flow altering devices (e.g. charge motion valves, variable valve timing, etc.). A method combining experimental data with a turbulent combustion model was developed to provide a turbulence intensity estimate for any operating condition. Required model inputs are calculated mass-fraction burned and experimentally measured residual gas fraction. A well-known turbulent combustion model is then solved in reverse yielding a representative value for in-cylinder turbulence. Model results were validated by comparison with an existing spark-ignition engine cycle-simulation. Data generated by the new model was used to derive a turbulence intensity prediction routine that is intended for use in an engine control unit. Results and findings are summarized as follows:

- The basic architecture and calculation methods used for calculating turbulence intensity from cylinder pressure data correlate to within 10% of cycle simulation values for the early stages of combustion.
- Uncertainty in calculated turbulence intensity is affected approximately one-to-one by residual gas fraction input uncertainty (±10%).
- Calculated turbulence intensity for the range from 5% to 10% mass fraction burned is averaged to generate a single characteristic value at each operating condition.

- Calculation results show that turbulence levels scale linearly with mean piston speed, which is in agreement with the observations of previous researchers. Spark timing, engine load, and valve overlap also have an impact on turbulence intensity.
- A model intended for use in an engine controller was generated, based on linear correlations, to calculated turbulence intensity throughout the engine operating range. The prediction accuracy of the model matched experimentally calculated turbulence levels with a RMSE of less than 1.0 m/s.

7.2.3 Combustion Duration Model Development

Observed combustion duration trends in high degree of freedom engines demonstrate the need for improved ignition timing control strategies. Previous attempts to develop model-based ignition timing prediction models have relied on complicated empirical equations. The equations used did not provide sufficient physical insight into combustion, and tend to hinder localized adjustments. To address these problems, the use of a simplified turbulent flame entrainment combustion model for an ignition timing prediction was proposed in this thesis. In addition to conventional engine variables, inputs for turbulence intensity and laminar flame speed were made available through newly developed techniques. The ignition timing prediction model is divided into two sub-models, one for calculation of combustion duration from ignition to CA50 and a second to properly phase combustion. Results and findings are summarized as follows:

- Combustion duration is calculated by determining a characteristic flame entrainment rate for each operating condition.
- Base-inputs are manipulated to yield the required entrainment rate according to newly developed models. Characteristic values of turbulence

intensity, laminar flame speed, flame area, and unburned charge density are held constant throughout the calculation.

- The characteristic gas density is calculated from the product of unburned charge density a density multiplier. Analysis of experimental data revealed that the density multiplier is linearly proportional to the instantaneous combustion chamber height at ignition.
- Flame area for each operating condition is calculated by an empirically fit equation. Accuracy of the empirical equation proved adequate, but improvements to the model are needed to associate physical meaning to the prediction and improve robustness.
- Combustion duration is estimated based on total in-cylinder mass (air, fuel, and residual) and a constant rate of mass entrainment. Using total in-cylinder gas partially accounts for changes in burn-up rate caused by different internal residual gas fraction quantities, and allows burn-up to be modeled by an offset that depends only on total entrainment duration.
- Using a characteristic flame entrainment rate greatly simplifies calculation and it re-predicts combustion duration of experimental data with an RMSE of 2.3 crank-angle degrees.
- To further validate the combustion duration sub-model a case study was investigated. Combustion duration using the base spark map from a fixed-cam version of the test engine was re-predicted. All of the operating conditions represented by the base ignition timing map were new and not previously recorded experimentally. Combustion duration is predicted to within six crank-angle degrees over a production engine ignition timing map which is within 10% of the actual value for each operating condition.
- The combustion phasing sub-model is used to determine the required ignition timing from combustion calculations performed over the entire

spark window of each operating condition. While overall performance of the combustion phasing model was good, more work is required to improve model accuracy. Of particular interest for improving accuracy is the flame area prediction over the spark window.

7.3 Future Work

Future research on several key topics could improve the robustness and predictive capability of the ignition timing routine discussed in this thesis. A list of suggested areas of improvement is as follows:

- Development of an improved residual gas fraction prediction method specifically for high degree of freedom engines is required. Experimental measurements using a fast response CO_2 analyzer in conjunction with high speed sample valves could extend the measurement range and increase the quantity of available data.
- Perform more extensive mapping of the engine operating range, including high speed as well as knock limited operation. Increasing the size and reach of the test data sample set will ensure that the prediction models are robust.
- Develop a new characteristic flame area prediction method for input to the combustion duration model. The new model should provide physical meaning to flame area prediction. Incorporating a new model will improve the predictive nature of the combustion model. Significant insight could be obtained by performing extensive spark timing sweeps while holding all other control actuators constant and analyzing flame area trends.

APPENDICES

APPENDIX A

IGNITION TIMING SELECTION CRITERIA

A.1 Overview of Ignition Timing Selection

Start of combustion in a spark-ignition engine is controlled by the timing of a spark discharge. The spark is generated by applying a large electrical potential (voltage) across gap filled with a combustible air and fuel mixture. After successful ignition, a flame propagates throughout the combustion chamber until it terminates at the chamber walls. Characteristics of the flame front, such as shape and velocity, are dependent on engine design and operating conditions. Timing of the spark ignition process must be adjusted to account for changes in combustion rate and the available time for combustion. For these reasons, required spark timing can vary significantly throughout the operating range of a given engine.

Ignition timing for a given operating condition is selected by considering fuel economy, torque, engine-out emissions, and catalyst condition. Spark timing can also influence the onset of engine damaging knock. The importance of each of these considerations changes throughout the engine operating range, and at a given operating condition each of the previous factors must be considered to generate optimal ignition timing. Examples of several important factors influencing spark timing throughout the engine operating range are shown in Figure A.1.

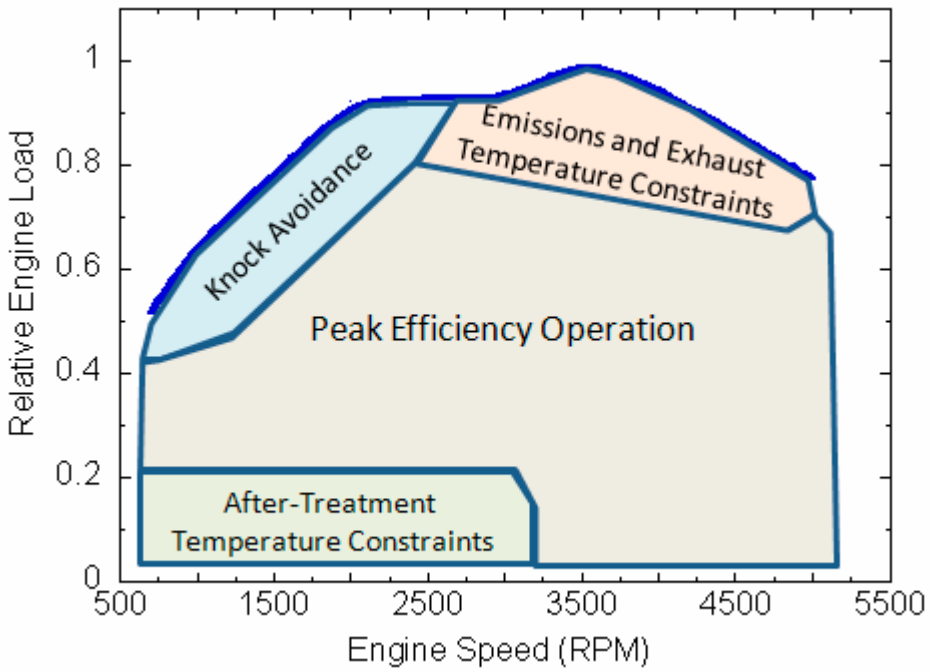

Figure A.1: The selection of spark timing is influenced by many factors. The importance of each factor can vary significantly throughout the engine operating range.

Ignition timing is defined by the number of crank angle degrees before top dead center (BTDC) of the compression stroke that the spark is initiated. Moving the spark timing so that is occurs earlier in the compression stroke is known as advancing the spark, while moving the spark later in the compression stroke is known as spark retard. The spark timing at that generates maximum torque at a given operating condition is known as maximum brake torque timing, or MBT timing. Even though MBT timing generates the maximum torque and efficiency for a given operating condition it is not always desirable, or even possible, to maintain MBT due to emissions and knock constraints. An in-depth discussion of spark timing selection criteria is provided in the following section.

A.2 The Factors Affecting Spark Timing Selection

In-cylinder gas pressure during the engine cycle provides significant insight into ignition timing selection. Three cylinder pressure curves recorded with different spark

timings are shown in Figure A.2. Peak cylinder pressure increases as the spark is advanced earlier in the compression stroke, and decreases when combustion is phased later. Peak cylinder pressure increases with spark advance because the bulk of heat release occurs in the compression stroke and the gas is compressed into a smaller cylinder volume than it would if combustion were phased later. Pressure during the expansion stroke increases as spark is delayed because combustion phasing is shifted.

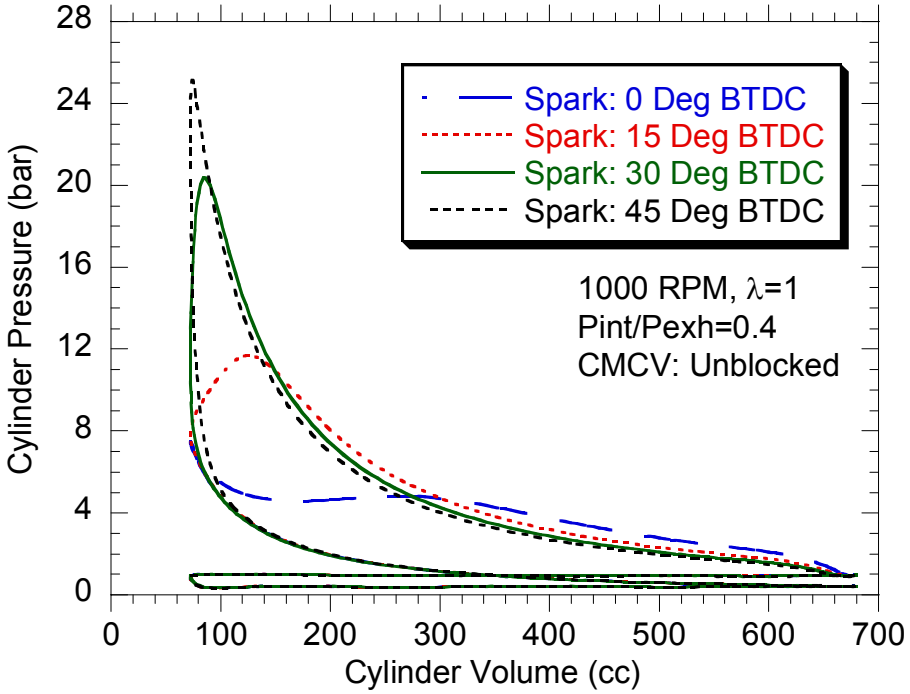

Figure A.2: P-V diagram of a typical spark sweep. Peak cylinder pressure is a function of spark timing; advancing the spark increases and retarding lowers peak pressure.

Zooming into the high pressure section more detail about the affects of spark timing can be observed in Figure A.3. When the spark is advanced (45° BTDC), pressure begins to significantly rise prior to TDC of the compression stroke. Late spark timing (0° and 15° BTDC) exhibits a late pressure rise, and consequently higher pressure late in the expansion stroke. Very late spark timing (0° BTDC) generates a 'double-hump' in cylinder pressure because significant pressure rise due to combustion occurs after TDC. In the case of very late spark timing it is possible for compression pressure to be higher than peak combustion pressure.

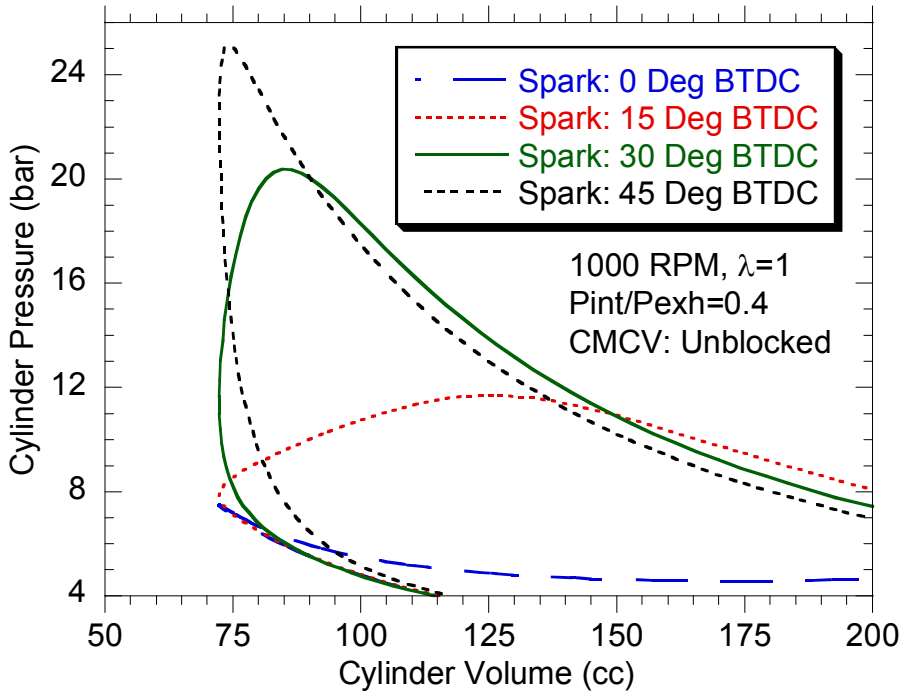

Figure A.3: The high pressure section of the P-V diagram. Pressure rise due to combustion occurs before TDC of the compression stroke for early spark timing and after TDC when spark is delayed.

The mass fraction burned (MFB) profiles for several spark locations, in Figure A.4, show the phasing and duration of combustion. Advanced spark timings cause the bulk of combustion to occur early and fast. For the most advanced spark timing, 45° BTDC, over 70% of the fresh air and fuel are burned prior to the end of compression. The most retarded spark timing (0° BTDC) is phased such that all of the combustion occurs in the expansion stroke. The rate of combustion is indicated by the crank angle duration from the spark to 10% and from10% to 90% MFB. Combustion durations for the entire spark sweep are shown in Figure A.5. The minimum spark to 10% MFB duration occurs for an ignition timing prior to TDC. The duration of initial combustion is dependent on overall phasing and in-cylinder conditions at the time of spark. In general, higher pressures and temperatures create more favorable ignition conditions, so early ignition for a spark near TDC should occur faster than an earlier or later spark. The minimum spark to 10% duration does not necessarily occur at TDC however; spark

phasing also determines the pressure and temperature at which early combustion occurs. As previously discussed, combustion occurring prior to TDC generates higher peak cylinder pressures, increasing combustion rate. The balance to ignition conditions and early rate of combustion favor the minimum spark to 10% MFB duration to occur prior to TDC. The duration of 10% to 90% MFB is primarily driven by the relative cylinder volume where the bulk of combustion occurs. Releasing significant portions of heat prior to TDC (advanced spark) greatly increase the rate of combustion, reducing 10% to 90% MFB duration. Late combustion phasing (retarded spark) generates long 10% to 90% duration because the bulk of heat release occurs during expansion, lowering overall pressure and temperature and slowing combustion.

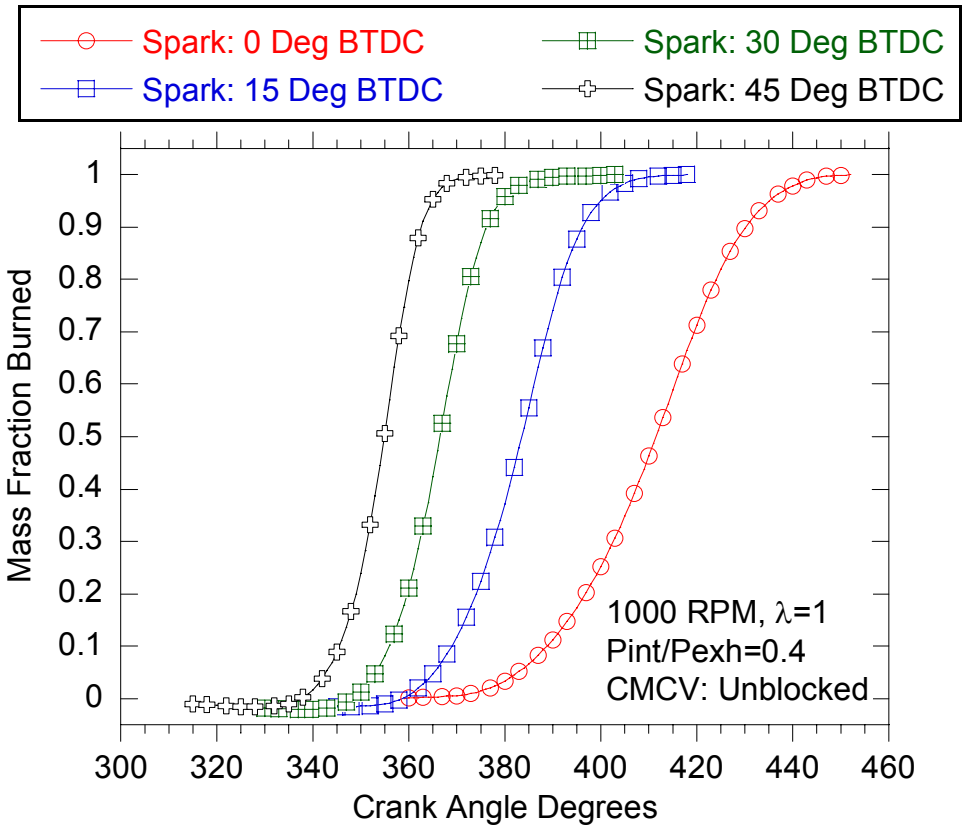

Figure A.4: Spark timing selection affects the phasing and duration of combustion.

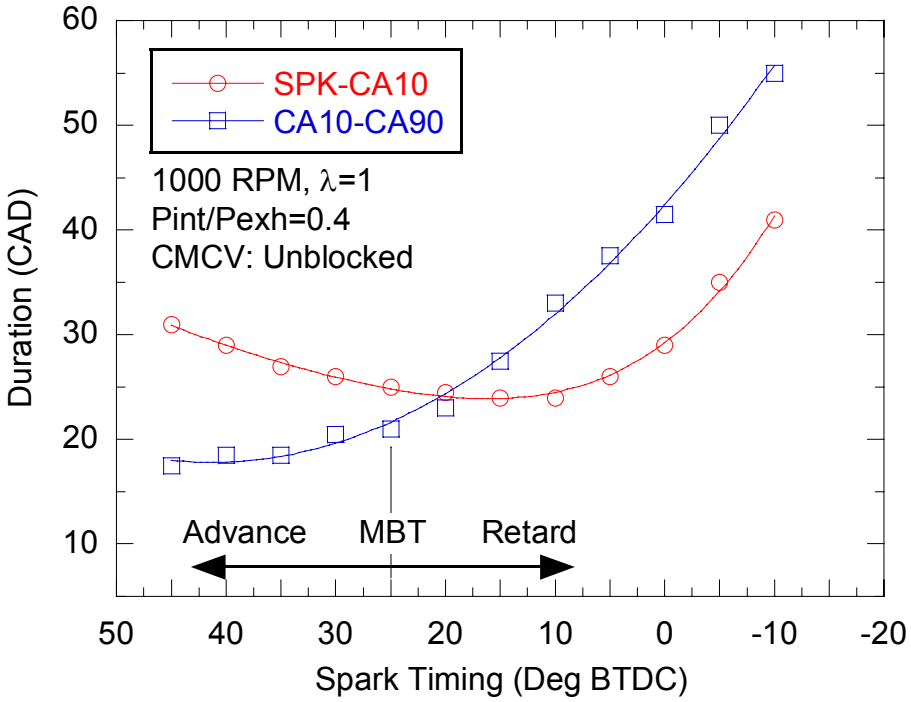

Figure A.5: Combustion durations from spark to 10% and from 10% to 90% MFB are a function of spark timing

Figure A.6 shows $IMEP_{net}$ for 86 consecutive cycles at several spark timings versus the location at which half of the fresh in-cylinder charge is burned, known as CA50. CA50 is an indication of relative combustion phasing. In general, MBT spark timing usually generates a CA50 location around 8-10° ATDC (Heywood 1988). Spark sweep data in Figure A.6 is recorded at the same operating condition, with constant fuel and air mass flow rate. Peak $IMEP_{net}$ occurs when CA50 is approximately 8° ATDC. A similar trend is followed throughout the operating range of the test engine. Retarding spark 10° from MBT decreases $IMEP_{net}$ by approximately 5% in this case. Spark timings advanced from MBT suffer from high heat transfer to the cylinder walls caused by high gas temperatures generated from high peak pressures, reducing net work extracted from the cylinder. Retarding spark timing from MBT reduces work output because energy is released later in the expansion stroke where it cannot be fully expanded, effectively reducing the engine expansion ratio. The trade-off between heat losses at advanced spark

timings and expansion losses at late spark timings generates an optimal spark location for peak efficiency (MBT) for a given set of operation conditions.

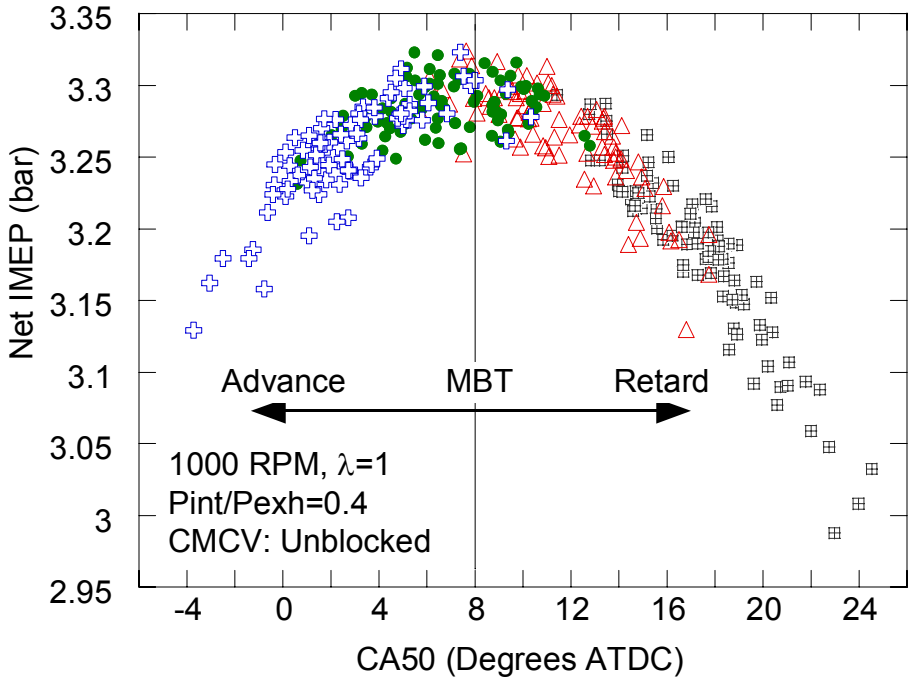

Figure A.6: Spark timing selection influences combustion phasing and determines IMEP for a given amount of fuel energy

Under certain conditions engine-damaging knock can occur. Knock results when unburned gases ahead of the flame front (end gases) ignite independent of flame propagation. Auto-ignition occurs when end gases reach temperatures capable of combustion with sufficient time for initial reactions to develop. When end gases ignite prior to flame front arrival heat release rate greatly increases and high frequency pressure oscillations propagate throughout the cylinder. The pressure fluctuations are often audible, leading to the term 'knock.' Knock is most likely to occur with the combination of low engine speed and high load. Low engine speed allows time for reactions to occur in the end gases, and high engine loads increase the pressure and temperature of the end gases. Under these conditions knock occurs at a spark timing that is retarded from the ideal MBT timing, therefore MBT timing is not possible. Spark retard is used to avoid knock when occurrence is likely. Delaying combustion lowers end gas temperatures by

shifting combustion into the expansion stroke. The use of spark retard to avoid knock decreases engine efficiency, so accurate knock detection and spark timing control techniques are important for fuel economy.

Fuel conversion efficiency, for a given operating condition, is a strong function of spark timing. Peak efficiency occurs at MBT timing, as shown in Figure A.7. Efficiency decreases when spark is advanced from MBT because heat transfer to the cylinder walls increases. Spark retard from MBT reduces efficiency because combustion is shifted into the expansion stroke and the effective expansion ratio of burned gases is reduces. Retarding spark from MBT has a greater impact on efficiency than an equal spark advance.

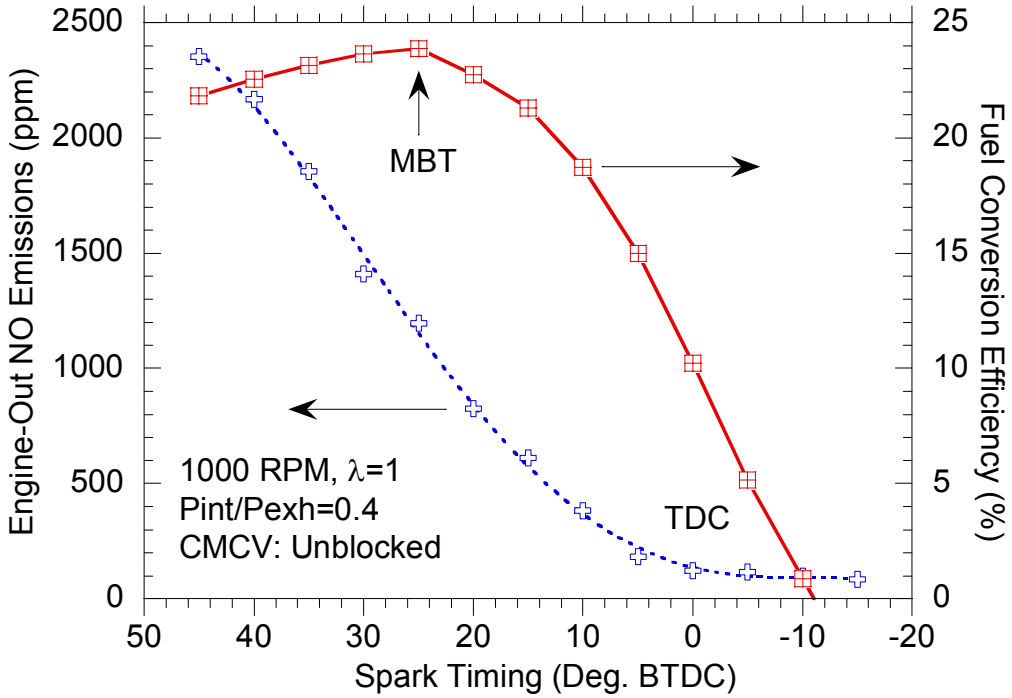

Figure A.7: Peak efficiency occurs at the MBT timing. NO emissions increase with spark advance because peak combustion pressures and temperatures rise.

Engine-out exhaust NO emissions are shown as a function of spark timing in Figure A.7. Chemical dissociation reactions occurring at high temperatures are responsible for in-cylinder NO production. In general, lowering combustion temperatures will reduce NO concentration in the exhaust. The relationship between

spark timing and peak cylinder pressures allows reduction of NO emissions using spark retard. Due to the fuel efficiency and torque penalties associated with spark retard, this control strategy is only used to control NO emissions at high engine loads.

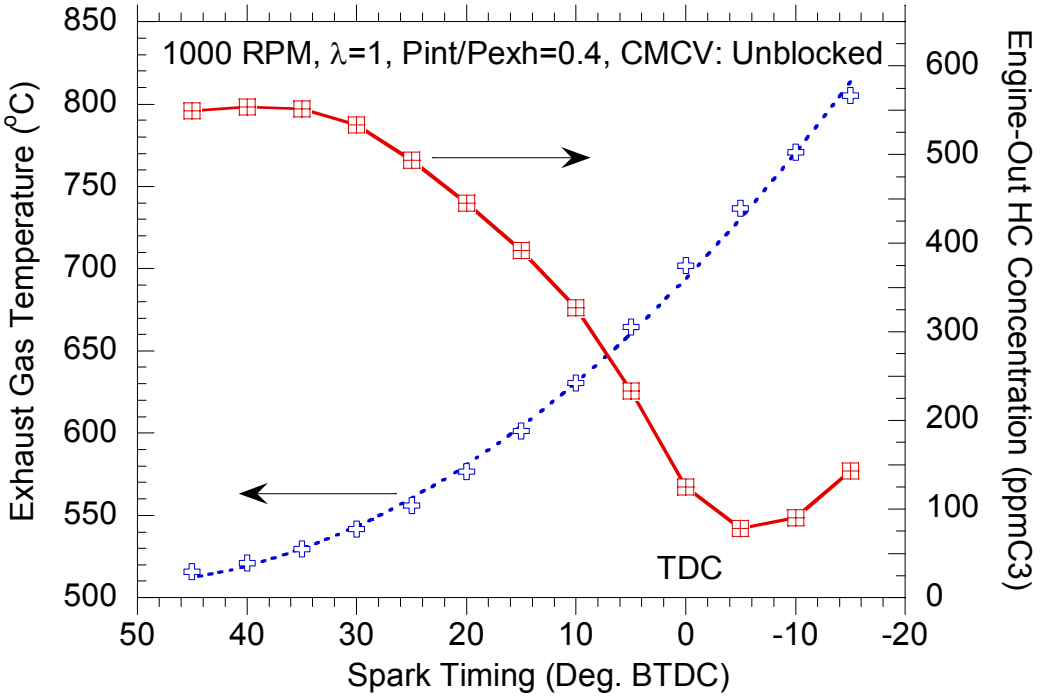

Figure A.8: Phasing combustion later in the expansion stroke increases exhaust gas temperatures, aiding in the burn-up of exhaust HC. The increases in HC emissions at spark timings after TDC are a result of poor combustion conditions.

Exhaust temperature (Figure A.8) is influenced by heat transfer to cylinder walls and the overall expansion to work of in-cylinder contents. Advanced spark timings reduce exhaust temperature because more of the fuel energy is transferred to the engine coolant through the cylinder walls and heat is released early allowing for ample expansion and work production. High exhaust temperatures are generated with late combustion phasing because heat transfer to coolant and the effective expansion ratio is reduced. Spark retard is a commonly used tool to heat and maintain the temperature of the three-way catalyst.

High exhaust gas temperatures created by spark retard are useful for reducing engine-out HC emissions. The cylinder pressure reduction generated by late combustion

reduces the amount of HC that escapes combustion by hiding in crevice volumes, further lowering HC. The reduction of HC emissions with spark retard couples well with increased exhaust gas temperatures and is used to heat the three-way catalyst to an activation temperature during cold-start. HC emissions are generally the constraining species of the regulated emissions during cold-start because cylinder walls are cold and flame quench zones are large (Cheng et al. 1993; Russ et al. 1995; Takeda et al 1995; Stanglmaier et al. 1999). As shown in Figure A.8, excessive spark retard causes an upswing in HC emissions because combustion becomes more erratic.

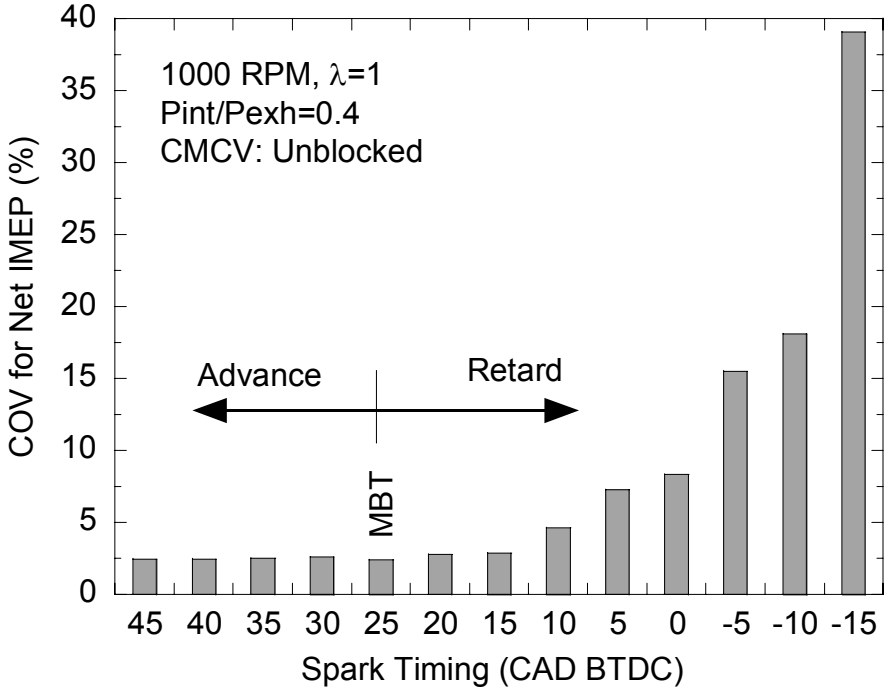

Figure A.9: Variability in Net IMEP increases dramatically at very late spark timings.

The reduction of combustion quality with excessive spark retard from MBT is clearly visible in Figure A.9. COV_{IMEP} is low around MBT timing, and advanced, because combustion temperatures and pressures are high enough to support stable combustion. As spark retard increases COV_{IMEP} begins to increase significantly. High COV_{IMEP} is caused by cycle-to-cycle variations in burn rate in the expanding combustion chamber. (Russ et al. 1999).

Spark-ignition engine load is controlled by varying inlet air flow with a throttle plate while maintaining a constant air-to-fuel ratio. Opening the throttle increases the pressure and density in the intake manifold. The increase in manifold pressure tends to reduced internal residual gas fraction, increasing burn rate. Unburned charge density also affects burn rate. Lower charge density slows flame propagation. Burn duration for the operating condition in Figure A.10 changes by nearly a factor of two throughout the load range. Spark timing must therefore be adjusted as a function of engine load to ensure proper combustion phasing.

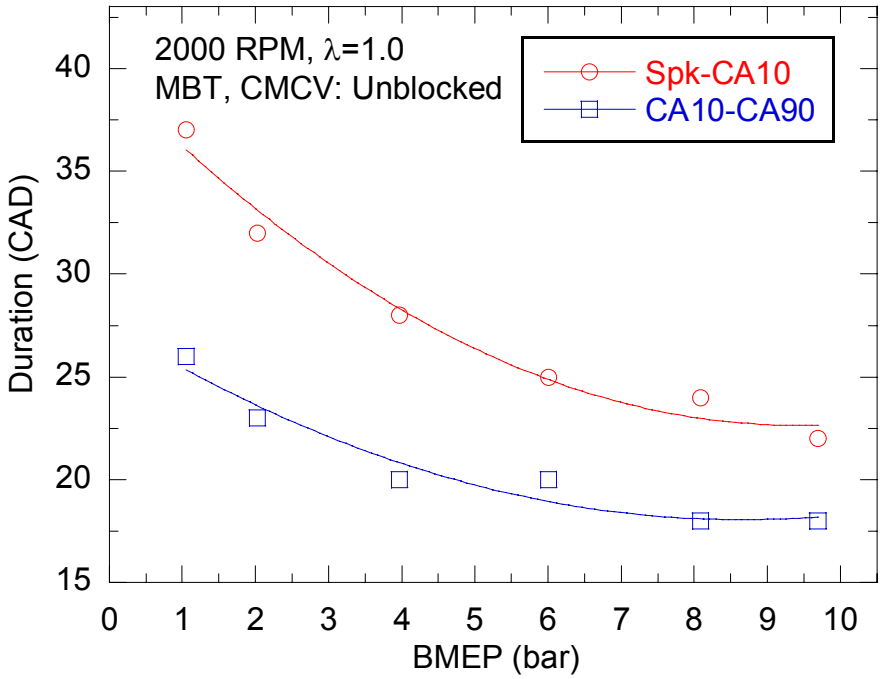

Figure A.10: Combustion duration is a function of engine load. The spark must be advanced as load decreases to maintain MBT timing.

Combustion duration described on a crank-angle basis increases with engine speed (See Figure A.11); however, it increases at a rate less than one-to-one. Combustion occurs in less overall time as engine speed increases, this trend is observed by converting duration to a time-basis (See Figure A.12). Combustion duration changes significantly because in-cylinder charge motion is influenced by engine speed. Average piston velocity is proportional to the flow velocity through the intake valves; increasing

engine speed generates high in-cylinder charge motion elevating the rate of combustion. The change in combustion duration with engine speed requires spark timing adjustment to maintain the desired combustion phasing.

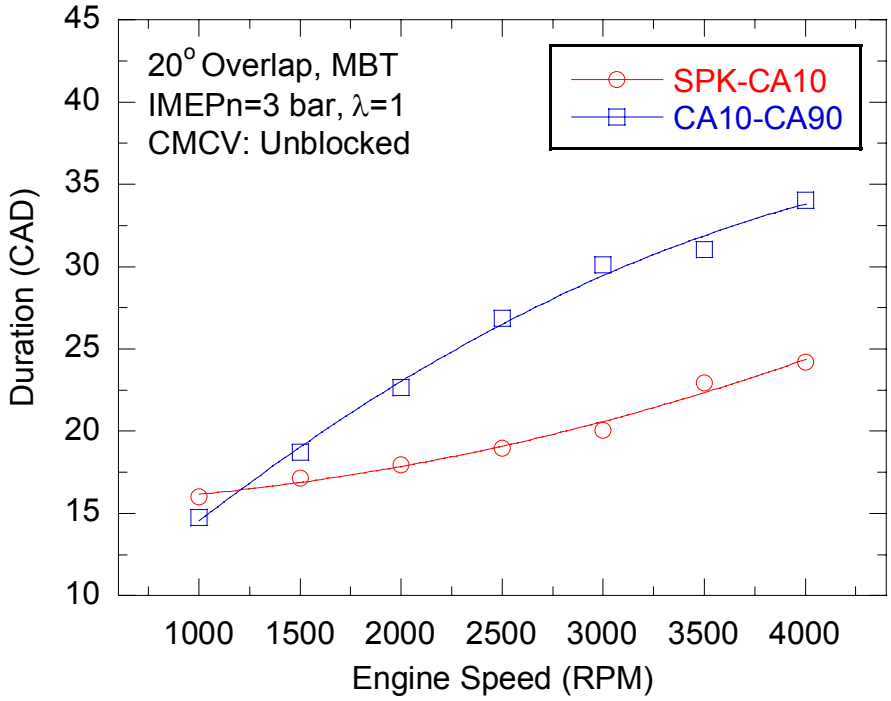

Figure A.11: Combustion duration, reported in CAD, increases with engine speed.

Combustion duration is a function of air-to-fuel ratio at a given engine operating condition. Air-to-fuel ratio affects the laminar flame speed of the in-cylinder mixture. Peak laminar flame speed occurs at a relative air-to-fuel ratio, λ, which is slightly fuel rich. The specific air-to-fuel ratio that creates peak burning velocity is a fuel property and usually occurs from rich mixture (Heywood 1988). Minimum combustion duration occurs at the point of maximum laminar flame speed in Figure A.13. Combustion duration can change by a factor to two depending upon air-to-fuel ratio and spark timing must be adjusted accordingly.

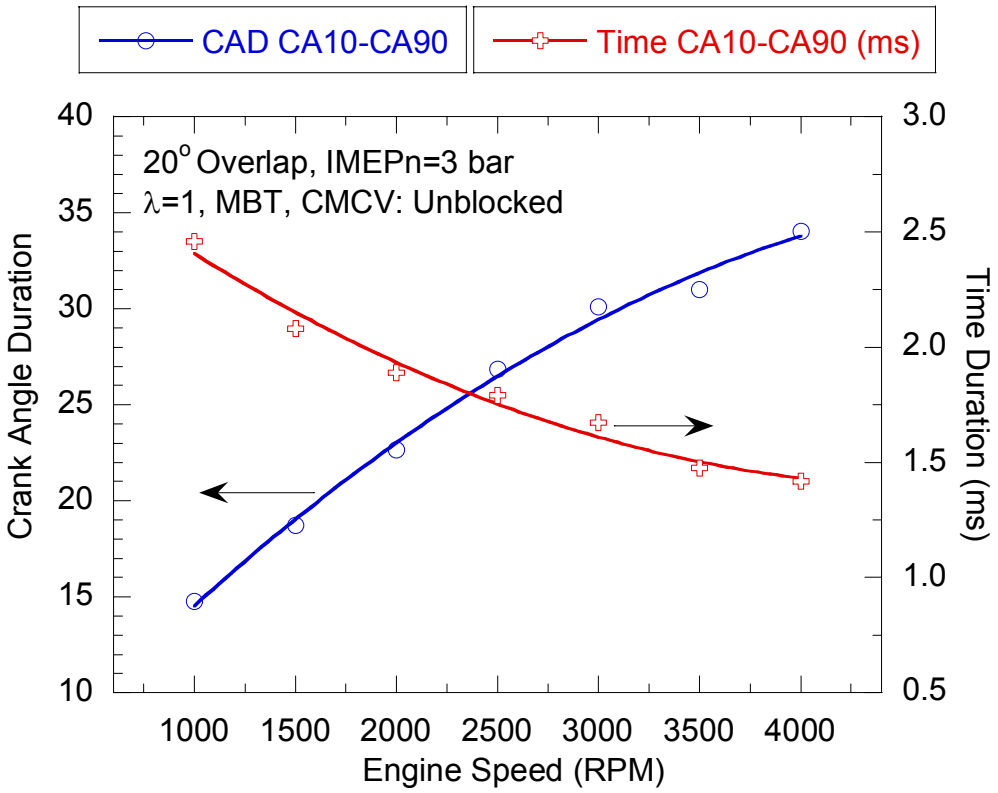

Figure A.12: Combustion duration increases with engine speed when reported in crank angle degrees, but decreases on an overall time basis.

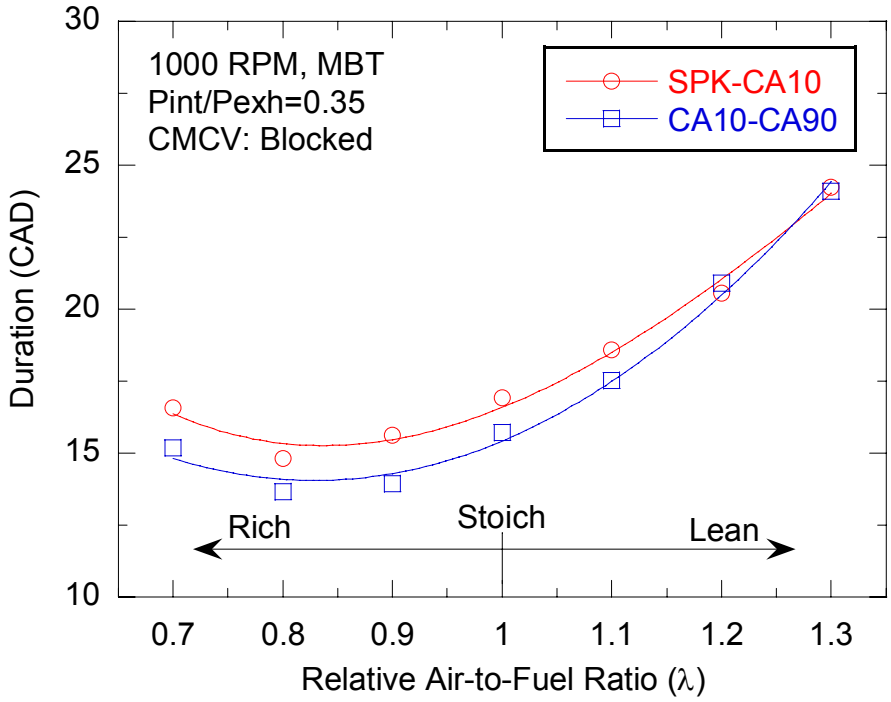

Figure A.13: Relative air-to-fuel ratio alters the laminar flame speed of the in-cylinder mixture and affects burn duration

Combustion duration for a valve overlap duration sweep is shown in Figure A.14. Overlap duration can change combustion duration by approximately a factor of two. Valve overlap affects residual gas fraction, altering laminar flame speed. Laminar flame speed reduces as residual fraction increases. High levels of either positive or negative overlap generate high levels of residual fraction. High levels of positive overlap create exhaust backflows generated by the pressure differential between the intake and exhaust manifold. High negative overlap elevates internal residual gas fraction because exhaust valve closing occurs at a larger cylinder volume, trapping more exhaust gases.

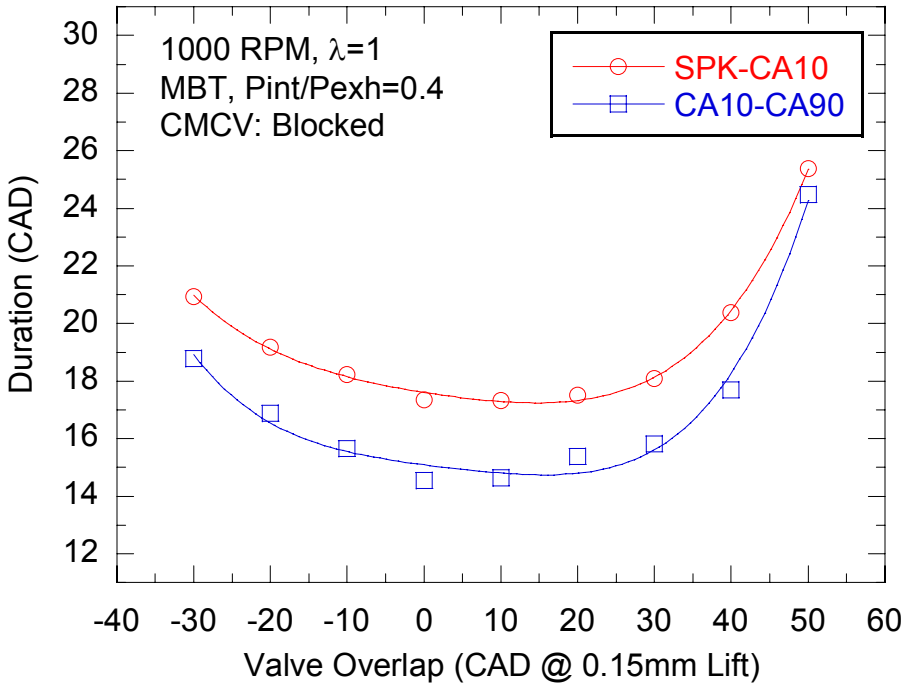

Figure A.14: Valve overlap duration affects combustion duration by changing residual gas fraction. Increasing residual gas fraction decreases laminar flame speed, increasing combustion duration.

The location of overlap centerline affects combustion duration and therefore the required spark timing. Cylinder volume change during the overlap period affects the flow processes that determine internal residual gas fraction. Shifting overlap centerline to the exhaust stroke creates a net decrease in cylinder volume during the valve overlap. Intake stroke centerline bias experiences a net cylinder volume increase during overlap.

At the operating condition in Figure A.15 combustion duration increases around 20% from minimum to maximum. The minimum combustion duration occurs when overlap centerline is located at TDC and increases as bias is shifted to either the intake or exhaust stroke.

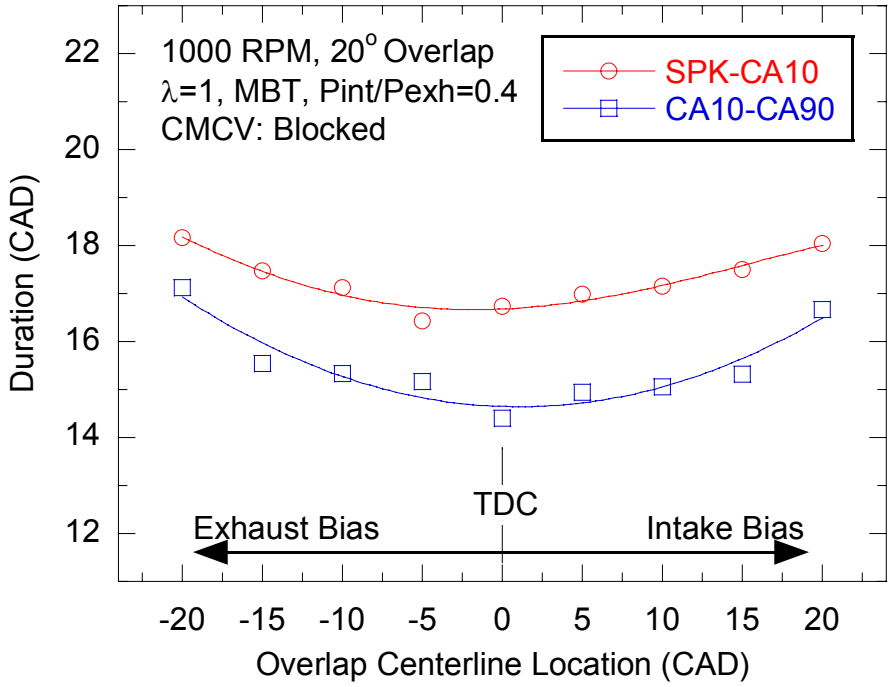

Figure A.15: The location of valve overlap centerline influences residual gas fraction and charge motion, affecting burn duration.

APPENDIX B

AN OVERVIEW OF GAS EXCHANGE AND VALVE TIMING

B.1 An Overview of the Gas Exchange Process

To create a complete understanding of spark ignition engine operation, an in-depth understanding of the gas exchange process is required. Gas exchange processes largely influence engine performance and emissions. The following sections describe general characteristics of the intake, exhaust, and valve overlap processes in a naturally aspirated spark-ignition engine. Diagrams of the intake and exhaust process are shown in Figure B.1 and Figure B.2 respectively.

B.1.1 The Intake Process

There are five general steps that occur to make up the intake process. Mixture preparation and fuel injection are included as one step since they are affected by the intake process. The process steps below represent those of standard cam timing having a valve overlap period during which the intake and exhaust valves are open simultaneously; referred to as positive overlap.

Fuel Injection

While both intake and exhaust valves are closed, fuel is injected into the intake port. Fuel is rarely injected while the intake valve is open. Around 20% (Chen 1996) of the fuel injected during this cycle is vaporized and pulled into the cylinder. The

remaining fuel that is not vaporized collects on the relatively cool intake port walls. The additional 80% of fuel/fuel vapor needed to maintain the proper air fuel ratio for each cycle evaporates or flows in from the port walls.

Hot Exhaust Backflow

Also known as valve overlap backflow, the hot exhaust backflow consists of hot post-combustion gases from the cylinder flowing into the intake manifold during the first few degrees of intake valve opening. Valve overlap backflows provide a large amount of heat to the intake port in a short period of time. The backflow is caused by a combination of valve-overlap and a negative pressure difference between the intake and exhaust manifolds. Since the intake manifold pressure is a function of throttle position and engine speed, the amount of exhaust backflow into the manifold will vary throughout the load and speed range of the engine. Heywood et al. (1991) suggest a critical pressure ratio of 0.54 across the intake valve will choke the backflow and create sonic flow in the valve-seat area. The valve-overlap backflow step in the intake process is also very important for providing heat to evaporate fuel in the intake port (Shin et al. 1995).

Forward Induction

After the exhaust backflow event a mixture of the backflow gases, fuel, and air from the intake is pulled through the intake runner and into the cylinder. Piston motion is the primary driver of flow into the cylinder during forward induction. Gas dynamic effects on cylinder pressure are noticeable during this time and influence cylinder flow to some extent.

Displacement Backflow

The intake valve generally closes several degrees after bottom dead center (BDC) of the intake stroke to take advantage of charge momentum that will continue to allow air into the cylinder at high engine speeds. Since valve timing is generally fixed, there is only a narrow speed range where the engine can benefit from extra charging while the piston is rising toward top dead center (TDC). For this reason, at most engine speeds there is a second backflow of pre-flame cylinder contents that are pushed back into the intake port just before intake valve closing. The displacement backflow is greater in magnitude at slower engine speeds, and decreases as the intake flow momentum increases at higher engine speeds. Displacement backflows remain in the intake manifold area until the next intake process.

Quiescent Phase/Valve Leakage

This is the time when the intake valve is closed and before injection. Fuel films evaporate during this time increasing HC concentration in the intake port. While cylinder pressure is high there is a possibility of leakage of combustion gases back into the intake manifold. Valves generally leak if deposits form between the valve and the valve seat preventing proper sealing. Bad valve sealing can also occur if the cylinder head is warped due to thermal or mechanical stress. Valve leakage is not the focus of this experiment, but it can be an important event because it can be significant enough to change the intake manifold vacuum.

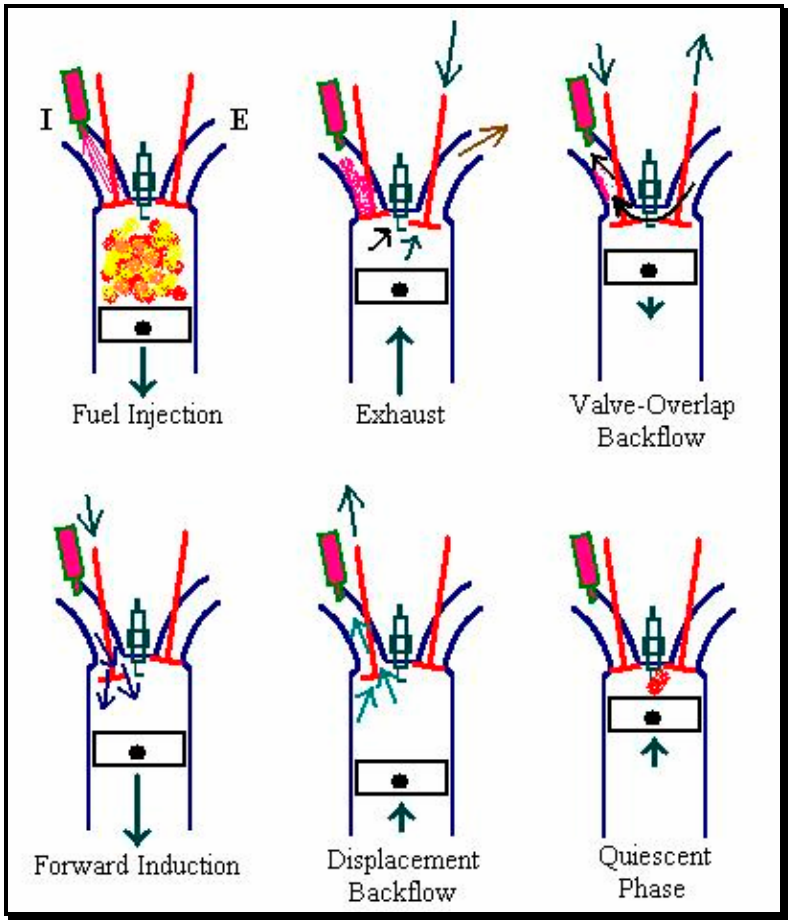

Figure B.1: The intake process in a naturally-aspirated spark-ignition engine

B.1.2 The Exhaust Process

There exist three distinct processes that make up the exhaust process in a conventional fixed-cam four-stroke engine: blow-down, displacement flow, and the overlap period. The blow-down period occurs just after exhaust valve opening (EVO) and consists of a flow created by a pressure imbalance between the engine cylinder and the exhaust port. The second process, the displacement flow, represents the flow created out of the cylinder by the piston sweeping the cylinder from BDC to TDC (otherwise known as the exhaust stroke). The final exhaust process is the overlap period when both intake and exhaust valves are open concurrently. Since the cylinder and exhaust port are generally at a different pressure than the intake port, flows can develop that influence the

residual fraction of the next operating cycle. The use of variable valve actuation can create situations that eliminate or accentuate each of these processes described above. The details of each process affect the temperature and mass flow of exhaust products.

Exhaust Blow-Down

The blow-down period is considered the beginning of the exhaust process. The duration and strength of the blow-down is strongly dependent upon engine speed and load. Generally, the blow-down flow is from the cylinder into the exhaust manifold (under-expansion of in-cylinder gases). However there are occasions where the exhaust pressure can be higher than the cylinder pressure and mass will flow into the cylinder from the exhaust manifold (over-expansion of in-cylinder gases). Blow-down is characterized by a fast equalization of pressures between the cylinder and exhaust manifold. The blow-down period is generally characterized as being choked flow (Heywood 1988) and lasting more than 150 crank-angle degrees in some cases. Due to high gas velocities during the blow-down period, heat transfer to the exhaust valve(s) and port(s) from the hot exhaust gases is extremely high.

Displacement Exhaust Flow

After the blow-down period, the displacement flow period will begin that primarily consists of flows determined by the movement of the piston in the cylinder. Some gas dynamic effects will be present during this process although piston motion primarily influences flow magnitude and direction. If the blow-down period finishes prior to the piston reaching BDC of the expansion stroke, then there can be a displacement flow into the cylinder until the piston reaches BDC. After the piston reaches BDC and starts to travel back toward TDC all displacement flow will be in the direction out of the cylinder. Heywood (1988) states the total flow rate magnitude during

the displacement phase remains nearly constant with varying load at a given engine speed. Therefore, the increased mass of exhaust gas at higher loads will be accounted for during the blow-down period.

Valve Overlap Period

Standard fixed-cam engines generally have a period when both the intake and exhaust valves are open simultaneously known as valve overlap. Valve overlap is designed into fixed-cam engines as a compromise that will allow function throughout the speed and load range of the engine. High valve lift is desired to improve volumetric efficiency at high engine speed and load. However, high valve lift requires longer overall valve opening duration so that valve acceleration levels are acceptable for durability and sound level considerations. Consequently, increasing duration results in increased valve overlap so that high lift sections of the cam lobes continue to align with the intake and exhaust strokes.

The coupling between valve lift and opening duration creates a dilemma when trying to design a fixed cam engine for good performance over a wide operating range. Low valve overlap is desired for low speed and load applications where there is a lot of time for overlap along with a large pressure differential between the intake and exhaust manifolds. Under such conditions, large back-flows of exhaust gases can flow into the intake manifold (which is generally throttled to a pressure below the exhaust system pressure in a SI engine) increasing the residual fraction for the next cycle. High residual levels can severely deteriorate combustion stability at low engine speeds and loads. At high speeds there is not a lot of time for the gas exchange processes to take place. This is why it is important to open the intake valve early so that the valve can be at a high lift by the time the intake stroke begins. Opening the intake valve early and closing the exhaust valve late leads to high levels of valve overlap. As a compromise, fixed-cam engines are

generally designed with the maximum amount of valve overlap that will still allow low enough levels of internal residual to maintain acceptable idle quality. Such a compromise decreases potential peak power levels, but allows for a wide range of stable operation.

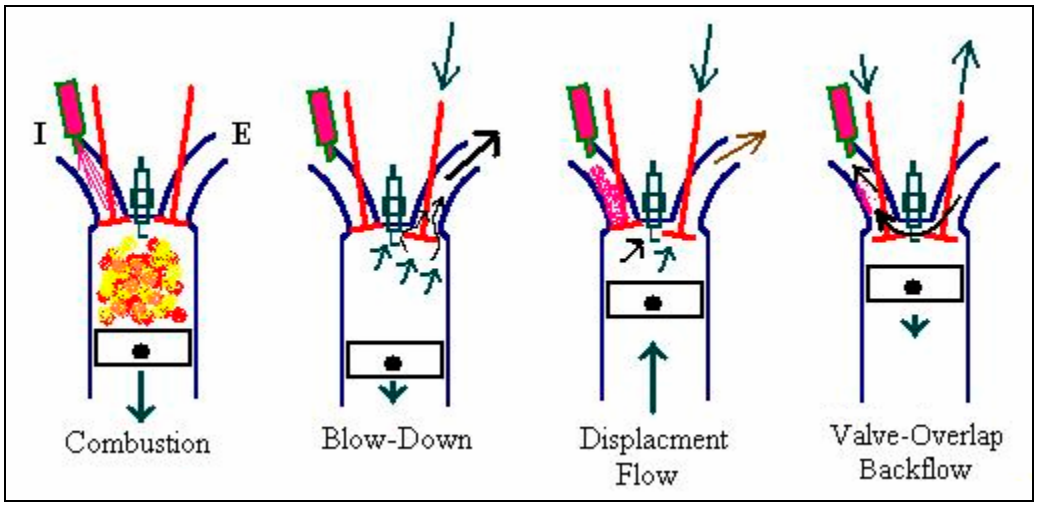

Figure B.2: The exhaust process in a naturally-aspirated spark-ignition engine

B.1.3 Individual Valve Events and Valve Lift

The location of individual valve events and valve lift is critical to engine performance. Each event, whether it is exhaust valve opening (EVO), exhaust valve closing (EVC), intake valve opening (IVO), or intake valve closing (IVC), influences specific engine operating parameters. Flows generated through valves are determined both by pressure gradients and the rate of cylinder volume change. Therefore, it is important to note that valve events should be discussed on the basis of changes in cylinder volume in a phase relationship with the valve opening profile (Asmus 1982). To better understand variable valve timing strategies it is first important to become familiar with the factors affected by the locations of individual valve events.

Exhaust Valve Opening (EVO)

Traditionally, EVO occurs well before BDC of the expansion stroke to allow sufficient time for blow-down to occur, which aids the scavenging process (Asmus 1982; Assanis and Polishak 1990). If EVO is timed close to BDC of expansion it could significantly increase cylinder pressure during the first part of the exhaust stroke, increasing pumping work. Early EVO decreases the effective expansion ratio of the engine which lowers thermal efficiency. Loss of efficiency with either early or late EVO creates an optimum EVO timing that is found between both extremes. For fixed cam engines, the optimum position is chosen as a compromise between high speed and load performance and low speed and load fuel efficiency. The location of EVO also limits either EVC or the maximum valve lift due to the coupling between duration and valve lift. Asmus (1982) reports that for fixed cam engines late EVO can decrease efficiency from 0.07-0.12% per degree of retard. Engines equipped with variable valve timing systems reduce the need for a large compromise of EVO timing.

Exhaust Valve Closing (EVC)

EVC marks the end of the exhaust stroke and valve overlap period when positive valve overlap is present. For fixed cam engines the exhaust valve typically closes between 8 and 20 crank-angle degrees after TDC of the exhaust stroke (Asmus 1982). The location of EVC affects the amount of trapped residual gases since it can determine the length of the overlap period. At low loads, with high pressure gradients from the exhaust to the intake manifold, early EVC will decrease residual and lead to improved cycle-to-cycle variability. Thus early EVC can improve idle quality. Early EVC decreases the engine's ability to scavenge exhaust gases at high engine speeds. For fixed cam engines Asmus (1982) suggests that late EVC decreases low speed volumetric

efficiency from 0.15-0.35% per degree of retard. EVC timing is therefore a trade-off between idle quality and high engine speed performance (Assanis and Polishak 1990).

Intake Valve Opening (IVO)

IVO is the beginning of both the intake stroke and the valve overlap period (if present). The intake valve opening is generally timed 10-25º prior to TDC of the exhaust stroke for fixed cam engines. Early IVO increases the length of the overlap period and therefore increases residual gas fraction. The increase in residual gas fraction is due to increased backflows into the intake manifold from the cylinder during overlap caused by pressure gradients created by throttling. Exhaust backflows may increase residual gas fraction, but they can also aid intake port fuel preparation. The high temperatures and velocities of exhaust gas backflows can help to break-up and evaporate intake manifold fuel films. Delaying IVO reduces the residual gas fraction, but shortens the intake stroke. Asmus (1982) suggests that late IVO may increase pumping work slightly, but it does not have a major effect on volumetric efficiency since there is adequate time for flow recovery during the remainder to the intake process. Therefore, late IVO has very little effect on engine power, but it can significantly affect fuel preparation and residual gas fraction.

Intake Valve Closing (IVC)

IVC is generally located past BDC of the intake stroke during the early part of the compression stroke. Closing the intake valve during the compression stroke allows more time for high momentum gases from the intake manifold to flow into the cylinder at high engine speeds (Assanis and Polishak 1990). At low engine speeds IVC during the compression stroke creates a displacement backflow of cylinder charge back into the intake manifold. Displacement backflows decrease engine volumetric efficiency at low

engine speeds. For fixed cam engines, Asmus (1982) reports that late IVC creates an efficiency loss from 0.42-0.65% per degree of retard for the typical IVC range from 40-60º ABDC at low engine speeds. Therefore, IVC timing is twice as important as EVC location, pertaining to engine output.

Valve Lift

As previously discussed, valve lift and opening duration are linked due to valve acceleration limitations. As with valve timing, optimum valve lift is dependent on engine operating conditions. Intake valve lift is very important to the development of in-cylinder flow fields during the intake stroke. Low valve lift has been shown to increase in-cylinder turbulence and improve combustion at low engine speeds and loads (Assanis and Polishak 1990; Jung et al. 2004). However, low valve lift severely reduces volumetric efficiency at high engine speed and load. Increasing valve lift improves high speed/load performance to a point. Valve lift that is too high can actually reduce volumetric efficiency in some cases due to intake port separation (Annand and Roe 1974). It is also important to note that increasing valve lift will generally increase valve overlap, and therefore residual gas fraction.

B.1.4 Variable Valve Timing Systems and Operating Strategies

Variable valve timing (VVT) devices allow for significant variations in the general gas exchange processes described above. Variations to the gas exchange process under certain conditions can allow for significant improvements in engine performance, fuel economy, and exhaust emissions. An understanding of individual valve events and their influence on engine operation is useful when studying VVT systems. The following sections describe various forms of VVT systems and their operating strategies.

Overview of Variable Valve Timing Systems

Terminology, specific to valve train systems, has been developed to describe the functions of specific systems. Many names have been used to describe these systems, but the three most common are: variable valve timing (VVT), variable valve actuation (VVA), and variable cam timing (VCT). Each of these names are general terms and do not refer to a specific mechanical arrangement of the valve train. All three names can be used to describe strategies that vary cam phasing, lift, or duration or some combination of the three options. Specific functions of each process named VVT, VVA, or VCT must therefore be defined to gain a full understanding of their function. The term VVT will be used throughout this report.

As described previously, VVT, VVA, and VCT are all names used to describe systems that can be used to vary cam phasing, lift, and duration. Cam phasing is the name of the process done when the valve-lift profile is not altered, but the location of the profile is altered with respect to the crankshaft. Otherwise stated, cam phasing shifts both the valve opening and closing locations in the same direction by an equal amount without changing valve lift or opening duration. Variable lift refers to changing the maximum height the valve is opened during a valve event. Variable lift systems may also incorporate the capability to change the shape of the valve lift profile as well. Variable duration refers to adjusting the number of crank-angles in which the valve is open. Variable valve duration is related to variable lift since valve accelerations must be controlled closely to avoid valve failure and seating problems.

Many types of variable valve timing systems have been developed that control from one to all of the options described above (phasing, lift, and duration). The type of system implemented on an engine depends on specific engine requirements, including cost. Most VVT systems in production today allow phasing of either the intake cam or the exhaust cam, but not both simultaneously. However, systems that allow the

adjustment of both cams independently are becoming more common. Most VVT systems in production allow the adjustment of only cam phasing. Variable lift and durations systems add significant complexity and cost which greatly limits their use in high volume production vehicles.

Engines designed with a separate camshaft for intake and exhaust valves have been designed to vary only one cam while keeping the other cam fixed. These systems are usually limited to cam phasing adjustment only, but they can influence engine operation substantially. Generally, intake valve phasing allows for a performance increase by extending the range for which intake tuning is effective. Exhaust valve phasing can be used to increase fuel economy by adjusting the trade-off between expansion losses and pumping losses by adjusting the timing of the blow-down process.

The advantages of phasing both intake and exhaust cams can be combined using a dual-independent cam phasing strategy. Such a system encompasses intake cam only, exhaust cam only and dual-equal strategies along with allowing additional possibilities. Dual-equal strategies are often found on engines with a single camshaft for both intake and exhaust valves. The four major cam phasing systems are discussed in the following sections.

Variable valve timing strategies can be used to optimize engine operation over a broader range than is allowed by fixed cam systems. The main characteristics of engine operation affected by VVT systems are volumetric efficiency, burn rate, expansion ratio, pumping losses, and mechanical efficiency (Asmus 1991). Many mechanical systems available offer variable valve timing capabilities.

Intake Cam Phasing

Phasing of the intake cam only can extend the effective range of intake tuning. Since IVC generally has a greater impact on engine operation than IVO intake cam only

phasing can produce performance benefits. Asmus (1991) suggests intake cam phasing benefits are limited. IVC retardation to take advantage of gas dynamic charging at high engine speeds will also delay IVO. IVO timing influences the speed and timing of intake recompressions due to manifold tuning. Therefore, retarding IVC to gain high engine speed power will only work over a limited range until intake duration is not sufficient to capture intake recompression.

Leone et al. (1996) suggests using intake cam advance at low engine loads to increase trapped mass and residual gas fraction. High overlap decreases HC emissions by drawing high HC concentration gases back into the cylinder late in the exhaust stroke. NOx reductions were also demonstrated due to high levels of residual creating lower combustion temperatures. Intake stroke pumping benefits were also realized. Early IVC tends to trap more mass in-cylinder by reducing displacement backflows into the intake manifold. Increased trapped mass will decrease the required manifold pressure needed to maintain a certain load level, but Leone suggests that the early IVC effect on MAP is more than offset by the benefits if increasing residual. A slightly increased effective compression ratio with intake cam advance is also desirable.

Exhaust Cam Phasing

The ability to phase only the exhaust cam allows for an adjustable expansion ratio and valve overlap period. At low speeds and loads the exhaust cam can be retarded to allow for greater expansion and higher efficiency. Exhaust cam retard generally increases residual gas fraction through the increase in valve overlap. Increased residual gas fraction is known to deteriorate idle quality creating a tradeoff.

Leone et al. (1996) suggests exhaust cam retard at low engine loads to increase expansion work and residual gas fraction. Similar to findings using advanced intake cam timing, high overlap decreased HC emissions by drawing high HC concentration gases

back into the cylinder late in the exhaust stroke. NOx reductions were also demonstrated due to high levels of residual creating lower combustion temperatures. Intake stroke pumping benefits were also realized.

Seabrook et al. (1996) suggests the main benefit of exhaust cam only phasing is emission control. He suggests that both early and late exhaust valve closure reduce HC as well as NOx emissions through retention and re-circulation of end-of-stroke exhaust gases. Seabrook also suggests that exhaust valve timing can be used to increase exhaust gas temperature and reduce catalyst light-off.

Dual-Equal Cam Phasing

Engines utilizing a common camshaft for both intake and exhaust valves can be used to experiment with dual-equal cam phasing strategies. Dual-equal phasing strategies allow the adjustment of desired valve events, such as IVC or EVO, but since all valve events change benefits of such a system can be compromised Asmus (1991). Dual-equal phasing strategies can offer benefits since some valve events influence engine operation more than others.

Leone et al. (1996) recommends that camshaft events be significantly retarded under light load conditions. This strategy delays the overlap period, increasing residual, while reducing pumping work using late IVC and increasing expansion ratio with late EVO. Leone reported that delayed overlap produced three favorable effects, (1) reduced NOx emissions due to higher residual, (2) reduced HC emissions since gases high in HC concentration late in the exhaust stroke were recaptured, and (3) a reduction in intake pumping work. Late IVC reduced effective compression ratio, which could lower combustion temperatures, but this effect was offset by high levels of hot internal EGR. Leone also suggested improved HC emissions were due to a longer post-flame oxidation period brought about by late EVO.

Dual-Independent Cam Phasing

Mechanisms allowing the independent phasing of both intake and exhaust cams provide the greatest range of phasing flexibility. Dual-independent phasing systems can be used to operate with any of the previously discussed strategies as well as a large number of new conditions. Leone et al. (1996) suggests that at part load conditions a dual-independent cam phasing strategy will be very similar to a dual-equal strategy, but with adjustable valve overlap. Leone further suggests that dual-independent strategies have larger benefits over dual-equal strategies at medium and high load conditions.

Kramer and Philips (2002) found significant NOx reductions at part load using a high overlap strategy. He also reported a 10% reduction in HC emissions at part load by retarding the exhaust cam more than the intake cam. The HC reduction is attributed to longer expansion that provides increased post-flame oxidation.

Cold-Start Valve Phasing Strategies

Variable valve timing systems can be leveraged to improve cold-start emissions performance. VVT control strategies that decrease catalyst light-off time as well as reduce engine out hydrocarbons have been studied, but are not well understood. Intake cam phasing strategies have been studied as a means of enhancing engine cold-start performance. Roberts and Stanglmaier (1999) reported a significant drop in COV of IMEP with 19 CAD of intake cam retard under cold conditions. However, Roberts also reported that HC emissions rise dramatically when the intake cam is retarded or advanced beyond 20 CAD. These results may be skewed however since fuel/air ratio was not closely controlled during this testing.

Seabrook et al. (1996) used a model to predict that exhaust temperature will increase with increased exhaust cam retard. Seabrook sites higher residual levels, generated by high valve overlap, as the reason for the exhaust temperature increase

because of reduced burn rate. Burn rate reduction will shift more combustion to later in the expansion stroke when there is less time for heat transfer prior to EVO. Seabrook found an increase of around 20ºC for every 5º of exhaust cam retard.

Kramer and Philips (2002) outlined three requirements of a cold-start cam phasing strategy. They first suggest a moderate valve overlap during cold-start to decrease residual and maintain combustion stability. A second stated requirement is that IVC must be sufficiently early to provide a high enough compression ratio to allow ignition under very cold conditions. Lastly, Kramer suggested that some valve overlap should be present to create hot backflows that will increase mixture preparation and decrease engine-out HC emissions.

Bohac (2003) found that catalyst light-off time could be reduced by applying an early EVO with varied exhaust valve duration. Results using motoring cold-start experiments showed a significant decrease in light-off time over standard timing using two exhaust cams each with EVO 60º advanced while one maintained standard EVC and the second advanced EVC by 40º. The exhaust cam with early EVO and standard EVC produced the fastest light-off, but produced higher HC mass emissions prior to light-off than the other two cams tested. Bohac (2003) sites higher residual levels using early EVC as the reason for different light-off times between the two cams using early EVO. The cam using 60º advanced EVO and 40º advanced EVC produced the lowest HC emissions prior to light-off. Lower HC emissions from the cam using early EVC were attributed to the trapping of HC rich gases that would exit near the end of the standard exhaust process.

APPENDIX C

CALIBRATION OF THE SPARK-IGNITION ENGINE SIMULATION

C.1 Calibration of the Cycle Simulation

The cycle simulation, described in Chapter 3, is calibrated to experimental data by matching burn rate and IMEP. Simulation-specific input parameters are given in Table C.1, geometric engine parameters are given in Chapter 2. The simulated combustion period is of primary interest because the experimental prediction model only calculates turbulence intensity during combustion. To aid in the cycle simulation calibration to experimental data the turbulence dissipation constant (c_β) is fixed at 1.5 and the turbulence multiplier (c_{mult}) is adjusted for burn rate matching at each operating condition and CMCV activation state. The CMCV blocks approximately 85% of the intake port cross-sectional area, therefore if data outside of the combustion period were of interest then turbulence dissipation rate and other geometric parameters would require adjustment to accurately model other engine processes (e.g. gas exchange). The step-by-step process for calibrating the simulation to experimental data is as follows:

1. Adjust valve timing locations (IVO, IVC, EVO, and EVC) to represent the ICL/ECL camshaft positions.
2. Match the experimental spark timing, RPM, and equivalence ratio.
3. Input the experimentally-measured average intake manifold pressure
4. Set turbulence multiplication constant (c_{mult}) to match burn rate to experimental results.

5. Run the simulation to verify the predicted internal residual gas fraction, and adjust the simulated EGR flow to match the measured RGF.
6. Iterate intake manifold pressure settings to match the recorded cylinder pressure.

Model calibration was performed at several operating conditions for each CMCV activation state. The turbulence multiplication constant was set to provide sufficient correlation with experimental burn rate and cylinder pressure over the engine speed and load range tested. Data comparisons for both blocked and unblocked CMCV states spaced throughout the testing range are shown in the Figures below.

Table C.1: Simulation-Specific Input Parameters

Turbulence Dissipation Constant (c_β)	1.5
Intake Valve Diameter	3.72 cm
Intake Flow Area (per valve)	8.40 cm^2
Exhaust Valve Diameter	2.59 cm
Exhaust Flow Area (per valve)	6.66 cm^2

C.2 Calibration Points for Unblocked CMCV Operation

The spark-ignition simulation program calculates burn rate and cylinder pressure to within a couple percent of experimental data when the CMCV is unblocked, or non-active. At low engine speed the simulation predicts slightly longer combustion duration than experimental measurements. As engine speed increases the simulated combustion duration is reduced relative to experiment, and at high engine speeds the predicted burn rate is slightly faster. In general, the combustion event duration is predicted very well for both the flame development (Spark-10% MFB) and bulk combustion (10-90% MFB). The following Figures show simulation correlations with experimental data for several operating conditions with an unblocked CMCV throughout the test range.

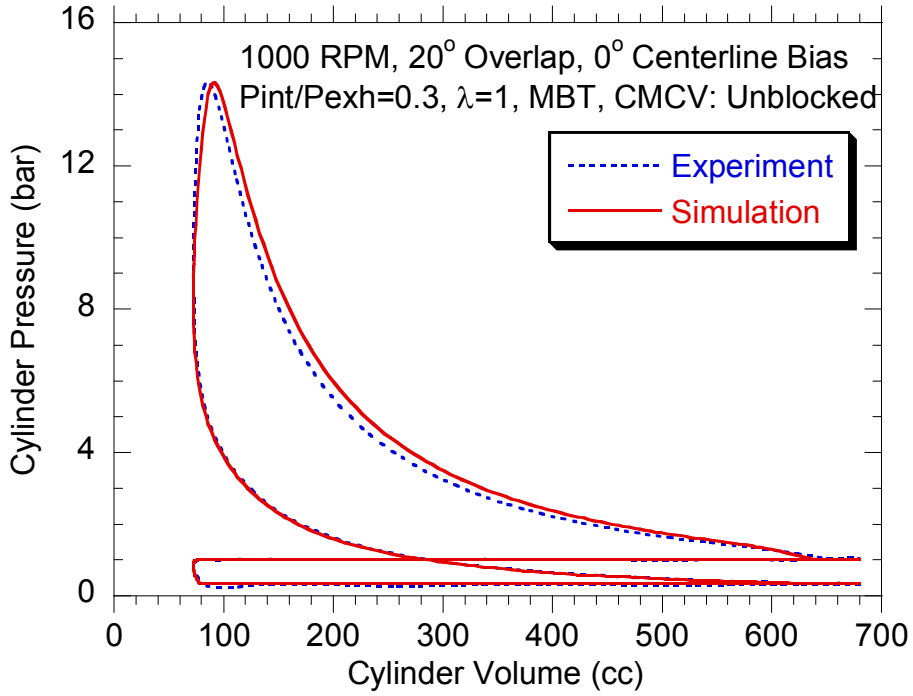

Figure C.1: At low engine speed and load, cylinder pressures correlate quite well because burn rates are closely matched.

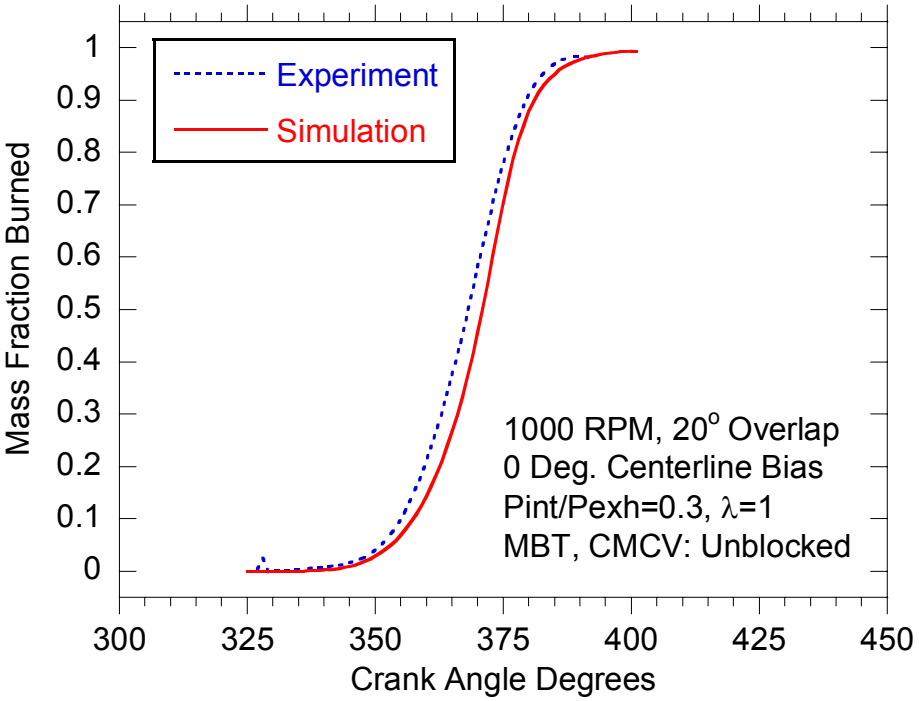

Figure C.2: Simulation results at low engine speed and load predict a slightly slower burn rate for early combustion.

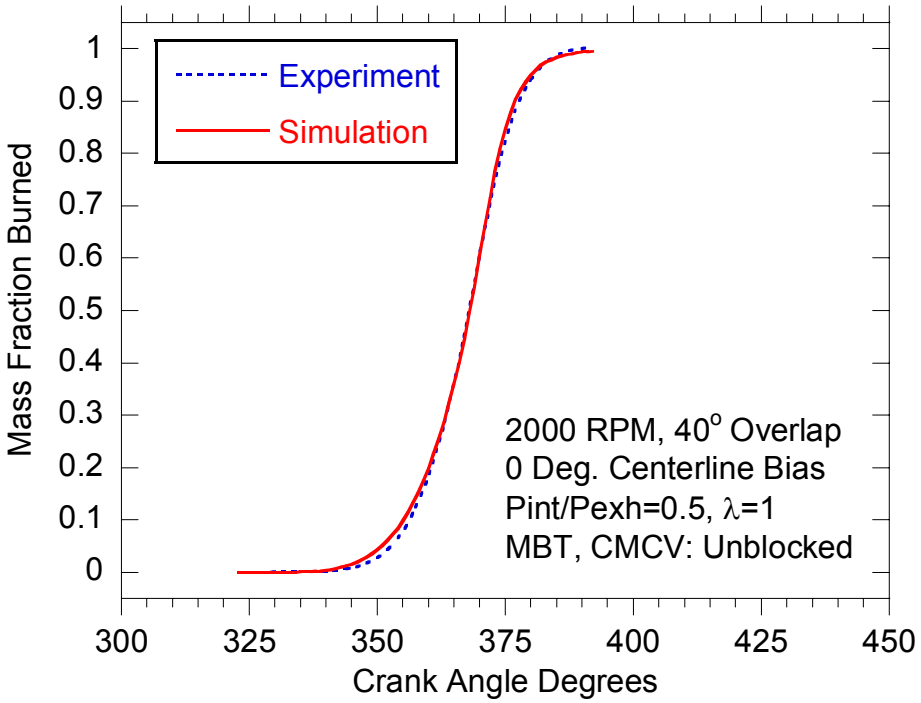

Figure C.3: At medium engine speed and load with increased valve overlap the correlation between simulation and experiment is very good.

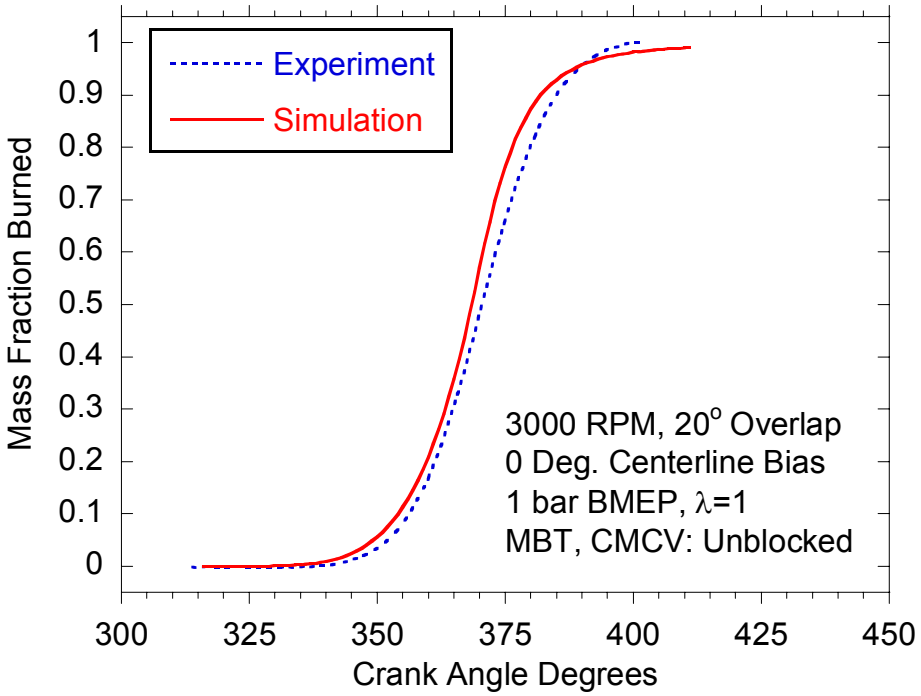

Figure C.4: Simulated burn rate is slightly higher than is experimentally measured at high engine speeds.

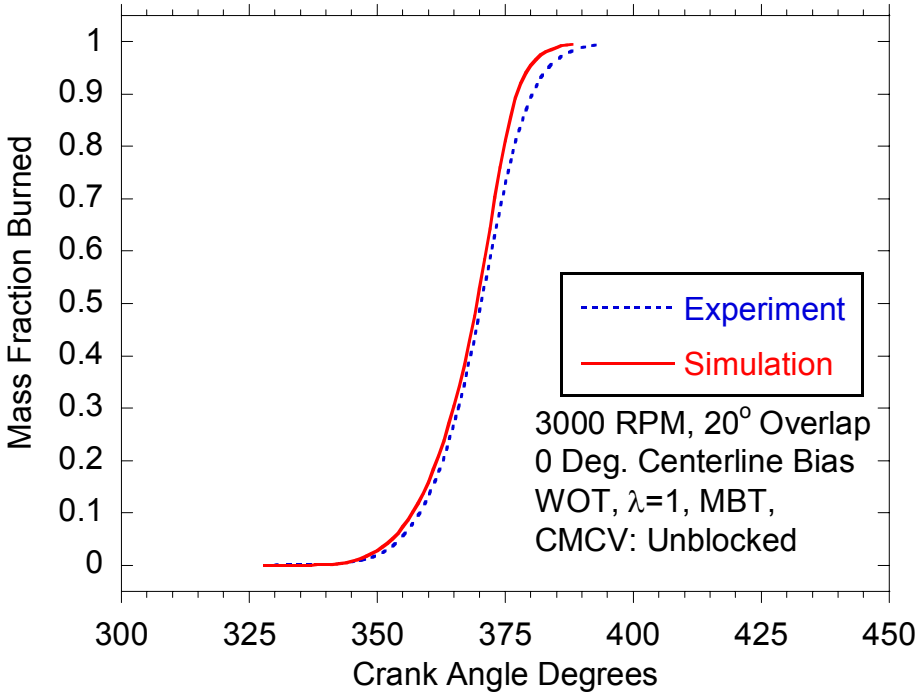

Figure C.5: High speed wide-open throttle operation is properly captured by the simulation.

C.3 CMCV Blocked Simulation Calibration

The spark ignition simulation predicts burn rate and cylinder pressure very well when the CMCV is blocked, or active. Burn rate is predicted within several percent of experimentally determined values. In general, the total combustion event duration is predicted very well; although the proportion of flame development to bulk combustion duration can vary slightly. The following Figures show simulation correlations with experimental data for several operating conditions throughout the test range.

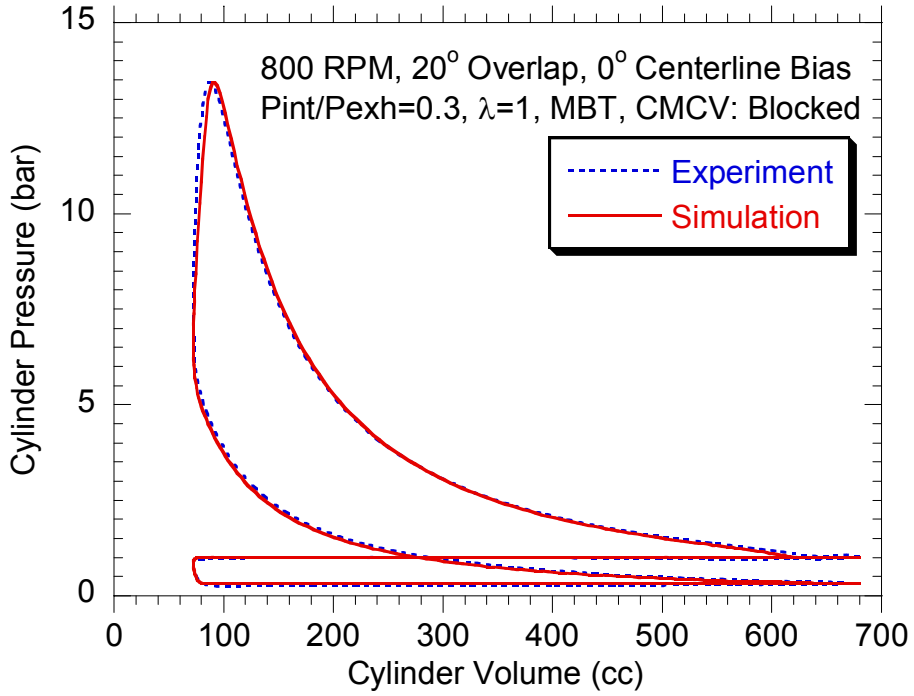

Figure C.6: Cylinder pressure at low speed and load is well predicted by the spark-ignition engine simulation.

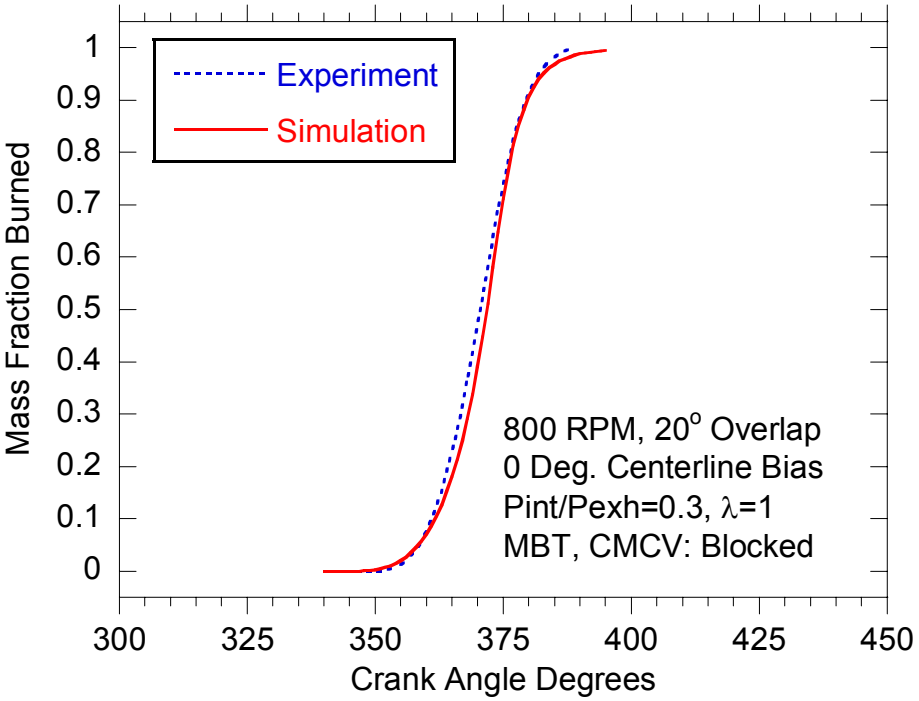

Figure C.7: The duration of flame development is well predicted when the CMCV is blocked. The bulk of combustion (10-90% MFB) is only two percent faster than the simulation prediction.

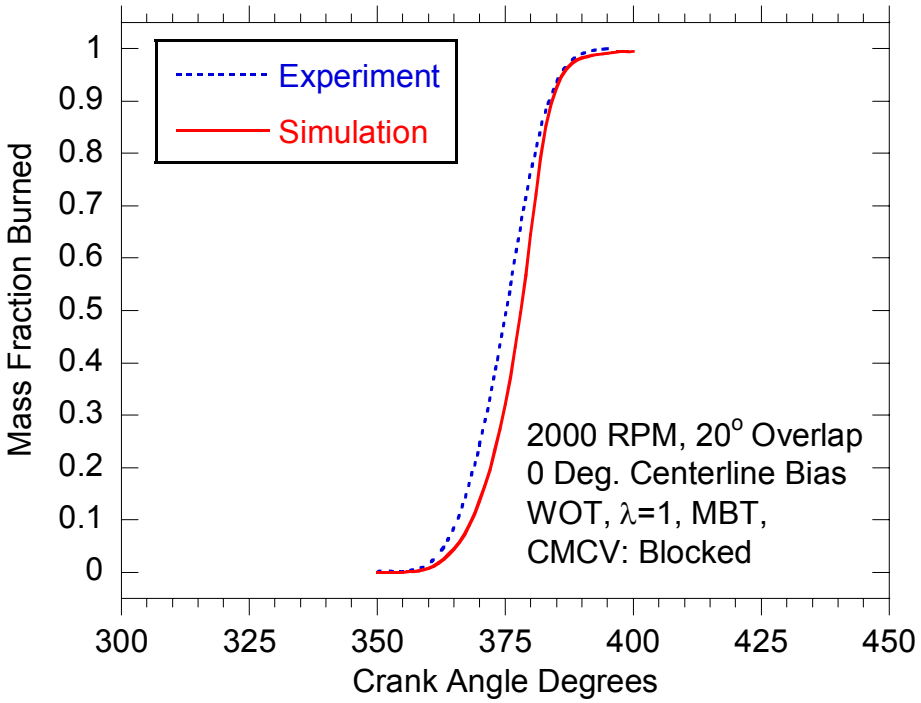

Figure C.8: At full load and medium engine speed the simulation predicts a slightly longer flame development period and a shorter 10-90% duration making the total combustion length very similar to experimental results.

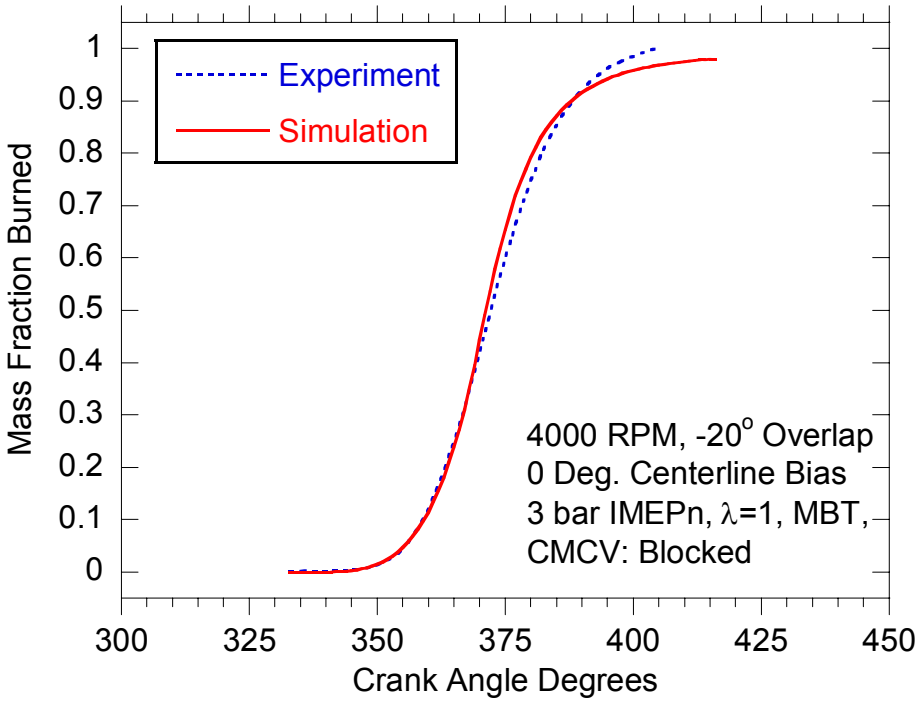

Figure C.9: Overlap variation is well captured by the simulation. In this case, the flame development period (Spark-10% MFB) and bulk combustion (10-90% MFB) match experimental results to within a couple percent.

BIBLIOGRAPHY

Abraham, J., Williams, F., Bracco, F., "A Discussion of Turbulent Flame Structure in Premixed Charges," SAE Paper No. 850345, 1985.

Albert, B., Ghandhi, J., "Residual Gas Measurements in a Utility Engine," SAE Paper No. 2004-32-0029, 2004.

Alger, T., Wooldridge, S., "Measurement and Analysis of the Residual Gas Fraction in an SI Engine with Variable Cam Timing," SAE Paper No. 2004-01-1356, 2004.

Amer, A., Zhong, L., "A Semi-Empirical Model for Fast Residual Gas Fraction Estimation in Gasoline Engines," SAE Paper No. 2006-01-3236, 2006.

Annand, Roe, "Gas Flow in the Internal Combustion Engine," Haessner, Newfoundland, 1974.

Asmus, T., "Valve Events and Engine Operation," SAE Paper No. 820749, 1982.

Asmus, T.W., "Perspectives on Applications of Variable Valve Timing", SAE Paper No. 910445, 1991.

Assanis, D., Polishak, M., "Valve Event Optimization in a Spark-Ignition Engine," Journal of Engineering for Gas Turbines and Power, Vol. 112, pg. 341-347, 1990.

Ayala, A., Bailey, G., "In-Cylinder Measurements of Intake Generated Turbulence in a Steady Flow Rig," ASME Fall Technical Conference, 2000.

Bailey, G., Kuhlman, J., "Intake Turbulence Generated by a Steady Valve - Cylinder Flow," ASME Internal Combustion Engines Vol. 39, pgs 201-209, ICEF2002-498, 2002.

Blizard, N., Keck, J., "Experimental and Theoretical Investigation of Turbulent Burning Model for Internal Combustion Engines," SAE Paper No. 740191, SAE Transactions 86, 1974.

Bohac, S., "Reduction of Spark-Ignition Engine Hydrocarbon Emissions and the Associated Local Ozone Production Through Variable Exhaust Valve Timing", PhD. Thesis, University of Michigan, 2003.

Bozza, F., Gimelli, A., Tuccillo, R., "The Control of a VVA-Equipped SI Engine Operation by Means of 1D Simulation and Mathematical Optimization," SAE Paper No. 2002-01-1107, 2002.

Cains, T., "Measurement of Trapped Residuals in an SI Engine Through Skip-Firing," IMechE Future Engine and Systems Technologies, Paper S490/015/97, 1997.

Cavina, N., Suglia, R., "Spark Advance Control based on a Grey Box Model of the Combustion Process," SAE Paper No. 2005-01-3760, 2005.

Chen, G., Asmus, T., Weber, G., “Fuel Mixture Temperature Variations in the Intake Port”, SAE Paper No. 961194, 1996.

Cheng, W., Hamrin, D., Heywood, J., Hochgreb, S., Min, K., Norris, M., “An Overview of Hydrocarbon Emissions Mechanisms in Spark-Ignition Engines”, SAE Paper No. 932708, 1993.

Cho, H., Lee, J., Lee, K., “Measurements of HC Concentration near Spark Plug and Its Effects on Combustion,” SAE Paper No. 981431, 1998.

Cho, H., Lee, K., Lee, J., Yoo, J., Min, K., “Measurements and Modeling of Residual Gas Fraction in SI Engines,” SAE Paper No. 2001-01-1910, 2001.

Davis, P., Peckham, M., “Measurement of Cycle-by-Cycle AFR using a Fast Response NDIR Analyzer for Cold Start Fuelling Calibration Applications,” SAE Paper No. 2006-01-1515, 2006.

Davis, P., Peckham, M., “Measurement of Cycle-by-Cycle AFR using a Fast Response NDIR Analyzer for Cold Start Fuelling Calibration Applications,” SAE Paper No. 2006-01-1515, 2006.

Davis, R., Patterson, G., “Cylinder Pressure Data Quality Checks and Procedures to Maximize Data Accuracy,” SAE Paper No. 2006-01-1346, 2006.

Depcik, C., Jacobs, T., Hagena, J., Assanis, D., “Instructional Use of a Single Zone, Pre-mixed Spark-ignition Heat Release Simulation,” Accepted by International Journal of Mechanical Engineering Education, 2006.

Durbin, P., Zeman, O., “Rapid Distortion Theory for Homogeneous Compressed Turbulence with Application to Modelling,” J. Fluid Mechanics, Vol. 242, pg. 349-370, 1992.

Filipi, Z., Assanis, D., “Quasi-Dimensional Computer Simulation of the Turbocharged Spark-Ignition Engine and its Use for 2- and 4-Valve Engine Matching Studies,” SAE Paper No. 910075, SAE Trans., 100. Sect. 3., 1991.

Filipi, Z. "Investigation of Variable Valve Area Strategies for a Turbocharged SI-Engine", Proceedings of the IMechE 1994-6, 5th International Conference on Turbocharging and Turbochargers, London, 1994, pp. 93–102.

Filipi, Z., Assanis, D., “The Effect of the Stroke-to-Bore Ratio on Combustion, Heat Transfer and Efficiency of a Homogenous Charge Spark Ignition Engine of Given Displacement,” Int. Journal of Engine Research, Vol. 1, No. 2, 191-208, 2000.

Ford, R., Collings, N., “Measurement of Residual Gas Fraction using a Fast Response NO Sensor,” SAE Paper No. 1999-01-0208, 1999.

Fox, J., Cheng, W., Heywood, J., "A Model for Predicting Residual Gas Fraction in Spark-Ignition Engines," SAE Paper No. 931025, 1993.

Galliot, F., Cheng, W., Cheng, C., Sztenderowicz, M., Heywood, J., Collings, N., "In-Cylinder Measurements of Residual Gas Concentration in a Spark Ignition Engine," SAE Paper No. 900485, 1990.

Gatowski, J., Balles, E., Chun, K., Nelson, F., Ekchian, J., Heywood, J., "Heat Release Analysis of Engine Pressure Data," SAE Paper No. 841359, 1984.

Giansetti, P., Perrier, C., Higelin, P., Chamaillard, Y., Charlet, A., Couet, S., "A Model for Residual Gas Fraction Prediction in Spark Ignition Engines," SAE Paper No. 2002-01-1735, 2002.

Goldwitz, J., Heywood, J., "Combustion Optimization in a Hydrogen-Enhanced Lean-Burn SI Engine," SAE Paper No. 2005-01-0251, 2005.

Guerrier, M., Cawsey, P., "The Development of Model Based Methodologies for Gasoline IC Engine Calibration," SAE Paper No. 2004-01-1466, 2004.

Hall, M., Zuzek, P., Anderson, R., "Fiber Optic Sensor for Crank Angle Resolved Measurements of Burned Gas Residual Fraction in the Cylinder of an SI Engine," SAE Paper No. 2001-01-1921, 2001.

Ham, Y., Chun, K., Lee, J., Chang, K., "Spark-Ignition Engine Knock Control and Threshold Value Determination," SAE Paper No. 960496, 1996.

Hands, T., Peckham, M., Campbell, B., Sutela, C., "Transient SI Engine Emissions Measurements on the FTP75 Drive Cycle with a Fast Response CO Instrument," SAE Paper No. 2001-01-3450, 2001.

Hardenberg H. O., "The Middle Ages of the Internal-Combustion Engine 1794-1886," SAE International, Warrendale, 1999.

Hassaneen, A., "Prediction of Optimum Ignition Timing in a Natural Gas-Fueled Spark Ignition Engine Using Neural Network," SAE Paper No. 2006-01-1347, 2006.

Heywood J.B, "Internal Combustion Engine Fundamentals" McGraw-Hill, Inc. New York, 1988.

Heywood, J., "Fluid Motion Within the Cylinder of Internal Combustion Engines – The 1986 Freeman Scholar Lecture," Journal of Fluids Engineering, pg 109, 1978.

Heywood, J., Internal Combustion Engine Fundamentals, McGraw-Hill, Inc., New York, New York, 1988.

Heywood, J.B., Cheng, C., Cheng, W.K., Maroteaux, D., Collings, N., "Intake Port Phenomena in a Spark-Ignition Engine at Part Load." SAE Paper No. 912401, 1991.

Hinze, P., Miles, P., "Quantitative Measurements of Residual and Fresh Charge Mixing in a Modern SI Engine Using Spontaneous Raman Scattering," SAE Paper No. 1999-01-1106, 1999.

Hohenberg, G., "Advanced Approaches for Heat Transfer Calculations," SAE Paper No. 790825, 1979.

Iizuka, M., Kato, N., Kasashima, K., Muto, H., "Carbon Dioxide Measuring Technology in Engine Combustion Chambers," SAE Paper No. 2004-01-1340, 2004.

Ishizawa, S., "Analysis if HC in Residual Gas and Combustion Efficiency on Spark Ignition Engine," SAE Paper No. 972939, 1997.

Jang, J., Yeom, K., Bae, C., "Effects of Exhaust Throttling on Engine Performance and Residual Gas in an SI Engine," SAE Paper No. 2004-01-2974, 2004.

Jung, H., Stein, R., Leone, T., "Comparison of Dual Retard VCT to Continuously Variable Event Valvetrain," SAE Paper No. 2004-01-1268, 2004.

Karagiorgis, S., Collings, N., Glover, K., Coghlan, N., Petridis, A., "Residual Gas Fraction Measurement and Estimation on a Homogeneous Charge Compression Ignition Engine Utilizing the Negative Valve Overlap Strategy," SAE Paper No. 2006-01-3276, 2006.

Kolmel, A., Spicher, U., "Analysis of Mixture Conditions Close to Spark Plug Location using a Time Resolved Gas Sampling Valve," SAE Paper No. 982473, 1998.

Kramer, U., Phlips, P., "Phasing Strategy for an Engine with Twin Variable Cam Timing", SAE Paper No. 2002-01-1101, 2002.

Krieger, R., Borman, G., "The Computation of Apparent Heat Release for Internal Combustion Engines," ASME Paper 66-WA/DGP-4, 1966.

Kuratle, R., Marki, B., "Influencing Parameters and Error Sources During Indication on Internal Combustion Engines," SAE Paper No. 920233, 1992.

Lee, K., Lee, C., Park, H., Kim, D., "Effects of Tumble and Swirl Flows on the Turbulence Scale Near The TDC in a 4-Valve S.I. Engine," ASME 2001, 2001.

Leone, T.G., Christenson, E.J., Stein, R.A., "Comparison of Variable Camshaft Timing Strategies at Part Load", SAE Paper No. 960584, 1996.

Lygoe, R., "Fitting Automotive Microprocessor Control Look-Up tables to a Response Surface Model using Optimization Methods," SAE Paper No. 981459, 1998.\

Mansouri, S., Heywood, J., Radhakrishnan, K., "Divided-Chamber Diesel Engine, Part 1: A Cycle-Simulation Which Predicts Performance and Emissions," SAE Paper No. 820273, 1982.

Mehta, P., Achuth, M., "Characterization of Tumble Motion in SI Engines – A New Parameter," ASME Internal Combustion Engines Vol. 39, pgs 185-191, ICEF2002-496, 2002.

Metghalchi, M, "Laminar Burning Velocity of Isooctane-Air, Methane-Air, and Methanol-Air Mixtures at High Temperature and Pressure," M.S. Thesis, Departement of Mechanical Engineering, MIT, 1976.

Miles, P., Hinze, P., "Characterization of the Mixing of Fresh Charge with Combustion Residuals Using Laser Raman Scattering with Broadband Detection," SAE Paper No. 981428, 1998.

Miller, R., Russ, S., Weaver, E., Kaiser, E., Newman, C., Davis, G., Lavoie, G., "Comparison of Analytically and Experimentally Obtained Residual Fractions and NOx Emissions in Spark-Ignited Engines," SAE Paper No. 982562, 1998.

Mladek, M., Onder, C., "A Model for the Estimation of Inducted Air Mass and the Residual Gas Fraction using Cylinder Pressure Measurements," SAE Paper No. 2000-01-0958, 2000.

Munson, B., Young, D., Okiishi, T., "Fundamentals of Fluid Mechanics, 4th Edition" John Wiley & Sons, Inc., Hoboken, 2002.

Obert, G., "Internal Combustion Engines," International Textbook Company, Scranton, 1968.

Onder, C., Geering, H., "Model-Based Engine Calibration for Best Fuel Efficiency," SAE Paper No. 950983, 1995.

Page, V. W, "Questions and Answers Relating to Modern Automobile Design, Construction, Driving and Repair," The Norman W. Henley Publishing Co., New York, 1921.

Peckham, M., Hands, T., Burrell, J., Collings, N., Schurov, S., "Real Time In-Cylinder and Exhaust NO Measurements in a Production SI Engine," SAE Paper No. 980400, 1998.

Poulos, S., Heywood, J., "The Effect of Chamber Geometry on Spark-Ignition Engine Combustion," SAE Paper No. 830334, 1983.

Quader, A., Majkowski, R., "Cycle-by-Cycle Mixture Strength and Residual-Gas Measurements During Cold Starting," SAE Paper No. 1999-01-1107, 1999.

Randolph, A., "Cylinder-Pressure-Transducer Mounting Techniques to Maximize Data Accuracy," SAE Paper No. 900171, 1990.

Rassweiler, G., Withrow, L., "Motion Pictures of Engine Flames, Correlated with Pressure Cards," SAE Transactions, Vol. 42, Paper No. 5, 1938.

Ribbens, W., Badalament, M., "Balancing IC Engine Torque Via Individual Cylinder Spark Control," SAE Paper No. 970026, 1997.

Roberts, C. Stanglmaier, R., "Investigation of Intake Timing Effects on the Cold Start Behavior of a Spark Ignition Engine", SAE Paper No. 1999-01-3622, 1999.

Russ, S., Kaiser, E., Siegl, W., Podsiadlik, D., Barrett, K., "Compression Ratio and Coolant Temperature Effects on HC Emissions from a Spark-Ignition Engine", SAE Paper No. 950163, 1995.

Russ, S., Lavoie, G., Dai, W., "SI Engine Operation with Retarded Ignition: Part 1 – Cyclic Variations," SAE Paper No. 1999-01-3506, 1999.

Russ, S., Thiel, M., Lavoie, G., "SI Engine Operation with Retarded Ignition: Part 2 –HC Emissions and Oxidation", SAE Paper No. 1999-01-3507, 1999.

Sandquist, H., Wallesten, J., Enwald, K., Stromberg, S., "Influence of Valve Overlap Strategies on Residual Gas Fraction and Combustion in a Spark-Ignition Engine at Idle," SAE Paper No. 972936, 1997.

Schwarz, F., Spicher, U., "Determination of Residual Gas Fraction in IC Engines," SAE Paper No. 2003-01-3148, 2003.

Schweitzer, P.H., Collins, T.W., "Electronic Spark Timing Control for Motor Vehicles," SAE Paper No. 780655, 1978.

Seabrook, J., Nightingale, C., Richardson, S., "The Effect of Engine Variables on Hydrocarbon Emissions – An Investigation with Statistical Experiment Design and Fast Response FID Measurements", SAE Paper No. 961951, 1996.

Sellnau, M., Matekunas, F., Battiston, P., Chang, C., Lancaster. D, "Cylinder-Pressure-Based Engine Control Using Pressure-Ratio-Management and Low-Cost Non-Intrusive Cylinder Pressure Sensors," SAE Paper No. 2000-01-0932, 2000.

Senecal, J., Xin, J., Reitz, R., "Predictions of Residual Gas Fraction in IC Engines," SAE Paper No. 962052, 1996.

Shayler, P., Lai, W., Brown, N., Harbor, N., "Limits of Charge Dilution, Fuel and Air Proportions for Stable Combustion in Spark Ignition Engines," SAE Paper No. 2004-01-1533, 2004.

Shayler, P., Winborn, L., Hill, M., "The Influence of Gas/Fuel Ratio on Combustion Stability and Misfire Limits of Spark Ignition Engines," SAE Paper No. 2000-01-1208, 2000.

Shimasaki, Y., Maki, H., Sakaguchi, J., Nishizawa, K., Kato, A., Suzuki, H., Kondo, N., Yamada, T., "Study on Combustion Monitoring System for Formula One Engines Using Ionic Current Measurement," SAE Paper No. 2004-01-1921, 2004.

Shin, Y., Min, K., Cheng, W., "Visualization of Mixture Preparation in a Port Fuel Injected Engine During Engine Warm-up", SAE Paper No. 952481, 1995.

Sonntag, R., Borgnakke, C., Van Wylen, G., "Fundamentals of Thermodynamics", John Wiley & Sons, New York, 1998.

Stanglmaier, R., Li., J., Matthews, R., "The Effect of In-Cylinder Wall Wetting Location on the HC Emissions from SI Engines," SAE Paper No. 1999-01-0502, 1999.

Sutela, C., Collings, N., Hands, T., "Fast Response CO2 Sensor for Automotive Exhaust Gas Analysis," SAE Paper No. 1999-01-3477, 1999.

Sutela, C., Collings, N., Hands, T., "Real Time CO2 Measurement to Determine Transient Intake Gas Composition under EGR Conditions," SAE Paper No. 2000-01-2953, 2000.

Suzuki, K., Nemoto, M., Machida, K., "Model-Based Calibration Process for Producing Optimal Spark Advance in a Gasoline Engine Equipped with a Variable Valve Train," SAE Paper No. 2006-01-3235, 2006.

Tabaczynski, R., Ferguson, C., Radhakrishnan, K., "A Turbulent Entrainment Model for Spark-Ignition Engine Combustion," SAE Paper No. 770647, 1977.

Tabaczynski, R., Trinker, F., Shannon, B., "Further Refinement and Validation of a Turbulent Flame Propagation Model for Spark Ignition Engines," Combustion and Flame, 39, 111-121, 1980.

Takeda, K., Yaegashi, T., Sekiguchi, K., Saito, K., Imatake, N., "Mixture Preparation and HC Emissions of a 4-Valve Engine with Port Fuel Injection During Cold Starting and Warm-Up" SAE Paper No. 950074. 1995.

Tang, D., Chang, M., Sultan, M., "Predictive Engine Spark Timing Control," SAE Paper No. 940973, 1997.

Tennekes, M., Lumley, J.L., *A First Course in Turbulence*, MIT Press, Cambridge, Massachusets, 1972.

Toda, T., Nohira, H., Kobashi, K., "Evaluation of Burned Gas Ratio (BGR) as a Predominant Factor to NOx," SAE Paper No. 760765, 1976.

Turns, S., "An Introduction to Combustion: Concepts and Applications, 2nd Edition" McGraw-Hill, Boston, 2000.

Ward's Automotive Yearbook: 2007. Southfield, MI: Penton Media Inc.

Winstead, W. P., "A Production Computerized Engine Timing Control System," SAE Paper No. 770854, 1977.

Wong, V., Hoult, D., "Rapid Distortion Theory Applied to Turbulent Combustion," SAE Paper No. 790357, 1979.

Wu, B., Filipi, Z., Assanis, D., Kramer, D., Ohl, G., Prucka, M., DiValentin, E., "Using Artifical Neural Networks for Representing the Air Flow Rate through a 2.4 Liter VVT Engine," SAE Paper No. 2004-01-3054, 2004.

Wu, B., Prucka, R., Filipi, Z., Kramer, D., Ohl, G., "Cam-phasing Optimization Using Artificial Neural Networks as Surrogate Models – Maximizing Torque Output," SAE Paper No. 2005-01-3757, 2005.

Wu, B., Prucka, R., Filipi, Z., Kramer, D., Ohl, G., "Cam-phasing Optimization Using Artificial Neural Networks as Surrogate Models – Fuel Consumption and NOx Emissions," SAE Paper No. 2006-01-1512, 2006.

Yoon, P., Park, S., Sunwoo, M., Ohm, I., Yoon, K., "Closed-Loop Control of Spark Advance and Air-Fuel Ratio in SI Engines Using Cylinder Pressure," SAE Paper No. 2000-01-0933, 2000.

Zeng, P. Prucka, R., Filipi, Z., Assanis, D., "Reconstructing Cylinder Pressure of a Spark-Ignition Engine for Heat Transfer and Heat Release Analyses," ASME Internal Combustion Engines Fall Conference 2004, Paper No. ICEF2004-886, 2004.

Zhu, G., Daniels, C., Winkelman, J., "MBT Timing Detection and its Closed-Loop Control Using In-Cylinder Pressure Signal," SAE Paper No. 2003-01-3266, 2003.

Zhu, G., Haskara, I., Winkelman, J., "Closed-Loop Ignition Timing Control for SI Engines Using Ionization Current Feedback," IEEE Transactions on Control Systems Technology, Vol. 15, No. 3, 2007.